Integrated Analysis of the Scavenging Process in Marine Two-Stroke Diesel Engines

PhD Thesis

$$(EIv'')'' = q - \rho A \ddot{v}$$

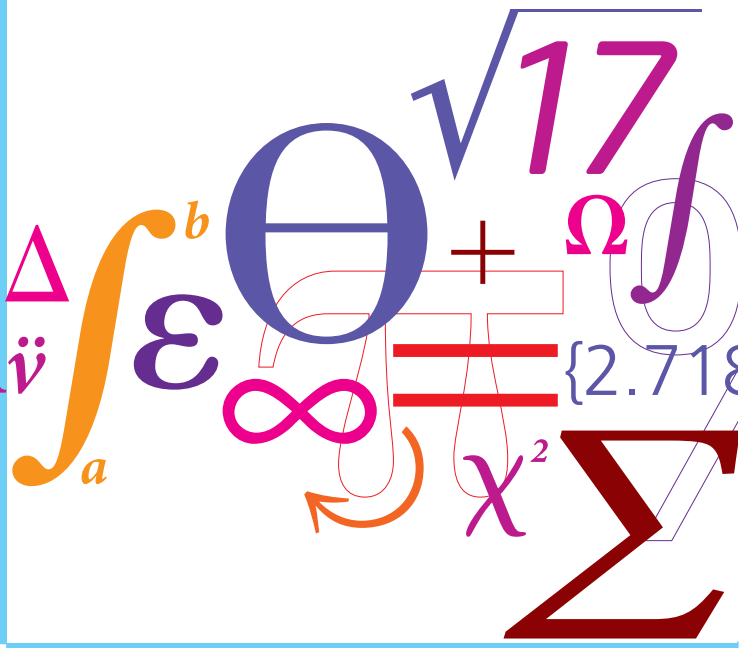

Fredrik Herland Andersen
DCAMM Special Report No. S191
August 2015

DTU Mechanical Engineering
Department of Mechanical Engineering

Integrated Analysis of the Scavenging Process in Marine Two-stroke Diesel Engines

Fredrik Herland Andersen

Ph.D. thesis

Kongens Lyngby, August-2015

Integrated Analysis of the Scavenging Process in Marine Two-stroke Diesel Engines

Fredrik Herland Andersen

A dissertation submitted in partial fulfilment of the degree of Doctor of Philosophy (Ph.D.)

Supervisors:
Jens Honoré Walther, Technical University of Denmark
Stefan Mayer, MAN Diesel & Turbo
Simon Matlok, MAN Diesel & Turbo

ISBN 978-87-7475-433-6

DCAMM Special Report no. S191

Pages: 176

This thesis is typeset using LaTeX

August, 2015

Technical University of Denmark
Section of Fluid Mechanics, Coastal and Martime Engineering
Niels Koppels Allé, building 403,
2800 Kongens Lyngby, Denmark
Phone +45 4525 2525
info@mek.dtu.dk
www.mek.dtu.dk

Abstract

Large commercial ships such as container vessels and bulk carriers are propelled by low-speed, uniflow scavenged two-stroke diesel engines. An integral in-cylinder process in this type of engine is the scavenging process, where the burned gases from the combustion process are evacuated through the exhaust valve and replaced with fresh air for the subsequent compression stroke. The scavenging air enters the cylinder via inlet ports which are uncovered by the piston at bottom dead center (BDC). The exhaust gases are then displaced by the fresh air entering the cylinder. The scavenging ports are cut with an angle to introduce a swirling component to the flow. The in-cylinder swirl is beneficial for air-fuel mixture, cooling of the cylinder liner and minimizing recirculation zones where pockets of exhaust gas are trapped. However, a known characteristic of swirling flows is an adverse pressure gradient in the center of the flow, which might lead to a local deficit in axial velocity and the formation of central recirculation zones, known as vortex breakdown.

Ever more stringent emission legislations over the last 10-15 years have changed the engine lay out diagram in the pursuit of an engine which is both fuel effective and within the current emission legislations. To achieve this goal, a fundamental understanding of the in-cylinder processes, and the interactions between them are needed. This thesis aims at providing in-depth knowledge of the scavenging process and to identify the parameters that governs its performance.

This thesis will present a CFD model that is tested and validated with quantitative data obtained from a dedicated test engine and during engine commissioning on location at the shipbuilder. The CFD model comprises the full geometry of a single cylinder from scavenge receiver to the exhaust receiver for a two-stroke diesel engine. Time resolved boundary conditions corresponding to measurements obtained from an operating engine as well as realistic initial conditions are used in the simulations. The CFD model provides a detailed description of the in-cylinder flow from exhaust valve opening (EVO) to exhaust valve closing (EVC).

A string of studies are included in this thesis. An engine load sweep is included to evaluate the scavenging process as function of engine load. The engine load sweep follows the propeller curve, where the engine speed varies with the engine load. This implies that the pressure in the scavenge and exhaust receivers increase while the scavenge port exposure time, t_{scav}, decrease. Further the scavenging pressure is varied while the engine speed is kept constant. From the perspective of the scavenging process this will resemble a load sweep following a generator curve. The scavenge port angle is varied to investigate the influence of in-cylinder swirl. A total of 7 port angles is applied; $\alpha = 0°$, $\alpha = 10°$, $\alpha = 15°$,$\alpha = 18°$, $\alpha = 20°$, $\alpha = 25°$ and $\alpha = 30°$.

The CFD analysis shows that the bulk purity of air in the cylinder is proportional to the volumetric flow rate (mass flow rate divided by the air density) of scavenge air through the cylinder. The volumetric flow rate decreases with density for a given mass flow rate. When the engine load is increased, both the mass flow rate and the scavenging pressure is increased due to the turbocharger response. It is shown in this thesis that the increased density of the scavenge air, in conjunction with the reduced port exposure time, actually decrease the volume flow rate of air in the cylinders. This impairs the scavenging process at high engine loads. The CFD model also shows that the scavenging process consist of two sub processes. The volumetric scavenging, where the scavenge air displace the exhaust gas. And the push out process, where the piston displace the scavenge air and exhaust gas mixture between inlet port closing, IPC, and exhaust valve closing, EVC. The port angle study shows that the scavenging process is unaffected by the changes in the in-cylinder swirl. Visualization of a passive scalar shows some influence of the in-cylinder distribution of scavenge air and exhaust gas, but volumetric displacement is the prime mover in the scavenging process.

The CFD simulations is in good agreement with a simple perfect displacement model proposed by Sher (1990). The perfect displacement model is used as the basis for a simplified scavenging model in conjunction with a model to predict the contribution from the push out process. The model is modified to fit the CFD results to account for mixing between the scavenge air and the exhaust gas and can therefore only be considered as a preliminary model. However, this model shows that it is possible to obtain a simple model which can be used to ensure adequate scavenging based on turbocharger characteristics and exhaust valve lift profiles.

The CFD model described in this Ph.D. thesis is used to investigate the response of key parameters on the scavenging process and gives detailed and profound insight to an integral in-cylinder process in the two-stroke diesel engine cycle. Further, the results from the CFD model is a valuable part of the R&D strategy of "full cycle CFD modelling" where the scavenging CFD model shall be coupled together with a combustion CFD model to simulate the complete engine cycle.

Resumé

Store kommercielle skibe så som containerskibe og tankskibe fremdrives af langsomtgående, længdeskyllede, to-takts diesel motorer. En afgørende cylinderproces for denne type motor er skylleprocessen, hvor de brændte gasser fra forbrændingsprocessen evakueres gennem udstødningsventilen og erstattes af skyllelufte n der entrer cylinder via indløbsporte der afdækkes af stemplet ved bund død punkt (BDC). Udstødningsgassen bliver fortrængt af den friske luft der strømmer ind i cylinderen. Skylleportene er vinklet for at introducere en roterende strømning. Den roterende strømning er fordelagtig for opblandingen mellem brændstof og luft, køling af cylinderforingen og for at minimere recirkulerende strømningsstrukturer hvor lommer af brændte gasser bliver fanget. En kendt egenskab ved roterende strømninger er potentialet for en modsatrettet trykgradient i centrum af strømningen. Denne trykgradient kan føre til et lokalt fald i den aksiale hastighed og danne en centralt placeret recirkulations zone, også kendt som en vortex breakdown.

Stadigt strengere emissionskrav de sidste 10-15 år har ændret motorudlægningerne i jagten efter stadig mere brændstoføkonomiske motorer der lever op til emissionskraverne. For at nå dette mål er det afgørende at oparbejde en fundamental forståelse for processerne der finder sted. Denne afhandling har som mål at give en dybtgående forståelse af skylleprocessen, samt at identificere nogle af de parametre der påvirker den.

Der vil i denne afhandling blive præsenteret en CFD model der er blevet testet og valideret med data fra dedikerede motor tests. Den modellerde geometri inkluderer den fulde motor fra skylleluftreceiveren til udstødningsgasreceiveren for en enkelt cylinder. Tidsopløste randbetingelser, svarende til måleresultater fra en motor i service samt realistiske initialbetingelser er blevet brugt i simuleringerne. CFD modellen giver en detaljeret beskrivelse af strømningen i cylinderen fra udstødningsventilens åbning (EVO) til udstødningsventilens lukning (EVC).

Forskellige motor driftsforhold er inkluderet i denne afhandling. Indflydelsen

af motorens last er blevet undersøgt for at vurdere hvordan skylle processen blev påvirket af denne. Motorlastkurven fulgte propellerkurven hvor både motorens omdrejningstal og MEP (mean effecitve pressure) følger lasten. Endvidere blev indflydelsen af skylletrykket undersøgt for konstant omdrejningstal. Skylleportvinkelen blev også varieret for at undersøge indflydelsen af graden af rotation i strømning. I alt 7 skylleports vinkelkombinationer blev undersøgt ; $\alpha = 0°$, $\alpha = 10°$, $\alpha = 15°$,$\alpha = 18°$, $\alpha = 20°$, $\alpha = 25°$ and $\alpha = 30°$.

Resultaterne fra den numeriske analyse har vist en stærk korrelation mellem volumenstrømmen og renhedsgraden af luften i cylinderen. Ved stigende motorlast, stiger skylletrykket og følgelig skylleluftens densitet. Massestrømmen fra turboladerens kompressor vil, grundet et højere ladningstryk, også øges, men skylleluftens øgede densitet vil, trods dette, reducere volumenstrømmen igennem motoren. CFD modellen har også vist at skylleprocessen kan opdeles i to separate processer. Den første er en volumetrisk skylnings process, hvor de brændte gasser fortrænges af skylleluften og den anden er "push out" processen hvor cylinderens indhold vil fortrænges af stemplets bevægelse fra skylleportlukning (IPC) og til udstødningsventillukning (EVC). Studiet hvor skylleporternes vinkel er varieret viste, at skylleprocessen ikke blev forringet af variationer af rotationsstyrken i cylinderen. Hvilket bla kan ses ved en visualisering af en passiv skalær der viste tydelig forskel på strømningen i cylinderen. For at opnå en god skylning er det den volumetriske fortrængning der er afgørende for skylleprocesses.

Et første bud på en simplificeret algebraisk skyllemodel bliver foreslået i afhandlingen. CFD modellen kræver lange simuleringstider og det er ønskelig at udnytte den viden man har fået fra CFD modellen til at lave en simplificeret model. Denne model kan implementeres i udviklingsprocessen af fremtidige motordesign og udlægningsstrategier.

CFD modellen er blevet valideret og brugt til at belyse skylleprocessen under forskellige betingelser. Dette har givet en god forståelse for de processer der optræder i cylinderen og er verdifuld til videre udvikling af motoren. Endvidere er det en del af MAN Diesel & Tubro's udviklingsstrategi at bedrive "full cycle CFD", dvs simulere hele motor syklusen ved hjælp af CFD. Skyllemodellen presenteret i denne afhandling kan bruges til at generere randbetingelser for en forbrændings CFD model og dermed bidrage til at lave "full cycle CFD".

Preface

This dissertation is submitted as partial fulfilment of the requirements for the degree of Doctor of Philosophy (Ph.D.). The dissertation is based on research carried out between September 2011 and August 2015, with a 12 months sabbatical leave from December 1'st 2013 to November 30'th 2014. The project is part of the Industrial Ph.D. programme and is carried out in cooperation between the department of Mechanical Engineering at the Technical University of Denmark and the Danish branch of MAN Diesel & Turbo SE. The project is funded partly by MAN Diesel & Turbo and the Danish Ministry of Science, Technology and Innovation with project number 11-109504. The project was carried out under the supervision of the head of the Engine Rrocess Research group at MAN Diesel & Turbo, Stefan Mayer, Ph.D. and Professor MSO Jens Honoré Walther at the section for Fluid Dynamics, Coastal and Maritime Engineering.

An external stay was conducted at the Internal Combustion Engine Group at Dipartimento di Energia, Politecnico di Milano from September to December 2012. The external research stay was under the supervision of Associate Professor Federico Piscaglia and Associate Professor Tommaso Lucchini.

Conference papers

During the project, three conference papers have been published. The papers can be found in appendix A.

Paper I Andersen FH, Hult J, Nogenmyr K-J, Mayer S. Numerical Investigation of the Scavenging Process in Marine Two-Stroke Diesel Engines. In Technical papers presented at the SAE/KSAE 2013 International Powertrains, Fuels & Lubricants Meeting. Society of Automotive Engineers, Incorporated. 2013. (S A E Technical Papers; No. 2013-01-2647). Available from: 10.4271/2013-01-2647

Paper II Andersen FH, Hult J, Nogenmyr K-J, Mayer S. CFD analysis of the scavenging process in marine two-stroke diesel engines. In Proceedings of the ASME 2014 Internal Combustion Engine Division Fall Technical Conference (ICEF 2014). American Society of Mechanical Engineers. 2014. ICEF2014-5438.

Paper III Andersen FH, Mayer S. Parametric Study of the scavenging process in marine two-stroke diesel engines. In Proceedings of the ASME 2015 Internal Combustion Engine Division Fall Technical Conference (ICEF 2015). American Society of Mechanical Engineers. 2015. ICEF2015-1075.

Authorship declarations

Paper I Fredrik Herland Andersen has performed the majority of all work related to the paper, including evaluating the initial and boundary conditions, running the simulation, post-processing the results and writing the paper. Johan Hult provided the PIV data and Karl-Johan Nogenmyr supervised the work in collaboration with Stefan Mayer. Fredrik Herland Andersen presented the paper at the SAE Powertrains, Fuels and Lubricants meeting in October 2013.

Paper II Fredrik Herland Andersen has performed the majority of all work related to the paper, including evaluating the initial and boundary conditions, running the simulation, post-processing the results and writing the paper. Johan Hult provided the PIV data and Karl-Johan Nogenmyr supervised the work in collaboration with Stefan Mayer. Fredrik Herland Andersen presented the paper at the ICEF2014 ASME conference in October 2014.

Paper III Fredrik Herland Andersen has performed the majority of all work related to the paper. Generating mesh, evaluating boundary conditions, running the simulations and post-processing the results. Stefan Mayer supervised the work. Fredrik Herland Andersen will present the paper at the ICEF2015 ASME conference in November 2015.

Acknowledgements

I want to thank my supervisors Stefan Mayer, Ph.D. and Professor MSO Jens Honoré Walther for their excellent guidance and support throughout the project. I would like to thank all my colleagues in the Engine Process Research group (LFD1) for interesting discussions and helpful input to my project. I will like to extend a special thanks to Karl-Johan Nogenmyr which was extremely helpful in the first stages of the project where he assisted in developing the CFD model and provided technical guidance. I will also like to thank my colleague Eric Baudoin, Johan Hult, Jens Dahl Kunoy, Henrik Christensen and Mark Hoffmann for proof reading my thesis. Further I wish to thank my colleagues at DTU, Kristian Mark Ingvorsen and Casper Schytte Hemmingsen for our technical discussions and exchange of ideas. Further I owe my family endless gratitude for always believing in me and supporting me. I would not have made it this far without their support. At last I wish to thank my girlfriend for supporting me and for bringing love and happiness to my life.

Kgs. Lyngby, August-2015

Fredrik Herland Andersen

Contents

Chapter 1

Introduction and background

In the 1850's, the advent of large scale production of petroleum spawned a series of inventions and patents which today is known as the internal combustion engine. The spark-ignition (SI) engine was invented by Nikolaus Otto in 1876, while in 1892 the compression-ignition (CI) engine was invented by Rudolf Diesel (Heywood, 1988). The first automobile, the horse less carriage, propelled by a small SI engine was invented by Karl Benz in 1885. The first two-stroke engine was patented in England by Sir Dougal Clerk in 1881 (Blair, 1996).

History from the second half of the 19'th century and throughout the 20'th century is littered with technological achievements such as the above, which in turn paved the way for increasing globalization of the world economy. The internal combustion engine eventually replaced the steam engine to become the preferred engine type for transport, power production and various industrial applications.

Today it is approximated that 90% of world trade is transported by shipping at sea and that shipping of cargo at sea is responsible for 2-4% of the world annual fuel consumption (Corbett, 2004). The majority of these ships are container ships or bulk carriers which are propelled by low speed marine two-stroke diesel engines as this engine type offers the best compromise between operational cost, power output, reliability and size of the total propulsion system.

In addition to competition with respect to power output and specific fuel oil consumption (SFOC), ever more stringent emission legislations is forcing the industry to invest heavily into R&D to develop the technology needed to meet

the emission requirements within the given time line. In 1973 the International Maritime Organisation (IMO) adopted the "International Convention for the Prevention of Pollution from Ships" now known as MARPOL. The latest update was in 1997 which include Annex VI: "Regulations for the Prevention of Air Pollution from Ships" (International Maritime Organization, 2009). The MARPOL Annex VI describe limitation to the emission of nitrogen oxide (NOx) and sulphur oxide (SOx). The reduction takes place in three stages: Tier I (2000), Tier II (2011) and Tier III (2016).

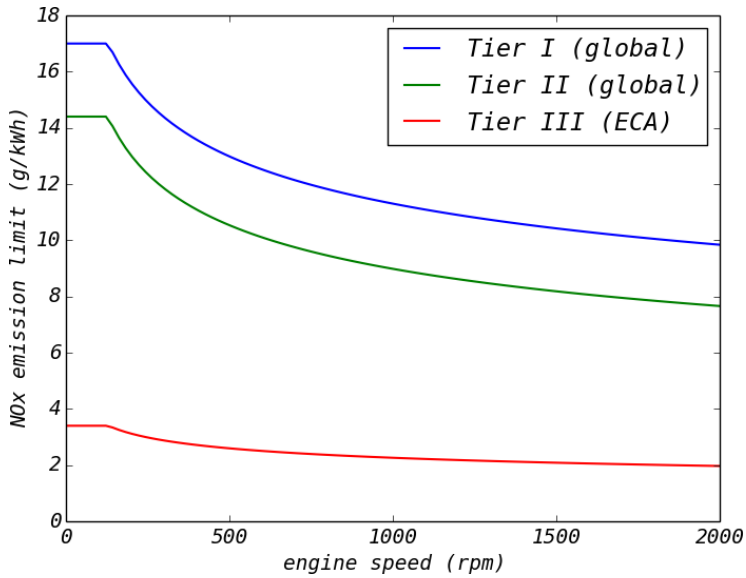

Figure 1.1: Max NOx emission limits for new ships complying with Tier I, II and III, IMO

The NOx emission limits are shown in figure 1.1. The regulation of Tier I and Tier II went into effect January 1st 2000 and 2011 respectively and applies to all ships commissioned on or after those dates. The NOx reduction from Tier I to Tier II is approximately 20%. Tier III is planned to take effect January 1st 2016 and require a NOx reduction of 80% for all ships operating within Emission Control Areas (ECA). Outside of the Emission Controlled Areas Tier II emission regulations apply.

Complying with NOx emission legislations and adjusting to demands from the market have affected the layout and operating conditions for the MAN B&W two-stroke engines. The introduction of the **ME** engine in 2003 allowed for electronically controlled fuel injection and exhaust valve timing. This freedom allows development engineers to optimise the combustion process to produce the highest possible fuel economy within the MARPOL regulations. Electron-

ically controlled, hydraulically actuated exhaust valve and fuel supply system provide a higher degree of control of the combustion process as the compression pressure and fuel injection rates can be optimized. This development has led to a change in engine and turbocharger layout where the pressure in the scavenge receiver is increased. This allow late closing of the exhaust valve (two-stroke Miller timing). Furthermore, increased focus on part load optimization and slow steaming, influences the gas exchange process in the cylinder.

Traditionally, the engine design and lay out have not influenced the scavenging efficiency as the air amount delivered by the turbo charger have usually been sufficient to adequately flush the cylinder clean with scavenge air. Experiences in the industry the later years indicate that the engine design and lay out is no longer guaranteeing an adequate air flow to successfully scavenge the cylinder. Sub optimal scavenging is characterized by high thermal loads on the exhaust valve, as it is not sufficiently exposed to cool scavenge air. For this reason there has been an increased focus on the scavenging process in the later years. Further the introduction of waste heat recovery (WHR) systems affect the scavenging process as the energy extracted to the WHR system comes from the same source as the energy which drives the turbine side of the turbo charger. This implies that an optimized scavenging process is important for the overall engine efficiency.

Two-stroke engines are used in both ends of the engine size spectrum. The smallest engines, such as the ones found in garden utilities, usually operate by the two-stroke engine cycle. The mid-range engine size found in automotive, transport, marine and light power plant applications are usually operated by the four-stroke engine cycle. However, the largest engines in the world today are operated according to the two-stroke engine cycle. The low-speed, two-stroke, marine engine is regarded as the most efficient engine type in the world today and is used primarily as the main engine in container vessels, tankers and bulk carriers. The ship design is optimized in terms of cargo space, where it is desired to have a small engine room. Marine two-stroke diesel engines have direct drive, where the crank shaft is directly coupled with the drive shaft which drives the propeller. This means that the engine speed matches the rotational speed of the propeller and a large transmission box can be omitted. The rotational speed of the propeller is limited by cavitation at high tip speed. The maximum tip speed for a given propeller is adjusted with the stroke of the engine. A large stroke yields a low engine speed, which is why marine two-stroke diesel engines have very high stroke to bore ratios (4-5). The two-stroke engine also have a high power density as each cylinder has a power stroke per revolution. Figure 1.2 show a cross section and a side view of a large bore uniflow scavenged marine two-stroke diesel engine.

The economic recession following 2008 led to a decline in world trade which in turn influenced the marked for container vessels. In the "boom years" up to the recession "short stroke" engines with high engine speed were in high demand as it was beneficial at the time to sail fast to maximize capacity. In the years

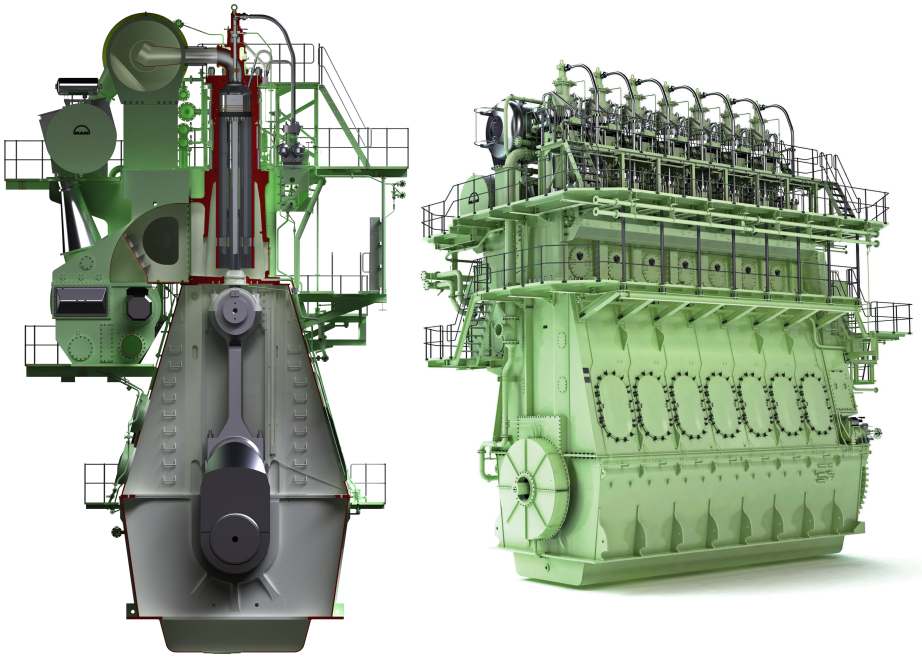

Figure 1.2: Cross section and side view of a MAN B&W G90ME-C (ultra long stroke) uniflow scavenged engine. (MAN Diesel & Turbo, 2015)

following the recession the trend shifted and "slow steaming" become popular (MAN Diesel & Turbo, 2015). The G-type engine was developed to meet this demand. The G70ME engine has a stroke of 3.256 meters and engine speed in the range of $46 - 73\,rpm$ which in conjunction with a large propeller diameter saves up to 7% fuel (Ingenioren, 02.05.2014).

1.1 Working principles of two-stroke diesel engines

The two-stroke engine is today used in a wide range of applications from the small scale engines such as those found in model air planes, garden utilities, mopeds and up to large bore marine diesel engines. Its high power to weight ratio, due to a combustion process for every engine cycle and the simple design makes the two-stroke engine the designers choice when simplicity and reliability are important factors.

The absence of separate induction and exhaust strokes in the two-stroke engine is the main difference from the four-stroke engine. The in-cylinder gas exchange in two-stroke engines is called the scavenging process where the induc-

tion and exhaust process happens simultaneously. Consequently, the scavenging process in two-stroke engines is one of the most important factors influencing the efficiency and performance of two-stroke engines. The scavenging process and the most common scavenging arrangements will be discussed in greater detail in section 1.2. First a short description of the two-stroke engine cycle is given.

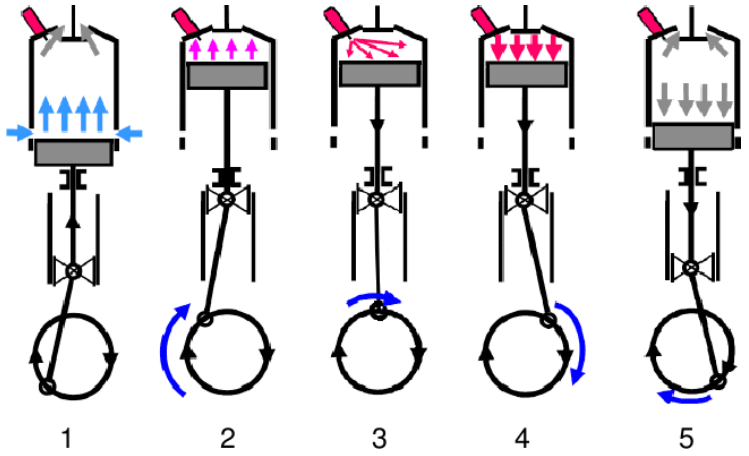

Figure 1.3: Uniflow scavenged two-stroke diesel engine cycle (MAN Diesel & Turbo, 2015)

As mentioned above, the two-stroke engine cycle differs from the four-stroke cycle as it does not have separate intake and exhaust strokes. This arrangement enables one combustion process per cylinder per crankshaft revolution compared to one combustion process every second revolution for the four-stroke engine. Figure 1.3 shows 5 processes that occur during one engine cycle.

1. The piston is located near bottom dead center (BDC). Inlet ports (scavenge ports) are milled into the cylinder liner in the bottom. When the scavenge ports are uncovered, the pressurized scavenge air enters the cylinder indicated by the blue arrows in the figure. The cylinder is filled with exhaust gas from the previous combustion process. The scavenge port opens and compressed scavenge air will displace the exhaust out through the exhaust valve and occupy the cylinder. This is known as the scavenging process. A more elaborate description can be found in section 1.2.

2. The second image in figure 1.3 shows the compression stroke where both the scavenge ports and the exhaust valve is closed. The piston displacement compresses the cylinder content which yields a high in-cylinder pressure and temperature.

3. The diesel fuel is injected into the combustion chamber when the piston approaches TDC. In MAN Diesel & Turbo's two-stroke diesel engines,

the fuel is injected through two, and sometimes three, atomizers located along the engine cover azimuthal. The fuel is is then injected in the same direction as the in-cylinder swirl which is believed beneficial for the mixing of fuel and air.

4. The combustion of fuel increases the pressure and temperature of the cylinder content. The piston is forced down to expand the cylinder volume. This is the working stroke where the force acting on the piston is converted to mechanical work by rotating the crank shaft.

5. Before the scavenge ports are uncovered close to BDC the exhaust valve is opened to adjust the in-cylinder pressure with the pressure of the scavenge air. This is essential for the scavenging process to prevent back flow from the cylinder to the scavenge box. The flow trough the cylinder is driven by a pressure difference between the scavenge receiver and the exhaust receiver, figure 1.5. If the in-cylinder pressure at scavenge port opening (IPO) is higher than the pressure in the scavenge receiver, hot exhaust gases from the cylinder will enter the scavenge box and prevent the scavenge air from entering the cylinder.

1.2 Scavenging process in two-stroke engines

The scavenging process in two-stroke diesel engines is responsible for clearing the cylinder from the exhaust gas from the previous combustion process and replacing it with fresh air for the subsequent compression stroke and combustion. This is done by increasing the inlet pressure by either a blower or a turbo charger (Heywood, 1988). The piston uncovers the intake port and the pressure difference between the intake and exhaust manifolds, the scavenging gradient, will displace the exhaust gases in the cylinder. A two-stroke engine can either have ports connecting the cylinder to the intake and exhaust manifolds or the exhaust port can be replaced with one or several poppet valves (Heywood, 1988). Three configurations for the scavenge process is shown in figure 1.4.

Figure 1.4a and figure 1.4b show cross and loop scavenging respectively. Both configurations use inlet and exhaust ports, milled into the cylinder liner, which are uncovered when the piston approach BDC. The difference between cross and loop scavenging is the orientation of the ports. A cross scavenged engine has the inlet and exhaust port on opposite sides. When the induction port is uncovered the fresh air flows across the cylinder, displacing the exhaust gas. To avoid short circuiting, i.e. fresh air travelling across the cylinder leaving pockets of exhaust gases untouched, a deflector is mounted on the piston crown. The deflector alters the direction of the introduced air as show in figure 1.4a. Cross scavenging is the least efficient of the scavenging configurations (Heywood, 1988).

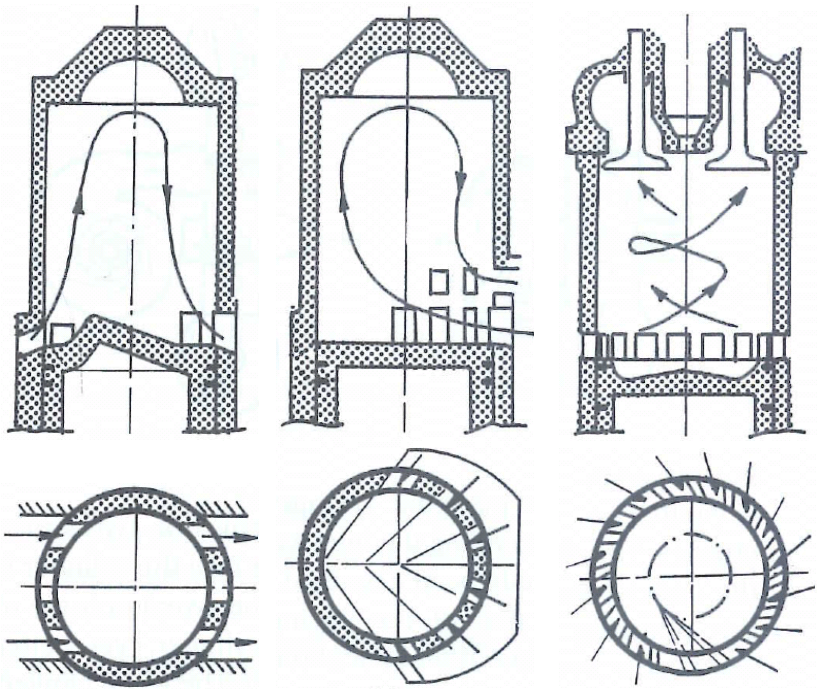

(a) cross scavenging **(b)** loop scavenging **(c)** uniflow scavenging

Figure 1.4: Scavenging systems (Stone, 1999)

Figure 1.4b shows loop scavenging port configuration. Loop scavenged engines also have ports for both inlet air and exhaust gas, but the configuration is different from cross scavenging. Inlet and exhaust ports are milled into the cylinder on the same side. This configuration forces the airflow to change direction inside the cylinder which will prevent short-circuiting of the fresh air in the cylinder. The deflector can be omitted which reduces the heat load on the piston compared to a cross scavenged engine. Cross and loop scavenging are normally found in small engines such as in garden utilities, mopeds and small motorcycles. As mentioned earlier, the scavenging process in two-stroke engines must be driven by an external force. Cross and loop scavenged engines normally use the underside of the piston and the crankcase as a pump to compress the inlet air. When the piston moves upwards in the compression stroke, air enters the crankcase through a non-return valve. During the working stroke the piston compress the air in the crank shaft generating a positive pressure difference between the inlet air and the pressure in the exhaust manifold (Blair, 1996).

Figure 1.4c shows the uniflow scavenging configuration. The uniflow scavenging configuration employs inlet ports milled into the cylinder liner at bottom

dead center and one or several exhaust ports located in the cylinder cover. This configuration concentrates the airflow through the cylinder uniformly in the axial direction. The ports are angled with respect to the local radius in order to create a confined swirling flow in the cylinder. The uniflow scavenging arrangement is the most effective of the three principles presented in this section. The inlet port and exhaust valve configuration render short circuiting nearly impossible as they are located in opposite ends of the cylinder. The exhaust poppet valve increases the complexity of the engine, but offers flexibility and performance optimization. Large marine two-stroke diesel engines are build according to the uniflow scavenging configuration. A large stroke to bore ratio, up to 4-5, make the uniflow scavenging configuration the most obvious choice for marine diesel engines as cross and loop scavenging will short circuit when the stroke is long. High scavenging efficiency at moderate delivery ratios and the possibility to optimize engine performance with exhaust valve timing makes the uniflow scavenging principle well suited for large marine diesel engines. The uniflow scavenging principle was introduced in MAN B&W engines in 1927 (Soerensen, 2008).

1.3 Air flow in uniflow scavenged two-stroke diesel engines

The air flow is integral to engine performance in uniflow scavenged marine diesel engines. The scavenging process is responsible for replacing the exhaust gas with fresh air as mentioned earlier. This implies that the scavenging process is responsible for setting the initial conditions for the combustion process. In this light, it is clear that the scavenging process indirectly affects engine performance, specific fuel oil consumption and emission of hazardous gases.

The air flow through a MAN B&W engine is shown in figure 1.5. Ambient air enters the compressor side of the turbo charger where it is pressurized. The air then travels through a diffuser into the cooler unit where the air is cooled down to a pick point temperature. The air is dehumidified by the water-mist catcher before entering the scavenge receiver. The scavenge receiver is a large volume designed to damp out pressure fluctuations created by the cylinder firing order and to produce a stable scavenge pressure.

After the combustion process follows the working stroke where the high in-cylinder pressure forces the piston down towards BDC. Approximately 120-130 crank angle degrees after top dead center (CADATDC) the exhaust valve opens to equalize the in-cylinder pressure with the scavenge receiver pressure, this process is called the blow-down process. The optimal initial conditions for scavenging are fulfilled if the cylinder pressure and scavenge pressure are equal at inlet port opening (IPO). Then no blow-back will occur and the fresh air from the scavenge receiver will enter the cylinder immediately after IPO. The blow-back gas contains lubrication oil and will over time lead to fouling in the

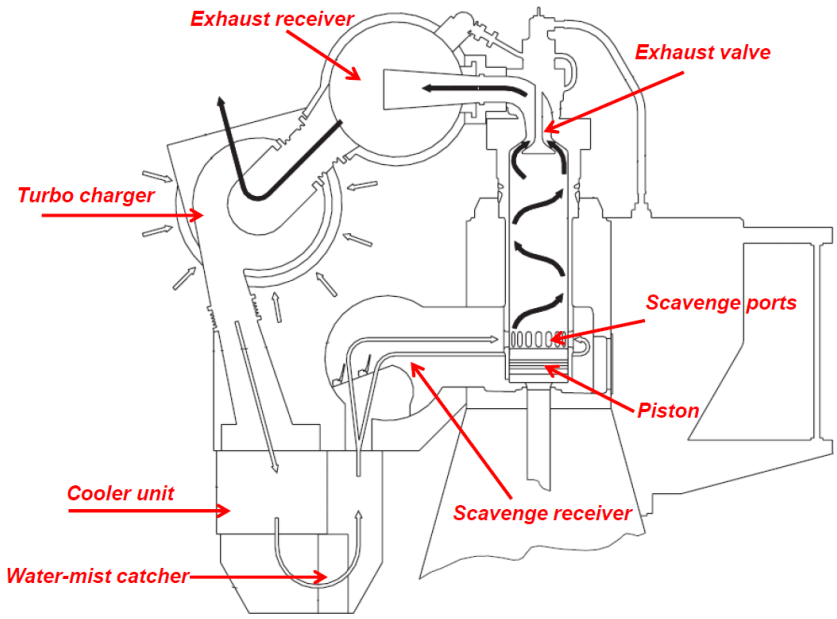

Figure 1.5: Air flow through a MAN B&W engine (MAN Diesel & Turbo, 2015)

scavenge receiver. This can reduce the service interval for the engine. However, due to fuel optimization, some blow back is accepted to maximize the force acting on the piston. The ME control system is set to allow approximately 1% of the cylinder mass to blow back into the scavenge box.

When the ports are uncovered the scavenge air inters the cylinder. The ports are angled with respect to the local radius to introduce a tangential velocity component to the flow. The air then moves up the cylinder in a swirling, helical, motion. The in-cylinder swirl is beneficial for the mixture of air and fuel as the fuel is injected into the combustion chamber in the same direction as the swirl. The in-cylinder swirl also minimizes the recirculation zones at the sharp top and side corner of the scavenging ports where the flow separates due to the sharp edges. The swirl also reduce the effect of the asymmetric inlet to the cylinder. The scavenge receiver is located to one side of the cylinder which will bias the velocity distribution in the cylinder to one side. The swirl is expected to redistribute the velocity field more evenly across the cylinder cross section due to the angular momentum.

There are also some drawbacks involved with confined swirling flow. A known characteristic of swirling flow is vortex breakdown (Lucca-Negro and O'Doherty, 2001). Even at low swirl levels, radial pressure gradients are present at any axial position due to centrifugal effects. At low swirl levels, these gra-

dients do not give rise to more than a slight axial pressure gradient which is not strong enough to cause axial recirculation. When increasing the swirl, these adverse pressure gradients increase causing a central recirculation zone. This phenomenon affects the mixing of exhaust gases and fresh air during the scavenging process as exhaust gases are being trapped in the center of the cylinder. Ideal scavenging is performed by pure displacement where the scavenge air simply replaces the exhaust gas without any mixing. Mixing of exhaust gas and scavenge air increase the air amount needed to fully flush the cylinder as the mixture must also be evicted from the cylinder. The scavenging process is also responsible for cooling the cylinder liner, engine cover and especially the exhaust valve. The scavenge air moves in a helical motion through the cylinder before exiting through the exhaust valve as shown in figure 1.5. The exhaust gas and scavenge air mixture enters the exhaust receiver which is a large volume designed to damp out pressure oscillations and provide a stable boost pressure for the turbine side of the turbocharger.

1.4 Two-stroke, uniflow scavenged, engine cycle

The working principles of the two-stroke diesel engine was presented in section 1.1. This section will act as a supplement, focusing specifically on the uniflow scavenging principle.

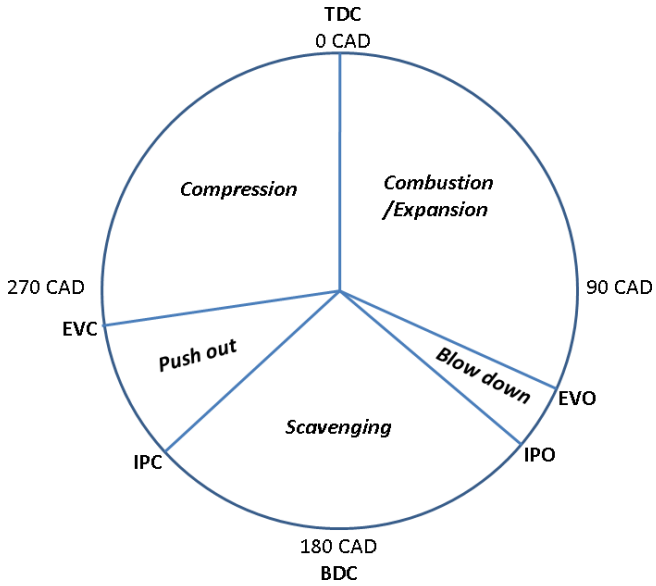

Figure 1.6: Two-stroke, uniflow scavenged, engine cycle

Figure 1.6 shows a schematic diagram of the main processes that takes place

during one engine cycle. The engine cycle can be divided into 2 phases consisting of 5 processes.

1. **Closed volume phase**
   (a) Compression
   (b) Combustion and expansion
2. **Open volume phase**
   (a) Blow down
   (b) Scavenging
   (c) Push out

The first phase is the closed volume phase where there is no transfer of mass to or from the cylinder, except for the injected fuel. This phase starts at exhaust valve closing (EVC) and ends at exhaust valve opening (EVO). During this phase the compression, combustion and expansion occur. The second phase starts at EVO and ends at EVC and is called the open volume phase. This part of the engine cycle is characterized by transfer of mass to and from the cylinder. The open volume phase is subdivided into three sub processes: The blow down, volumetric scavenging and push out process. As mentioned in section 1.3 the blow down process is responsible for adjusting the cylinder pressure with the scavenge pressure to control blow back. The scavenging process is responsible for flushing the cylinder for exhaust gas, replacing it with fresh air before the compression stroke. The push out process is used to determine the compression ratio p_{comp}/p_{scav}, the compression pressure and the charge mass in the cylinder. The ME engine control system use the ratio $^{p_{comp}}/_{p_{scav}}$ to determine the timing of EVC.

1.5 Scavenging Parameters

This section will introduce some engine parameters that can be relevant for the analysis of the scavenging process. Computational Fluid Dynamics makes it possible to quantify the amount and composition of the mixture in the cylinder continuously during simulation of the physical process. The CFD model keeps track of the amount of air that enters the cylinder by integrating the flux across the scavenge ports. The CFD code is also able to distinguish between the scavenge air and the exhaust gas, which is used to evaluate the composition of the cylinder content. The most common parameters used to evaluate the scavenging process is the scavenging, charging and trapping efficiency and the delivery ratio (Stone, 1999) and they are defined as follow,

$$\eta_{scav} = \frac{mass\ of\ delivered\ air\ retained}{mass\ of\ trapped\ cylinder\ charge}, \tag{1.1}$$

$$\eta_{charge} = \frac{mass\ of\ delivered\ air\ retained}{reference\ volume \times ambient\ density}, \tag{1.2}$$

$$\eta_{trap} = \frac{mass\ of\ delivered\ air\ retained}{mass\ of\ delivered\ air}, \tag{1.3}$$

$$DR = \frac{mass\ of\ delivered\ air}{reference\ volume \times ambient\ density}, \tag{1.4}$$

where η_{scav} , η_{charge} and η_{trap} are the scavenging, charging and trapping efficiency respectively. The scavenging efficiency is a direct measure of the ratio of fresh air to mixture in the cylinder at EVC. The charging efficiency is a measure of the amount of scavenge air delivered, compared to the theoretical mass needed to fill the cylinder at ambient conditions, which in case of large bore, two-stroke, cross-head engines are the conditions in the scavenge receiver. The reference volume is equal to the swept volume plus the nominal compression volume minus the piston shims,

$$V_{ref} = V_{swept} + V_{nom\,comp} - V_{shims}.$$

The trapping efficiency measures how much air flows directly into the exhaust system, also known as short-circuiting. Trapping efficiency states the amount of air trapped in the cylinder compared to the total amount of air that entered the cylinder. DR is the delivery ratio which is a measure of the total amount of air that is introduced into the cylinder compared with a theoretical reference mass. The delivery ratio is the mass of delivered air divided by the density of the delivered air so it depicts the total volume added to the cylinder compared to a reference volume. The delivery ratio is a generalised quantity as it refers to the swept volume instead of the actual volume that must be flushed. Most marine two-stroke engines built the last 10-15 years are ME engines, which means that the exhaust valve lift operation is electronically controlled and hydraulically operated. The timing of the exhaust valve lift and closing is therefore a tool which can be used for engine performance optimisation. Exhaust valve closing (EVC), figure 1.6, is not a fixed parameter, but changes as function of engine load or engine lay out. Intuitively, ideal scavenging is performed by simply displacing the burned gases in the cylinder without any mixing. In the original DR definition, equation 1.4, the volume required to flush is defined to be equal to the swept volume. It could be appropriate to include the push out phase where cylinder content is pushed out of the cylinder by the piston motion. This means that an alternate formulation for the delivery ratio, based on the actual reference volume which shall be displaced can be formulated like:

$$DR_{corr} = \frac{m_{scav}}{\rho_{scav} \cdot V_{cyl@EVC}}. \tag{1.5}$$

1.6 Simple algebraic model for the scavenging process

Simple models for the scavenging process can be found in the literature. The most common being the perfect displacement model and the perfect mixing model. Both models are described in detail in Stone (1999).

The perfect displacement model serves as an upper bound of the scavenging process, it assumes that no mixing occurs between the exhaust gas and the introduced scavenging air. Further, the model assumes that the process occurs under constant volume and pressure without heat transfer. The two gases are also assumed to have the same density. The introduced scavenge air will act as a piston purely displacing the burned gas. The bulk purity of fresh air in the cylinder is equal to the delivery ratio in the perfect displacement model.

The other model is the perfect mixing model which acts in the opposite manner compared to the perfect displacement model. It assumes that the two gases are instantly homogeneously mixed within the cylinder. The process occurs at constant volume and pressure without any heat transfer from the walls to the gas. The fresh scavenge air and the exhaust gas have equal and constant densities. The reader is referred to Stone (1999) for the complete derivation of the model.

Sher (1990) expanded the perfect displacement model to include the difference in density between the compressed scavenge air and the hot exhaust gases in the cylinder. The model still assumes that the scavenging process occurs at constant volume and pressure and that there is no transfer of heat or mass between the scavenging air and exhaust gas.

The following relation form the basis of the model:

$$\psi = \frac{m_{scav}}{m_{scav} + m_{ex}}, \tag{1.6}$$

where ψ is the purity of air in the cylinder and

$$DR = \frac{m_{scav}}{m_{cyl}}, \tag{1.7}$$

is the delivery ratio. The model assumes constant volume and therefore the cylinder volume can be described as $V_{cyl} = V_{scav} + V_{ex}$. Further $m_{scav} = \rho_{scav} \cdot V_{scav}$, and $m_{ex} = \rho_{ex} \cdot V_{ex}$. For a uniflow scavenged engine the cylinder mass can be described with the density of the scavenge air and the volume of the cylinder $m_{cyl} = \rho_{scav} \cdot V_{cyl}$. From these relations the exhaust mass can be expressed as

$$m_{ex} = \rho_{ex} \left(\frac{m_{cyl}}{\rho_{scav}} - V_{scav} \right). \tag{1.8}$$

Inserting 1.8 into 1.6, gives the following expression for the purity of scavenge air:

$$\psi = \frac{\rho_{scav} V_{scav}}{\rho_{scav} V_{scav} + \rho_{ex} \left(\frac{m_{cyl}}{\rho_{scav}} - V_{scav} \right)}. \tag{1.9}$$

Further rearranging 1.9 gives the final model equation:

$$\psi = \left[1 + \frac{\rho_{ex}}{\rho_{scav}} \left(\frac{1}{DR} - 1 \right) \right]^{-1}, \tag{1.10}$$

where the bulk purity of scavenge air in the cylinder is a function of the delivery ratio and includes the density ratio between the exhaust gas and fresh air.

1.7 Literature survey

This section will present some of the research, relevant to the scavenging process, in marine two-stroke diesel engines available in literature. The literature on research for large marine two-stroke diesel engines are scarce compared to smaller engines due to the size, cost and complexity involved with research on large ship engines. The market for large bore two-stroke diesel engines for marine applications is significantly smaller in turns of units compared to smaller engines for e.g. automotive applications and there are few manufacturers world wide. A consequence of this is that research is often conducted on scaled down models of engines. Only a short overview of research relevant for two-stroke diesel engines will be accounted for in this section, a more comprehensive description can be found in (Heywood and Sher, 1999).

Early studies of the scavenging process, based on visualization, include (Ferro, 1958), (Rizk, 1958) and (Dedeoglu, 1971). More quantitative investigations were performed by Percival (1955) who used various Pitot instruments to measure the pressure at various points in the cylinder and computed the corresponding velocity components. He then varied the inlet port angles to investigate the influence on the in-cylinder, radial, velocity profiles. The influence of the exhaust valve region was investigated by Sung and Patterson (1982), who used a Laser Doppler Anemometer (LDA) device to measure the internal flow fields in a Detroit Diesel 6VB-92. Sher et al. (1991) studied the scavenging process in a scaled down model of a uniflow scavenged engine using a hot-wire anemometry technique to evaluate radial velocity profiles as well as turbulent parameters during steady flow conditions. He further compared this data with predictions from a slightly modified version of the computer program DICE-2. Nakagawa et al. (1990) used Laser Doppler Velocimetry (LDV) to measure velocity profiles in an uniflow scavenged model engine. He investigated both CSS (Controlled Swirl Scavenging) ports and regular ports and used the experimental results as input for a numerical model. The controlled swirl scavenging ports, CSS, has

a varying port geometry which was employed to promote improved scavenging (Woodyard, 2009). A typical CSS port angle varies from 38° angle at IPO to 2° at BDC. The sharp angle in the top of the scavenging ports generated a strong swirl which will discharge the exhaust gas located at the liner wall. The bottom part of the CSS part is directed towards the center of the cylinder and was designed to clear the piston top and the central region of the cylinder. The influence of inlet port angle was investigated by Litke (1999) who used a model engine of $^1/_4$ scale and liquid as the working fluid. He quantified the scavenging efficiency as a function of delivery ratio and concluded that the optimum port angle is in the range of 15-25°. He further investigated different scavenge port geometries. The standard port which has a constant angle and smooth machined edges, the second port also has a constant angle but is not machined after being milled into the liner, the third port configuration corresponds to a CSS port.

Haider (2011) investigated the velocity profiles in a stationary model of the T50ME-X test engine using stereoscopic Partice Image Velocimetry (PIV) and CFD. The model engine did not include a moving piston, but the influence of piston position was investigated at steady flow conditions (Haider et al., 2013). Obeidat et al. (2014) performed CFD analysis of the influence of piston position using a Large Eddy Simulation (LES) turbulence model. The model engine was modified to include a moving piston and a more realistic port geometry by (Ingvorsen, 2013). He analysed in-cylinder velocity profiles at steady state and transient conditions as well as the influence of scavenge port angle using PIV and LDA (Ingvorsen et al., 2014)(Ingvorsen et al., 2013). His work revealed that for 20° the in-cylinder flow is dominated by a concentrated vortex structure with a well defined vortex core that extends the cylinder length and vortex breakdown in the bottom of the cylinder. For the dynamic case central recirculation zones, or vortex breakdown, occurs in the bottom of the cylinder briefly when the piston uncovers the scavenge ports due to peak velocities at IPO.

Al-Mousawi (2012) performed CFD analysis on the transparent model engine using both Reynolds Averaged Navier-Stokes (RANS) and Large Eddy Simulation (LES) turbulence models. Hemmingsen (2014) extended the CFD model to include convective heat transfer from the scavenging air to the liner surface.

Sigurdsson et al. (2014) performed CFD analysis including convective heat transfer on a 12° sector of the T50ME-X test engine located at the Diesel Research Center in Copenhagen. The model included a simplified scavenge box geometry, exhaust duct and moving piston and valve. The CFD model performs multiple cycles including the a heat and momentum source to account for combustion process. The study included conjugate heat transfer on the piston crown.

Some CFD studies in the literature exist where the full geometry is included. Lamas and Vidal (2012) investigated the scavenging process in a MAN B&W 7S50MC engine using ANSYS Fluent. The study included a complete cylinder liner, exhaust valve and exhaust bend, but the scavenge box with the asymmet-

ric inlet was omitted. RANS turbulence model was used and a passive scalar was used to distinguish the exhaust gas from the scavenge air during the gas exchange. The study only include the open volume part of the engine cycle, from EVO to EVC.

1.8 Thesis statement

The research discussed in section 1.7 mostly comprise scaled engine like models or relatively simplified CFD models of a two-stroke, uniflow scavenged diesel engine at operating conditions. However, there is a void in the literature where the models are used to investigate the scavenging process more in depth by changing operating conditions and geometry corresponding to realistic, full scale engines.

This industrial Ph.D. project aims to investigate the scavenging process in marine two-stroke diesel engines, primarily by use of Computational Fluid Dynamics (CFD). A CFD code capable of handling shape and topological changes to the mesh due to the piston and valve motion is used to investigate the gas exchange process in the cylinder during scavenging. The model includes the full 3D geometry of one cylinder from the scavenge receiver to the exhaust receiver. The initial conditions consist of a combination of time resolved and cycle averaged data from test bed, and values calculated on the basis of experimental data. A validation of internal flow fields is done by comparison with in-cylinder velocity measurements (Hult et al., 2014). The validated model is then applied to various operating conditions as well as geometrical changes in the pursuit of an in-depth understanding of which parameters that influence the scavenging process. Both the T50ME-X test engine, located in the Diesel Research center in Copenhagen and a production engine with experimental data obtained at test bed is used in this study to investigate if the scavenging process is sensitive to engine type, lay out and geometry. A engine load sweep is conducted on both the propeller curve and what would correspond to a generator curve as well as a sensitivity study of the in-cylinder flow field where the angle of the scavenge ports are varied. All the results are then analysed and coupled together with simple scavenging models from literature to produce a conclusive understanding of the scavenging process in marine two-stroke diesel engines.

The activities in this project was carried out primarily at the R&D facilities at MAN Diesel & Turbo SE, Low Speed business unit in Copenhagen, Denmark as well as at the section of fluid mechanics, coastal and maritime engineering at the Technical University of Denmark. Some of the results obtained during the project have been published in (Andersen and Mayer, 2015), (Andersen et al., 2014) and (Andersen et al., 2013).

The objective for this Ph.D. project can be summarized as:

1. Develop a CFD model which is capable to predict in-cylinder behaviour during the scavenging process in marine two-stroke diesel engines.
2. Embed the model into the existing MAN Diesel & Turbo R&D research environment and development pipe line.
3. Apply model to strengthen the knowledge of in-cylinder processes and to asses sensitivities to engine lay-out strategies and design changes.
4. Generate knowledge of the initial velocity field, thermodynamic properties and composition of the in-cylinder air/gas mixture for subsequent combustion CFD.
5. Develop a simple model for the scavenging process which can be used to evaluate the engine lay out at an early stage of the engine design process.

Chapter 2

Numerical model

This chapter contains an overview of the governing equations that form the basis of the numerical model applied in this thesis. The code used in this study is an extended version of the open source C++ tool box OpenFOAM® which contains the functionality to solve the Navier-Stokes equations by the Finite Volume Method (FVM). An additional engine wrapper class is developed to handle uniflow scavenged two-stroke engines. The computational domain is subjected to shape and topological changes due to the motion of the piston and the exhaust valve. Furthermore, the scavenge box and the cylinder must be coupled together when the piston uncovers the scavenging ports during scavenging (IPO-IPC).

2.1 Governing equations

The governing equations used by the CFD solver are the compressible Navier-Stokes equations, the continuity equation and the energy equation. All of which can be seen as conservation equations of the given properties. If ϕ is any conserved property (ϕ=1 for mass, ϕ=$\vec{v}$ for momentum, ϕ=h for enthalpy and ϕ=Y for passive scalar), then a conservation equation known as the Reynolds' transport theorem (Ferziger and Perić, 1996) can be applied.

$$\frac{d}{dt}\int_{\Omega\,CM}\rho\phi d\Omega = \frac{d}{dt}\int_{\Omega\,CV}\rho\phi d\Omega + \int_{S\,CV}\rho\phi\vec{u}\cdot\vec{n}dS \tag{2.1}$$

where Ω_{CV} denotes the control volume, Ω_{CM} stands for the volume occupied by the mass and S_{CV} is the surface enclosing the control volume. $\vec{n}$ is the unit

vector orthogonal to S_{CV}, ρ is the fluid density and ϕ is the conserved quantity. By defining conservation of mass as

$$\frac{dm}{dt} = 0 \tag{2.2}$$

and inserting equation 2.2 as the left hand side of equation 2.1, one obtained an integral form of the continuity equation:

$$\frac{d}{dt}\int_{\Omega\,CV} \rho d\Omega + \int_{S\,CV} \rho\vec{u}\cdot\vec{n}dS = 0. \tag{2.3}$$

Equation 2.3 states that the rate of change in the control volume equals the convective flux of the conserved property across the CV boundary. By applying the Gauss divergence theorem to the convective term, the surface integral is converted into a volume integral. The continuity equation can then be written in differential form using index notation as

$$\frac{\partial\rho}{\partial t} + \frac{\partial\rho u_i}{\partial x_i} = 0, \tag{2.4}$$

where $i = [1, 2, 3]$, $x_i = [x, y, z]$ are the Cartesian coordinates and $u_i = [u_x, u_y, u_z]$.

The Navier-Stokes equations govern the conservation of momentum in fluid flow are based on Newton's second law:

$$\frac{dm\vec{u}}{dt} = m\vec{a} = \sum \vec{f}, \tag{2.5}$$

which states that the sum of the forces acting on a control mass equal the mass multiplied with the acceleration. Applying equation 2.5 as the left hand side of equation 2.1 gives a momentum conservation equation in an integral form

$$\frac{\partial}{\partial t}\int_{\Omega\,CV} \rho\vec{u}d\Omega + \int_{S\,CV} \rho\vec{u}\vec{u}\cdot\vec{n}dS = \sum \vec{f}. \tag{2.6}$$

Again the left hand side of equation 2.6 states that the rate of change equals the flux across the CV boundaries. The right hand side equals the sum of forces acting on the CV. The forces can be divided into:

$$\vec{f} = \vec{f}_{surface} + \vec{f}_{body},$$

where the surface forces are forces acting on the CV boundary such as shear stresses and pressure (White, 2006). Body forces act on the entire CV such as gravitation and Couriolis forces. Body forces are neglected in the following derivation of the governing equations as well as in the simulations presented in this thesis. For a Newtonian fluid, the surface forces can be accounted for with a stress tensor. The stress tensor is included in equation 2.6 to form the integral form of the momentum conservation equation

$$\frac{\partial}{\partial t}\int_{\Omega} \rho\vec{u}d\Omega + \int_{S} \rho\vec{u}\vec{u}\cdot\vec{n}dS = \int_{S} T\cdot\vec{n}dS. \tag{2.7}$$

The stress tensor is written with Einstein notation as:

$$T_{i,j} = -\left(p + \frac{2}{3}\mu\frac{\partial u_j}{\partial x_j}\right)\delta_{i,j} + 2\mu D_{i,j}, \tag{2.8}$$

where p is the static pressure, μ is the dynamic viscosity, $\delta_{i,j}$ is the Kronecker delta ($\delta_{i,j}$=1 if i=j and $\delta_{i,j}$=0 if $i \neq j$) and D is the rate of strain tensor (Ferziger and Perić, 1996).

The viscous stress tensor, $\tau_{i,j} = T_{i,j} + p\delta_{i,j}$, written in Einstein notation reads

$$\tau_{ij} = 2\mu D_{i,j} - \frac{2}{3}\mu\frac{\partial u_i}{\partial x_i}\delta_{i,j} \tag{2.9}$$

where $\delta_{i,j}$ is the Kronecker delta ($\delta_{i,j}$=1 if i=j and $\delta_{i,j}$=0 if $i \neq j$), and the rate of strain

$$D_{i,j} = \frac{1}{2}\left(\frac{\partial u_i}{\partial x_j} + \frac{\partial u_j}{\partial x_i}\right). \tag{2.10}$$

After applying Gauss divergence theorem, the conservation of momentum can be written using Einstein notation as

$$\frac{\partial \rho u_i}{\partial t} + \frac{\partial \rho u_i u_j}{\partial x_j} = \frac{\partial \tau_{i,j}}{\partial x_j} - \frac{\partial p}{\partial x_i}. \tag{2.11}$$

The last of the governing equations is the conservation of energy. The energy equation is the first law of thermodynamics applied to a control volume. The law states that energy can be transported to and from a CV, but cannot be created and destroyed. The change in energy in a CV equals the sum of added work or heat

$$dE = dQ + dW \tag{2.12}$$

where Q is the heat added and W is the work done to the system (White, 2006). the left hand side of equation 2.12 can be evaluated for enthalpy instead of internal energy

$$h = e + \frac{p}{\rho}$$

and inserted into the Reynolds transport theorem, equation 2.1

$$\underbrace{\frac{\partial}{\partial t}\int_\Omega \rho h \, d\Omega + \int_S \rho h \vec{u}\cdot\vec{n}\, dS}_{\mathrm{dE}} = \underbrace{\int_S \lambda \nabla T \cdot \vec{n}\, dS}_{\mathrm{dQ}} + \underbrace{\int_\Omega (\vec{u}\nabla p + \tau_{i,j}\nabla\vec{u})\, d\Omega + \frac{\partial}{\partial t}\int_\Omega p\, d\Omega}_{\mathrm{dW}} \tag{2.13}$$

where the heat term is given by Fourier's law $q = \lambda\nabla T$ where λ is the thermal conductivity (Cengel, 2007). Note that T in Fourier's law denotes temperature.

The net work done on the volume is given by the pressure and the viscous stress. Radiative heat transfer is neglected in this study.

Applying Gauss divergence theorem, the energy equation, 2.13, can be written in Einstein notation as

$$\frac{\partial \rho h}{\partial t} + \frac{\partial \rho h u_j}{\partial x_j} = \frac{\partial p}{\partial t} + \frac{\partial p u_j}{\partial x_j} + \tau_{i,j}\frac{\partial u_i}{\partial x_j} + \left(\lambda \frac{\partial^2 T}{\partial x_i^2}\right) \tag{2.14}$$

The three governing equations: the continuity equation 2.4, the momentum equation 2.11 and the energy equation 2.14 form the basis of the CFD model used in this report.

In addition to the governing equations, a transport equation for a passive scalar has been implemented into the top level solver to distinguish between the exhaust gas and the introduced scavenge air in the computational domain. The passive scalar Y is derived using the Reynolds transport theorem, equation 2.1

$$\frac{\partial}{\partial t}\int_\Omega \rho Y d\Omega + \int_S \rho Y \vec{u}\cdot\vec{n} dS = \sum f_Y. \tag{2.15}$$

Equation 2.15 states that the rate of change and the convective transport of the quantity Y equals the sum of other transports such as diffusion. Fick's law of mass diffusion (Ferziger and Perić, 1996) is used for $\sum f_Y$, using the dynamic viscosity as the diffusion flux yields the following expression:

$$\frac{\partial}{\partial t}\int_{\Omega\,CV} \rho Y d\Omega + \int_S \rho Y \vec{u}\cdot\vec{n} dS = \int_{S\,CV} \mu \nabla Y \cdot \vec{n} dS. \tag{2.16}$$

Applying the divergence theorem to equation 2.16 yields the following equation, written in Einstein notation

$$\frac{\partial \rho Y}{\partial t} + \frac{\partial \rho Y u_{i,j}}{\partial x_j} = \frac{\partial}{\partial x_j}\left(\mu \frac{\partial Y}{\partial x_i}\right). \tag{2.17}$$

2.2 Turbulence modelling

The flow in internal combustion engines is highly turbulent which implies that resolving all the energy carrying scales of fluid motion is not fasible, therefore a turbulence model is needed. A turbulence model is used to account for the effects of turbulence which is not resolved by the mesh. The Reynolds number is a non dimensional quantity that relates the ratio of inertial forces to the viscous forces. For high Reynolds numbers the inertial forces due to convection are more dominant.

$$Re = \frac{\rho \cdot U \cdot D}{\mu} \tag{2.18}$$

The Reynolds number is shown in equation 2.18. The Reynolds number for in-cylinder flow during scavenging in a marine two-stroke diesel engine is typically in the order of millions which is well within the turbulent regime. For comparison, experiments have shown that the transition between laminar and turbulent flow in a fully developed pipe flow is in the range of $2300 < Re < 5000$.

Turbulence can be understood as an irregular, chaotic state of fluid motion that occurs when the instabilities present in the initial or the boundary conditions are amplified, and a self-sustained cycle is established where turbulent eddies are created and destroyed (Piomelli, 2012). The turbulent structures are coherent, but random in terms of location and time of occurrence. Turbulence is usually characterised by its properties. Turbulent flows are highly unsteady and three dimensional. Turbulence increases mixing through turbulent diffusion. The increased mixing is due to contact between fluids carrying different momentum. The shear between the fluid structures reduce the velocity gradients and the kinetic energy. The turbulence is dissipative as the large energy carrying structures are reduced and broken up into smaller structures until the energy is irreversibly lost to internal energy (heat) (Ferziger and Perić, 1996).

Due to the wide scales of turbulent structures, it is in most engineering applications not feasible to resolve the smallest spatial and temporal scales of turbulence, but rather use models to account for these scales. The two most common approaches to model turbulence is Large Eddy Simulation (LES) and Reynolds Average Navier-Stoke (RANS) formulation.

2.2.1 RANS turbulence modelling

In Reynolds Averaged Navier-Stokes (RANS) modelling, following the idea of Reynolds (1894), it is assumed that the fluid is in a randomly unsteady turbulent state which can be decomposed into a mean and fluctuating component.

$$\phi = \overline{\phi} + \phi^{'} \tag{2.19}$$

where the overbar represents the average and the prime represents the fluctuating component, time average of the quantity ϕ is given by

$$\overline{\phi}(x_i) = \lim_{T\to\infty} \frac{1}{T} \int_0^T \phi(x_i, t). \tag{2.20}$$

Time averaging for unsteady flows, which are not statistically steady state, is done by ensemble averaging (Wilcox, 1998)

$$\overline{\phi}(x_i, t) = \lim_{N\to\infty} \frac{1}{N} \sum_{n=1}^{N} \phi(x_i, t), \tag{2.21}$$

where N is the number of members to the ensemble. For compressible flow it is convenient to apply a density weighted averaging procedure when establishing the time average equations. This procedure was suggested by Favre (1965). The mass weighted average of the quantity ϕ is then written

$$\widetilde{\phi} = \frac{\overline{\rho\phi}}{\overline{\rho}}, \tag{2.22}$$

and the fluctuation reads

$$\phi'' = \phi - \widetilde{\phi}. \tag{2.23}$$

The governing equations (2.4), (2.11) and (2.14) are averaged according to equations (2.22) and (2.23) to form the Favre Averaged Navier-Stokes equations (FANS).

$$\frac{\partial\overline{\rho}}{\partial t} + \frac{\partial\overline{\rho}\widetilde{u}_i}{\partial x_i} = 0 \tag{2.24}$$

$$\frac{\partial\overline{\rho}\widetilde{u}_i}{\partial t} + \frac{\partial\overline{\rho}\widetilde{u}_i\widetilde{u}_j}{\partial x_j} = \frac{\partial}{\partial x_j}\left[\overline{\tau_{i,j}} - \overline{\rho}\widetilde{u_i''u_j''}\right] - \frac{\partial\overline{p}}{\partial x_i} \tag{2.25}$$

$$\frac{\partial\overline{\rho}\widetilde{h}}{\partial t} + \frac{\partial\overline{\rho}\widetilde{h}\widetilde{u_j}}{x_j} = \frac{\partial}{\partial x_j}\left(\overline{\lambda}\frac{\partial\widetilde{T}}{\partial x_i} - \overline{\rho}\widetilde{u_i''h''}\right) + \frac{\partial\overline{p}}{\partial t} + \widetilde{u_j}\frac{\partial\overline{p}}{x_i} + \overline{\tau_{i,j}}\frac{\partial\widetilde{u_i}}{\partial x_j} \tag{2.26}$$

The averaging procedure introduced some additional terms in equation 2.25 and 2.26 which cannot be represented uniquely in terms of mean quantities. The additional terms $\overline{\rho}\widetilde{u_i''u_j''}$ and $\overline{\rho}\widetilde{u_i''h''}$ are the Reynolds stress, augmenting the viscous stress and the Reynolds heat flux, augmenting the heat flux. Both terms introduce unknowns which require modelling in order to close the set of equations. The turbulence model applied in this report is known as an eddy viscosity model where the Reynolds stress tensor $R_{i,j}$ can be written like

$$R_{i,j} = -\overline{\rho}\widetilde{u_i''u_j''} = 2\mu_t\left(\widetilde{D}_{i,j} - \frac{1}{3}\frac{\partial\widetilde{u}_k}{\partial x_k}\right) - \frac{2}{3}\overline{\rho}k\delta_{i,j} \tag{2.27}$$

where μ_t is the turbulent or eddy viscosity, modelled by the turbulence model and k is the turbulent kinetic energy

$$k = \frac{1}{2}\widetilde{u_i''u_i''}. \tag{2.28}$$

The exact Reynolds heat flux is replaced by a model heat flux

$$Q_i = \overline{\rho}\widetilde{u_i''h''} = -\lambda_t\frac{\partial\widetilde{T}}{\partial x_i}, \tag{2.29}$$

where k_t is the turbulent thermal conductivity. This quantity can be obtained from the turbulent viscosity, μ_t and a turbulent Prantl number, Pr_t which is assumed constant. The turbulent thermal conductivity can be written as

$$\lambda_t = \frac{c_p \mu_t}{Pr_t}, \tag{2.30}$$

further, for a perfect gas with constant c_p, the enthalpy can be expressed by $\widetilde{h} = \overline{c}_p \widetilde{T}$ and a thermal diffusivity as $\alpha_t = \mu_t / Pr_t$. The closure hypothesis for the energy equation is obtained by inserting 2.30 into 2.29 and rearranging

$$Q_i = -\alpha_t \frac{\partial \widetilde{h}}{\partial x_i} \tag{2.31}$$

2.2.1.1 RNG k-ϵ turbulence model

The Renormalized k-ϵ model by Yakhot et al. (1992) is a common turbulence model used for engineering problems. The model is based on the standard k-ϵ model by Jones and Launder (1972). The k-ϵ model belongs to the class of "two-equation" models, in which two model transport equations are solved for two turbulent quantities: turbulent kinetic energy and turbulent dissipation rate ϵ (Pope, 2000). From the turbulent kinetic energy and the dissipation rate, it is possible to express a length scale, $l = k^{\frac{3}{2}}/\epsilon$, a time scale, $t = k/\epsilon$ and a quantity of dimension $\mu_t = f(\frac{k^2}{\epsilon})$. The RNG k-$\epsilon$ uses a Re-Normalization Group to renormalize the governing equations to account for smaller scales of motion. While the standard k-ϵ model evaluates the eddy viscosity on a single length scale, the RNG k-ϵ tries to include the contribution of other scales. The RNG k-ϵ model solves two transport equations. The turbulent kinetic energy,

$$\frac{\partial \overline{\rho} k}{\partial t} + \frac{\partial \overline{\rho} k \widetilde{u_j}}{\partial x_j} = \frac{\partial}{\partial x_j} \left[\left(\mu + \frac{\mu_t}{\sigma_k} \right) \frac{\partial k}{\partial x_j} \right] + P_k - \overline{\rho}\epsilon, \tag{2.32}$$

where the term P_k is the production of turbulent kinetic energy

$$P_k = -\overline{\rho} \widetilde{u_i'' u_j''} \frac{\partial \widetilde{u_i}}{\partial x_j}, \tag{2.33}$$

which includes the Reynolds stress tensor from equation 2.27 and is modelled with the turbulent viscosity, μ_t. $\overline{\rho}\epsilon$ is the destruction of turbulent kinetic energy. σ_k is a model constant, acting as a turbulent Prantl number. The turbulent dissipation rate,

$$\frac{\partial \overline{\rho} \epsilon}{\partial t} + \frac{\partial \overline{\rho} \epsilon \widetilde{u_j}}{\partial x_j} = \frac{\partial}{\partial x_j} \left[\left(\mu + \frac{\mu_t}{\sigma_\epsilon} \right) \frac{\partial \epsilon}{\partial x_j} \right] + C_{1\epsilon} \frac{\epsilon}{k} P_k - C^*_{2\epsilon} \rho \frac{\epsilon^2}{k}, \tag{2.34}$$

where $C^*_{2\epsilon}$ is a modified constant which includes the RNG contribution.

$$C^*_{2\epsilon} = C_{2\epsilon} + \frac{C_\mu \eta^3 \left(1 - \frac{\eta}{\eta_0}\right)}{1 - 1\beta\eta^3} \tag{2.35}$$

where

$$\eta = D\frac{k}{\epsilon} \tag{2.36}$$

and

$$D = \sqrt{2D_{i,j}D_{i,j}} \tag{2.37}$$

is included to account for the interaction between turbulent dissipation and mean shear.

2.3 Modelling engine flow

CFD analysis of the scavenging process in uniflow scavenged engines is not straight forward. The scavenging process is highly transient and include motion of engine components which must be accounted for in the CFD model. A special engine wrapper class is developed in order to accommodate the shape and topological changes to the mesh. This class is an extension of the native two-stroke engine class to include a central poppet valve and 30 individual scavenging ports. Three primitive mesh modifiers are used to facilitate the motion of the piston and exhaust valve.

1. **Sliding interface**
   Connecting scavenge port patches between cylinder mesh and scavenge box mesh allowing the fluid to pass from the scavenge box mesh over to the cylinder mesh.

2. **Add / Remove layers**
   Motion of exhaust valve. Hexahedral cells in a uniform layer are stretched/compressed to a certain point at witch an additional layer of cells is added if stretched or removed if compressed.

3. **Generalized Grid Interface (GGI):**
   Communication over the interface between two regions sliding across each other. Used when the valve region is moving down into the cells in the cylinder region.

Time is also handled differently for engine simulations, the userTime is reported in crank angle degrees rather than seconds. An engine dictionary is included in the case directory containing geometrical properties of the engine

as well as the operating conditions. The engine class reads the engine dictionary and converts the user time from seconds to crank angles with the following expression,

$$CAD = \frac{360}{60} \cdot RPM \cdot t. \tag{2.38}$$

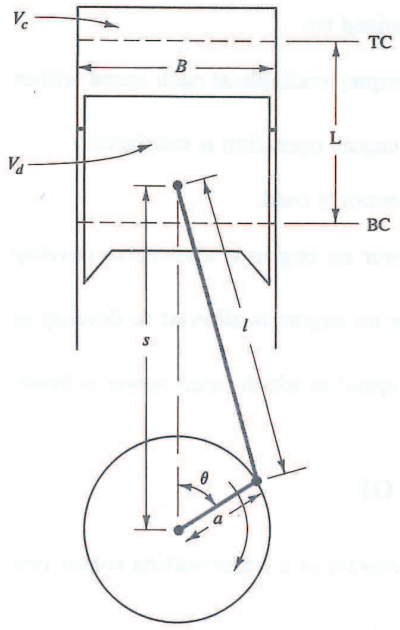

Figure 2.1: Geometry of cylinder, piston, connecting rod and crank shaft (Heywood, 1988)

Figure 2.1 shows a schematic representation of a cylinder with a piston, piston rod , connection rod and a crank shaft where B is the bore, a is the crank radius (0.5· Stroke), l is the length of the connecting rod and θ is the crank angle. These properties are given in an engine geometry dictionary and used to calculate the position of the piston at any given time in the simulation.

$$piston_{pos}(\theta) = l + a - \left(a \cdot cos(\theta) + \sqrt{l^2 - a^2 sin^2(\theta)}\right) \tag{2.39}$$

2.3.1 Sliding interface

In section 1.4, the two-stroke engine cycle was divided into two phases, open volume and closed volume. The simulations presented in this thesis start at EVO and ends at EVC. During the blow down process, the valve is opened but

the scavenge ports are not uncovered by the piston and the mesh consists of two separate regions. At IPO, the piston will uncover the scavenging ports, allowing air from the scavenge receiver to enter the cylinder. Numerically, this implies that the faces on the patches representing the scavenge ports must change their boundaries from a boundary type patch to an internal face. This is managed by using the sliding interface mesh modifier. The motivation for the sliding interface algorithm is to allow two non conformal interfaces to slide across each other where the two interfaces are coupled together. The algorithm is based on the identification of two corresponding, overlapping patches and creates a third patch consisting of the overlapping faces from the master and slave patch respectively. The algorithm require two corresponding patches, a master and a slave. The algorithm searches across the faces in the two patches and creates a new, temporary, internal patch consisting of the overlapping faces. For the next time step, the sliding interface detaches and reverts to it original configuration. In detail the process is as follows:

1. Project the points from the "slave" patch onto the master patch. The stationary patch is by convention the master patch and the sliding patch is the slave patch. The master patch will therefore conserve its shape.

2. Identify the part of the patches where master and slave overlap. For those faces, the original master and slave boundary should be replaced by a set of internal faces which couple the two regions together.

3. If part of the master patch remain uncovered, it should remain in the master patch and support its original boundary condition.

4. Likewise for the slave patch

5. If the two meshes move relative to each other, the sliding interface should be able to recover the original definition (faces) and re-couple the meshes.

Figure 2.2 shows an example case with two scavenge ports being connected to a liner patch. It is important to note that each of the scavenge ports has a patch on the scavenge box side and a corresponding one on the cylinder side yielding a total of 60 patches involved in the sliding interface operations given the 30 scavenge ports for a MAN B&W engine.

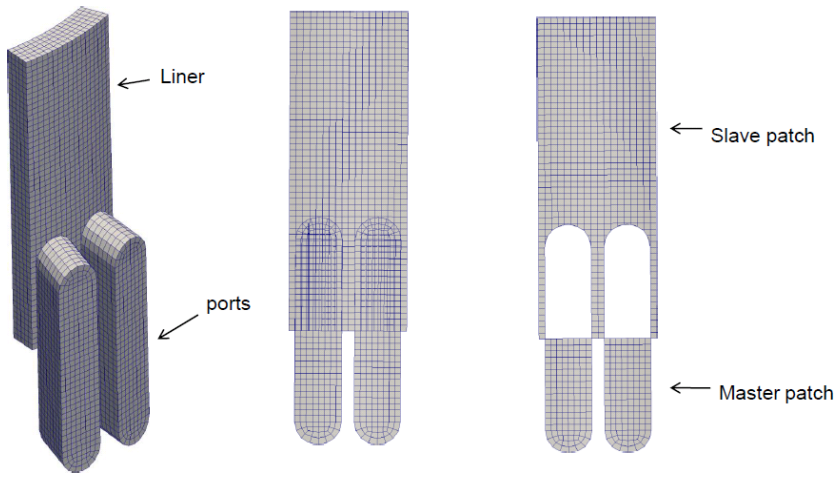

Figure 2.2: Sliding interface example case

2.3.2 Add/remove layers

Opening and closing the exhaust valve without topologically changing the mesh would require the mesh to deform heavily, producing highly distorted cells. Another strategy is to move a block of cells and compensate for the motion by adding or removing layers of cells. This requires some attention when generating the mesh as a plane surface of pure hexahedral cells is required by the mesh modifier in order to add a complete layer of cells. An uneven plane of cells will cause the algorithm to diverge.
Figure 2.3 shows the cells that are affected by the motion of the valve. When setting up the simulation the user must generate cell and face sets to define which cells and cell faces the mesh modifiers should act on. The sets are generated by the user to accommodate the valve motion.

faceSets

- valveLayeringFacesTop
- valveLayeringFacesBottom

cellSets

- valveCells

The engine class will read the user generated sets and convert them to zones run time and the code will update the zones as the mesh is subjected to topological changes. A tabulated lift profile for the exhaust valve is also to be provided by the user.

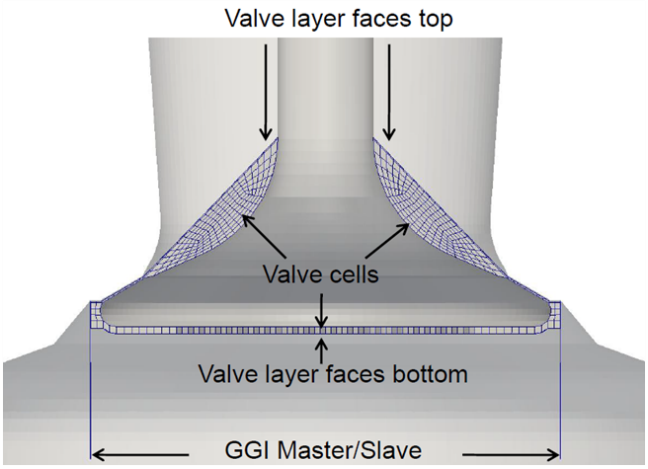

Figure 2.3: Cross section of the exhaust valve region of the mesh, the visible cells are the cells subjected to topological changes by the mesh modifiers

2.3.3 Generalized Grid Interface (GGI)

A consequence of the valve motion is that a part of the mesh will be sliding across the stationary cells in the engine cover. To accommodate this, the mesh must be considered as two regions with an interface. A utility implemented in the extended version of openFOAM is called Generalized Grid Interface (GGI) (Beudoin and Jasak, 2008). It was originally designed for turbomachinery applications to handle a sliding interface between the stator and rotor. Although the GGI at first glance, has the same application as the sliding interface algorithm, described in section 2.3.1, it does not make any adjustments to the topology of the mesh but performs communication between the two regions on a matrix level. Two faceZones must be defined to mark the interface between the stationary and the translating region. The two interfaces are called ggiMaster and ggiSlave and can be observed in figure 2.3. The analogy of the stationary part being denoted master is also the case for the GGI as it is for sliding interface.

Figure 2.4 shows an example of a non conformal interface between two mesh regions. As the faces does not perfectly overlap, it is necessary to cut the interface into smaller **facets** which are consistent for the master and shadow faces. The facets are seen in figure 2.4 (shaded area). The total face area is then replaced with facets. Discretisation on the interface can be rewritten as a sum of facets operations. Introducing shadow neighbour values, ϕ_N^s, for the front of the face, creating the effect as if the interface is integrally matched. The

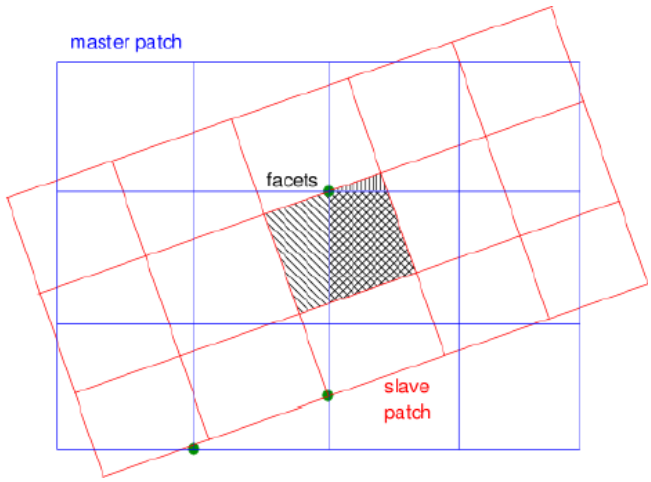

Figure 2.4: Non conformal mesh interface showing the master and slave patches and the facets needed to interpolate the face values across the interface, (Jasak, 2011)

flux transfer from the master to the shadow patch is then given by

$$\phi_N^s = \sum_t w_t \phi_t, \tag{2.40}$$

where w_t is a weighting function evaluated to account for the difference in facets area. To ensure that the interface discretization remains conservative the following constrains must be obeyed:

$$\sum_t w_t = 1,$$

the sum of facet area must equal the total face area. The perceived facet area must also be equal for both the shadow and the master patch face. If face A touches face B, the perceived facet area must be equal to:

$$w_{A \to B} S_A = w_{B \to A} S_B,$$

where S_A and S_B are the face area of face A and B respectively. The weighting functions are usually evaluated geometrically

$$w_t = \frac{S_{facet}}{S}, \tag{2.41}$$

where S is the total face area.

2.4 Top level solver

The top level solver is based on the Pressure Implicit with Splitting of Operators (PISO) algorithm. The solver also includes an option for running the solver loop several times with under-relaxation between the outer iterations and the internal PISO iterations. This makes the solver a merge between the Semi Implicit Method for Pressure Linked Equations (SIMPLE) and the PISO algorithm where the under-relaxation is intended to increase stability and allow higher time steps. The solver is in OpenFOAM known as the PIMPLE algorithm (OpenFOAM-UserGuide). A flow chart of the top level solver is shown in figure 2.5.

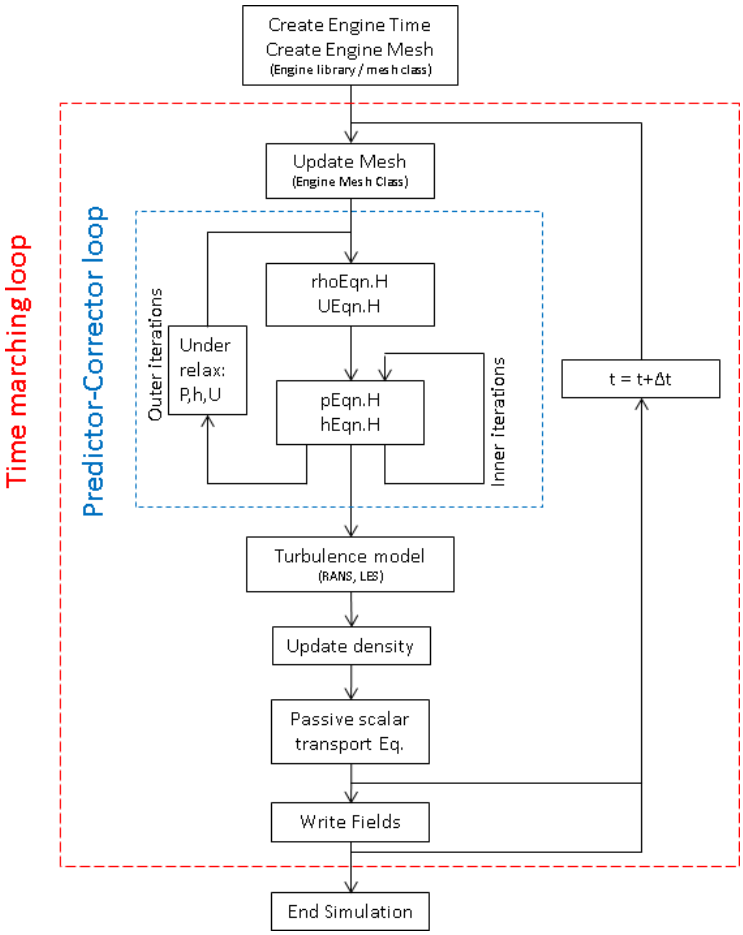

Figure 2.5: Solver flow chart

The flow chart is created as a representation of the main events in the code. Declarations, auxiliary and sub processes performed by the code are omitted from figure 2.5. When the solver executable is called, a number of declarations and header files are called to link with the central engine library. The Solver enters the time marching loop where the mesh is updated according the motion of piston and valve. The engine library will calculate the piston position based on equation 2.39 and read the relative valve lift from a table provided by the user. The engine class will adjust the position of piston and valve using the respective mesh modifiers. Special attention must be made to the fluxes when applying a moving grid. Before the `mesh.update()` function is called the fluxes is made absolute by adding the flux from the mesh motion to the face fluxes $\phi = \phi + \phi_{mesh}$, where the flux is defined as

$$\phi = \rho \cdot U \cdot S_f \tag{2.42}$$

where S_f is the surface normal face area and U is the velocity perpendicular to the face. The mesh is updated and a space conservation law is solved to ensure conservation of mass when the mesh is morphed (I. Demirdzic, 1988),

$$\frac{\partial}{\partial t}\int_V dV - \int_S \vec{u}_b \cdot \vec{n}\, dS = 0, \tag{2.43}$$

where $\vec{u_b}$ is the velocity of the moving mesh boundary. After the mesh is updated the thermodynamic library is called to update the fields for temperature, pressure, viscosity and thermal diffusivity according to the updated volume. The mesh flux is calculated, $\phi_{mesh} = \rho \cdot U_b \cdot S_f$, where U_b is the boundary velocity. The relative flux is then calculated according to 2.42 and the mesh flux, ϕ_{mesh}, is stored in memory to be used to make the flux absolute in the next time step.

The solver then enters the pressure velocity coupling where the governing equations 2.24, 2.25 and 2.26 is solved. It is natural to use equation 2.24 to calculate the density and the equation 2.26 to derive the temperature. The pressure is calculated from an equation of state like the perfect gas law,

$$p = \rho R T, \tag{2.44}$$

where T is the absolute temperature and R is the gas constant.

The UEqn.H routine is called which sets up a solution for the momentum predictor, a discretised form of the momentum equation, equation 2.25, reads

$$A_p \vec{u}_p = \vec{H} - \nabla p \tag{2.45}$$

where A_p is the coefficients of the linear system of equations and $\vec{H}$ is short hand notation for the convective and diffusive transport plus additional source terms, (Jasak, 1996):

$$\vec{H} = -\sum_l A_l \vec{u}_l + \frac{\partial \rho \vec{u}}{\partial t}. \tag{2.46}$$

The discretised momentum predictior has the form

$$\vec{u} = \frac{\vec{H}}{A_p} - \frac{\rho}{A_p}\nabla p. \tag{2.47}$$

The momentum predictor, equation 2.47, is solved using the pressure from the previous time step. This does not ensure conservation of mass and a pressure equation is derived in pEqn.H to correct the fluxes from equation 2.47. The following pressure equation is specified in pEqn.H

$$\nabla \cdot \frac{\rho}{A_p}\nabla p = \nabla \cdot \left(\frac{\vec{H}}{A_p}\right). \tag{2.48}$$

Equation 2.48 is used to calculate an estimate for pressure and the fluxes is updated based on the new pressure field,

$$\phi = \vec{S}_f \cdot \left[\frac{\vec{H}}{A_p} - \frac{\rho}{A_p}\nabla p\right]. \tag{2.49}$$

When the fluxes is updated, the rhoEqn.H is called again from inside pEqn.H to ensure mass continuity before the velocity from equation 2.47 is recalculated with the updated pressure from equation 2.48. The energy equation, 2.26, is solved when hEqn.H is called.

The coupling between the pressure and velocity presented above is known as the PISO algorithm. The PISO consists of one predictor step and a prescribed number of corrector steps. The algorithm can be summed up as follows:

1. Set the boundary conditions.
2. Solve the discretised momentum equation to compute a intermediate velocity field, equation 2.45.
3. Calculate a new pressure with the pressure equation, equation 2.48.
4. Correct the fluxes, equation 2.49.
5. Correct the velocities on the basis of the new pressure field, equation 2.45.
6. Update the boundary conditions.
7. Repeat from 3 until convergence.
8. Perform time step and repeat from 1.

The PIMPLE algorithm provides the user to run the entire PISO loop multiple times, under-relaxing the equations in every outer iteration loop. This makes the solver more stable, allowing for a larger time step, but also the equations

are solved several times so the CPU time per time step is larger. The user specifies the number of outer corrector steps (SIMPLE) and inner corrector steps (PISO) the solver should take. Default values would be 3 outer correctors and 4 inner correctors. If the user choose to have one outer corrector and 2 inner corrector the solver runs like a standard PISO algorithm. At the initial stages of this project, due to increased stability, the solver was run in PIMPLE mode with 3 inner and 4 outer iteration loops. However, as the mesh quality was improved it was possible to run the solver in PISO mode without a reduction in quality. Moving from a PIMPLE to a PISO mode significantly reduced the computational cost since the equations was solved fewer times.

After the predictor corrector loop, the turbulence model is called to calculate the turbulent viscosity and thermal diffusion. If the simulation is run using the RNG k-ϵ turbulence model, this call will solve the two transport equations 2.32 and 2.34 and calculate the turbulent viscosity. When the turbulent viscosity is calculated the density is updated using the ideal gas law 2.44.

The transport equation for a passive scalar, equation 2.17, is then solved to distinguish between the hot exhaust gas in the cylinder and the cooled scavenge air which is introduced into the cylinder at IPO. Some run time post processing is also implemented into the routine containing the transport equation for the passive scalar. The engine mesh class has the cells comprising the cylinder region of the mesh, in a cellZone, and these cells can be obtained by the top level solver to calculate in-cylinder properties. Volume weighted averages of properties such as pressure, temperature and density can be calculated and outputted to log files. The volume weighted average of an arbitrary quantity ϕ is calculated with the following equation:

$$\overline{\phi} = \frac{1}{V} \int_V \phi \, dV. \tag{2.50}$$

The cylinder bulk purity of scavenge air is evaluated at each time step and outputted to a log file. The scavenging efficiency from equation 1.1 can be evaluated based on the passive scalar, Y, and calculated with the following expression

$$\psi = \frac{\int_V Y\rho \, dV}{\int_V (1-Y)\rho \, dV} \tag{2.51}$$

where $\eta_{scav} = \psi$ at exhaust valve closing (EVC).

Further, the axial and angular momentum in the cylinder are calculated to quantify the in-cylinder field. The volume integrated axial momentum is calculated with

$$G_z = \int_V \rho u_z \, dV, \tag{2.52}$$

where u_z is the axial velocity component and the angular momentum with

$$L = \int_V r\rho u_\theta \, dV, \tag{2.53}$$

where u_θ is the tangential velocity component.

After the routine including the transport equation for the passive scalar is called, the solver either performs a time step, writes the fields or terminates depending on where in the process the simulation is.

Chapter 3

Simulation process

While chapter 2 aimed to provide a description of the numerical model, this chapter will give an overview of the procedures and processes involved with IC-engine CFD. It was decided in the incipient stage that since this is an industrial Ph.D. project, the processes involved with generating a mesh, generating boundary conditions and initial conditions should be embedded in the existing MAN Diesel & Turbo engine research framework. The scavenging simulation package should be compatible with established interfaces to internal data bases and 0/1 dimensional simulation tools as well as related CFD activities performed within the R&D department.

3.1 Mesh generation

Generating the computational domain for IC-engine CFD is not straight forward due to the requirements from the mesh modifiers described in section 2.3. Special attention must be given to the mesh generation in the valve region due to the add/remove layers mesh handling strategy. Pure layers of hexahedral cells must exist in order for the addition and removal of cells to be successful. Further the GGI interface must be defined. The mesh generation strategy was therefore to split the mesh into regions that are meshed separately and then coupled together afterwards using a native OpenFOAM utility called stitchMesh (OpenFOAM-UserGuide). The computational domain was generated in four separate parts: the exhaust bend, exhaust valve, the cylinder and the scavenge box as shown in figure 3.1.

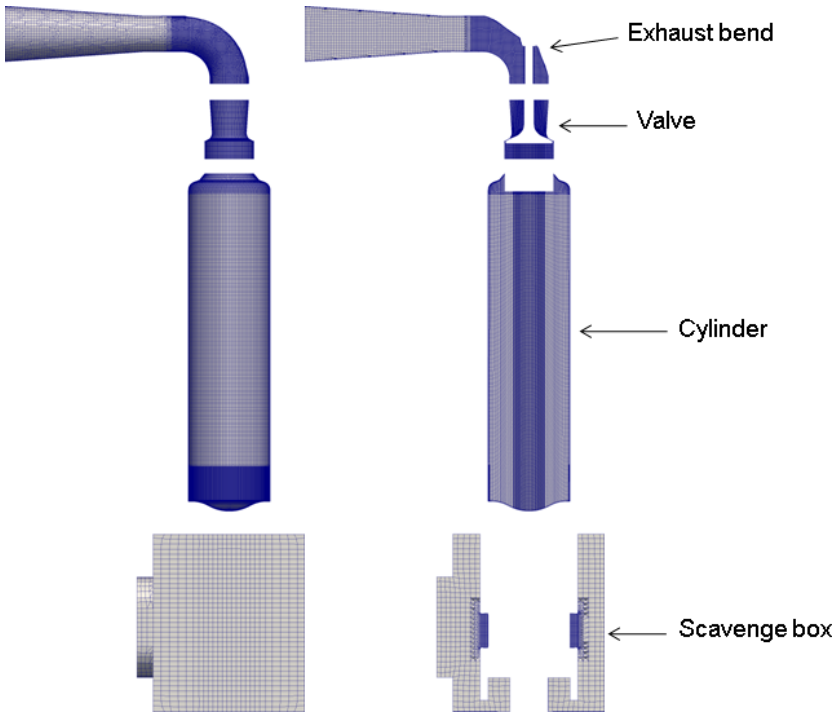

Figure 3.1: Mesh components and cross section

OpenFOAM has two native mesh generation tools, snappyHexMesh and blockMesh, both produce hexahedral dominated meshes. The valve and cylinder meshes are generated using blockMesh where the input file is generated with an in-house code which reads an input file containing geometric data from drawings and represents the shape in terms of splines. The spline objects are then parsed into the blockMesh input format along with a specification of mesh density.

The exhaust bend and scavenge box regions are created with the snappyHexMesh utility. The snappyHexMesh utility uses a hexahedral background mesh (usually generated with blockMesh) with a geometric surface description, e.g. a stereo lithographic (STL) file, embedded in the background mesh. The algorithm then projects the existing mesh onto the prescribed geometry. Cells which lie outside the computational domain are removed and the end result is a body fitted grid. Local grid refinement and layering are functionalities that produce high quality meshes. SnappyHexMesh can bee considered to be a mesh sculptor rather than a mesh generator as it requires the presence of a mesh to begin with. The snappyHexMesh mesh generator is rather experimental and case dependent which require a certain amount of trial and error in the mesh generation process. Especially the scavenging ports were challenging to generate

as each port cuts through the hexahedral background mesh with a different angle due to the ports azimuthal orientation. The mesh quality of the scavenging ports are very important as the slidingInterface algorithm, which will operate on the scavenge port patch, require a high quality mesh. While the scavenge box is disconnected from the cylinder when the simulation starts, the exhaust bend, exhaust valve and cylinder mesh must be merged into a single mesh. This is done by two native OpenFOAM functions, mergeMesh and stitchMesh. The mergeMesh algorithm will join two meshes together into a single mesh. The interface between the two regions will however remain, acting as internal baffles. The stitchMesh algorithm is then used to couple the interface together, removing the internal baffles. The algorithm have the same functionality as the slidingInterface algorithm when it couples two mesh interfaces together.

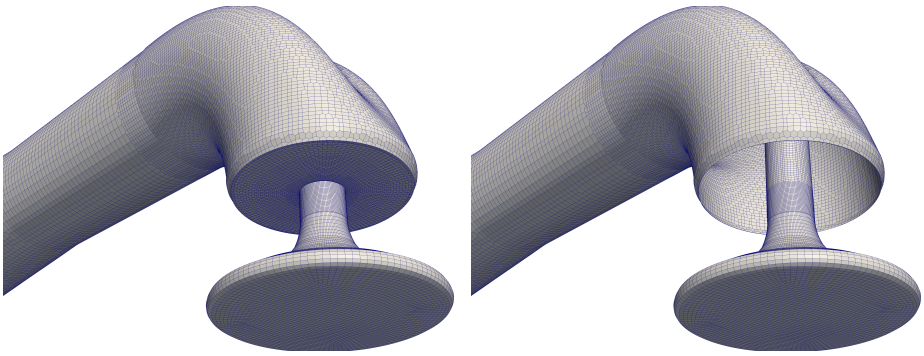

(a) Before stitched together **(b)** After stitched together

Figure 3.2

Figure 3.2 shows the interface between the exhaust valve and exhaust bend meshes before and after they have been stitched together. Both figures only show selected surface meshes, the internal mesh is not shown. Figure 3.2a show the two overlapping boundaries before they are stitched together. In figure 3.2b the two boundaries have been stitched together and changed into internal faces. The base size for the mesh is 13 mm for the cylinder and 4 mm for the valve region. This size give a good compromise between computational time and numerical accuracy.

3.2 Initial and boundary conditions

The initial conditions and the boundary conditions influence the CFD analysis heavily and have been an area of focus through out the course of the Ph.D. project. The CFD model uses experimental data obtained from dedicated test engines in Copenhagen, Japan, Korea or at test bed where the engines are com-

missioned. At these facilities, the engines are fitted with pressure transducers and temperature gauges which provide valuable input for the CFD model. The initial flow field must be initialized to include the initial swirl, which originates from the previous scavenging process and the swirl added by the injected fuel. Further the initial temperature field in the cylinder must be calculated, which require knowledge of the initial mass in the cylinder.

3.2.1 Pressure fields and mass flow correction

The flow trough the cylinder is driven by a pressure difference between the scavenge receiver and the exhaust receiver, known as the scavenging gradient. In a typical test engine configuration there is one probe measuring the absolute pressure in the scavenge receiver. Pressure transducers mounted in the scavenge box, cylinder lubrication hole, cylinder head and exhaust receiver record pressure traces which are scaled with the absolute pressure measurement in the scavenge receiver. Cycle averaged pressure traces are therefore obtainable for the scavenge box pressure and the in-cylinder pressure. The exhaust receiver pressure is a time averaged quantity (instead of a cycle averaged) since it is influenced by multiple cylinders. The CFD simulations in this thesis only comprise single cylinder simulations, so the cylinder interactions are only included in the inlet pressure boundary condition. The transient pressure signal from the scavenge box is used as input for the inlet boundary. The pressure sensor used to obtain the transient pressure signals is the Kistler 4260A100BCFD00R0 which produce a pressure signal with a tolerance of about 4 millibar (MAN Diesel & Turbo, 2015).

An example of a cycle averaged pressure trace used as the input boundary condition is shown in figure 3.3. The pressure trace show the cycle averaged transient pressure measured in the scavenge box (see figure 3.1). The pressure trace show the fluctuations that originate due to influence from other cylinders and dynamic effects of opening and closing of exhaust valve and scavenging ports. The signal shows four fluctuation periods during the scavenging period which can influence the actual driving pressure across the cylinder. The exhaust pressure boundary condition is defined as a time averaged fixed pressure which is calculated from the mean scavenge inlet pressure subtracted the pressure drop across the engine.

$$p_{ex} = \overline{p}_{scav} - \Delta p_{engine} \tag{3.1}$$

The pressure drop over the cylinder, Δp_{engine}, is a measured quantity and can be obtained from the engine performance data base. However, preliminary simulations showed a discrepancy between the mass flow in the CFD analysis and the mass flow indicated by emission measurements. The simulations under predicted the mass flow rate, which heavily impaired the scavenging process. Deviations up to 30% in air mass flow were observed in the CFD simulations which

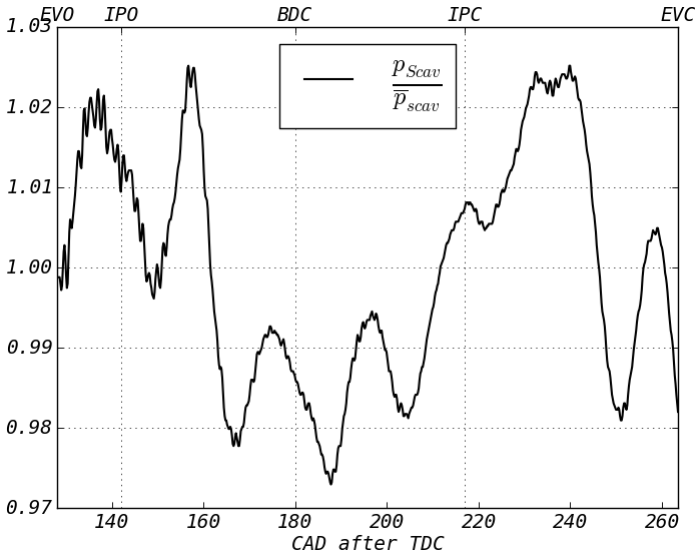

Figure 3.3: Cycle averaged pressure trace from the scavenge box used as input for the CFD model

are unacceptable when investigating a process which rely heavily on the mass flow rate. To overcome this source of error, it was decided to use the mass flow rate obtained with emission measurements to calculate a corresponding pressure drop according to engine geometry and scavenge port kinematics. Initially, a iterative approach was employed where the scavenging gradient, Δp_{engine}, was varied to investigate the sensitivity to the mass flow rate. However, this approach was ineffective as each iteration loop was very time consuming.

The strategy for correcting the mass flow rate was to calculate the effective restricting area in the cylinder as a function of crank angle and calculate the integrated engine area. The engine area is equal to the minimum of the exhaust valve area and the scavenging port area as shown in figure 3.4. The exhaust valve is fully open during the scavenging process, IPO-IPC, and the flow area trough the exhaust valve does not change. The scavenging ports act as the flow restricting area in the cylinder for 5 CAD after IPO and before IPC. The exhaust valve area is the restricting flow area for the remainder of the scavenging process.

If the cylinder is considered to be a flow restricting orifice between the scavenge receiver and the exhaust receiver, a simple expression can be used to evaluate the mass flow rate of scavenge air through the cylinder:

$$\dot{m} = \rho_{scav} \cdot U_b \cdot A. \tag{3.2}$$

Where ρ_{scav} is the density of the scavenge air, U_b is a bulk velocity during

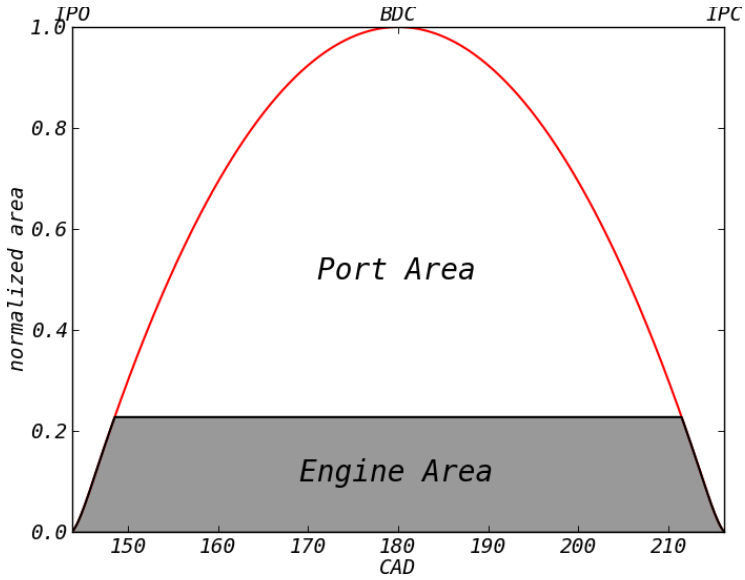

Figure 3.4: Normalized engine area showing both the scavenge port area and the effective exhaust valve area. The effective flow restricting area in the cylinder is the minumum of those two quantities.

the scavenging and A represents the flow restricting area in the cylinder. The integrated engine area is calculated with

$$A_{engine} = \int_{t_{scav}} A\,dt = \sum_{t_{scav}} A \cdot dt, \tag{3.3}$$

where A is the restricting flow area in the cylinder, $A = min(A_{ex\,valve}, A_{scav\,ports})$. The restricting flow area is the minimum value of the port area and the exhaust valve flow area shown as the grey area in figure 3.4. The scavenging time t_{scav}, is the time from IPO to IPC, and depends on engine speed as:

$$t_{scav} = \frac{60}{360} \frac{CAD_{(IPC)} - CAD_{(IPO)}}{rpm}. \tag{3.4}$$

The integrated mass flow for the engine test is measured and can be obtained from the engine data base. The integrated engine area, A_{engine}, from equation 3.3 is used to obtain an expression of the integrated mass flow

$$m = \dot{m} \cdot t_{scav} = \rho_{scav} \cdot U_b \cdot A_{engine}. \tag{3.5}$$

The bulk velocity, U_b, can be estimated using Bernoulli's equation (R. Fox and

Pritchard, 2004)

$$\int \frac{dp}{\rho} + \frac{U^2}{2} + gz = constant, \tag{3.6}$$

where gz is the gravitational contribution which is neglected in this calculation. Equation 3.6 can be solved with respect to the bulk velocity potential between the exhaust and scavenge receivers

$$U_b = \sqrt{\frac{2\Delta p_{engine}}{\rho_{scav}}}. \tag{3.7}$$

The integrated mass, m, flow rate over the cylinder during one scavenging process is obtained from the data base and the corrected pressure drop , Δp_{engine}, is calculated by combining equation 3.5 and 3.7

$$\Delta p_{engine} = \frac{\rho_{scav}}{2} \left(\frac{m}{\rho_{scav} \cdot A_{engine}} \right)^2 \tag{3.8}$$

The corrected pressure drop is used in the CFD analysis. This approach improved the mass flow rates significantly and reduced the error in mass flow for the CFD simulation from 30% under prediction to a deviation in the range of -1.56% to 3.83% depending on operating conditions. The method was applied to a load sweep test where four simulations corresponding to engine loads: 25%, 50%, 75% and 100% on a propeller curve was run with the data base Δp_{engine} and with the corrected $\Delta p_{engine,\,corr}$.

Engine load:	**100%**	**75%**	**50%**	**25%**	
m	3.85	3.68	3.13	2.42	kg
p_{scav}	3.877	3.416	2.429	1.614	bar
ρ_{scav}	4.36	3.90	2.76	1.81	kg/m^3
Uncorrected:					
Δp_{engine}	120	110	90	70	$mbar$
m_{CFD}	2.73	3.06	2.75	2.32	kg
Deviation	-29.1	-16.8	-12.1	-2.9	%
Corrected:					
$\Delta p_{engine\,corrected}$	187.7	160.9	123.7	70	$mbar$
m_{CFD}	3.79	3.77	3.25	2.35	kg
Deviation	-1.56	2.45	3.83	-2.9	%

Table 3.1: Integrated mass flow over the engine for the CFD analysis

A comparison of the CFD simulations using the corrected and uncorrected Δp_{engine} is shown in table 3.1. It shows a clear improvement in the prediction of mass flow for the CFD model. The under prediction of mass flow is most dominant for the high load cases where the scavenging pressure, p_{scav} and air density are the highest.

3.2.2 Temperature fields

The initial and boundary conditions regarding pressure was described in section 3.2.1. This section will describe how the initial and boundary temperature are determined. Temperature probes are mounted in the exhaust receiver and scavenge receiver, which makes it easy to set the boundary condition for the inlet and outlet patches of the computational domain. Furthermore there are three temperatures to be initialized in the computational domain: the scavenge box region, the cylinder region and the exhaust bend region. The scavenge box is initialized with the measured temperature in the scavenge receiver and the exhaust bend region is initialized with the measured temperature in the exhaust receiver. The latter is slightly uncertain as the content of the exhaust bend is a mixture of exhaust gas and scavenge air at IPC. The actual temperature of the mixture in the exhaust bend is probably lower than the gas temperature in the exhaust receiver. However, it is believed not to be of influence as the initial air content in the exhaust bend is displaced by the cylinder content within the first 5-15 CAD after EVO. When the scavenge ports are opened, the initial condition in the exhaust bend have left the computational domain.

The cylinder temperature is not directly measured, but can be calculated, using the ideal gas law

$$T_{cyl} = \frac{p_{cyl}}{\rho_{cyl} \cdot R}. \tag{3.9}$$

Where p_{cyl} and ρ_{cyl} is the in-cylinder pressure and density at EVO respectively. R is the specific gas constant ($R = R_u/M_m$, where M_m is the molecular mass and R_u is the universal gas constant). The density, ρ_{cyl}, is unknown and must be evaluated. As the exhaust valve is still closed at EVO, the total mass in the cylinder must be equal to the amount of air trapped in the cylinder at EVC during the previous scavenging process plus the added mass due to the injected fuel. The trapped cylinder mass can be calculated by an in-house tool that performs an isentropic compression of air with thermodynamic properties of the scavenge air to the compression pressure, p_{comp} and calculates the mass of air based on the compression volume and thermodynamic state. The amount of mass added by the fuel from the measured engine fuel consumption is calculated by the following formula,

$$m_{fuel} = \frac{SFOC \cdot P}{rpm \cdot 60 \cdot n_{cyl}} \left[\frac{g}{kWh} \cdot kW \cdot \frac{min \cdot h}{min} \right], \tag{3.10}$$

where $SFOC$ is the specific fuel oil consumption, P is the power output and n_{cyl} is the number of cylinder. The air density is then calculated by

$$\rho_{cyl@EVO} = \frac{m_{air} + m_{fuel}}{V_{cyl@EVO}}. \tag{3.11}$$

The in-cylinder temperature at EVO is calculated by equation 3.9 using equation 3.11 to determine the density and p_{cyl} is extracted from the pressure trace.

3.2.3 Velocity field

The in-cylinder swirl is important for the scavenging process in marine two-stroke diesel engines. A tangential component to the in-cylinder flow field is generated by the angled scavenge ports. The swirl then decays due to wall friction during compression. Some additional swirl is then added by the fuel spray before the swirl again decays due to wall friction. The initial flow field is difficult to predict. Hult et al. (2014) performed PIV measurements of the in-cylinder velocity during scavenging in the T50ME-X test engine using a special cover with optical access. This allowed for the angular and axial velocity component for a single point in the combustion chamber to be extracted as function of crank angle.

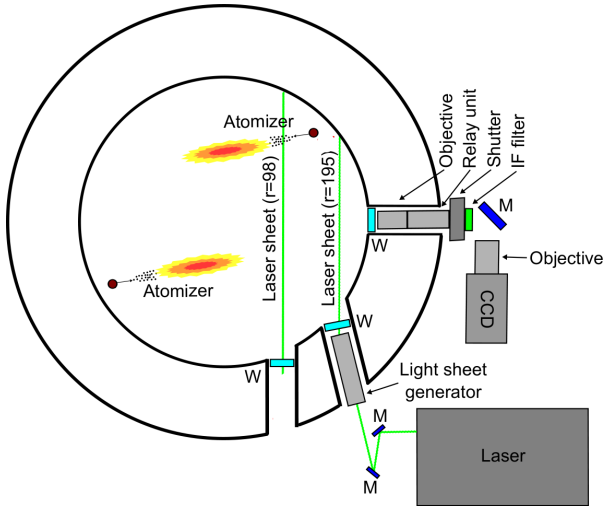

Figure 3.5: Schematic of experimental arrangement for PIV (Hult and Matlok, 2013)

Figure 3.5 shows a schematic of the PIV arrangement used in the experiment. The figure shows a cross section of the optical cover and the location of the two

laser sheets in relation to the exhaust valve, atomizers and liner wall. Only the laser sheet closest to the wall (r=195) was used to evaluate the initial swirl. The PIV arrangement was able to resolve a 50x50 mm field of view. The velocity vectors in this small sheet were found to be homogeneous and the sheet average value is used to evaluate the in-cylinder flow. Both the axial and tangential components are extracted as an average of the 50x50 mm field, rendering the measurements to be point measurements. A more detailed description of the experimental setup is published in Hult et al. (2014). The PIV data is cycle averaged with a temporal resolution of 10 CAD. The PIV data is also used in section 4.1.

A solid body rotation is initialized in the cylinder according to the angular velocity, obtained with PIV, from the experiment. The solid body rotation was scaled so that the tangential velocity matches the known value at the laser sheet location. The code use a definition of the swirl number as input to match the tangential velocity:

$$S_w = \frac{60}{\pi} \frac{V_\theta}{rpm \cdot B}. \tag{3.12}$$

Where V_θ is the tangential velocity component, RPM is the engine speed and B is the engine bore. This version of a swirl number quantify the time it takes a particle to complete a full rotation of the cylinder azimuthal compared to the engine frequency. The swirl number, S_w, is a user input to the CFD solver. The axial velocity component is initialized to be quiescent at the exhaust valve and increase linearly to match the piston velocity at the piston position. This is to avoid non-physical pressure waves initialized by the sudden piston motion. Figure 3.6 show the velocity distribution in the computational domain after adjusting the velocity field after PIV data and piston velocity. The air in the exhaust bend and the scavenge box is initialized as quiescent due to lack of information about the flow. The pressure difference when opening the exhaust valve accelerate the air in the exhaust bend rapidly and this assumption is not likely to effect the scavenging process. The transient pressure boundary condition will also generate motion and fluctuations in the scavenge box before IPO.

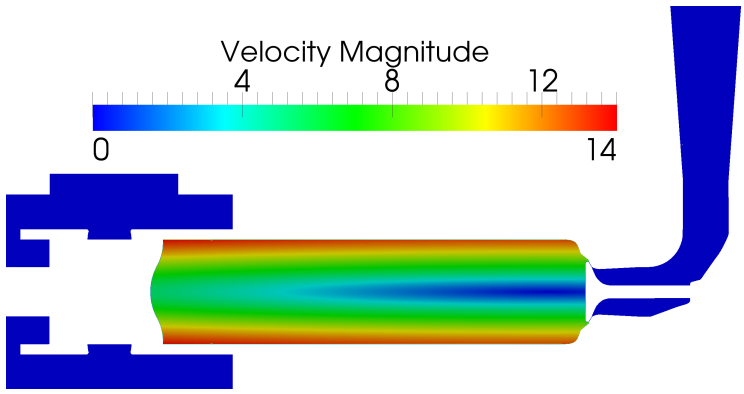

Figure 3.6: Initial velocity field

3.3 Subdomain decomposition for parallelisation

This section will describe the process of decomposing the computational domain into smaller partitions which can be solved in parallel on a computer cluster. The mesh modifiers, described in section 2.3, impose restrictions to the distribution of cells which in turn require the mesh to be decomposed manually by the user. The user define cellSets containing the cells which should be distributed to the different processors. Manual decomposition further complicates the process of conducting the CFD analysis as the user must manually attempt to optimize the load balancing.

There are several conflicts in the mesh modifiers that renders automatic mesh decomposition algorithms, such as scotch, unsuited for scavenging simulations. For example, a GGI patch cannot exist on the same processor as a Sliding Interface patch. This restriction alone states that the mesh must be decomposed into a minimum of two domains where the GGI and the Sliding Interface is located on separate partitions. The Add/Remove layer algorithm cannot remove or receive cells across processors. The Add/Remove layer mesh modifier require a column type mesh perpendicular to the face where cells are added or removed so the processor boundaries must be perpendicular to the layering surface. The GGI patch should normally be fully parallelized by letting the complete GGI surfaces be present on each processor as a global faceZone. This is unfortunately not possible as the GGI is not compatible with other sliding interfaces. The solution is to run the GGI in "local parallel" mode, meaning that each GGI stays local on each processor. This only works if the decomposition is done such that the two patches using GGI are fully overlapping each other on each processor.

The manual decomposition allows the user to manually allocate cells to processors in a way that meets the requirements above. This is done by generating

"**sets**" of cells which is then distributed to different processors. A python script is developed that generates the input script for the OpenFOAM utility "**setSet**" which is used to generate the processor sets. The simplest way of decomposing the domain would be to simply divide the domain into slices along the axial direction. This could also fulfil the formal requirements from the mesh modifiers, but is not the most practical as it would isolate all the sliding interface patches in a single processor. Instead is was decided to divide the scavenge box mesh into sectors with only a limited number of scavenge ports on each processor. This would result in a speed up as each processor will only operate on a limited number of patches. To minimize the size of the processor boundaries the mesh is divided into 5 regions which is divided into sectors. The 5 regions are: one for the scavenge box and lower part of the cylinder, two regions for the main cylinder region, one for the valve region and the last region covers the exhaust bend.

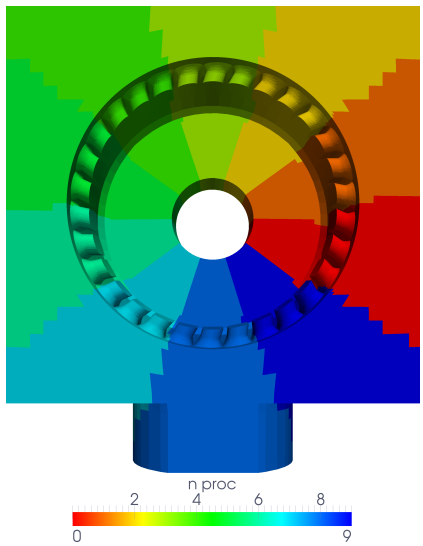

Figure 3.7: Cross section of the scavenge box showing the sector based mesh decomposition

Figure 3.7 show the decomposition of the scavenge box. The scavenge box and the lower part of the cylinder is divided into 10 sectors, containing 3 scavenge port patch pairs on each processor. Keeping few scavenge port patch pairs on each processor is beneficial as the sliding interface algorithm will iterate over all of the faces on the patch pairs to perform the coupling and topological change. This process should be distributed onto many processors to optimize load balancing. Figure 3.8 show a side view of the computational domain indicating the processor distribution. The color scheme is scaled from processor 11

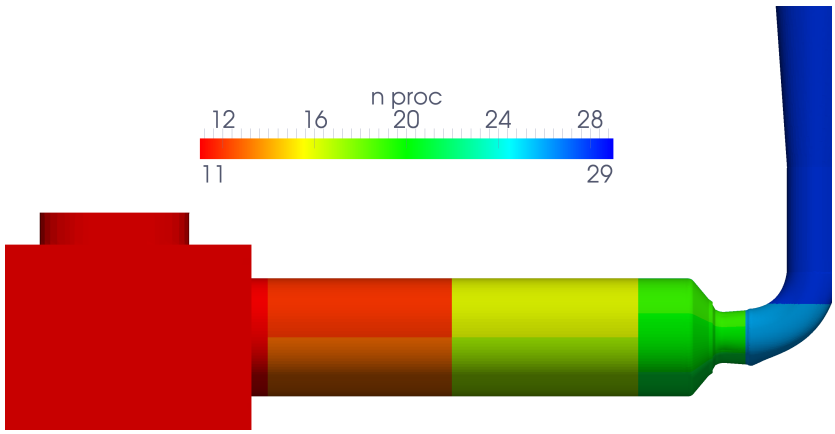

Figure 3.8: Side view of the computational domain showing mesh decomposition

to 29. This is done to highlight the distribution of partitions above the scavenge box. The cylinder region is divided into two times 4 sectors while the exhaust valve region is divided into 6 sectors. The exhaust bend region is divided into 4 components. The ligth blue and dark blue region in figure 3.8 is subdivided in half. Two additional partitions is used to make the load balancing process easier. A circular partition is located in the bottom of the cylinder. This partition is used to balance the number of cells in the scavenge box sectors with the rest of the partitions. Adjusting the radius of the central partition in the lower part of the cylinder will adjust the number of cells in the sectors. Likewise a circular partition is located under the exhaust valve to make the process of load balancing easier. The simulations in this report is decomposed into 30 partitions and solved in parallel on a computer cluster.

Chapter 4

Validation study of CFD model

As mentioned in the introduction, the research on large marine two-stroke diesel engines is modest compared to smaller engine types found in the automotive and truck industry, light power production units and garden utilities due to the size, cost and complexity involved with test facilities and operation of large engines. The large stroke to bore ratio in combination with the uniflow scavenging principle (compared to valve controlled gas exchange found in four-stroke engines) increases the length and time scales. This in turn increases the Reynolds number significantly compared to smaller engines which complicates CFD modelling. Further, research on an engine in service is not feasible within a university framework due the cost, size and manpower required for operation. The research on marine engines is usually conducted on, simplified and scaled model engines. A consequence of this is that the amount of validation data for a CFD model of a full size operating two-stroke marine engine is limited. These factors complicate the validation process of the CFD model since high quality data is scarce and difficult to obtain. There are several aspects into the validation of the CFD model used in this project.

First the engine library, described in section 2.3, have been inspected to make sure that the piston follows the prescribed motion.

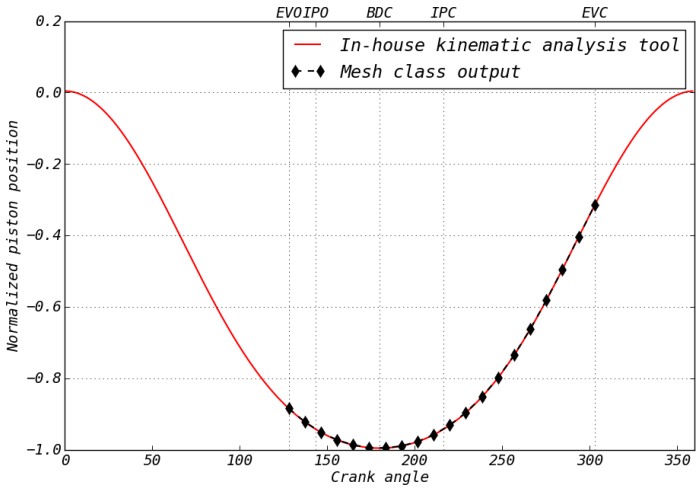

Figure 4.1: Comparison of piston position as function of CAD ATDC generated with the engine mesh class and an in-house piston kinematics analysis tool

The piston position is written to a log file from the CFD analysis and compared to an in-house piston kinematics analysis tool. The comparison is shown in figure 4.1 which validates the mesh class in terms of piston kinematics. The piston position is crucial for the scavenging simulations as it dictates the correct timing for opening and closing of the scavenge ports as well as ensuring the correct cylinder volume. The cylinder volume must be correct otherwise the density of the air in the cylinder will be incorrect as it is initialized with a measured p_{cyl} and the calculated T_{cyl} from equation 3.9.

Comparing the pressure trace from the experiment and the CFD model is a good indication for the CFD results accuracy. The pressure trace from EVO to EVC for an engine case corresponding to data obtained at test bed from a production engine is shown in figure 4.2. The black line corresponds to the simulated cylinder bulk average pressure from a 100% engine load case which will be presented in section 5.1. The bulk average pressure is calculated with equation 2.50. The red line is measured on an operating engine at test bed at Hyundai Heavy Industries (Korea) with a pressure transducer located in one of the lube oil lubrication nozzle, located roughly 1/3 of the liner length down from the cylinder cover. The agreement between the cylinder pressure for the CFD model and the experiment is good, where the CFD model predicts the blow down process with good accuracy. This is essential for the scavenging process as the conditions in the cylinder and scavenge box must be realistic at IPO. When the scavenge port opens, the cylinder pressure experiences fluctuations due to pressure waves propagating through the cylinder. Both the calculated

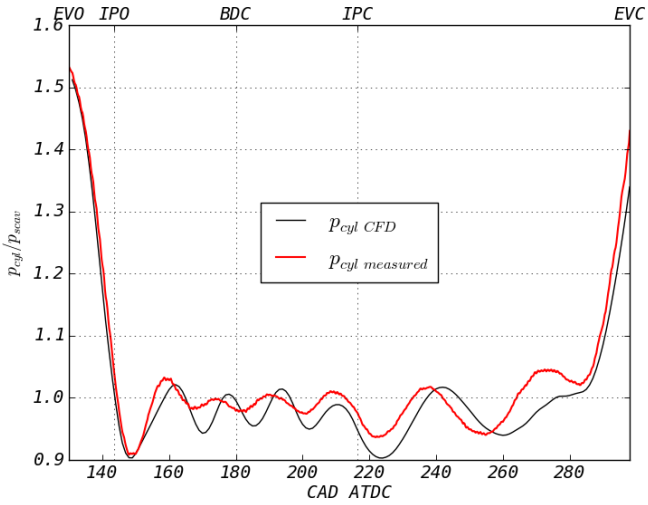

Figure 4.2: Comparison of normalized in-cylinder pressure as function of CAD ATDC between a CFD simulation and the measurement from a engine test case

and measured cylinder pressure experience four peaks during scavenging (IPO-IPC) and two peaks during the push out process. The frequency reduces by 50% when the scavenge port closes which is in agreement with the fundamental frequency for a cylinder with both ends open and a cylinder with one open and one closed end. The equations for the fundamental frequency for the cylinder is:

$$f_{IPO-IPC} = \frac{c}{2 \cdot L}, \tag{4.1}$$

during the scavenging process between IPO and IPC and,

$$f_{IPC-EVC} = \frac{c}{4 \cdot L}, \tag{4.2}$$

during the push out process between IPC and EVC. Where c is the speed of sound and L is the length scale. The length scale is the total distance travelled by the pressure wave which in the simulation is from the inlet patch to the outlet patch for the scavenging phase and piston to exhaust patch in the push out process. From equation 4.1 and 4.2 it is clear that the frequency observed in the cylinder during scavenging should be twice the frequency during the push out process.

The scavenging gradients Δp_{engine}, used in the CFD simulations, have been modified to match the measured mass flow rate of air for the different cases. The approach and the results was discussed in section 3.2. The mass flow

rates through the cylinder is acceptable for the CFD simulations, which ensure realistic conditions for predicting the scavenging process with the CFD model. It has been stated clearly that this thesis only comprises the open volume phase and that the closed cycle where the combustion process occurs is beyond the scope. However, it is in the R&D strategy of MAN Diesel & Turbo to perform full cycle CFD simulations in the near future. This implies that the results from the scavenging CFD model will be used as input to a combustion CFD model and vice versa. The validity of the results from the scavenging CFD model, in terms of initial conditions to a combustion CFD model can be evaluated by calculating an isentropic compression of the cylinder content at EVC to the cylinder volume at TDC and compare the compression pressure, p_{comp}, with the measured compression pressure. An in-house real gas thermodynamic code creates a gas based on the cylinder mass, bulk temperature and bulk pressure and calculates the corresponding pressure when compressing the gas volume to the compression volume at TDC.

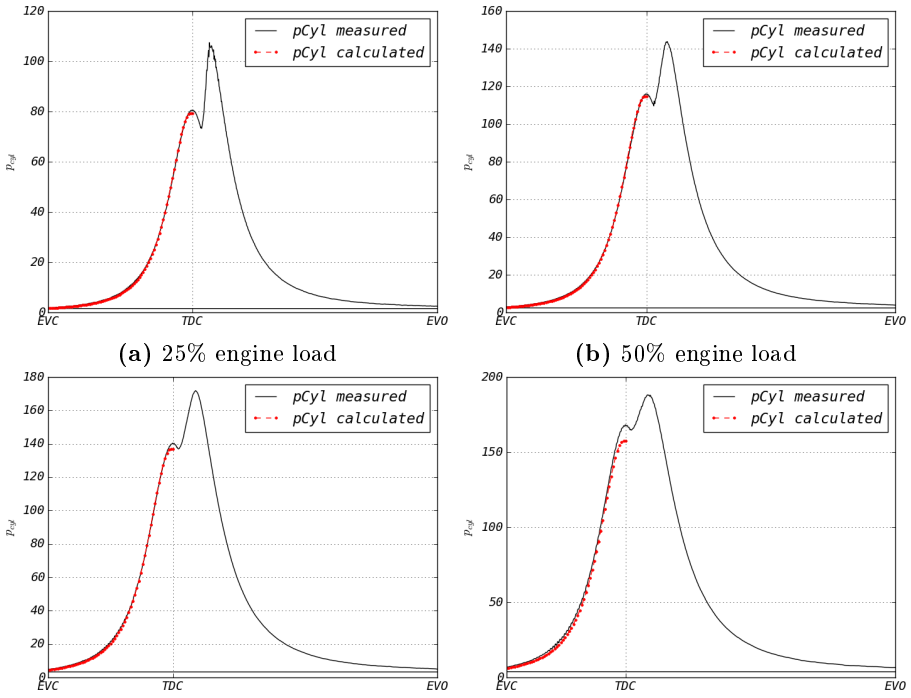

(a) 25% engine load

(b) 50% engine load

(c) 75% engine load

(d) 100% engine load

Figure 4.3: p_{cyl} vs CAD. Comparison between the cylinder pressure, calculated with the CFD model results and the measured p_{cyl} from experiments corresponding to an engine load sweep along the propeller curve.

Figure 4.3 shows the measured p_{cyl} pressure trace from the experiments plotted together with the isentropic compression, calculated with properties from scavenging CFD results corresponding to an engine load sweep (will be further investigated in section 5.1). The figure shows good agreement between the measured p_{comp} and the calculated p_{comp}, especially for the 25%, 50% and 75% engine load case where the calculated compression pressure is within 2% of the measured pressure. The 100% load case is somewhat under predicted, which might stem from the measured exhaust valve lift profile or the fact that the measured airmass and the calculated airmass is not 100% identical. Still it is clear that the scavenging CFD model is capable of predicting realistic and accurate initial conditions for the subsequent compression and combustion process.

4.1 Validation case with in-cylinder velocity measurements obtained with PIV

The validations in terms of pressure trace and mesh motion is good when evaluating the overall performance of the code. However, it does not directly say anything about the flow fields and the distribution of scavenge air compared to the exhaust gas. To evaluate the scavenging process, quantifiable data on the in-cylinder flow field should be used. Fortunately for this project, an optical measurement campaign was conducted by MAN Diesel & Turbo on the T50ME-X test engine in Copenhagen where a PIV setup was used to obtain what is, to the authors knowledge, the first quantified data on the in-cylinder velocity during the scavenging process in large two-stroke marine engines (Hult et al., 2014). These data have already been briefly discussed in section 3.2.3 where the data was used when generating the initial in-cylinder swirling flow field at EVO. In the initial stages of the Ph.D. project, two test cases from the optical measurement campaign were extensively used for validation. It was also used to develop best practices on how to run scavenging simulations effectively with the highest accuracy affordable.

4.1.1 Two test cases, varying the in-cylinder swirl

Part of the objective for the optical measurement campaign was to investigate the influence of in-cylinder swirl on the scavenging process. This was done by fitting a specially designed belt to blind every second scavenge port. This will increase the tangential momentum in the cylinder. The degree of swirl can be quantified by a swirl number, S_w. Gupta et al. (1984) suggested the following formulation for the swirl number:

$$S_w = \frac{2F_{\theta,z}}{F_{z,z}D}. \tag{4.3}$$

Where $F_{\theta,z}$ is the flux of angular momentum in the axial direction, $F_{z,z}$ is the flux of axial momentum in the axial direction and D is a geometrical scale, the cylinder bore in this case. As the velocity field usually is unknown it is difficult to determine an accurate swirl number a priori. A geometric swirl number, Ω, can be expressed using only geometric properties as

$$\Omega = \frac{A_{cyl}}{n_p A_p} sin(\alpha). \tag{4.4}$$

Where A_{cyl} is the cross sectional area of the cylinder, A_p is the area of one single scavenge port, n_p is the number of scavenge ports and α is the port angle.

(a) Belt not mounted **(b)** Belt mounted

Figure 4.4: The scavenge ports with and without the specially designed belt fitted, viewed through the scavenge port inspection hole.

The normal port arrangement is shown in figure 4.4a where all 30 scavenge ports are unrestricted. Figure 4.4b shows the scavenge port arrangement with the belt fitted. The belt will effectively reduce the flow area across the ports with 50%. Remembering that the engine flow area is still determined from the exhaust valve as it was demonstrated in figure 3.4. The geometric swirl number, Ω is listed in table 4.1.

Normal Swirl (NS)	**High Swirl (HS)**
$\Omega = 0.26$	$\Omega = 0.52$

Table 4.1: Geometric swirl number for the normal and high swirl case

T50ME-X is a four cylinder test engine located at the Diesel Research Center in Copenhagen. The test engine is a fully operational two-stroke uniflow scavenged diesel engine which is used for extensive testing and development of new engine concepts. Some technical specifications for the test engine is listed in table 4.2.

Bore	500 mm
Stroke	2 200 mm
Con rod length	2 885 mm
Cylinders	4
Ports per cyl	30(NS) / 15(HS)
Port angle	20°
Max Power	7 MW
Max engine speed	123 rpm
Valve operation	Electronic/Hydraulic
Max cylinder pressure	190 bar
Charging	Turbocharged

Table 4.2: Technical spesifications for 4T50ME-X

Case	**Normal Swirl**	**High Swirl**	
engine load	25	25	%
p_{scav}	1.53	1.84	bar
Δp_{engine}	204.3	250.8	mBar
Engine Speed	77.5	77.5	rpm
EVO	128	128	CAD atdc
EVC	257	261	CAD atdc

Table 4.3: Operating conditions for the NS and HS example cases

The operating conditions for the two cases are listed in table 4.3. It is important to note that only the instrumented cylinder (where the optical cover is fitted) has the belt mounted. Consequently the engine is more difficult to balance and some variations in operating conditions will occur. The intention was to run the engine under identical conditions. However, the reduction of port area increased the pressure drop from the scavenge box to the cylinder so p_{scav} is increased for the high swirl configuration. The increased scavenging pressure will affect the flow rate in the engine. The mass flow across the scavenge ports for the two cases is shown in table 4.4. The total mass flow rate across the cylinder is equal for the two test cases, but the increased density in the scavenge receiver influence the volumetric flow rate. The volume flow for the high swirl case is reduced by 15.6% due to the increased density of the scavenging air.

The mass flow rate for the two test cases is shown in figure 4.5. One can observe that both cases have the same total mass flow rate and that both experience the same oscillations as in the transient p_{scav} pressure trace used as inlet pressure boundary condition. An example of the inlet boundary pressure trace was shown in figure 3.3. The **NS** case has a lower scavenging pressure and

Parameter	Normal Swirl	High Swirl	
η_{scav}	99.9	98.0	%
m_{CFD}	1.13	1.13	kg
m_{CFD}/ρ_{scav}	0.65	0.54	m^3

Table 4.4: Scavenging efficiency and total mass flow for the normal and high swirl example cases

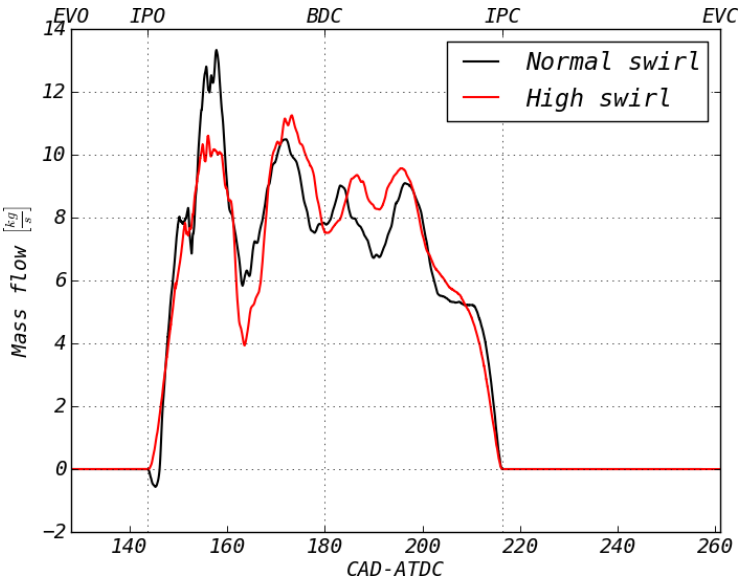

Figure 4.5: CFD result showing the mass flow rates across the scavenging ports in the CFD model for the NS and HS test cases

experience a blow back, where a portion of the exhaust gas in the cylinder is "expelled" into the scavenge box at IPO.

The relationship between the mass flow and volume flow is key to understand the scavenging process. The most important factor for the scavenging process is the volumetric displacement where the introduced scavenge air simply replaces the exhaust gas by displacement. In the start of the project, when the validation study was conducted, it was believed that the difference in η_{scav} observed in the simulations was a result of the increased mixing due to the elevated level of swirl. This was an obvious conclusion as the mass flow rate was identical in both cases. The accumulated flow across the scavenging ports is shown in figure 4.6a where it is clear that the increased p_{scav} did not influence the mass flow. Further investigating the volume flow reveals that the change in scavenge pressure actually imposes a rather large difference to the scavenging process.

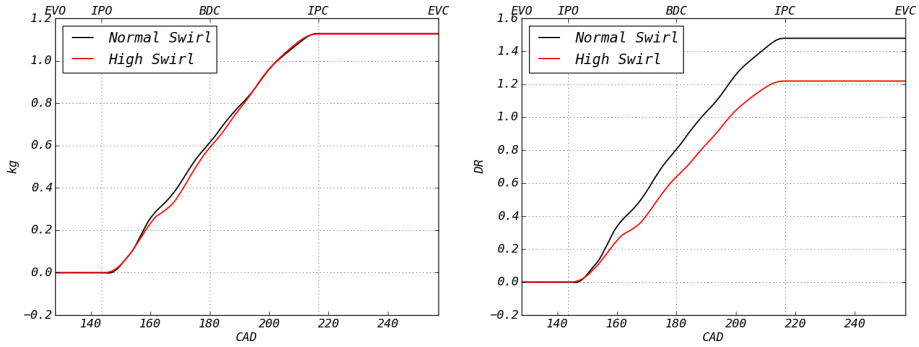

(a) Mass **(b)** Volume

Figure 4.6: CFD result showing the accumulated mass and volume flow for the NS and HS simulations. Volume flow represented in terms of delivery ratio, equation 1.4

Comparing the added mass and volume at BDC reveals that both the normal swirl and the low swirl cases have had approximately 0.6 kg of air added to the cylinder. The normal swirling case had $0.8 \cdot DR$ of air while the high swirling case only had $0.62 \cdot DR$ of air added to the cylinder. The reduction in volume flow decreases the displacement of exhaust gas.

The bulk purity of air, ψ, in the cylinder as function of the crank angle is shown in figure 4.7. The figure shows that the scavenging process for the high swirl case is suboptimal compared to the normal swirling case. Initially, it was believed to be caused by the difference in swirl level due to expected increase in mixing caused by vortex breakdown and central recirculation zones. However, further investigation on the quality of the added air revealed that the reduced air purity is not only a result of increased mixing, but is also strongly influenced by the reduced volume flow. Figure 4.8a and 4.8b shows the bulk purity of air as function of the added mass and volume of air (DR) to the cylinder respectively. The figure clearly show that the bulk purity of scavenge air in the cylinder is directly related to the volume flow. The bulk purity as function of added mass has the same characteristics as the bulk purity as function of crank angle where the high swirl configurations ability to flush the cylinder is lower than the standard port configuration. Dividing the mass flow with ρ_{scav} removes the discrepancy between the two configurations, demonstrating the strong link between the bulk purity and the volume flow (DR). The results shown in figure 4.6 shows that the purity of scavenge air in the cylinder, ψ, is directly governed by the volumetric displacement. This implies that the scavenging efficiency, η_{scav}, is a function of the delivery ratio. It also show that the pressure in the scavenge receiver, p_{scav}, influence the scavenging process as the volume flow or air varies, due to the density change, with the scavenging pressure.

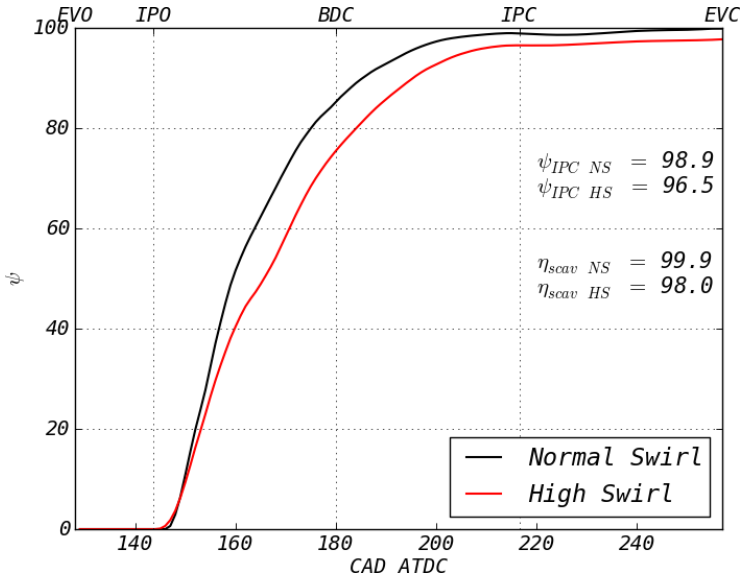

Figure 4.7: CFD result showing the bulk purity of scavenge air in the cylinder as function of the crank angle

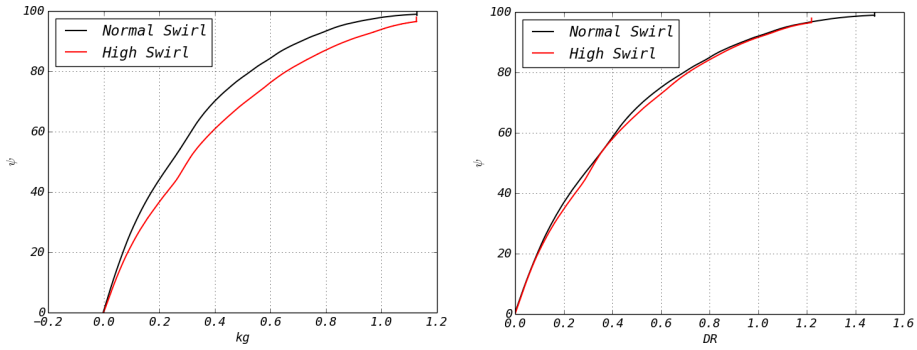

(a) Mass **(b)** Volume

Figure 4.8: CFD result showing the bulk purity of scavenge air in the cylinder as function of mass and volume flow

The angular transient momentum is evaluated to investigate the in-cylinder swirl. The angular momentum is calculated by the top level solver with equation 2.53 and shown in figure 4.9. The momentum is divided by the instantaneous total mass in the cylinder and is therefore the angular momentum per unit mass. The angular momentum presented in figure 4.9 therefore describe the influence

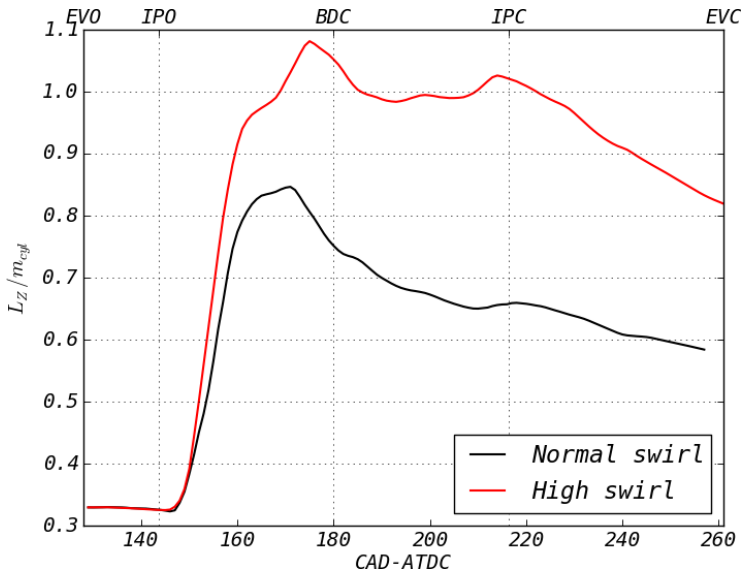

Figure 4.9: CFD result showing the angular momentum by unit mass in the cylinder as a function of crank angle for the NS and HS test case

of swirl on the in-cylinder flow. The angular momentum at EVO is a result of the initialization based on the solid body rotation described in section 3.2.3. There is a small reduction of the angular momentum until the scavenge ports are uncovered and the scavenge air enters the cylinder. The angular momentum then increases as the exhaust gas is flushed with the scavenge air. The peak in angular momentum is reached shortly before BDC when the cylinder is filled with fresh air. This is in agreement with the measured data which shows a sudden rise in the tangential velocity component at approximately 170 CAD after top dead center (shown in figure 4.13a and 4.13b). The angular momentum then decreases as the swirl decays due to wall friction. Shortly before IPC the angular momentum slightly increases for the high swirl case and stabilizes for the normal swirl case. This is due to the reduction in flow area when the scavenge ports are closing. As expected, the angular momentum for the high swirling case is higher than the normal swirling case.

The passive scalar from equation 2.17 is used to visualize the gas exchange in the cylinder during the scavenging process. The passive scalar acts as an indication of the mass fraction for the exhaust gas and the fresh air in the cylinder.

The passive scalar field for the normal swirling case is shown in figure 4.10. The color scheme is chosen in order to demonstrate the cold scavenge air as blue and the hot, exhaust gases, as red. From figure 4.10, it is clear that the scavenging process is dominated by displacement where the introduced scavenge

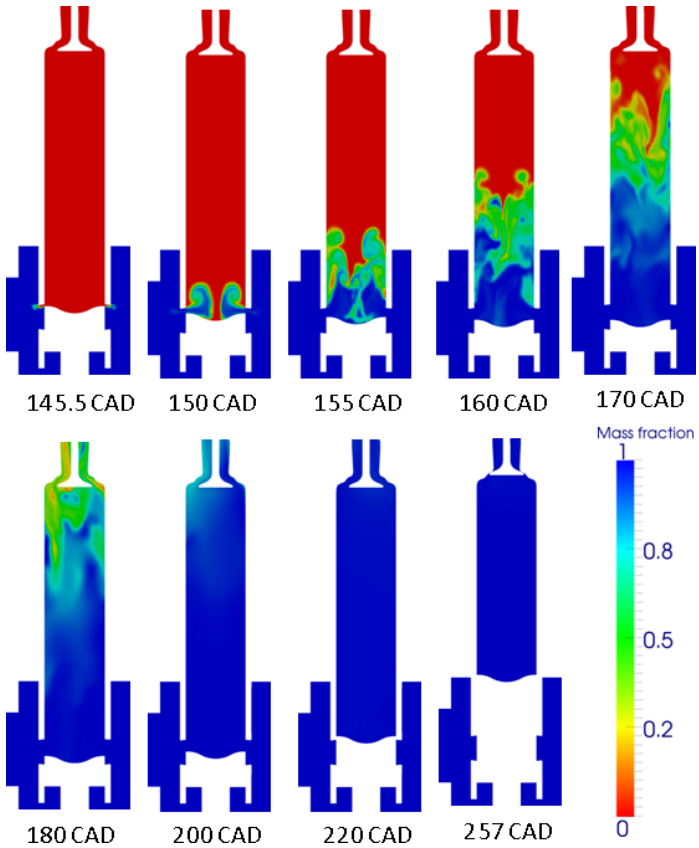

Figure 4.10: CFD result from the normal swirling case showing the distribution of the passive scalar in a cross sectional plane at relevant crank angles

air replaces the burned gas with only moderate mixing. Also it is clear that the cylinder is well scavenged shortly after 200 CAD ATDC.

The passive scalar field for the high swirl case is shown in figure 4.11. Comparing it with the normal swirl case from figure 4.10 it is appears that the increased swirl enhance the mixing of the two gases. As stated earlier the increased mixing of the two gases is the result from the adverse pressure gradient in the center of the swirling flow. The mass flow rates, and hence the axial momentum is similar for the two cases which implies that the high swirl is responsible for the increased mixing. The scavenging air travels axially at approximately the same rate in both figure 4.10 and 4.11 which can be seen as the scavenge air extends equally into the cylinder for both cases. The scavenge air reach the exhaust valve around BDC, but the purity of the cylinder gas is different. The

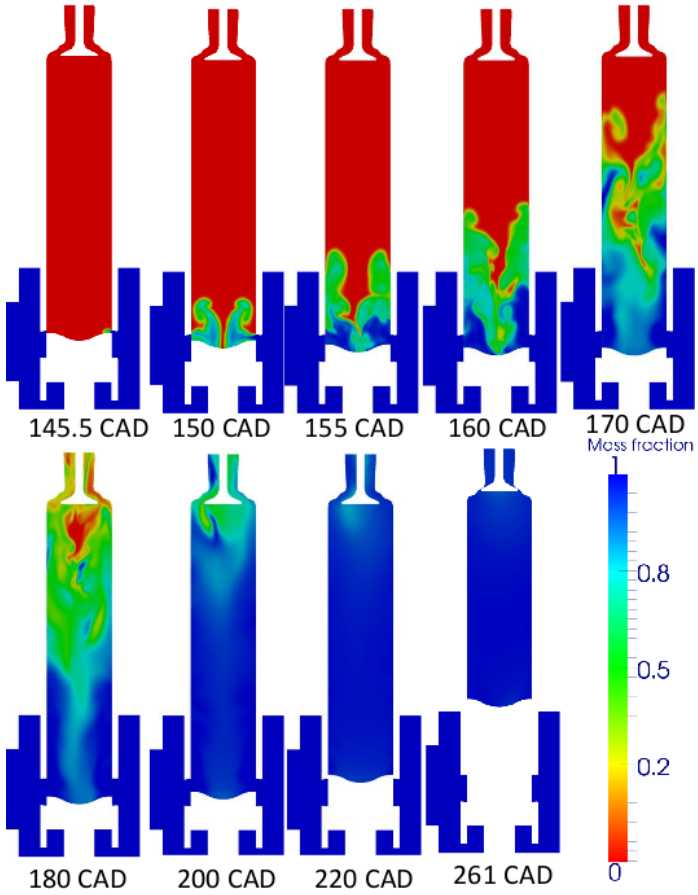

Figure 4.11: CFD result from the high swirling case showing the distribution of the passive scalar in a cross sectional plane at relevant crank angles

high swirl case has a larger amount of burned gases trapped along the center axis of the cylinder which is due to a central axial velocity deficit due to a vortex breakdown, the vortex breakdown region is shown in figure 4.12. Even at BDC, the high swirl case, figure 4.11, has a mixture in the order of $\psi = 0.7$ extending along the center axis to the piston surface while the normal swirling case has a mixture consisting of almost pure scavenge air covering most of the cylinder at BDC. A significant amount of burned gas is also trapped under the exhaust valve at BDC. The central recirculation zone for the normal swirl case and the high swirl case is shown in figure 4.12. The figure shows a volume-rendered threshold based on the negative axial velocity component at some relevant crank angles

during the scavenging process. The top row represents the normal swirl configuration and the bottom row represents the high swirl configuration. The normal swirl configuration experience recirculation above the scavenge ports at IPO. Then for the 160 CAD figure, a vortex breakdown is present along the center axis of the cylinder stretching from the piston surface and up half the length of the cylinder. The central recirculation zone is less prominent in the remainder of the scavenging process. The high swirling case also experience recirculation due to separation at the scavenge port sharp edge. A vortex breakdown is present at 160 CAD as for the normal swirl case. At 170 CAD the vortex breakdown at the piston surface is not very dominant and the central recirculation zone appears to be convected with the axial flow. However at 180 CAD and throughout the scavenging process a cone like vortex breakdown structure is present in the bottom of the cylinder. The vortex breakdown regions are consistent with the visualization of the passive scalar fields in figure 4.10 and 4.11 especially when considering the high swirling case at 180 CAD. A cone like structure in the scalar field is present in the bottom of the cylinder which is consistent with central recirculation zone in figure 4.12.

It is apparent, from this section, that the in-cylinder swirl has an influence on the mixing between the scavenge air and the exhaust gas during the scavenging process. The scalar fields in figure 4.10 and 4.11 in conjunction with the visualization of the vortex breakdown in figure 4.12 show a relation between in-cylinder swirl and mixing. However, it is important to remember that the bulk purity as function of delivery ratio is identical for the two cases as shown in figure 4.8b. These observations are somewhat contradictory as it renders the mixing process insignificant as both simulations follow the same displacement rate in terms of added volume flow. The conclusion from this observation must be that the mixing between the scavenge air and the exhaust gas is not as significant compared to the volume flow. If the cylinder receives an adequate amount of air, then both the exhaust gas and the mixture will be flushed out through the exhaust valve.

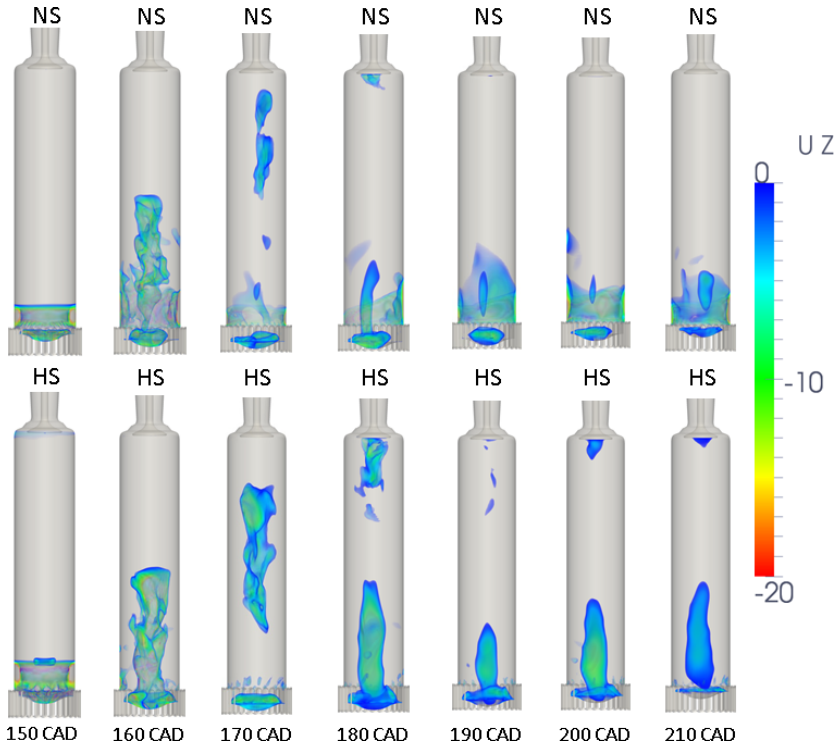

Figure 4.12: CFD result showing volume rendering of the vortex breakdown region for the NS and HS case at relevant crank angles. Top row correspond to the NS case and the bottom row correspond to HS case.

4.1.2 Comparison and validation with in-cylinder velocity measurements

The tangential and axial velocity components at a fixed location in space were measured as explained in section 3.2.3. The velocity components were measured using the non-intrusive optical method Particle Image Velocimetry (PIV). The PIV data have already been used to generate the initial flow field and will now be used as a validation tool for the CFD model. The measured velocities are located at a fixed point in the cylinder and can only provide information about the local velocity at this point. The in-cylinder radial velocity profiles are influenced by the port opening and closing, the central vortex core, the cylinder walls and the exhaust valve. The vortex core is particularly difficult to predict with RANS turbulence models as they are known to over predict the eddy viscosity in the vortex core. This implies that the CFD analysis will have difficulties

obtaining the correct radial velocity profiles and thus the absolute value in the probe locations. However, the tangential velocity component provides some useful information about the timing in the scavenging process. A sudden rise in the tangential velocity is observed when the scavenge air reach the probe location. Comparing the timing of this increase between the CFD model and the experiment can be used as a quantitative validation.

From the tangential velocities shown in figure 4.13, it is clear that the residual swirl is stable after the inlet ports are opened. Approximately 25-27 crank angle degrees after the ports opened, the tangential velocity suddenly rises. This indicates that the scavenging air that was introduced through the ports have reached the location of the probes in the cylinder head. This is a physical distance of about than two meters and can therefore be used to qualitatively determine the accuracy of the CFD analysis. It can be assumed that if the timing of this increase in tangential velocity matches between the PIV and the CFD analysis, then the mass flow rates should be reasonably well resolved. It should be noted that only every tenth crank angle is included in the PIV data while the CFD data includes every single crank angle in the data range. The axial velocity for the high swirl and the normal swirl case are very similar. The sudden increase in axial velocity is a direct response to the blow down process when the exhaust valve is opened to equalize the cylinder pressure to the scavenge receiver pressure. When the scavenge ports are uncovered at IPO, the pressure difference stabilizes and the axial velocity is relatively stable until the inlet ports close at IPC. Then the driving pressure difference for the scavenging process is removed and the axial velocity is reduced. The velocity increase observed close to exhaust valve closing is due to reduced flow area when the exhaust valve closes. The axial velocity for the NS case is slightly higher throughout the process with the exception of the final stages of the push out process. This trend is also observed in the axial velocity components from the CFD analysis. The tangential velocity components show a more significant difference between the high swirl case and the normal swirl case. The increase in tangential velocity appears to be earlier for the normal swirling case for both the PIV and CFD, but the high swirling case has the highest velocities throughout the scavenging process. After the increase, when the cylinder is filled with swirling air, the tangential velocity appears to decay. This is due to wall friction. The trend is clearly captured by the CFD model, but the tangential velocity appears to be over predicted in the high swirling case.

Figure 4.13a shows the comparison for the normal swirl case and it is clear that the CFD model predicts both the axial and tangential velocity with good accuracy. With the exception of a few data points the calculated velocity components are within the error bars. It captures the timing of the increase of tangential velocity very good as well as the swirl decay. The top and bottom peak that appear at the same time as the axial velocities are negative are more dominant in the CFD calculations than measured with PIV where they appear more vaguely. This is most likely due to the fact that the PIV measurements

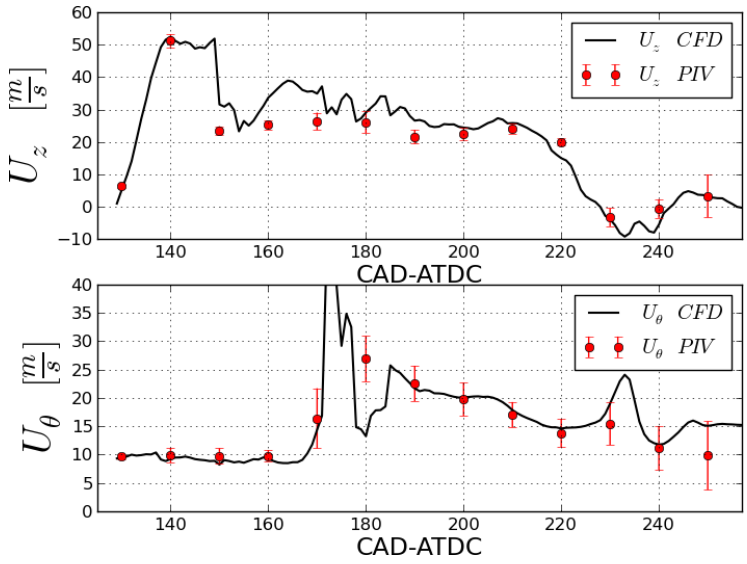

(a) Normal swirl

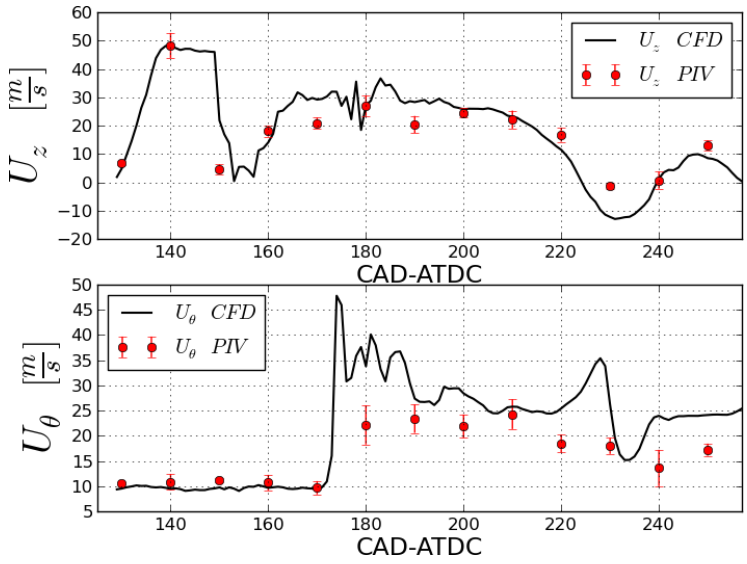

(b) High swirl

Figure 4.13: Comparison of measured PIV velocities and CFD calculations for the normal swirling and the high swirling case. Axial velocity component (top) and tangential velocity component (bottom)

are cycle averaged which have dampened out the fluctuations.

Figure 4.13b show the axial and tangential velocity component for the high swirl case. The axial velocity is reasonably well predicted by the CFD model with most of the data points being adjacent with the PIV measurements. Again the timing of the tangential velocity increase is well predicted, but the absolute values for the tangential velocity probes are over predicted by the CFD model. As mentioned earlier the CFD model is expected to struggle with predicting absolute values with high accuracy as the radial profile of the tangential velocity is hard to obtain numerically.

4.2 Comparison with a simple scavenging model

The purity of air calculated with equation 1.10 is plotted together with the bulk purity or air in the cylinder calculated with the simulation model in figure 4.14 and 4.15 for the NS and HS case respectively. The result show a very good agreement between the simple perfect displacement model and the CFD model. Especially in the initial stage of the scavenging process where no scavenge air can escape out of the cylinder due to the geometric arrangement of a uniflow scavenged engine. Since the scavenge air enters the cylinder close to BDC and leaves the cylinder through the exhaust valve in the cylinder head, the scavenging process in a uniflow scavenged engine will be governed by a pure displacement processes.

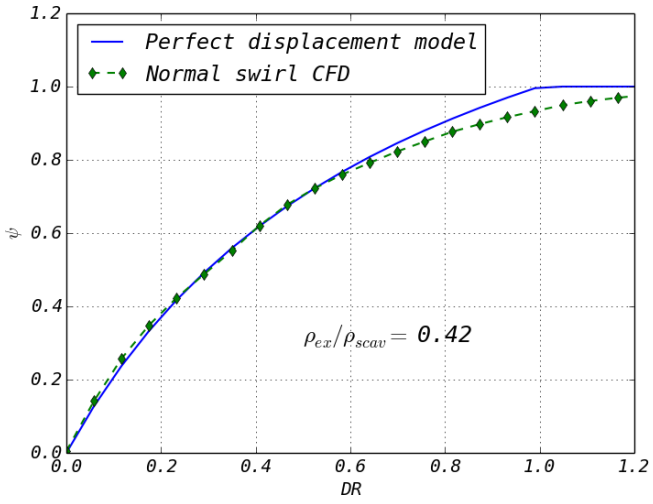

Figure 4.14: Purity of scavenge air in cylinder, comparison between Sher's theoretical model and the CFD simulation. Normal swirl port configuration case

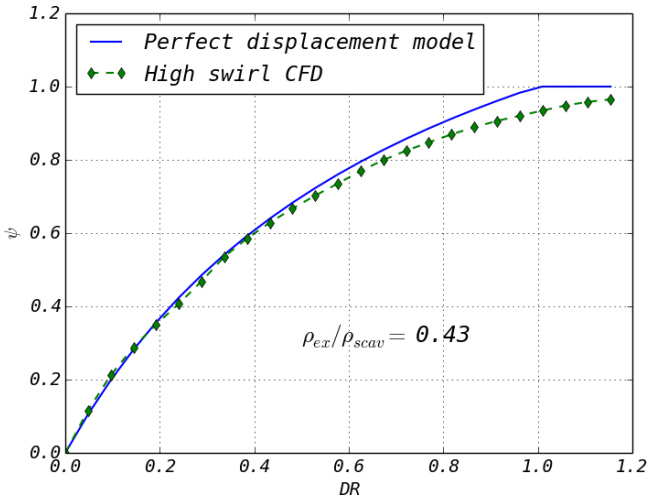

Figure 4.15: Purity of scavenge air in cylinder, comparison between Sher's theoretical model and the CFD simulation. High swirl port configuration case

Both the normal and high swirl configuration show good agreement with the pure displacement model up until approximately $DR = 0.6$ where they diverge slightly from the perfect displacement. The perfect displacement model from Sher is bounded at 1.0 as the purity of air cannot be higher than unity. The deviation between the perfect displacement model and the CFD model is due to mixing between the exhaust gas and the scavenge air at the interface between the two fluids and the mixing due to turbulence and in-cylinder swirl. The high swirl port configuration appears to have increased mixing which is consistent with phenomena such as vortex breakdown. The increased mixing due to swirl was also observed when comparing the scalar field in figure 4.10 and 4.11 where the high swirl configuration appeared to promote mixing of the two fluids. The ratio ρ_{ex}/ρ_{scav} influence the shape of the perfect displacement model and the density of the exhaust gas must be defined carefully.

The bulk average density of the cylinder content is shown in figure 4.16. The density in the figure is calculated with equation (2.50) and does not distinguish between the exhaust gas and the scavenge air. The figure shows that the density in the cylinder drops after the exhaust valve opens when the in-cylinder pressure is adjusted to the scavenge pressure. The minimal density is observed somewhat after the scavenge port opening (IPC) before the density increase as the cylinder is filled with the compressed scavenge air. The best correlation between the CFD model and the perfect displacement model is found using the lowest value of density in figure 4.16.

Figure 4.17 shows the purity of scavenge air in the cylinder for the CFD

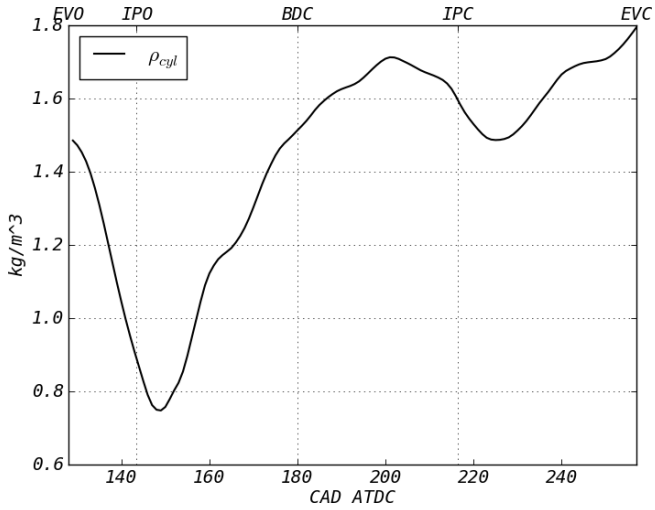

Figure 4.16: CFD result showing the bulk average density of the air/exhaust mixture in the cylinder as function of crank angle for the normal scavenge port configuration

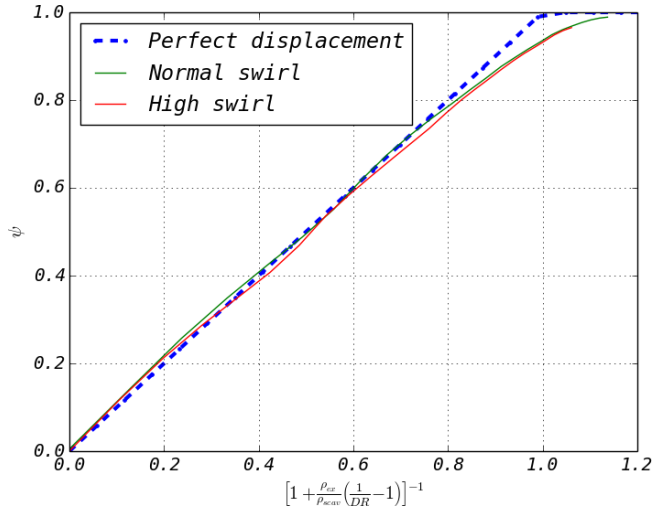

Figure 4.17: Purity of scavenge air in the cylinder. Comparison between the theoretical pure displacement model, (Sher, 1990), and the CFD mode.

model and the perfect displacement model. The perfect displacement model, equation 1.10, is used as the x-axis to clarify the CFD modelled results deviation

from the theoretical model. The figure shows that the theoretical model and the CFD model are in good agreement and that the CFD model for the first half of the scavenging process follows a perfect displacement before the mixing between the two fluids make the CFD diverge from the perfect displacement.

4.3 Mesh sensitivity

The mesh generation procedure and domain decomposition is described in section 3.1 and 3.3 respectively. There are several requirements to the mesh when conducting scavenging simulations, limitations from the mesh modifiers restrict the mesh generation and the decomposition process. Another important factor when conducting CFD analysis of the scavenging process in marine two-stroke diesel engines in an industrial framework is the time consumption when solving the equations. To minimize the time needed to conduct one simulation it is beneficial to run the simulations with as few mesh elements possible. In this section, three different meshes with increasing number of elements will be used to investigate if the relatively coarse mesh yield an acceptable accuracy.

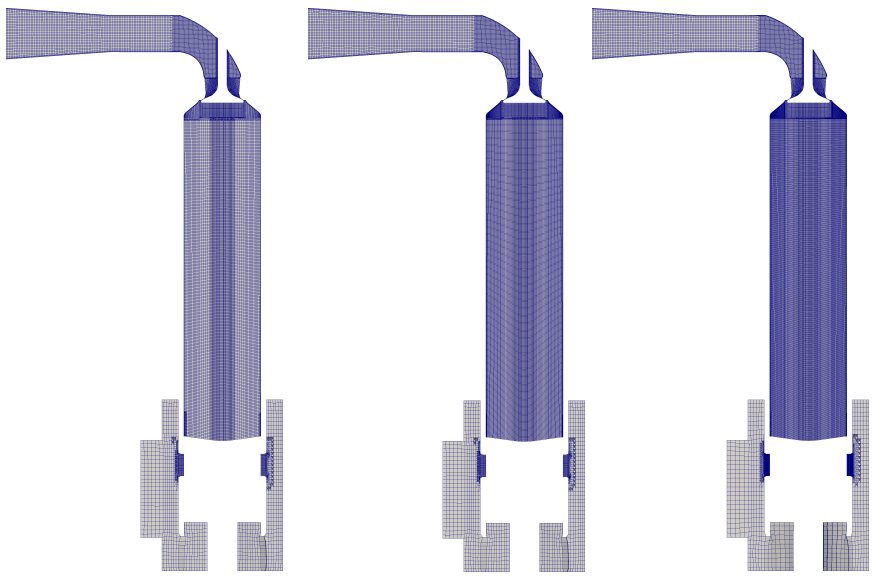

(a) $n_{cells} = 1.6$ mill **(b)** $n_{cells} = 3.0$ mill **(c)** $n_{cells} = 5.8$ mill

Figure 4.18: The three meshes used in the mesh sensitivity analysis

Three meshes was used in the mesh refinement study, the default mesh with approximately 1.6 million cells, a mesh with a total of approximately 3.0 million cells and one mesh with a total of 5.8 million cells. The three meshes is shown

in figure 4.19. The 1.6 million cell mesh is only refined in the cylinder region while the 5.8 million cell mesh is refined in both the cylinder region and the scavenge port region. The 1.6 million mesh is the default mesh, using a base size of 13 mm for the hexahedral cells in the cylinder region.

Parameter	1.6 mill	3.0 mill	5.8 mill
DR	0.77	0.73	0.74
η_{scav}	0.985	0.981	0.986
$\psi_{@\,EVC}$	0.886	0.880	0.882

Table 4.5: Results from the mesh validation study

The delivery ratio and the scavenging efficiency is shown in table 4.5. There are some differences in the delivery ratio which affect the scavenging efficiency. Some comparisons between the three simulations in the mesh refinement study is shown in figure 4.19. Figure 4.19a and 4.19b show the bulk average angular and axial momentum in the cylinder during the scavenging process. The in-cylinder momentums are of interest as they quantify on the flow field in the cylinder. Especially the angular momentum is interesting with respect to mesh sensitivity since it shows if the mesh is able to resolve the swirling motion. There are no apparent mesh dependence in terms of the axial momentum in figure 4.19b. There are some differences in the angular momentum in figure 4.19a where the 1.6 million mesh has a slightly higher angular momentum after BDC. This is partly due to the fact that the 1.6 million cell mesh yield a slightly higher mass flow rate than the two refined meshes. Figure 4.19c show the bulk purity of air as function of the delivery ratio. It is clear that the gas exchange is not mesh dependent as the lines for all three simulations are completely overlapping. Both figure 4.19b, 4.19a and 4.19c are all based on bulk average in-cylinder values. As the CFD analysis in this thesis is largely interested in bulk quantities, the results from the mesh sensitivity analysis is very good as the coarse mesh of 1.6 million cells produce the same results as the refined meshes.

So far the mesh sensitivity study has shown that the integral quantities is resolved with the coarse mesh. However, as the spatial resolution in the domain is changed the local flow field is changed. A sample probe is located close to the wall in the cylinder where the cylinder liner and cylinder cover intersects to sample the history of pressure and velocity locally in the cylinder. The pressure trace for the sampling probe can be seen in figure 4.19d. The local pressure trace shows very good agreement between the three meshes. The axial and tangential velocity was also sampled at the probe location and the trace of the axial and tangential velocity component is shown in figure 4.19e and 4.19f respectively. The local axial velocity trace shows good agreement between the three different mesh resolutions, except for a short period between BDC and IPC. The explanation for this discrepancy is that at this point the

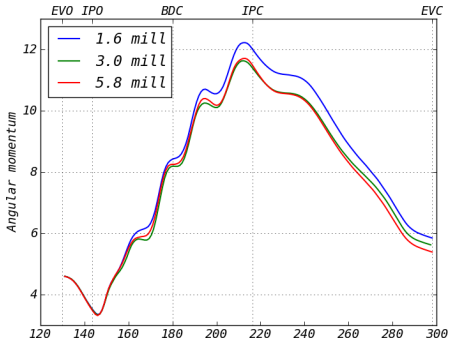

(a) Angular momentum

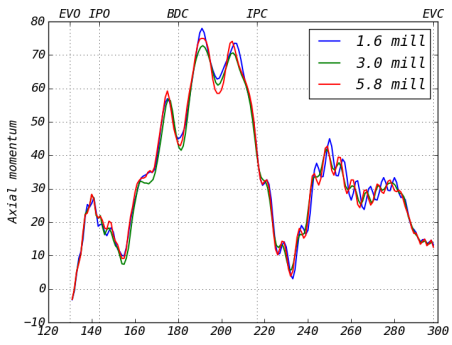

(b) Axial momentum

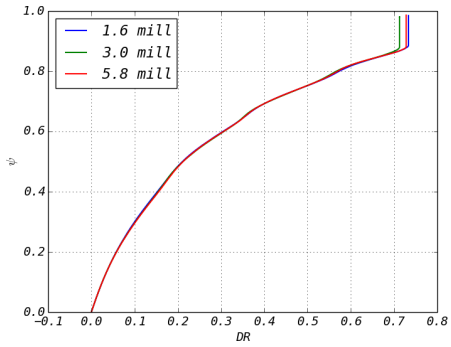

(c) Bulk purity

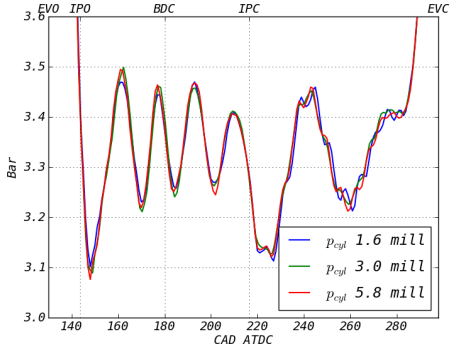

(d) In-cylinder pressure

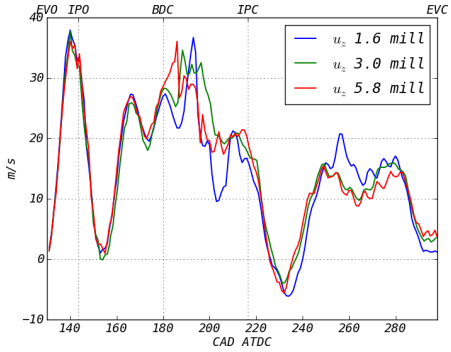

(e) Axial velocity

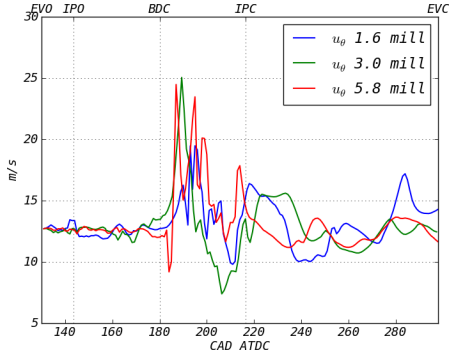

(f) Tangential velocity

Figure 4.19: Various results from the mesh sensitivity analysis

introduced scavenging air reach the probe location and cause fluctuations in the velocity field. There is a mixing region at the head of the scavenging air where large density variations can be expected. The period between BDC and IPC appears from the trace to be when the mixing region passes the probe. After the mixing region pass, the axial velocity trace for the three mesh resolutions is in good agreement again. The trace of the tangential velocity component at the probe location is shown in figure 4.19f. The tangential velocity trace is stable until the mixing region pass the probe location. The traces then start to fluctuate. After the scavenge ports close, the velocity traces become more stable. The difference between the three mesh resolutions is larger when analysing the tangential velocity component compared to the pressure trace and the axial velocity component trace.

The overall conclusion from the mesh sensitivity analysis is that when considering the bulk average properties the coarse mesh of 1.6 million cells adequately resolves the fluid problem and may be used for the CFD analysis. The coarse mesh is also adequate when analysing the trace of pressure and velocity locally in the domain. The velocity traces show that the flow field is indeed affected by changing the spatial discretization, but that increasing the number of cells in the domain does not provide a convergence as the traces are alike. It is therefore concluded to use the same base size as in the 1.6 million cell mesh when generating the meshes for the simulations presented in this thesis. This conclusion must be re-evaluated in the future when heat transfer analysis is to be included in the CFD model. Heat transfer is beyond the scope of this study which allows for the coarse mesh to be used.

Chapter 5

Results

5.1 Engine load sweep along propeller curve

In this section, the CFD model will be used to investigate the behaviour of the scavenging process as a function of engine load. Marine engines normally operate at constant load for extended periods of time. Several parameters, relevant for the scavenging process, are influenced by the engine load such as engine speed, scavenge pressure and the scavenging gradient. A total of four engine loads: 25%, 50%, 75% and 100% are presented in this section to investigate the scavenging process in marine two-stroke diesel engines. The engine load sweep refers to % of SMCR (specified maximum continuous rating) and follows the propeller curve where both the mean effective pressure (MEP) and the engine speed is varied to match the conditions for the engine, in service, when coupled to a propeller (Woodyard, 2009). The propeller law follows the following relation between power and engine revolution,

$$P = c \cdot rpm^3 \tag{5.1}$$

where P is engine break power and c is a constant.

Variations in engine load have an influence on the scavenging process primarily due to two factors. The increased RPM reduces the scavenging time, t_{scav}, where the scavenging ports are open. The scavenging time is shown in figure 5.1 where t_{scav} is normalized with the reference $t_{scav,ref}$ at 25% engine load. Increasing the engine load from 25% to 50% will reduce t_{scav} with almost 20%, t_{scav} further decrease with 30% when increasing engine load to 75% and t_{scav} is reduced by almost 40% when increasing the engine load to 100%.

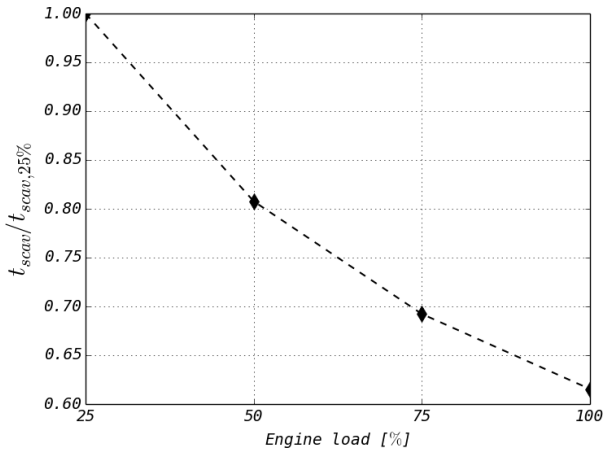

Figure 5.1: Scavenging time, t_{scav}. The time between scavenge port opening, IPO, and scavenge port closing, IPC.

The other load dependent factor is the pressure in the exhaust and scavenge receivers. The engine load is increased by burning more fuel, which leads to higher temperature and pressure in the cylinder, the energy containing exhaust gas is introduced into the exhaust receiver where it acts as the driving pressure for the turbocharger's turbine. This increases the pressure in the scavenge air receiver. Increasing p_{scav} leads to a higher mass flow rate needed to burn the additional fuel at high engine loads.

The scavenge pressure, density, engine speed and timing of the exhaust valve lift for the engine load sweep is shown in table 5.1.

Engine load	**100**	**75**	**50**	**25**	%
RPM	73.9	67.1	58.7	46.6	$\frac{1}{min}$
p_{scav}	3.877	3.416	2.429	1.614	bar
ρ_{scav}	4.36	3.90	2.76	1.81	$\frac{kg}{m^3}$
$\Delta p_{engine\,corrected}$	187.7	160.9	123.7	70.0	$mbar$
EVO	128	130	130	133	cad
EVC	303	298	286	281	cad

Table 5.1: Operating conditions and thermophysical properties for the CFD analysis.

In the later years, to comply with increasingly stringent emission legislation, a trend within the two-stroke marine industry has been to increase the scavenging pressure. High scavenge pressure in conjunction with late closing of the exhaust valve, known as two-stroke Miller timing, is beneficial as the method

can be optimized to reduce the formation of thermal NOx. The engine performance layout is determined by the maximum design pressure in the cylinder, which again is the sum of the compression pressure, p_{comp}, and the pressure rise, p_{rise}, due to the combustion. It implies that the compression ratio p_{comp}/p_{scav} is a determining factor in the exhaust valve closing strategy. There are two apparent advantages with late closing of the exhaust valve. Firstly, some of the compression work is moved from the piston to the turbocharger which is beneficial for the specific fuel oil consumption. Secondly, the compression temperature is lower due to the start conditions for the compression and the lower compression ratio p_{comp}/p_{scav}. The reduction of the temperature at p_{comp} leads to lower peak temperatures during the combustion process which reduces the production of thermal NOx. However, increasing the scavenge pressure also increases the density of the scavenge air. The definition of the delivery ratio, in equation 1.4, states a minimum volumetric requirement of air to fully scavenge the cylinder. The investigation presented in this section will show that a very important factor for the scavenging process is the volume flow rate, rather than mass flow rate. Ideal scavenging is by pure volumetric displacement of the cylinder content. The volume flow rate is equal to the mass flow rate divided by density, $\dot{V} = \dot{m}/\rho_{scav}$. The mass flow rate for the engine load sweep was shown in table 3.1 presented in section 3.2.1.

5.1.1 Scavenging efficiency

The scavenging efficiency is the most direct parameter for evaluating the scavenging process as it relates the bulk purity of the scavenging air in the cylinder to the exhaust gas at EVC. In the two cases used for validation purposes, section 4.1.1, both had good scavenging efficiencies where most of the cylinder content was replaced before IPC. Note that both these cases corresponded to an engine load of 25% and therefore the auxiliary blower was active. While the push out process in the validation case did not influence the scavenging significantly, the push out process in the engine load sweep presented in this section is far more important.

Engine load	100	75	50	25	%
η_{scav}	96.1	98.6	98.2	99.3	%
$\psi_{scav\,IPC}$	83.6	88.0	92.8	94.8	%
$\Delta\psi_{push\,out}$	12.5	10.6	5.4	4.5	%
m_{CFD}	3.79	3.77	3.25	2.35	kg

Table 5.2: Scavenging efficiency at different engine loads derived from the CFD analysis

The scavenging efficiency for the engine load sweep is shown in table 5.2.

The scavenging efficiency is acceptable from an engine performance perspective with the lowest $\eta_{scav} = 96.1\%$ for the 100 % engine load case. The scavenging efficiency for the 25% case is the highest with $\eta_{scav} = 99.3\%$. The low engine load case is expected to have the highest scavenging efficiency as the auxiliary blower is active in addition to increased volume flow due to the reduced p_{scav}.

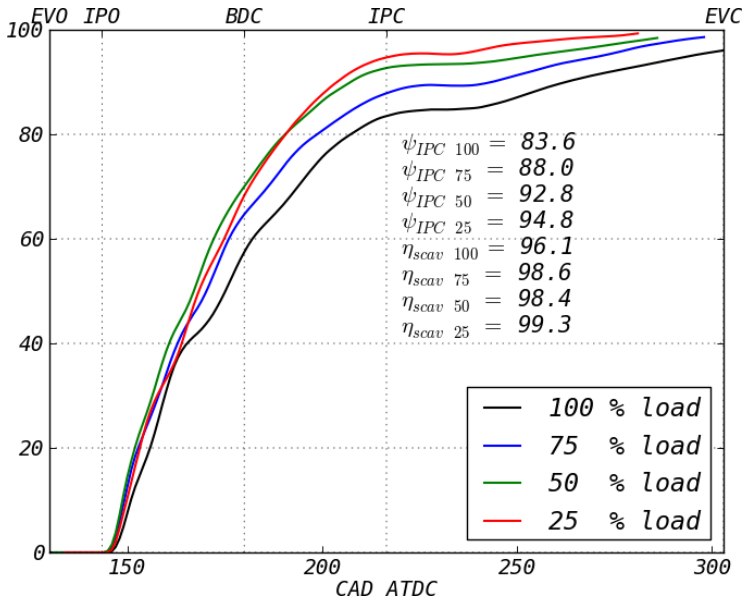

Figure 5.2: CFD result showing bulk purity of air in the cylinder as function of CAD ATDC

The CFD simulations show that the scavenging efficiency is highest for the low engine load case (25%) and then decreasing for higher loads. Figure 5.2 also shows the importance of the push out process. In the validation study only low engine load cases was investigated and the cylinder was close to fully scavenged at IPC and the push out process did not seem to influence the scavenging process significantly. In this case, it is showed that the push out process influence the overall scavenging process significantly, especially for the 100% and 75% case where the push out process is responsible for 12.5% and 10.6 % points of the scavenging efficiency respectively. The scavenging rate of change $\partial\psi/\partial\theta$ is significantly smaller during the push out process as the flow is only driven by displacement from the piston motion and not by a pressure difference.

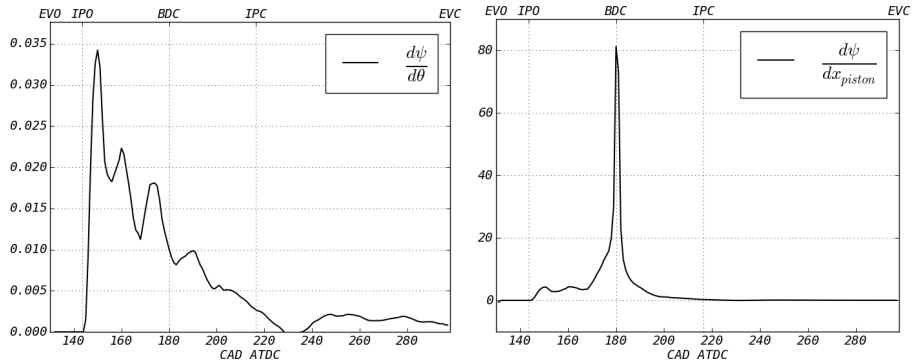

(a) Derivative of cylinder bulk purity ,ψ, with respect to crank angle

(b) Derivative of cylinder bulk purity ,ψ, with respect to piston position

Figure 5.3: CFD result showing the derivative of ψ with respect to crank angle and piston motion for the 75% engine load case

The derivative of the cylinder mixture purity as function of crank angle and piston motion is shown in figure 5.3a and 5.3b. The latter is the derivative of in-cylinder bulk purity of air as function of the crank angle. It shows that the gas exchange is faster in the early stages of the scavenging process, just after the ports are uncovered. The gradient peaks shortly after IPO and then decays until the ports close at IPC. When the scavenge ports close, the driving pressure difference between the scavenge and exhaust receiver is removed. The absence of driving pressure grinds the momentum to a halt as seen in the figure where $d\psi/d_\theta = 0$ some 10 crank angles after IPC before again increasing due to piston motion. The piston motion contributes to the rate of change by simply displacing the cylinder content. The plot in figure 5.3b shows the scavenging rate $d\psi/dx_{piston}$ which is the rate of change of air bulk purity as a function of piston motion. Fortunately for the scavenging process, the piston speed is lowest around the bottom dead center creating maximum "exposure time" for the scavenging ports. This can be seen in figure 5.3b, which has a very distinct peak value in BDC where the piston is momentary stationary.

5.1.2 Mass and volume flow rate

The delivery ratio can be used to evaluate the scavenging process before applying the CFD model as it only requires knowledge about the air amount and the thermodynamic state of the scavenge air. The delivery ratio is a measure of the volumetric consumption of air per cylinder compared to a reference volume. The delivery ratio was presented in section 1.5 and described in equation 1.4 and 1.5. The delivery ratio can be used as an initial investigation of the scavenging process as it relates the volume flow with the required volume to be replaced.

Engine load	100	75	50	25	%
DR	0.67	0.76	0.91	1.00	-
V_{scav}	0.87	0.98	1.18	1.30	m^3
$\dot{V}$	5.44	5.44	5.62	5.00	$\frac{m^3}{s}$
t_{scav}	0.16	0.18	0.21	0.26	s

Table 5.3: Correlations between volume flow and scavenge port exposure time derived from the CFD results

The delivery ratio and volume flow are listed in table 5.3. As expected, the delivery ratio is highest at low engine load. The total volume flow rate per cylinder is listed in table 5.3 as $\dot{V}$ and is defined as the total volumetric amount of air added to the cylinder divided by the scavenging time, t_{scav}, which is the time the scavenge ports are open:

$$\dot{V} = \frac{V_{scav}}{t_{scav}}. \tag{5.2}$$

The volume flow rate is close to equal for all engine loads. This is due to the turbocharger's nozzle ring which is designed to operate at choked flow condition where the velocity of the gas is equal to the speed of sound of the gas in the orifice. The variations in $\dot{V}$ comes from variations in the exhaust gas temperature which in turn influences the speed of sound of the gas. This shows that the engine speed has a significant influence one the scavenging process as it determines the delivery ratio. The scavenging time, t_{scav}, determines the volumetric flow to the cylinder as the volume flow rate from the turbocharger is constant for all loads. For the engine load sweep, where both the power output and the engine speed varies, it is clear that it is not just the scavenging pressure which influence the delivery ratio, but also the scavenging time, t_{scav}.

The mass flow and volume flow (shown as DR) are shown in figure 5.4a and 5.4b. It shows that the mass flow rate for high engine loads is higher than for low engine loads, which is logical as more air is required to burn the extra fuel. However, when increasing the scavenging pressure, the density, ρ_{scav}, increase which lower the volume flow across the cylinder. Comparing the mass flow and the volume flow in figure 5.4a and 5.4b, shows that the 25% engine load case has the smallest amount of air by mass, but the highest amount of air by volume and vice versa for the 100% case. It should be pointed out that the studied engine is fitted with an Exhaust Gas Bypass, **EGB**, system. The **EGB** system is designed to bypass some of the exhaust gas from the turbine side of the turbocharger. It is for the part load optimization strategy, where an undersized turbocharger can be mounted on the engine. The **EGB** valve is then opened at 100 % load to circumvent some of the energy from the exhaust gas. At 75% load and lower the **EGB** valve is closed. The turbocharger will be able to produce

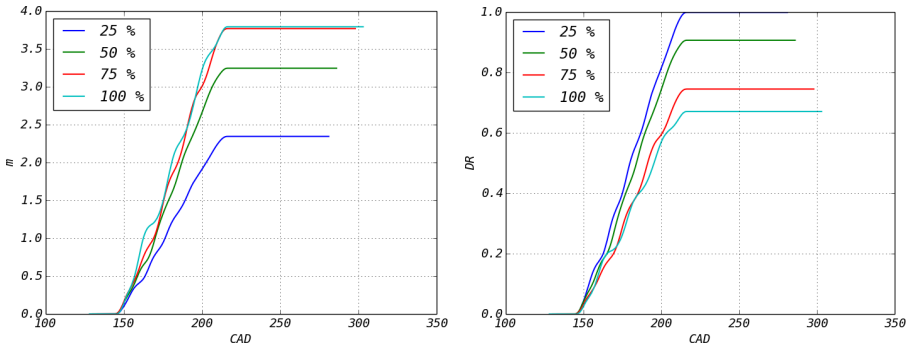

(a) Accumulated mass flow over scavenging ports for 100%, 75%, 50% and 25% engine load

(b) Accumulated volume flow divided by V_{ref} over scavenging ports for 100%, 75%, 50% and 25% engine load

Figure 5.4: CFD results showing a comparison of mass and volume flow for the engine load sweep

higher scavenging pressures at part load when the **EGB** valve is closed or partly closed. An engine with **EGB** is able to operate at higher scavenge pressures at part load compared to engine without the bypass option. A clear trend for the scavenging process is that the volume flow is more important than the mass flow for the scavenging process as the scavenging efficiency is decreasing with lower volume flow. This was also observed in the validation cases from section 4 where the difference in scavenging efficiency was caused by a reduction of volume flow.

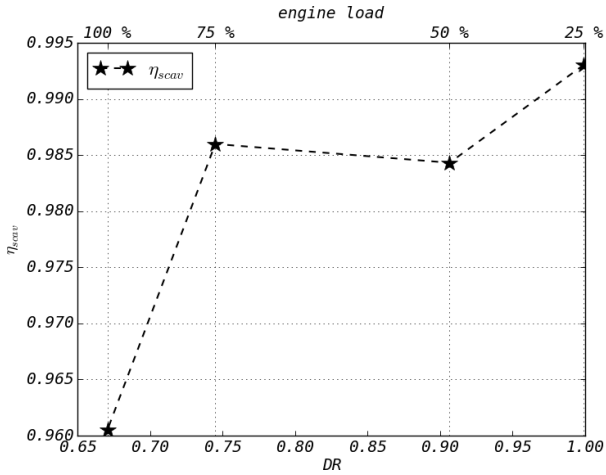

Figure 5.5: CFD result showing the scavenging efficiency for the engine load sweep

Figure 5.5 shows the scavenging efficiency for the engine load sweep as function of load and delivery ratio respectively. It has been established that the delivery ratio decreases with engine load as the scavenge pressure increases. The scavenging efficiency is highest for the 25% load case and lowest for the 100% load case. One interesting observation is that the scavenging efficiency for the 75% load case is higher than the 50% load case, despite a slightly lower delivery ratio. This artefact is due to the push out process as the scavenge air and exhaust mixture during the push out process can be stratified.

The bulk purity at scavenge port closing, IPC, is shown in figure 5.6a. This quantity is of interest as it represents the capacity of the flow driven part of the scavenging process to flush the cylinder for exhaust gas. This part of the scavenging process can be referred to as volumetric scavenging as is only takes the gas exchange between the scavenge air and exhaust gas into account. After IPC no air is added to the cylinder and the remaining of the scavenging process is driven by the piston motion, known as the push out process. Figure 5.6a shows the bulk purity at IPC as function of the delivery ratio. The figure shows that the purity of air at IPC scales with the delivery ratio. The increase in purity at IPC is close to linear when excluding the 100% engine load case (where the **EGB** valve is open). Figure 5.6b shows the contribution from the push out process on the bulk purity of air (scavenging efficiency). The change in purity is calculated as:

$$d\psi_{push\,out} = \eta_{scav} - \psi_{IPC}, \tag{5.3}$$

where η_{scav} is the bulk purity of air in the cylinder at EVC and ψ_{IPC} is the bulk purity of air in the cylinder at the start of the push out process. The change in volume is calculated by:

$$dV_{push\,out} = V_{IPC} - V_{EVC}, \tag{5.4}$$

where V_{IPC} and V_{EVC} is the cylinder volume at IPC and EVC respectively. The cylinder volume at IPC is geometrically bounded by the scavenge ports and is therefore constant for all engine loads, while the cylinder volume at EVC is dependent on the exhaust valve closing strategy. The crank angles for the exhaust valve closing for the engine load sweep are listed in table 5.1. The contribution from the push out process appears to be rather linear which is positive when attempting to create a generic, simple algebraic expression for the scavenging process.

Figure 5.7 and 5.8 show the purity, ψ, of air in the cylinder for the different engine loads as function of added mass flow and volume flow (delivery ratio) respectively. The trend is the same as for the validation cases in section 4.1.1 where the purity in the cylinder correlates with the added volume rather than with the added mass flow. Figure 5.7 shows the bulk purity as function of mass flow. The vertical portions at the end of the graphs is the contribution from the push out process. The purity as function of volume flow does not

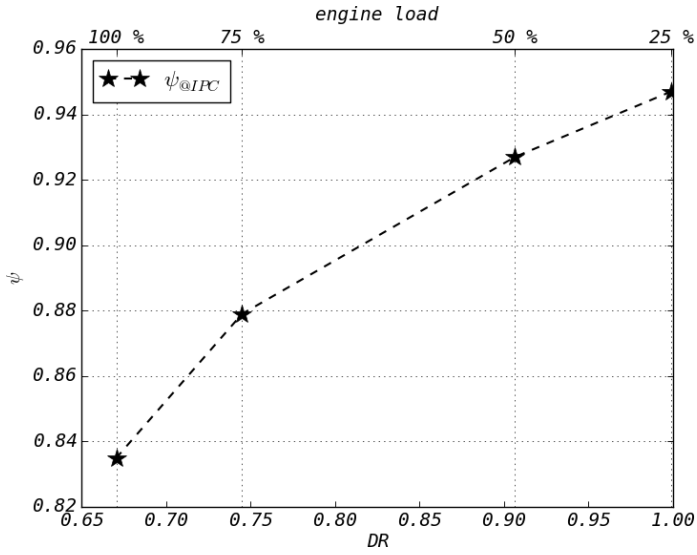

(a) Bulk puirity of scavenge air at scavenge port closing (IPC)

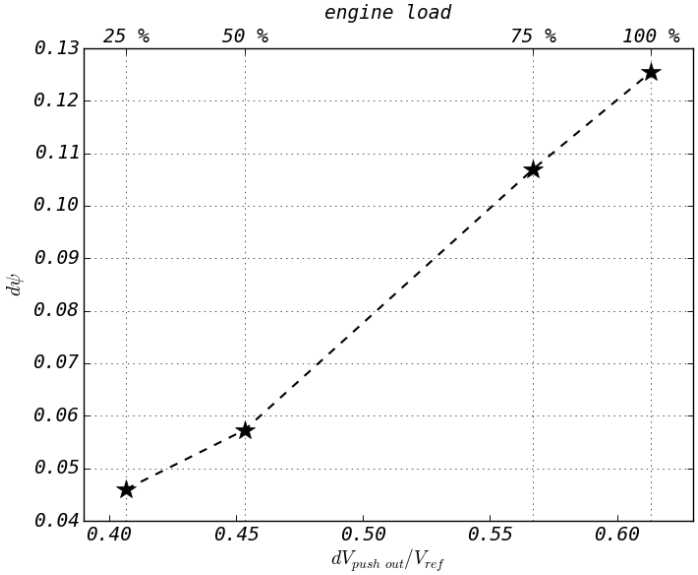

(b) Contribution to the bulk purity of air in the cylinder from the push out process

Figure 5.6: CFD result showing the contribution on the bulk purity of air from the push out process

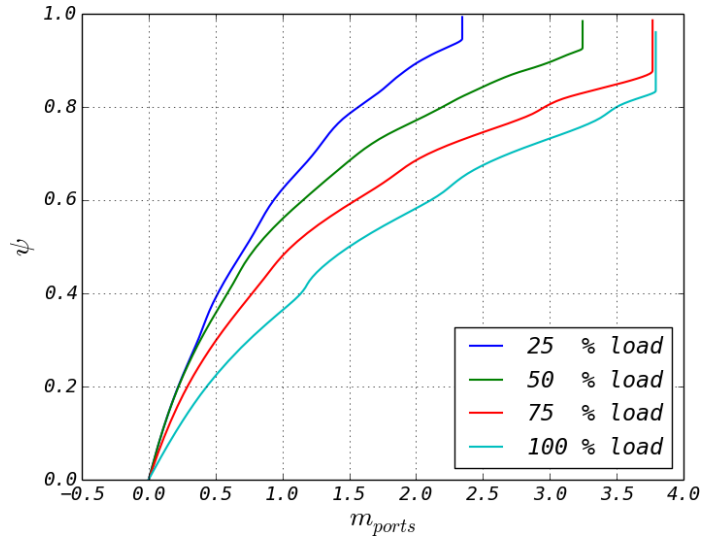

Figure 5.7: CFD results showing the bulk purity of scavenge air for the 100%, 75%, 50% and 25% engine load as function of mass flow.

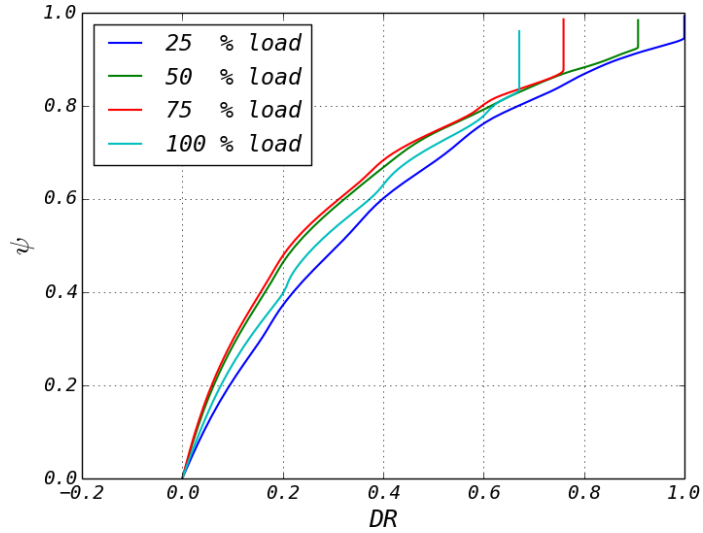

Figure 5.8: CFD results showing the bulk purity of scavenge air for the 100%, 75%, 50% and 25% engine load case as function of delivery ratio.

seem to match as well as in the validation case (figure 4.8b). There is a larger deviation between the individual purities in figure 5.8 although the curves appear

to converge onto the same line at the late stages of the scavenging process. The deviations observed in figure 5.8 are caused by the density difference between the scavenge air and the exhaust gas in the cylinder. At different engine loads, the density ratio between the exhaust gas and the scavenging air, ρ_{ex}/ρ_{scav}, varies which influences the shape of the curves observed in figure 5.8.

5.1.3 Perfect displacement model

The perfect displacement model from Sher (1990) was applied with good agreement to the two cases presented in section 4. The normal swirl arrangement and the high swirl port configuration cases were run under similar operating conditions was very similar with only small differences in the density ratio ρ_{ex}/ρ_{scav}. This ratio varies in the engine load sweep as the scavenge pressure increase with load as well as the in-cylinder pressure is affected by the engine load. The density ratios for the engine load sweep, used when calculating the purity with equation 1.10, are shown in table 5.4.

Engine load %	100	75	50	25
ρ_{ex}/ρ_{scav}	0.39	0.26	0.29	0.46

Table 5.4: Density ratios for the engine load sweep.

Figure 5.9, 5.10, 5.11 and 5.12 show the bulk purity of air in the cylinder as function of the delivery ratio calculated from the CFD results and with equation 1.10. As for the validation case, the CFD simulation and the perfect displacement model show good agreement. The CFD model and the perfect displacement model results are in perfect agreement when $DR < 0.2$ where the mixing of the scavenge air and exhaust gas starts to influence the bulk purity of scavenge air in the CFD model.

The results also show that the density ratio ρ_{ex}/ρ_{scav} can explain the differences observed in figure 5.8 where the purity as function of the delivery ratio showed differences in the gas exchange rate between the four CFD simulations. In figure 5.2 the bulk purity of scavenge air in the cylinder as function of the delivery ratio for all four simulations was shown in a single figure. The figure showed individual differences in the purity for $0 < DR < 0.6$. Since all the engine load cases follow the theoretical perfect displacement model of Sher (1990), the deviations in figure 5.2 must come from the ρ_{ex}/ρ_{scav} ratio. The bulk purity of scavenge air in the cylinder is defined as the ratio of the mass of scavenge air to the total mass in the cylinder. The delivery ratio is defined in terms of volume. The compressed and cooled scavenge air has a higher density than the hot exhaust gas. The density ratio therefore influences the shape of the purity as function of delivery ratio curve.

Figure 5.13 shows the perfect displacement model with different density ra-

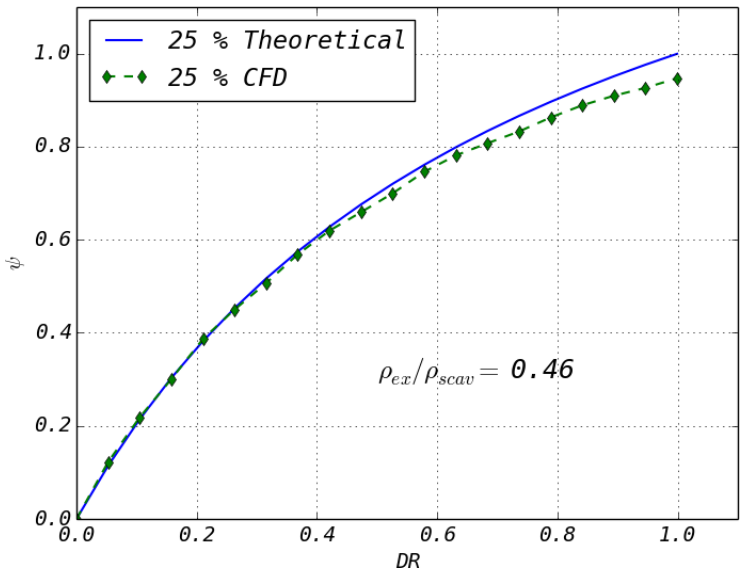

Figure 5.9: Bulk purity of scavenge air from CFD results and perfect displacement model (equation 1.10) for the 25% engine load case.

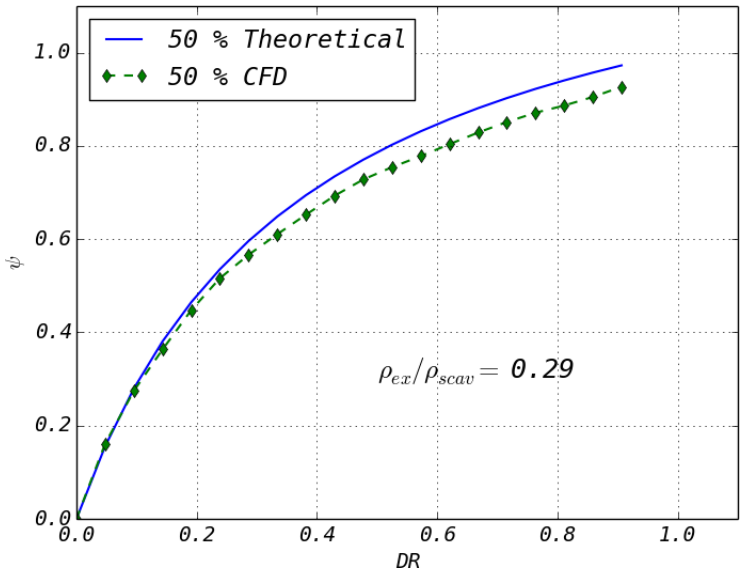

Figure 5.10: Bulk purity of scavenge air from CFD results and perfect displacement model (equation 1.10) for the 50% engine load case.

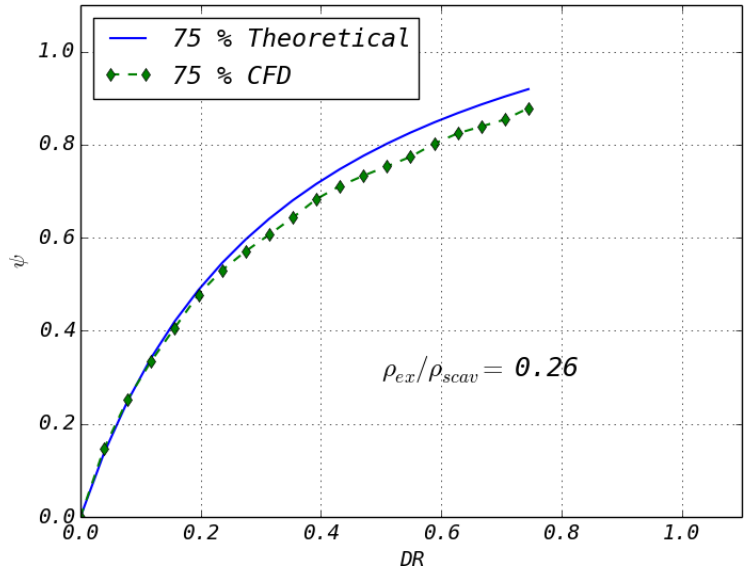

Figure 5.11: Bulk purity of scavenge air from CFD results and perfect displacement model (equation 1.10) for the 75% engine load case.

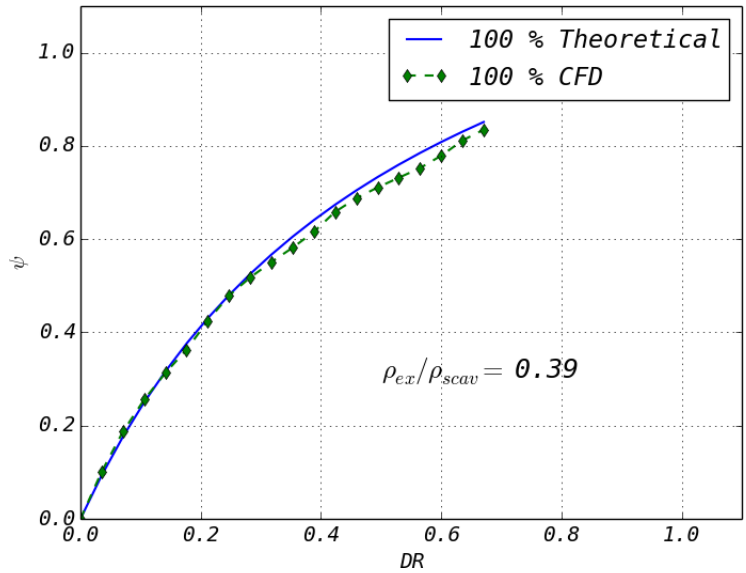

Figure 5.12: Bulk purity of scavenge air from CFD results and perfect displacement model (equation 1.10) for the 100% engine load case.

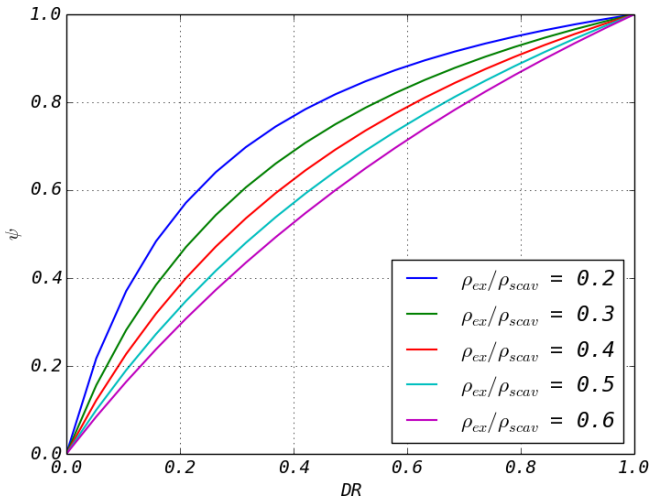

Figure 5.13: Varying the density ratio ρ_{ex}/ρ_{scav} in the perfect displacement model, equation 1.10.

tios to highlight the influence of ρ_{ex}/ρ_{scav}. The difference in density ratio also sheds light on the mixing process in the cylinder. The perfect displacement model of Sher (1990) does not take any mixing into consideration, indicating that the difference between the CFD model and the perfect displacement model represents the mixing of the introduced scavenge air and the exhaust gas in the cylinder. A comparison of figure 5.9, 5.10, 5.11 and 5.12 indicates that mixing increases with difference in density between the scavenge air and exhaust gas. The 50% and 75% engine load cases, shown in figure 5.10 and 5.11, are only accurate up until approximately DR = 0.2 before the perfect displacement model and CFD model starts to separate due to mixing. At 25% and 100% engine load, figure 5.9 and 5.12 do not diverge until approximately DR = 0.4. Even after this point the perfect displacement model and the CFD model are in good agreement and it appears to be less mixing between the scavenge air and the exhaust gas. The bulk purity of air is plotted against the perfect displacement model (equation 1.10) in figure 5.14. Using equation 1.10 as the abscissa creates a straight line from 0 to 1 witch represents the theoretical perfect displacement. By plotting the bulk purities calculated from the CFD results in the same manner show how the CFD model follows the theoretical perfect displacement model. Presenting the results in this way shows that the CFD model and the perfect displacement model of Sher (1990) are in good agreement.

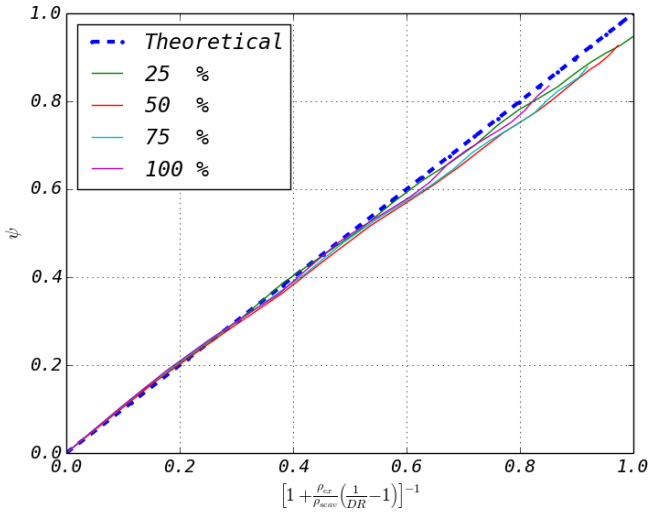

Figure 5.14: Bulk purity of air, ψ, in the cylinder. Comparison between the CFD model and the perfect displacement model of Sher (1990)

5.1.4 Flow visualization

The scavenge flow through the engine can be visualized with the passive scalar from equation (2.17). A cross section in the y-x plane is extracted and is used as a visual representation of the gas exchange and mixing process in the cylinder. Figure 5.15 shows a comparison between the four load cases at bottom dead center. This figure shows that the 25% and 50% case have scavenging air reaching almost the exhaust valve at BDC, while the 75% and 100% engine load cases have only roughly $50-60\%$ of the cylinder filled with fresh air.

Figure 5.16a, 5.16b,5.16c, 5.16e, 5.16f, 5.17a, 5.17b, 5.17c and 5.17d show the evolution of the gas exchange during the scavenging process for the engine load sweep. The scalar visualization of the scavenging process is shown in terms of delivery ratio rather than crank angle. It should be pointed out that it implies that the figure for the different engine loads does not correspond to the same crank angle. When comparing the scalar fields at the same crank angle, larger differences in the scalar distribution are observed due to differences in volume flow rate, as observed in figure 5.4b. Comparing the evolution of the scavenging process with the passive scalar field at the same delivery ratio gives a visual understanding of the mixing between the introduced scavenge air and the exhaust gas. There are individual differences between the scalar fields during the scavenging process. The scalar fields shows that a mixing region between the scavenge air and the exhaust gas is present in the cylinder during scavenging.

Figure 5.18 shows the contribution from the push out process. The top row of figures show a scalar visualization of the cylinder content at IPC and the bottom

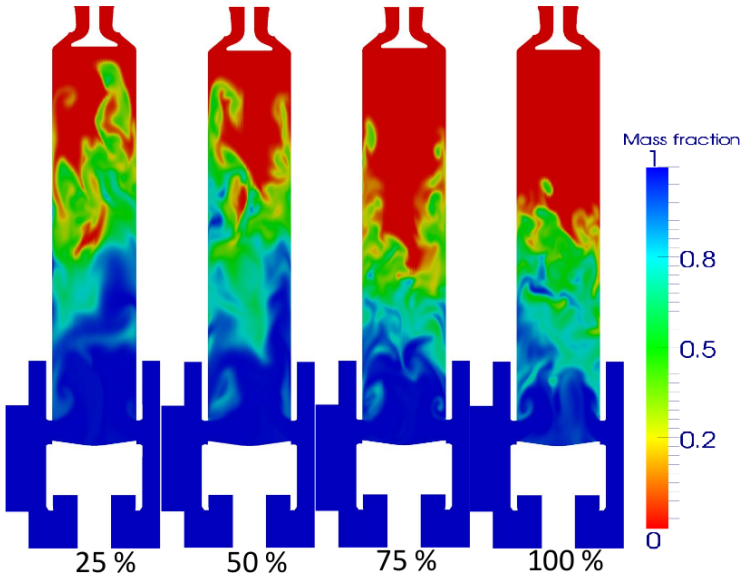

Figure 5.15: Mass fraction at BDC for the engine load sweep, CFD results

row show the cylinder content for the corresponding engine loads at EVC. The figure visualizes the push out process where the burned gases, primarily located in the cylinder head, is displaced by the piston motion. The figure also shows how the exhaust valve closing, EVC, affects the push out process. The figure shows that there are relatively large differences in the bulk purity of scavenge air in the cylinder when the scavenge ports close. The 25% and 50% load cases are almost fully flushed, while the 75% and 100% load cases still have a mixture of scavenge air and exhaust gas present in the top half of the cylinder.

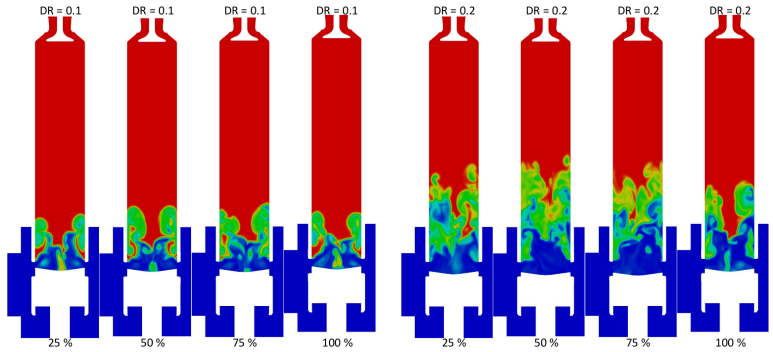

(a) DR = 0.1 (b) DR = 0.2

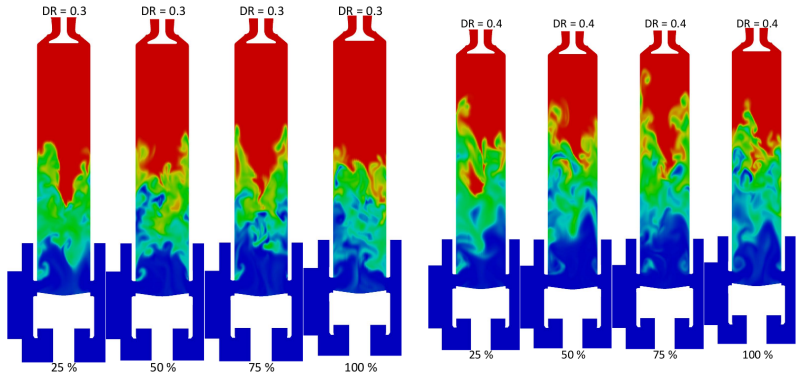

(c) DR = 0.3 (d) DR = 0.4

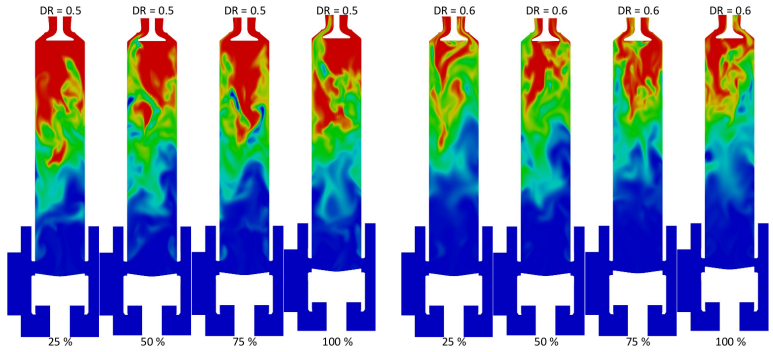

(e) DR = 0.5 (f) DR = 0.6

Figure 5.16: Visualisation of the passive scalar, CFD results

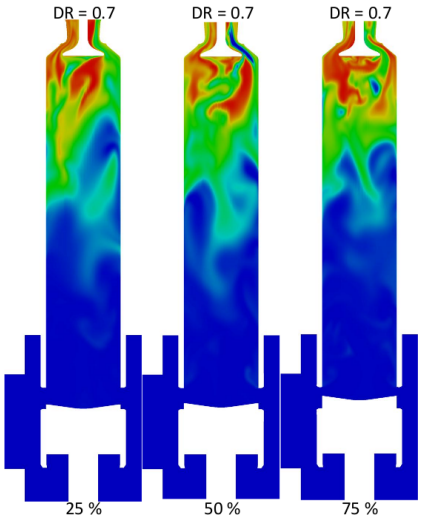

(a) DR = 0.7

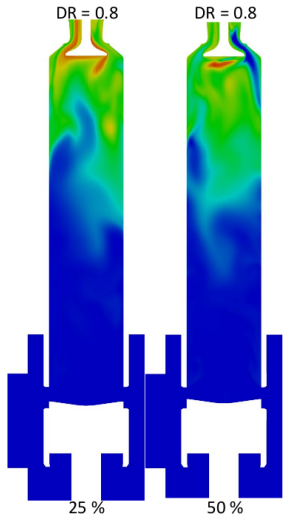

(b) DR = 0.8

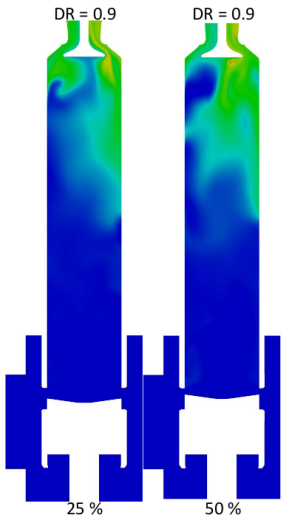

(c) DR = 0.9

(d) DR = 1.0

Figure 5.17: Visualisation of the passive scalar, CFD results

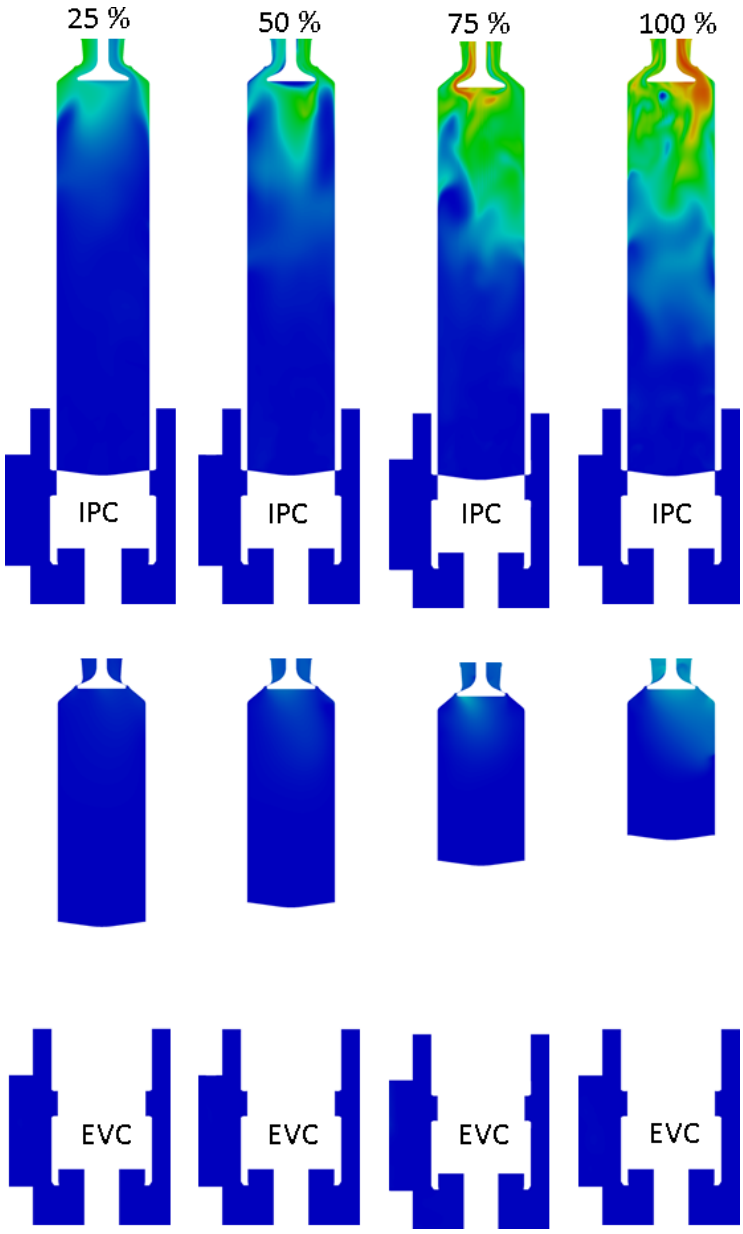

Figure 5.18: Scalar visualization of the push out process for the engine load sweep, CFD results

5.2 Scavenge pressure sweep

The previous section presented an engine load sweep following the propeller curve where both the mean effective pressure, scavenge pressure, exhaust pressure and engine speed varied. This section will investigate a parameter sweep where only the scavenge pressure is changed. Three test cases corresponding to a test series conducted on the T50ME-X test engine at the Diesel Research Center in Copenhagen is subjected to CFD analysis. As stated earlier in the report, a trend within the marine engine industry has been to introduce the two-stroke Miller cycle to reduce the formation of NOx emissions and to transfer some of the compression work from the piston to the turbocharger. This is done by increasing the scavenge pressure, p_{scav}. Increasing the scavenge pressure will increase the density, which in turn will decrease the volumetric flow rate across the engine. Both the validation case in section 4 and the engine load sweep in section 5.1 show that increasing the scavenge pressure has a negative effect on the scavenging process, as it reduces the volume flow.

Test nr	1	2	3	
Engine load	75	75	75	%
RPM	111.8	111.8	111.8	min^{-1}
EVO	116	125	129	$CAD\,atdc$
EVC	243	278	293	$CAD\,atdc$
p_{scav}	3.36	4.54	6.30	bar
ρ_{scav}	3.86	5.22	7.21	kg/m^3

Table 5.5: Operating conditions for the three cases where the scavenge pressure is varied

Table 5.5 shows the operating conditions for the three test cases presented in this section. Test 1 is a reference case where the engine is run at "normal" operating conditions so the scavenge pressure is representative for a typical two-stroke marine engine at the given engine load. The influence of increased scavenge pressure is readily seen in the table when evaluating the values of exhaust valve opening (EVO) and exhaust valve closing (EVC). When the scavenge pressure increases both EVO and EVC increase. Exhaust valve opening increases as the pressure difference between the cylinder pressure and the scavenge box pressure is inversely proportional with the scavenging pressure. This is beneficial for the specific fuel oil consumption as the compressed gas in the cylinder is allowed to perform work on the piston for a longer time. The exhaust valve closing increases with the scavenge pressure as the difference between p_{scav} and p_{comp} decreases. As stated earlier in the report, the engine control system determines the closing time for the exhaust valve based on the ratio p_{comp}/p_{scav}. The timing for the closing of the exhaust valve increases by 50 crank angles

when the scavenge pressure is increased from 3.46 bar to 6.30 bar.

5.2.1 Scavenging efficiency, delivery ratio and perfect displacement model comparison

Test nr	1	2	3	
η_{scav}	95.6	89.6	89.8	%
$\psi_{@IPC}$	93.8	81.0	75.4	%
$d\psi_{push\,out}$	1.8	9.6	14.4	%
DR	0.92	0.67	0.54	

Table 5.6: Results from the CFD analysis

The results from the CFD analysis is listed in table 5.6. As expected the increased scavenge pressure has a negative effect on the scavenging process. The "normal" case, test nr 1, has the highest scavenging efficiency, delivery ratio and purity at IPC. The case with the highest scavenging pressure, test 3, has the lowest scavenging efficiency and the smallest delivery ratio. According to the CFD analysis, the integrated volume flow only constitute 54% of the cylinder volume at BDC.

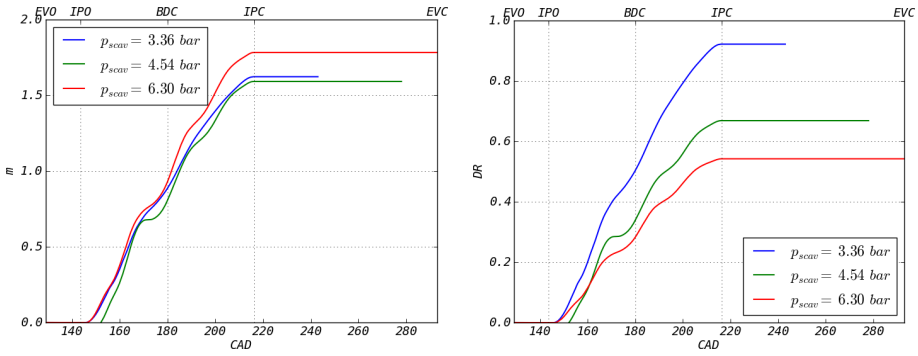

(a) Mass **(b)** Volume

Figure 5.19: CFD results shoing the integrated mass and volume flow for the three test cases

Figure 5.19 shows the integrated mass and volume flow rate for the three cases presented in this section. The results in the figures show that the increased scavenge pressure reduces the delivery ratio. There is one feature worth noticing in figure 5.19. Test nr 2, $p_{scav} = 4.54$ bar, appears to have a delay in terms of mass and volume flow. While test 1 and 3 experience a rise in mass and volume

flow rates shortly after the scavenge ports are uncovered. On the contrary test 2 has a delay of approximately 7 crank angles. This delay is caused by a large blow back, where the timing of the exhaust valve opening is not sufficient to balance the pressure in the cylinder and the scavenge receiver. A scalar visualization of the blow back is shown in figure 5.20. Snapshots at different crank angles show how the exhaust gases (red) is blown into the scavenge box due to the pressure difference between the cylinder and the scavenge box. The blow back last for several crank angles, from IPO until approximately 151 CAD where the scavenge air starts to enter the cylinder. The effective port area is blocked during the blow back which will reduce the integrated port area and thereby the flow rate across the scavenge ports.

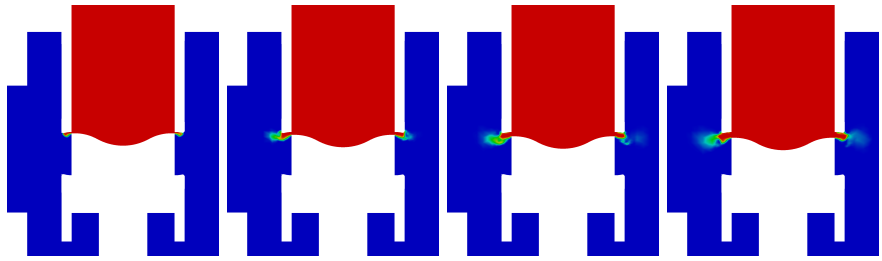

(a) 144.5 CAD **(b)** 145.5 CAD **(c)** 146.5 CAD **(d)** 147.5 CAD

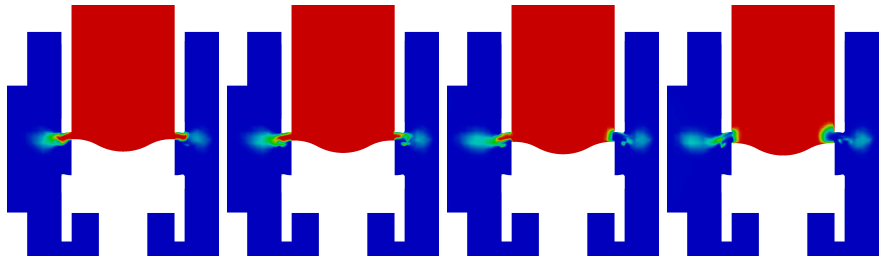

(e) 148.5 CAD **(f)** 149.5 CAD **(g)** 150.5 CAD **(h)** 151.5 CAD

Figure 5.20: Visualization of the blow back occurring between IPC and approximately 151 CAD atdc for test 2. CFD results

The volumetric and piston driven contribution to the scavenging process is shown in figure 5.21a and 5.21b where the bulk purity at scavenge port closing, IPC, and the $d\psi_{push\,out}$ is plotted separately. The observation from the figure is that the scavenging process is impaired at excessive scavenging pressures. Figure 5.21a verifies the trend observed in the engine load sweep (figure 5.6a) where the relationship between the purity of scavenge air in the cylinder and the delivery ratio were linear. The contribution from the push out process is also verified by this test series, where the trend is the same as for the engine

load sweep. The contribution to the scavenging efficiency is nearly linear with piston displacement, which indicate that the exhaust valve closing strategy is of importance for the overall scavenging process.

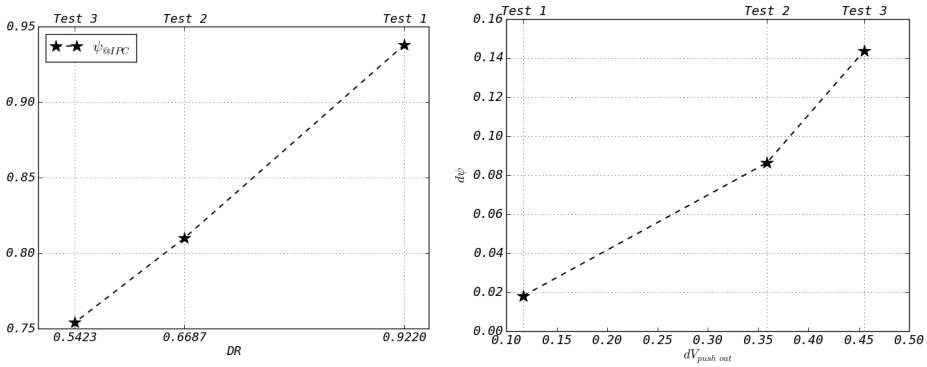

(a) Purity at scavenge port closing

(b) Scavenging by piston displacement

Figure 5.21: CFD results showing the volumetric contribution and the piston driven part of the scavenging process

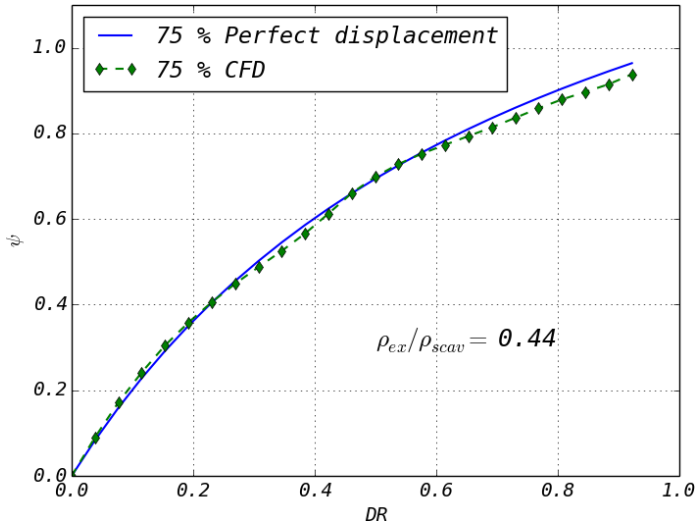

Figure 5.22: Comparison between the CFD model and the perfect displacemnt model of Sher (1990) for Test 1.

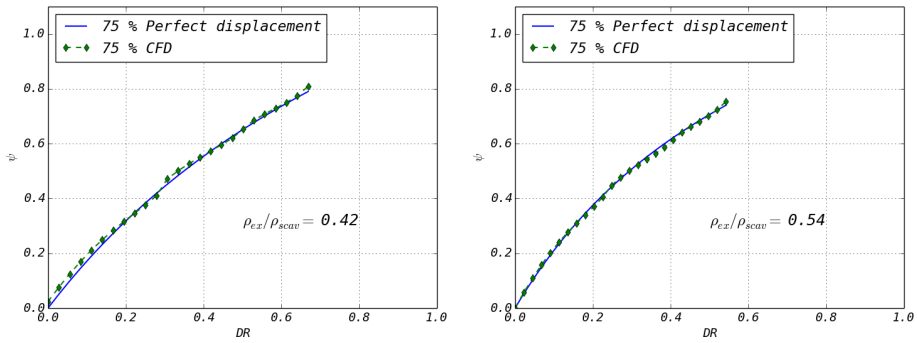

(a) Test 2 (b) Test 3

Figure 5.23: Comparison between the CFD model and the perfect displacement model of Sher (1990) for the three test cases presented in this section

Figure 5.22, 5.23a and 5.23b show a comparison between the CFD model and the perfect displacement model from equation 1.10. Again the CFD model and the theoretical perfect displacement model are in good agreement. Test case 2 and 3 have scavenging pressures in excess of normal operating conditions which reduce the delivery ratio significantly. The delivery ratio for the two test cases is so low that the CFD results and the perfect displacement model have not separated due to the influence of mixing between the scavenge air and the exhaust gas.

The influence of scavenge pressure has been investigated in this section. The intention was to further explore the close relationship between the delivery ratio and the scavenging efficiency in uniflow scavenged two-stroke diesel engines. The numerical analysis of the scavenging process so far has shown that increasing scavenge pressure, despite the positive effects on fuel consumption and NOx formation, may have an adversary effect on the scavenging process and thereby deteriorate the combustion process and increase engine component fatigue.

5.3 Sensitivity study of the scavenge port angle

This section will investigate the influence of the in-cylinder swirl on the scavenging process in uniflow scavenged two-stroke diesel engines. The validation case from section 4.1.1 did also contain a brief assessment of the in-cylinder swirl. This section will present a much more comprehensive study where the scavenge port geometry is varied from 0° to 30° to investigate the sensitivity of the scavenging process. The flow structure in the cylinder depends greatly on the in-cylinder swirl. A central jet like profile is expected to dominate the flow in the case of no in-cylinder flow while high swirl will generate a wake like

profile characterized by wall bounded jets and a central recirculation zone. The 75% engine load case from section 5.1 is used as baseline for the study. The boundary conditions are kept constant while only the port geometry is varied.

5.3.1 In-Cylinder swirl

This section aims to investigate if the in-cylinder swirl influences the scavenging process in marine two-stroke diesel engines. Section 4.1.1, 5.1 and 5.2 showed that the scavenging process in uniflow scavenged two-stroke diesel engines consist of three processes: perfect displacement, mixing between the exhaust gas and the scavenge air and by displacement due to piston motion (push out process). Ideally the cylinder should be fully scavenged by pure displacement without any mixing of scavenge air and the exhaust gas. Sources of mixing are; the jet impingement of scavenge air into the cylinder through the 30 individual scavenge ports, mixing due to flow separation located at the scavenging port's sharp top and side edges, diffusivity between the gas and scavenge air at the head of the flow and mixing due to central recirculation zones (vortex breakdown).

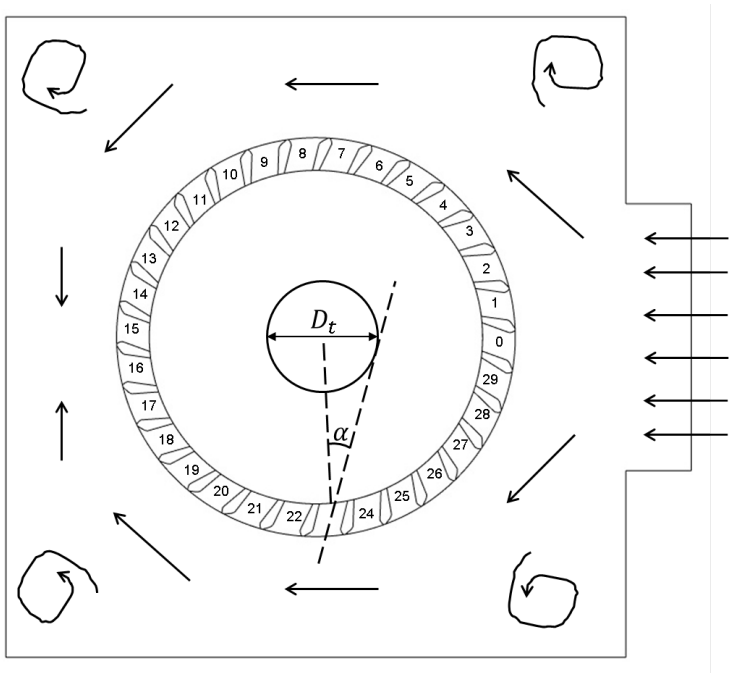

Figure 5.24: Cross section of the scavenging box, seen in the axial direction. The arrows indicate the distribution of scavenge air from the inlet (right side) and troughout the scavenge box. The numbers indicates the scavenge port numbers

A cross sectional drawing of the scavenge ports is shown in figure 5.24. The ports are angled with respect to the local radius. The port angle is defined as the angle between the line from the center of the cylinder to the midpoint of the inner port area, and the line along the port center axis. The center axis for the port will tangent an imaginary circle in the cylinder center, this circle has the diameter, D_t, which can be used to characterise the scavenge port geometry.

The scavenging ports are angled with respect to the local radius to introduce a tangential component to the in-cylinder flow. Swirling flow in the cylinder is beneficial with respect to the mixing of air and fuel as the fuel is injected in the same direction as the cylinder swirl. This facilitates the fuel droplets to be convected with the flow for a more homogeneous distribution of fuel droplets and air in the combustion chamber. The in-cylinder swirl can also minimize the recirculation zones at the sharp edges at the top and side corner of the scavenging ports where flow separation is likely to occur. The influence of the asymmetric inlet is also minimized by the swirling component of the in-cylinder flow. As the scavenge receiver is located at the side of the cylinder, the air will enter the scavenge box from one side only. This will bias the radial velocity profile for the axial component in the cylinder to the opposite side of the inlet. The cylinder swirl will distribute the introduced air more evenly across the cylinder cross section.

port angle (α)	**swirl number** (Ω)
0°	0
10°	0.215
15°	0.327
18°	0.396
20°	0.444
25°	0.568
30°	0.704

Table 5.7: Geometric swirl number for different port angles α

A total of 7 port geometries will be investigated in this study: 0°, 10°, 15°, 18°, 20°, 25° and 30°. The ports have been modified whereas the nominal area (port width) is kept constant. Keeping the nominal flow area constant should not influence the flow rate across the respective scavenge ports and discrepancies should in pressure drop should therefore be attributed to the increased in-cylinder increased swirl.

The geometric swirl number from equation 4.4 is used to quantify the in-cylinder swirl:

$$\Omega = \frac{A_{cyl}}{A_{ports}} \cdot sin(\alpha).$$

5.3.2 Initial conditions

As stated in the previous section, the 75% load case from section 5.1 is used as basis for this study. All temperatures, pressure boundaries and initial conditions are kept constant while the angle of the scavenge ports is changed. The initial velocity field in the cylinder must be modified to account for swirl. The procedures for generating the in-cylinder velocity field was described in section 3.2.3. The tangential component of the in-cylinder flow is initialized based on a PIV measurement corresponding to the standard port configuration. Changing the port angles will affect the swirl so the tangential velocity component was scaled to compensate for the variation in port angle.

It was decided to scale the swirl number from equation 3.12 with the change in angular momentum using the 75% engine load case as baseline. The bulk average angular momentum in the cylinder is calculated from equation 2.53. A steady state simulation with the piston at bottom dead center and the exhaust valve fully opened was conducted to produce an estimate of the in-cylinder bulk average angular momentum. The swirl number was then scaled with

$$Sw_{\alpha} = Sw \cdot \frac{L_{\alpha\, steady\, state}}{L_{ref\, steady\, state}}, \tag{5.5}$$

where $L_{\alpha\, steady\, state}$ is the angular momentum in the cylinder for the steady state simulation for port angle α, and $L_{ref\, steady\, state}$ is the angular momentum in the cylinder for the steady state simulation for the reference case (75% engine load from section 5.1). The steady state simulations were carried out using a compressible SIMPLE based solver where the driving pressure difference between the exhaust receiver and the scavenge receiver was replaced with an average volume flow rate. The average flow rate was calculated based on the mass flow rate obtained by the CFD model

$$\dot{V} = \frac{\dot{m}}{\rho_{scav}}, \tag{5.6}$$

where $\dot{m}$ is the average mass flow rate during the scavenging process for one cylinder. The CFD model evaluates the flux across the scavenge port patch faces and the average mass flow rate during scavenging can be calculated from the following

$$\dot{m} = \frac{\sum \dot{m}_{ports} \cdot dt}{t_{scav}}, \tag{5.7}$$

where $\dot{m}_{ports}$ is the instantaneous mass flow rate across the scavenging ports, dt is the current time step and t_{scav} is the scavenging time, the time between scavenge port opening and scavenge port closing.

The bulk average angular momentum is usually determined by integrating over the entire cylinder cell zone. It was decided in the steady-state simulations to exclude the regions close to the scavenging ports and the exhaust valve when

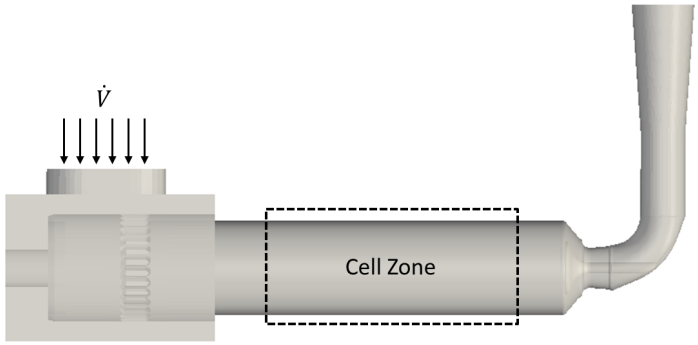

Figure 5.25: The stationary engine geometry at BDC showing the region where the angular momentum was evaluated.

evaluating the angular and axial momentum in the cylinder. A new cell zone was generated and the angular momentum calculated with equation 2.53 was only calculated for the cells within this zone. The cylinder and the corresponding cell zone are shown in figure 5.25.

α	0°	10°	15°	18°	20°	25°	30°
L/L_{ref}	0.18	0.56	0.83	1.00	1.16	1.56	1.95

Table 5.8: Scaling factors for the swirl number, Sw, used to generate the initial velocity field in the cylinder

The scaling factors for the swirl number used as input for the algorithm, which generates the initial in-cylinder velocity fields, are listed in table 5.8.

5.3.3 Flow visualization

In this section, one will visually inspect the distribution and mixing of the scavenge air and the exhaust gas with a passive scalar (equation 2.16). Figure 5.26 shows the scalar field (unity at inlet) in the cylinder at 155 CAD atdc which is 12.5 CAD after IPO. The figure shows a large diversity in the distribution of scavenge air and exhaust gas between the port configurations. For $\alpha = 0°$, a distinct central jet-like flow field is observed with a column of scavenge air stretching trough one third of the cylinder length. A recirculation zone at the liner wall is present, where pockets of exhaust gas are trapped at the sharp edges on the scavenging ports. For $\alpha = 30°$ the in-cylinder flow field is dominated by a wake like profile, where the introduced scavenge air is concentrated along the liner wall instead of the center axis. The wall jet structure is caused by a strong vortex, with possible vortex breakdown, located in the center of the

cylinder. The swirl is so strong in the $\alpha = 30°$ simulation that although the scavenge air stretches through approximately 20% of the cylinder the content in the center axis consists of 100% exhaust gas. The $\alpha = 0°$ and the $\alpha = 30°$ port configurations represent the extremities within the port angle study. The port configurations from $\alpha = 10°$ to $\alpha = 25°$ show a transition from a central jet like dominated profile to wall jet dominated profile.

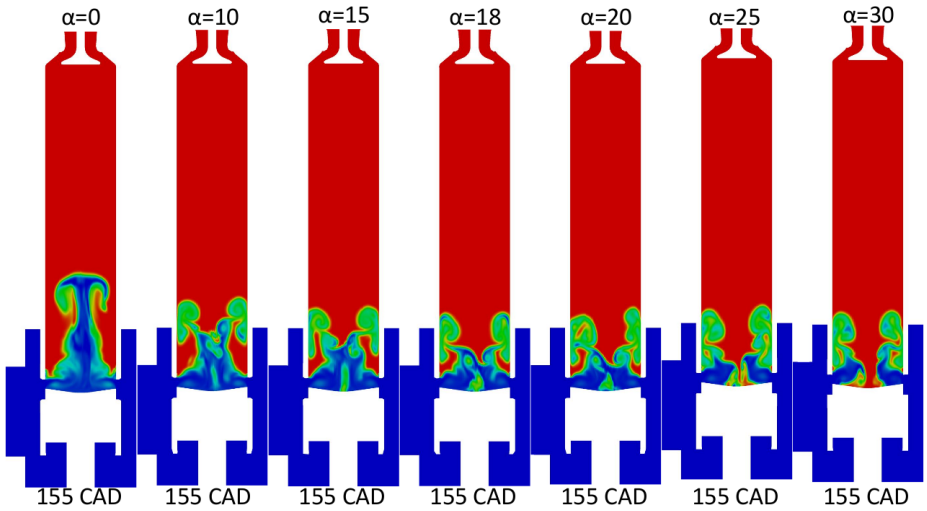

Figure 5.26: Visualization of the passive sclar for the 7 port angle configurations at 155 CAD atdc, CFD results

Figure 5.27 shows the distribution of the scavenge air and the exhaust gas at 170 CAD after top dead center. It appears that the $\alpha = 0°$ port configuration has the best performance as the scavenge air stretches further up the cylinder than in the simulations with a higher port angle. However, the $\alpha = 0°$ ports still have recirculation zones located above the scavenge ports where exhaust gas is trapped. The flow field is still dominated by a central jet like profile and the head of the introduced scavenge air is stratified. The $\alpha = 30°$ port simulation still has exhaust gas present in the center of the cylinder due to the vortex break down where a pocket of exhaust gas is trapped due to the central recirculation zone. The $\alpha = 0°$ and $\alpha = 30°$ port represent the two extremes, the port angles in between share the same characterizations, but they are less pronounced.

Figure 5.28 shows the distribution of the scavenge air and the exhaust gas at bottom dead center. A wake like profile is now present for the $\alpha = 15°$, $\alpha = 18°$, $\alpha = 20°$, $\alpha = 25°$ and $\alpha = 30°$ port angles. This is caused by the strong swirl with a radial deficit in the axial velocity component towards the vortex core. The vortex core increases with swirl, which is consistent with the observations in figure 5.28 where the interface between the scavenge air and the exhaust gas

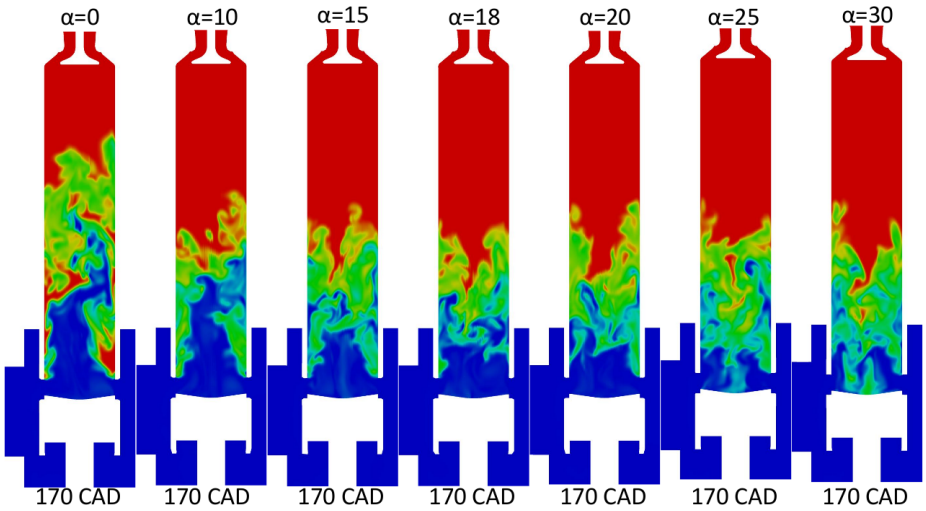

Figure 5.27: Visualization of the passive sclar for the 7 port angle configurations at 170 CAD atdc, CFD results

has a more distinct v-shaped profile for the high port angles.

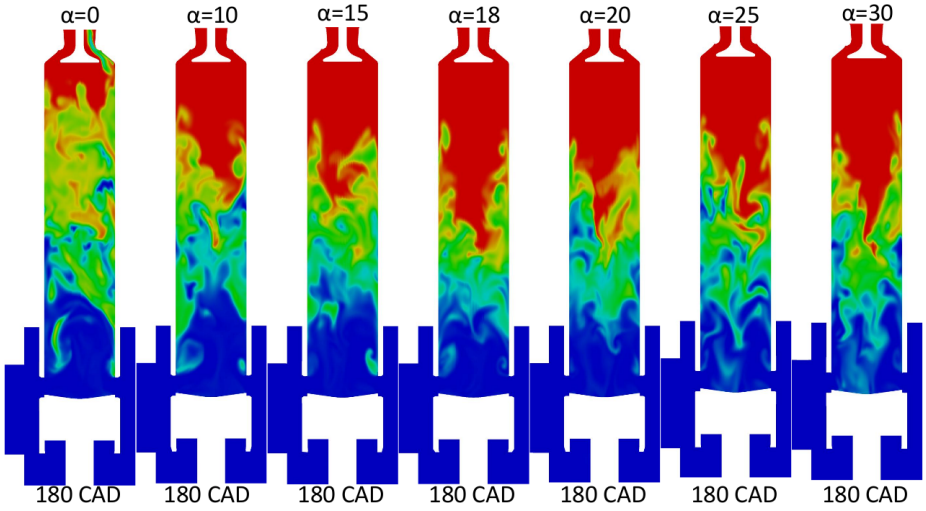

Figure 5.28: Visualization of the passive sclar for the 7 port angle configurations at 180 CAD atdc, CFD results

Figure 5.29 shows the scalar field (unity at inlet) at 200 CAD after top dead center. For $\alpha = 30°$ some residual exhaust gas is present along the center axis

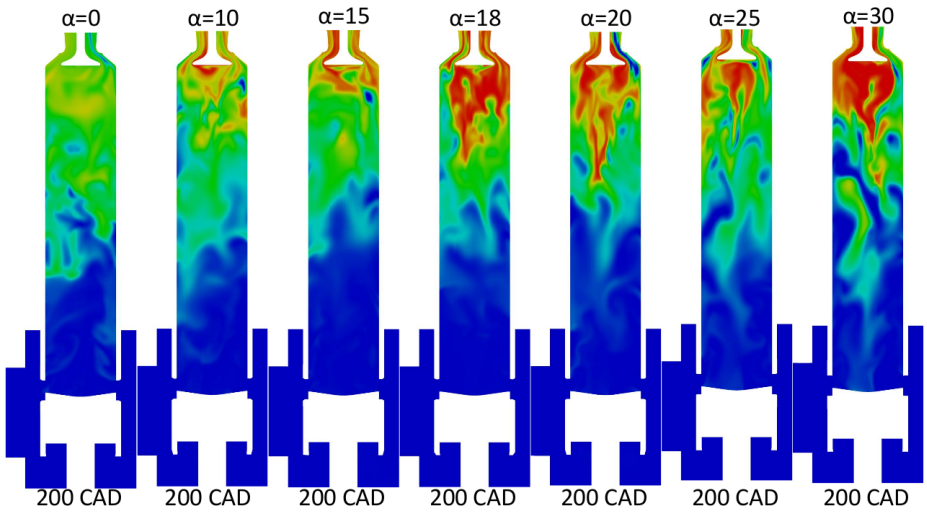

Figure 5.29: Visualization of the passive sclar for the 7 port angle configurations at 200 CAD atdc, CFD results

down to the piston. At this crank angle the simulations with a low swirl port configuration shows that the bottom 1/3 of the cylinder consists of pure scavenge air at 200 CAD. The largest stratification of scavenge air and exhaust gas is found in the top of the cylinder, especially for the high swirling port configurations. This is consistent with the reduced axial velocity component along the center axis of the cylinder for the high swirl cases. Figure 5.29 also visualizes the influence of the swirl on the component heat load. The low swirling port configurations appear to have a more uniform distribution of the cool scavenge air compared to the high swirling cases where the center part of the cylinder has a larger presence of exhaust gas in the mixture. The scavenging process is responsible for cooling the exhaust valve, which is known to be heavily subjected to thermal loads during the combustion process. Reducing the in-cylinder swirl and thereby transforming the wake-like profile to a jet like profile could benefit cooling of the exhaust valve.

Figures 5.30 and 5.31 show the distribution of the scavenge air and the exhaust gas at IPC and EVC respectively. The differences observed between figure 5.30 and 5.31 is caused by the push out process where the piston displaces the cylinder content. Observing the scalar fields in figure 5.30 does not reveal a large influence of the scavenge port arrangements in terms of the purity of scavenge air when the scavenging ports are closed. Figure 5.31 shows the scalar field at EVC. At exhaust valve closing the cylinder content is primarily scavenge air. Qualitatively, it appears that the $\alpha = 0°$ and the $\alpha = 30°$ port arrangements have some exhaust gas residue present in the cylinder.

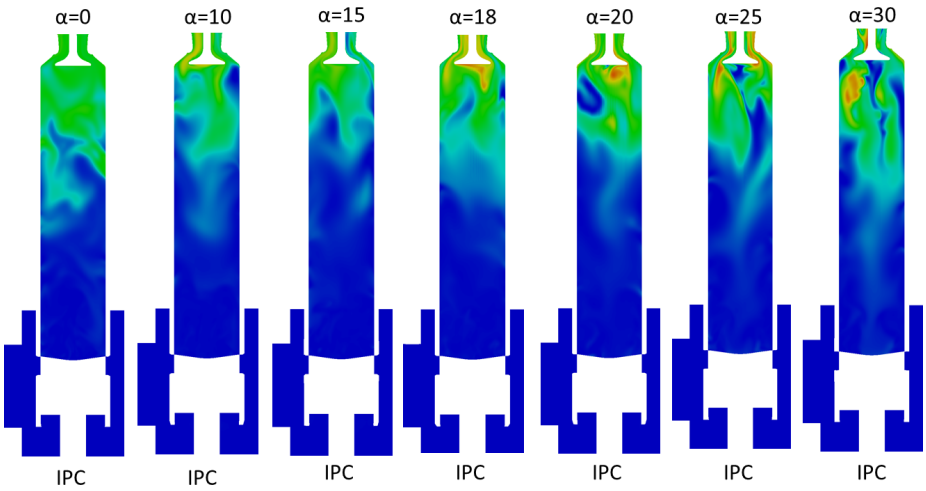

Figure 5.30: Visualization of the passive sclar for the 7 port angle configurations at IPC, CFD results

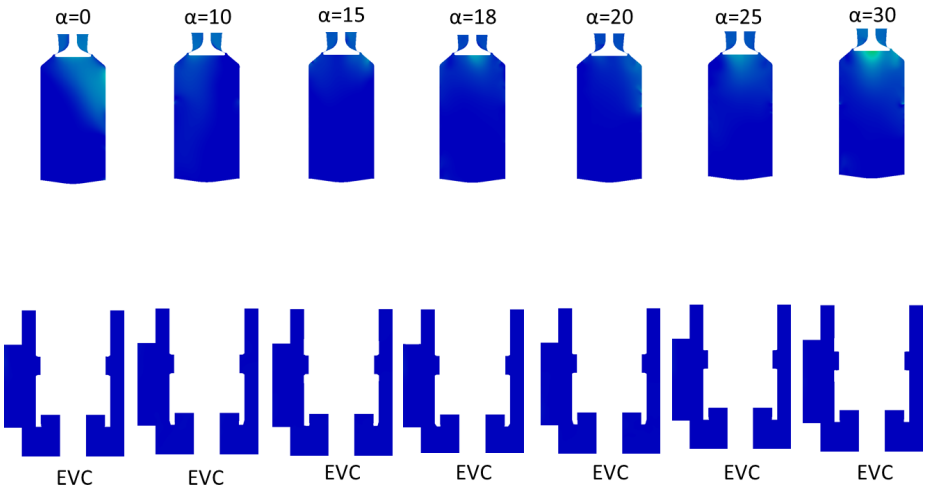

Figure 5.31: Visualization of the passive sclar for the 7 port angle configurations at EVC, CFD results

5.3.4 In-cylinder transient momentum

The transient in-cylinder momentum is used to investigate the in-cylinder flow during the scavenging process for the different port angles. The bulk average axial and angular momentum are calculated with equation 2.52 and 2.53, respectively.

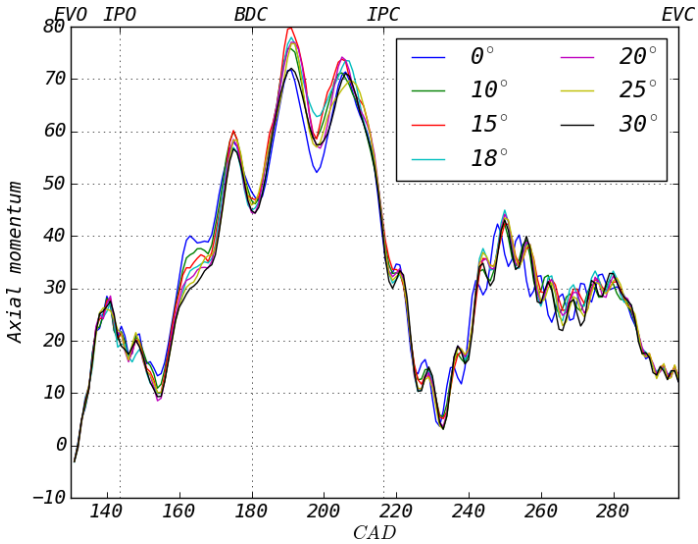

Figure 5.32: CFD result showing the transient bulk axial momentum in the cylinder

Figure 5.32 shows the bulk average axial momentum in the cylinder as function of the crank angle for all the different port angles. It is observed that the scavenge port angle does not significantly influence the axial momentum in the cylinder. It suggests that the mass and volume flow rates in the cylinder are independent from the port angle. The axial momentum trace is typical for a two-stroke uniflow scavenged engine. The axial momentum is slightly negative at EVO due to the piston motion during the expansion stroke. The axial momentum then rises due to acceleration of the cylinder content when the exhaust valve opens at EVO. Four peaks can be seen during the scavenging process, IPO-IPC, which corresponds to the fundamental frequency of a cylinder with both ends open (figure 4.2). The lowest value occurs after the closing of the scavenge port when the mass flow rate of scavenge air is removed. The piston motion accelerates the cylinder content, as seen by the increase in axial momentum after IPC.

The bulk average angular momentum trace in the cylinder is shown in figure 5.33. The influence of the scaling factor from table 5.8 is visible in figure 5.33 as the different port arrangements have different angular momentums at EVO. The $\alpha = 0°$ port arrangement has the lowest initial angular momentum and the $\alpha = 30°$ port arrangement has the highest. The scaling of the in-cylinder swirl appears to be sensible as all the simulations display similar behaviour. The swirl decays from exhaust valve opening to scavenge port opening due to wall friction. The angular momentum then increases due to the swirl generated by the port

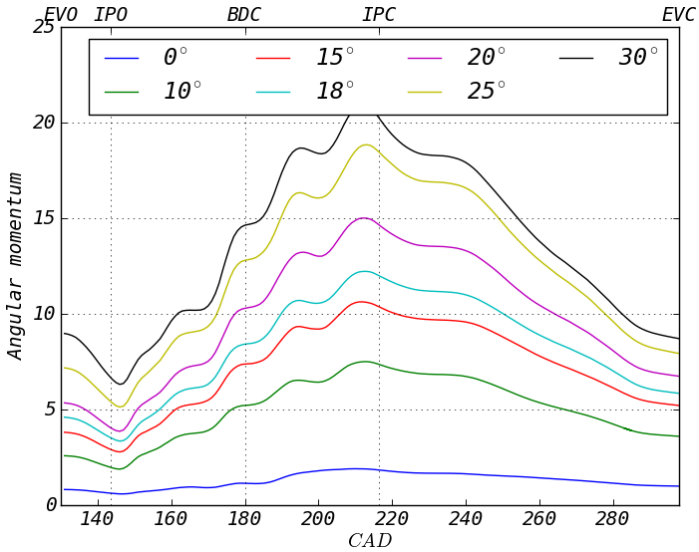

Figure 5.33: CFD results showing the transient bulk angular momentum in the cylinder

angle from scavenge port opening to scavenge port closing. The swirl then decays during the push out process. It is important to set the initial swirl as correctly as possible. If the swirl at scavenge port opening does not correspond to the swirl generated by the ports, then the mixing process between the scavenge air and the exhaust air can be affected due to increased shear stresses between the cylinder content and the introduced scavenge air.

5.3.5 Effect of port angle on scavenging efficiency

This section will comprise the results from the CFD analysis of the scavenging process when the scavenge port angles are varied. The reference port angle for this engine is $\alpha = 18°$. The working hypothesis was that the highest scavenging efficiency would be found somewhere around the reference port angle. Indeed a high swirl is expected to increase the central recirculation zone, trapping pockets of scavenge air in the center of the cylinder and the low swirling configuration is expected to leave dead zones where pockets of exhaust gas are trapped. Both effects should result in a decrease of scavenging efficiency. Figure 5.34 shows the scavenging efficiency as function of the port angle. As expected the scavenging efficiency has a peak value around the reference port angle. The scavenging efficiencies for all simulations are acceptable within an engine performance framework, however, it appears from figure 5.34 that the scavenging process is affected by angle of the scavenging ports.

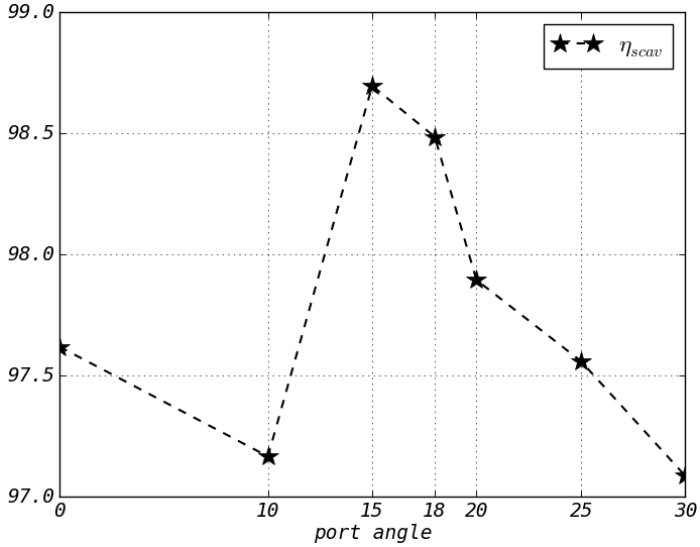

Figure 5.34: CFD result showing the scavenging efficiency for the different scavenge port angles

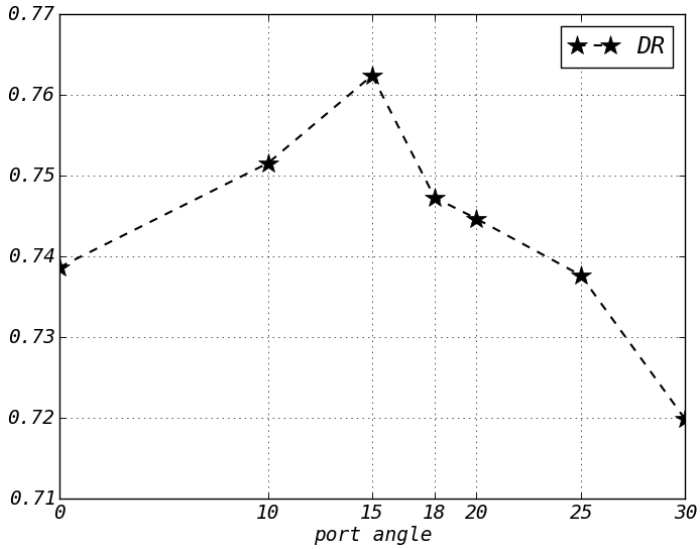

Figure 5.35: CFD result showing the delivery ratios for the different scavenge port angle simulations

The delivery ratios for the 7 CFD simulations are plotted in figure 5.35.

Comparing the shapes of the graphs in figure 5.34 and 5.35 reveals an apparent topological similarity. It appears that the peak value for the delivery ratio and the scavenging efficiency both appear at the same port angle configuration. Likewise for the $\alpha = 0°$ and $\alpha = 30°$ simulations where a decrease in delivery ratio corresponds to a decrease in the scavenging efficiency. The correlation between the delivery ratios in figure 5.35 and the scavenging efficiencies in figure 5.34 are in good agreement (apart from the 10° port angle simulation). This observation brings some clarity to the results presented in this section. It appears that the change in η_{scav} is not caused by any internal phenomenons in the cylinder, but rather by the flow resistance generated by the port geometry itself. All simulation set-ups is identical, except for the port geometry and the initial velocity field, so the scavenging gradient, Δp_{engine}, is identical for all simulations. The different port geometries have different resistance, which in turns lead to a small variation in mass flow rate. This discrepancy, caused the variations in the scavenging efficiencies.

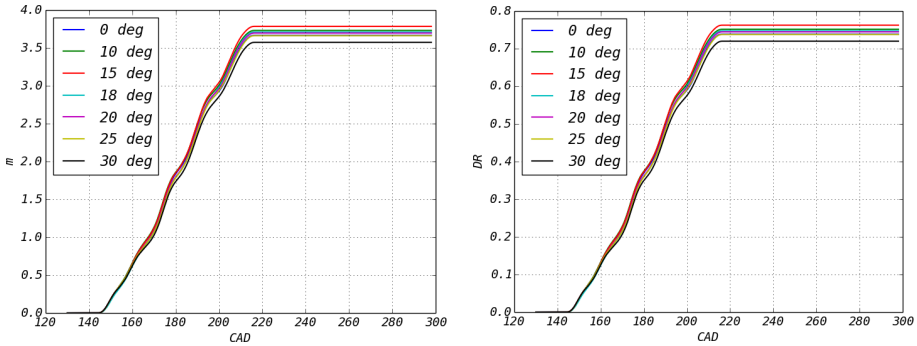

(a) Integrated mass flow rate as function of crank angle, CFD result

(b) Integrated volume flow rate (DR) as function of crank angle, CFD result

Figure 5.36

Figure 5.36a and 5.36b show the integrated mass flow rate and the integrated volume flow rate (DR), respectively. A lower mass flow rate for the high swirl and low swirl port configurations is observed, caused by the port topology. Figure 5.37 shows the mass flow for the 30 individual scavenge ports for the 15° and the 30° port configurations. It shows that the individual scavenge ports do not deliver the same amount of air to the cylinder. Ideally, the mass flow should be homogeneously distributed across the 30 scavenge ports, each port delivering the same amount of air. This is, however, not likely due to the asymmetric inlet condition, in-cylinder flow structures such as a preceding vortex core and pressure fluctuations between the exhaust and scavenge receivers. There are in fact significant differences between the scavenge ports. From figure 5.37 it appears that mass flux across port 3 is 3 times higher than across port 27 for

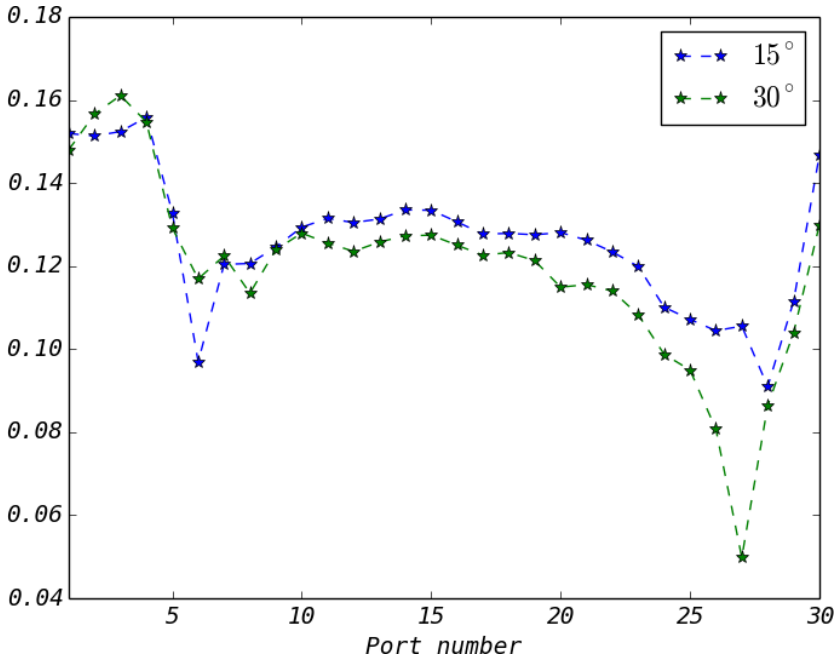

Figure 5.37: CFD result showing the integrated mass flow per port

the 30° port angle configuration.

The port configuration can be seen in figures 5.38a and 5.38b. The scavenge port numbered 0 is located perpendicular to the inlet (bottom of the scavenging box). The port numbering increments in a counter clockwise orientation. The velocity fields and vectors in figure 5.38a and 5.38b are instantaneous and can not be used to describe the port-to-port mass flow rate discrepancy. However, observations based on the geometry of the scavenge port arrangements can be made. The scavenging air enters the scavenge box through the inlet. The air flow will then split when being distributed around the cylinder. The ports are milled into the liner and subsequently the edges are rounded. The edges are not equally rounded and one side has a sharper edge than the other. The air that is distributed to the left side of the scavenge box will have to cross a sharper edge to enter the cylinder than the air that is distributed to the right. The sharper corner can make the air flow separate and form local recirculation zones which block the entrance to the cylinder. This theory is supported by the port to port mass flow rate variations seen in figure 5.37, where ports 0 to 5 have a higher mass flux than the remaining ports. The angle of attack between the air flow and the scavenge port generates flow separation. The scavenging ports located slightly downstream of the inlet, on the left side of the scavenge box, have the sharpest corner which makes these ports more sensitive to flow separation. This

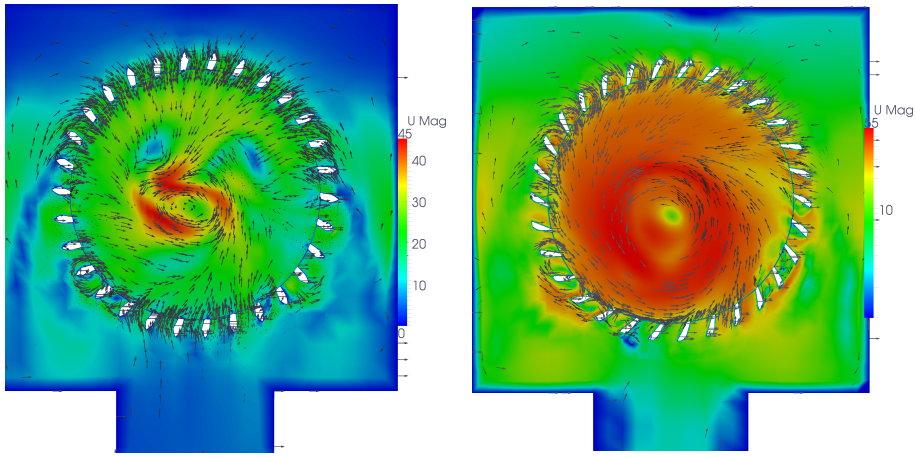

(a) 15° (b) 30°

Figure 5.38: Instentaneous velocity in a plane located in the middle of the scavengeport height at 180 CAD atdc. Inlet is shown at the bottom of the scavenge box.

is also shown in figure 5.37 where the ports in range 23-28 have a lower mass flux than the rest of the scavenge ports. The 30° ports have sharper edges than the 15° port arrangement, which is consistent with mass flow variations in figure 5.37 where the 30° ports consistently have a lower mass flow rate. The bias towards the right hand side of the scavenge box geometry also supports this theory.

The average bulk purity of scavenge air in the cylinder is shown in figure 5.39. The in-cylinder swirl has some influence on the scavenging process, but it is not as significant as expected. The air purity at IPC is roughly 86-89% and the contribution from the push out process is roughly 10%.

Figure 5.40 shows the bulk purity of scavenge air in the cylinder as function of the delivery ratio. The purity as function of delivery ratio includes the differences in mass flow rates and shows that the scavenging process is invariant to the scavenging port angle. The scavenging process follows the perfect displacement from equation 1.10 as seen in in figure 5.41.

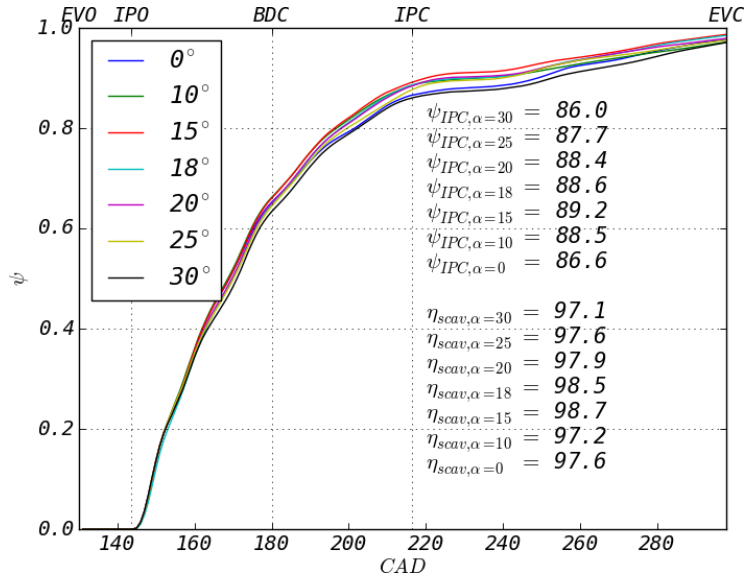

Figure 5.39: Bulk purity of scavenging air in the cylinder as function of crank angle (CFD result)

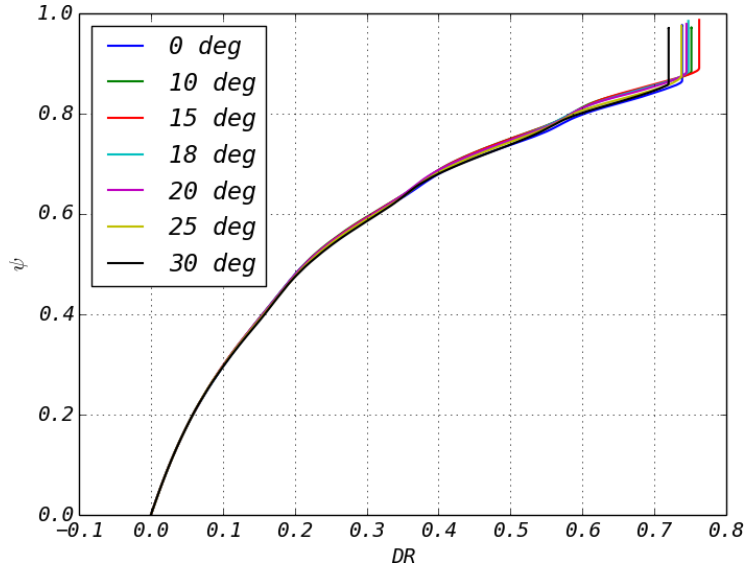

Figure 5.40: Bulk purity of scavenging air in the cylinder as fucntion of delivery ratio (CFD result)

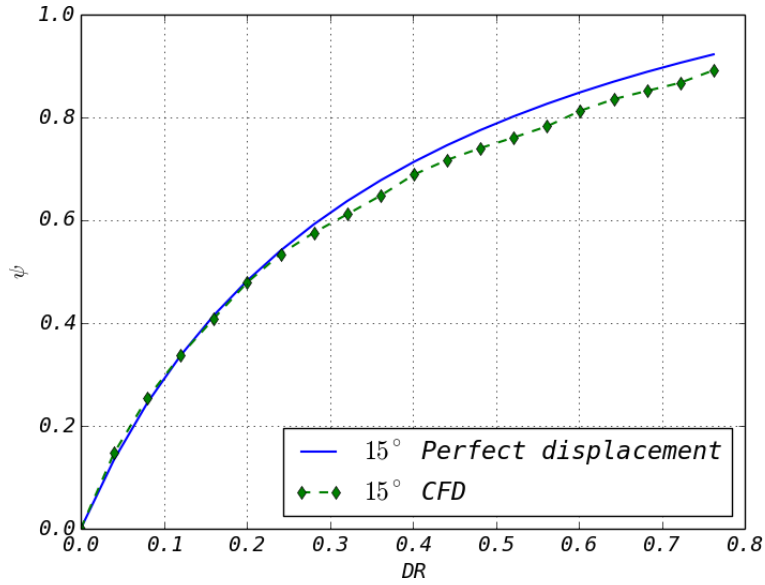

(a) 15°

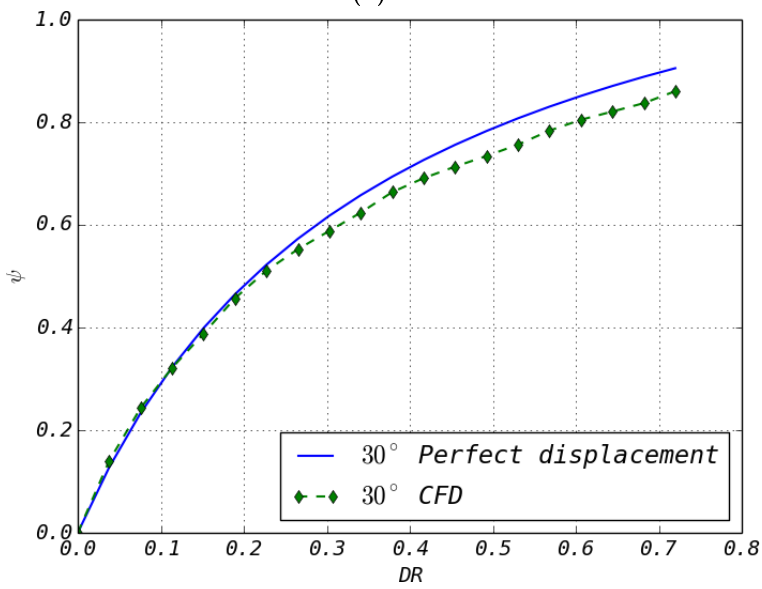

(b) 30°

Figure 5.41: Comparison between the perfect displacement model of Sher (1990) and the CFD model

Figure 5.42 shows a comparison between the perfect displacement model and the CFD model, where the perfect displacement model is used as the abscissa. The CFD model and the perfect displacement model is in good agreement up to DR = 0.6. The difference between the CFD and the perfect displacement model, is due to the mixing between the scavenge air and the exhaust gas. As all the curves are overlapping one can assume that the mixing is invariant to the in-cylinder swirl.

This knowledge is valuable from an engine designers perspective. The in-cylinder swirl is believed to be beneficial for the mixing of fuel and air. Furthermore, the swirl can be used to influence the cylinder heat transfer as the convective heat transfer increases with the tangential velocity at the wall. The port angle configuration can therefore be used as a tool to control the heat transfer to engine components such as the liner wall and to some degree the exhaust valve. The introduced scavenge air is cold, and therefore the effective cooling will increase with the swirl due to a higher convective heat transfer at the wall. The heat flux to the liner wall during the combustion and expansion stroke will also increase. It is beyond the scope of this project to assess the heat load in the combustion chamber. Based on the results presented in this section however, it can be concluded that the in-cylinder swirl can be used to influence the heat transfer without affecting the scavenging process.

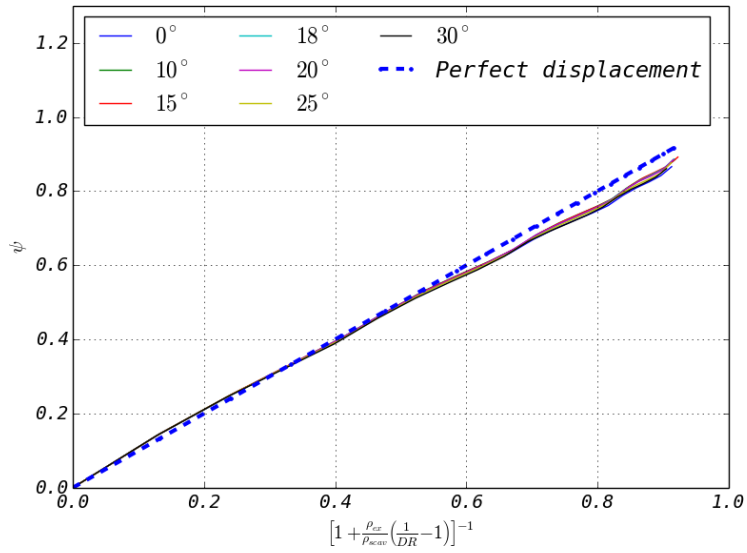

Figure 5.42: Comparison between the perfect displacement model of Sher (1990) and the CFD model.

5.4 Simple model to predict the scavenging process in marine two-stroke diesel engines

In this section, a preliminary algebraic scavenging model is presented. The objective is to derive an expression which includes the contribution from the volumetric part of the scavenging process and the contribution from the push out process. The volumetric scavenging is dependent on the volume flow (delivery ratio), while the push out process is dependent on the engine operating conditions, geometric properties and piston kinematics. The scavenging model has the generic form;

$$\eta_{scav} = d\psi_{vol} + d\psi_{push\,out}. \tag{5.8}$$

Where $d\psi_{vol}$ is the contribution from the volumetric scavenging and $d\psi_{push\,out}$ is the contribution from the push out process. It has been shown throughout this thesis that the volumetric part of the scavenging process (IPO-IPC) is well predicted with the theoretical perfect displacement model of Sher (1990). The perfect displacement model (equation 1.10) does not take the mixing between the scavenge air and exhaust gas into account. However, figures 5.14 and 5.42 shows that the bulk purity of air calculated from the CFD results is a linear function of the perfect displacement model (equation 1.10). A modified perfect displacement model, where the mixing is included, can be obtained by creating a linear fit to the plots in figure 5.14. A model fit for the CFD results in the engine load sweep case (section 5.1) is shown in equation 5.9 and in figure 5.43. The bulk purity of air for the engine load sweep is calculated with the modified perfect displacement model in equation 5.9. The results are shown in figure 5.44.

$$\psi = a \cdot \left[1 + \frac{\rho_{ex}}{\rho_{scav}} \left(\frac{1}{DR} - 1\right)\right]^{-1} + b \tag{5.9}$$

The modified perfect displacement model from equation 5.9 is in good agreement with the results from the CFD model and can be used to calculate the volumetric scavenging.

An expression for the push out process must be included in the scavenging model to obtain a complete scavenging model. The push out process for the engine load sweep study was shown in figure 5.6b. The figure shows that the change in purity and the swept volume is close to linear. This implies that information about the push out process from the CFD model can be used to create a model for the push out process. The exhaust valve closing is important when calculating the volume swept by the piston. The exhaust valve profile is measured at test bed for some engines, but it is desired to derive a generic expression where the cylinder volume at EVC can be calculated. The exhaust valve closing is determined by the engine control system according to the quantity p_{comp}/p_{scav} which is a key engine performance parameter. The following

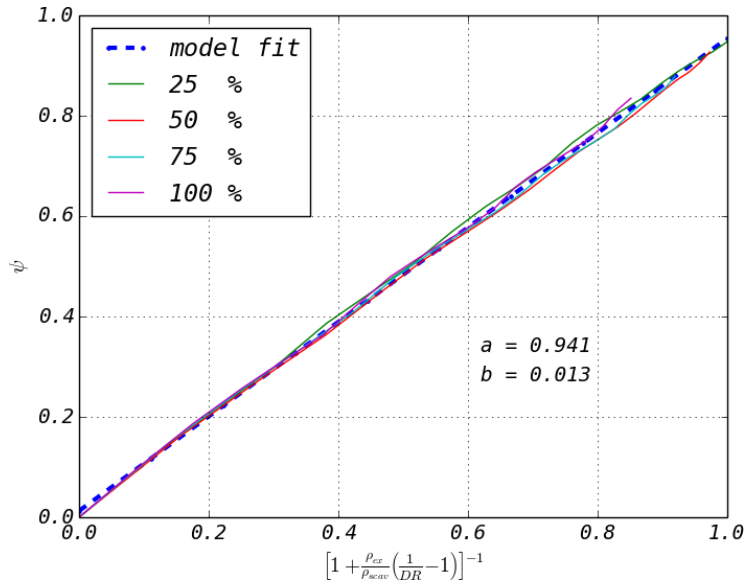

Figure 5.43: Model fit to the CFD results from the engine load sweep (section 5.1

relation between the in-cylinder pressure and volume can be made assuming isentropic compression,

$$V_{evc} = V_{comp} \cdot \left(\frac{p_{comp}}{p_{scav}} \right)^{1/\gamma}. \tag{5.10}$$

Where V_{evc} is the cylinder volume at exhaust valve closing, V_{comp} is the compression volume, p_{comp} is the compression pressure, p_{scav} is the scavenging pressure and γ is the ratio of specific heats. The volume swept by the piston during the push out process is defined as

$$dV_{push\,out} = V_{ipc} - V_{evc}, \tag{5.11}$$

where V_{ipc} is the cylinder volume at IPC. Equation 5.10 is used to calculate the exhaust valve closing timings for the engine cases used in the engine load sweep study. The EVC crank angles are listed in table 5.9

Engine load	25	50	75	100	%
Exhaust valve closing	283	285	291	289	CAD

Table 5.9: Exhaust valve closing timing, calculated with equation 5.10

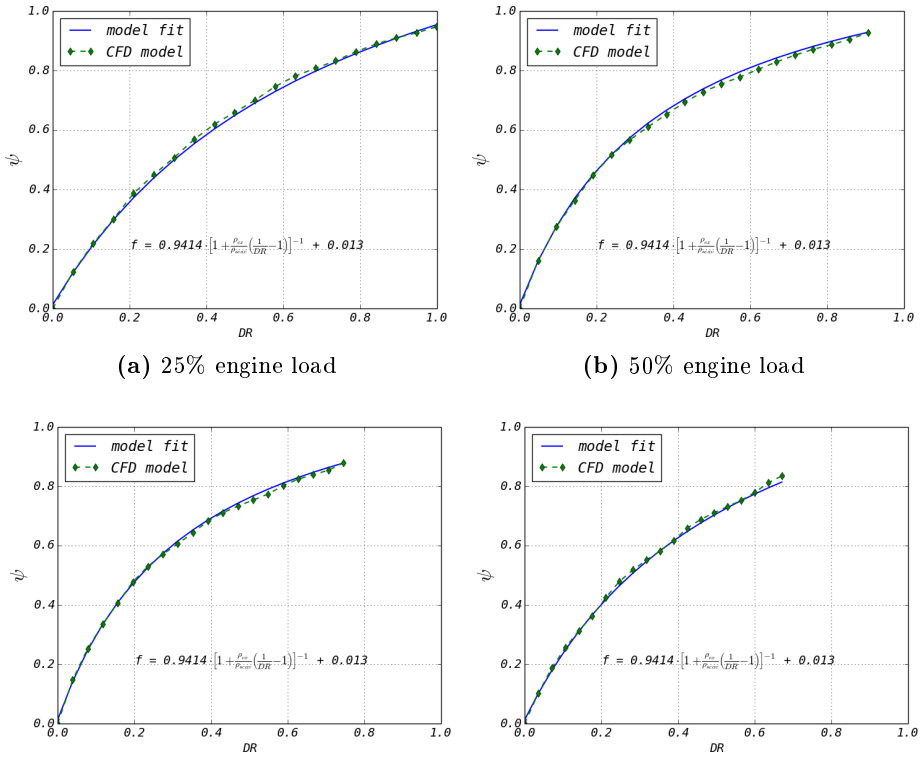

(a) 25% engine load

(b) 50% engine load

(c) 75% engine load

(d) 100% engine load

Figure 5.44: Bulk purity of air calculated with the CFD results and with the modified perfect displacement model (equation 5.9)

Comparing the exhaust valve closing angles in table 5.9 with the exhaust valve closing angles from the CFD models (table 5.1) show some differences. The difference observed between the CFD model and the isentropic compression model is caused by the p_{comp}/p_{scav} ratio. The istentropic compression starts at EVC and ends at TDC. Equation 5.10 calculates the initial volume required to istentropically compress air from p_{scav} to p_{comp}. The problem with this formulation is that the pressure in the cylinder at EVC is not equal to p_{scav}. The in-cylinder pressure will increase due to the piston motion between IPC and EVC, furthermore the exhaust valve needs 10-20 crank angles to close depending on the engine speed. The EVC value used in the CFD simulations corresponds to the angle where the exhaust valve is 2 mm open (when the CFD simulation ends). Some pressure increase is expected when the exhaust valve area is reduced from fully open to closed. This dynamic makes the EVC a difficult parameter to calculate.

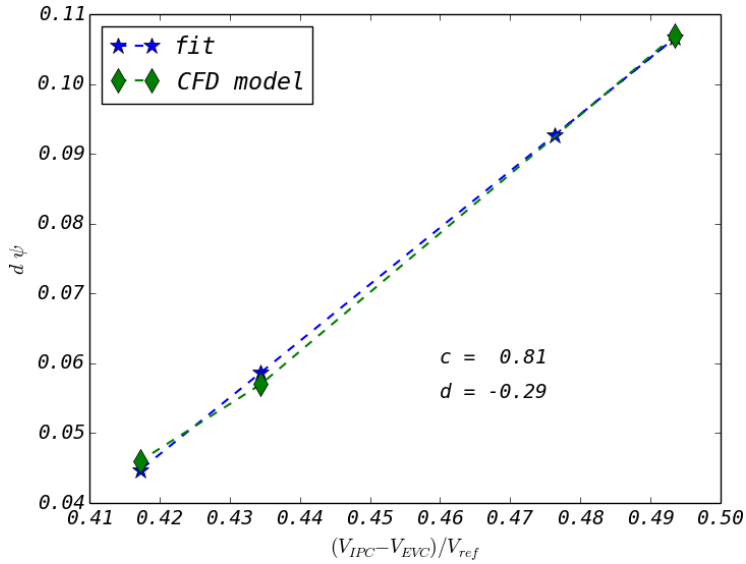

Figure 5.45: Model fit to the $d\psi_{push\,out}$ from the CFD results

A linear fit has been made based on the $d\psi_{push\,out}$ from equation 5.3 and the swept volume calculated with equation 5.11. The linear fit is shown in figure 5.45. The contribution from the push out process to the scavenging efficiency can be written as;

$$d\psi_{push\,out} = \frac{c}{V_{ref}} \cdot \left[V_{ipc} - V_{comp} \left(\frac{p_{comp}}{p_{scav}} \right)^{1/\gamma} \right] + d, \tag{5.12}$$

where V_{ref} is a reference volume, equal to the total cylinder volume at BDC. The expression depicting the volumetric contribution to the scavenging efficiency, equation 5.9, can now be combined with the expression depicting the contribution from the push out process, equation 5.12, to form the complete model for the scavenging efficiency,

$$\eta_{scav} = \underbrace{a \cdot \left[1 + \frac{\rho_{ex}}{\rho_{scav}} \left(\frac{1}{DR} - 1 \right) \right]^{-1} + b}_{d\psi_{vol}} + \underbrace{\frac{c}{V_{ref}} \cdot \left[V_{ipc} - V_{comp} \left(\frac{p_{comp}}{p_{scav}} \right)^{1/\gamma} \right] + d}_{d\psi_{push\,out}}. \tag{5.13}$$

Equation 5.13 only requires inputs which can be obtained, or estimated, a priori to a CFD model simulation or a full scale engine test. The model requires some data about the thermodynamic properties of the scavenge gas and the exhaust gas as well as the p_{comp}/p_{scav} ratio. A comparison between

the scavenging efficiency obtained from the CFD simulations and the simple scavenging model from equation 5.13 is shown in figure 5.46. The scavenging model, equation 5.13, and the CFD model shows good agreement for the 25%, 50% and 75% engine load case where the scavenging efficiency is within 1% deviation. The scavenge model also shows the same trend as the CFD model, where the 25% case has the highest scavenging efficiency followed by the 75% case, the 50% case and the 100% case.

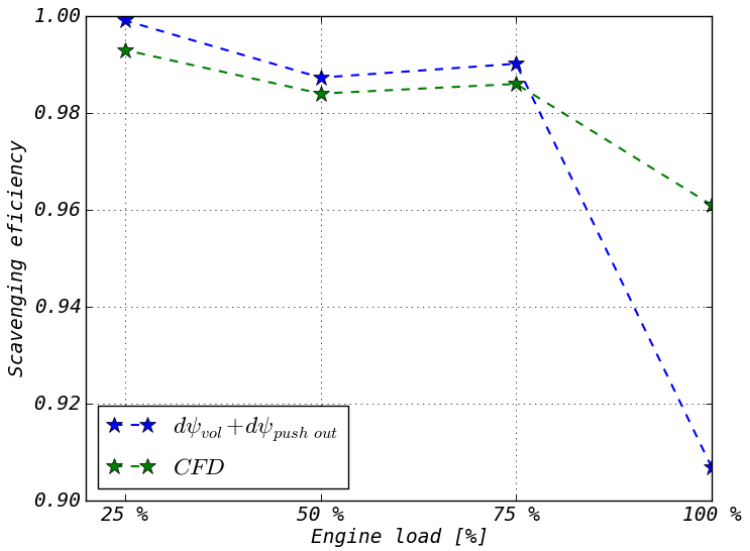

Figure 5.46: Scavenging efficiency obtained by the CFD model and with the scavenging model from equation 5.13

The 100% engine load case is under predicted by the scavenging model. The under prediction comes from the contribution from the push out process. Figure 5.44d shows that the volumetric contribution to the scavenging efficiency is in good agreement with the CFD results. When comparing the exhaust valve closing crank angles used in the CFD model (table 5.1 and the exhaust valve closing crank angles derived with equation 5.12 is shows that EVC for the 100% engine load case is under predicted by the push out model. The exhaust valve closing crank angle is 303 CAD in the CFD model while the push out model predicts an exhaust valve closing crank angle of 289 CAD. The difference of 14 crank angles constitutes a big difference in swept volume which causes the poor accuracy for the scavenging model at the 100% engine load case.

The scavenging model presented in this section is meant to serve as a first step towards a future scavenging model. Full scale CFD modelling of the scavenging process is costly and probably unfit to be part of an engine development process. It is therefore desired to create a simple model where engine data,

obtained from 0 and 1 dimensional engine simulation tools and a kinematic analysis of the geometry, to predict the scavenging process. The scavenging model presented here is not general, as it is tuned to match a specific engine at specified engine loads. A future model can be based on the same framework, but more general terms must be made for both the volumetric contribution and the push out process.

Chapter 6

Summary and conclusions

This thesis has presented the research conducted on the scavenging process in marine, two-stroke, uniflow scavenged, diesel engines during the course of the Industrial Ph.D. project: Integrated analysis of the scavenging process in marine two-stroke diesel engines. The project has been carried out at MAN Diesel & Turbo's facilities in Copenhagen, in collaboration with the department of Mechanical Engineering at the Technical University of Denmark.

The objective for the Ph.D. project was to build up a CFD model that was capable to describe the scavenging process with an acceptable accuracy. Such a model is beneficial for the engine designer as a tool to optimize the engine performance. Traditionally, the scavenging process has not been subjected to extensive research as the engine lay-out and turbocharger characteristics provided a sufficient flow of air to scavenge the cylinders. With the introduction of the MARPOL Annex VI (International Maritime Organization, 2009) in 1997, the engine builders was forced to optimize the combustion process and engine performance within the prescribed NOx emission legislations. The introduction of the ME engine program in 2003 opened up a whole new parameter space to optimize the engine performance as the fuel injection system and exhaust valve lift operation could be controlled electronically with hydraulic actuation. The ever more stringent emission legislations with Tier I, II and III have pushed the engine lay-out towards its maximum capacity in terms of the in-cylinder processes. Consequently, the scavenging process has been somewhat neglected and it has become apparent that comprehensive knowledge of this process is integral for further optimization of engine performance. Significant effort has been placed in the development of the CFD model, how to generate the mesh, initial-

ize the fields and running the simulations as efficient as possible. The simulation processes, pre-processing and post-processing is designed to be embedded in the research and development framework at MAN Diesel & Turbo. The CFD simulations presented in this report aims to give a comprehensive understanding of the scavenging process and the parameters that influence the performance of the scavenging process. The simulations was chosen as they represent a wide parameter space and would provide knowledge and understanding of the process that occurs during the scavenging process. CFD simulations are computationally expensive and inherently complicated so it is acknowledged that actively using CFD simulations in the design of every single engine layout is unfeasible. However, the knowledge manifested in this thesis give valuable insight to the processes that takes place during the scavenging process and the parameters that influence them.

6.1 Summary

The first three chapters in this thesis contains the problem formulation, background information, a description of the CFD model and a detailed description of the simulation process. The mesh generation process is described and the generation of the input and boundary conditions is presented. Preliminary simulations show that the CFD model under predicted the integrated mass flow when applying the scavenging gradient, Δp_{engine}, from the engine performance data base. A small utility was developed which calculated a corrected Δp_{engine} based on the mass flow of air obtained experimentally at the engine test. This modification significantly improved the results from the CFD analysis.

A validation study was conducted in chapter 4. Quantitative data on the in-cylinder velocity components was used to validate the CFD model. Two test cases were included in the validation study. Both cases where run with similar operating conditions, but the number of scavenge ports, and thereby the in-cylinder swirl, was modified. The simulations where in good agreement when comparing the CFD results with the velocity data obtained with PIV (particle image velocimetry). The validation study showed a very interesting feature with the scavenging process. The scavenging process shows a strong correlation with the volume flow (delivery ratio). The bulk purity of air in the cylinder calculated with the CFD results was compared to a theoretical model, based on the assumption of perfect displacement, proposed by Sher (1990). The CFD model showed good agreement with the perfect displacement model. The perfect displacement model does not, however, include the mixing between the scavenge air and the exhaust gas.

Three different studies was presented in section 5; a engine load sweep following a propeller curve, a sweep of the scavenging pressure at constant engine speed and an investigation of the scavenge port angle. These three studies were chosen to investigate how the scavenging process was influenced by changes in

operating conditions as well as the internal flow field in the cylinder.

The engine load sweep study comprise four CFD simulations corresponding to 25%, 50%, 75% and 100% engine load respectively. The highest scavenging efficiency is obtained at low engine loads. This is partly due to the increased pressure in the scavenge receiver for high engine loads. High scavenging pressure increases the density of the scavenge air which in turn reduces the volume flow rate across the cylinder. The mass flow rate through the engine increases with engine load as the turbocharger back pressure increase. However, the volume flow rate (delivery ratio) is decreasing due to the increased density of the scavenging air in conjunction with the reduced scavenging time, t_{scav}. As observed in the validation study, the bulk purity of air in the cylinder is a function of the delivery ratio which is reduced at higher engine loads. The results from the CFD analysis were compared with the perfect displacement model with good agreement. The engine load sweep also showed the influence of the push out process. For the 100% engine load case, 12.5% of the total bulk purity of air at EVC (η_{scav}) was obtained by the push out process.

The engine load sweep study followed the propeller curve, where the engine speed changes with load. A study where the engine speed was kept constant while increasing the scavenging pressure was also conducted. The study contained one reference case where the scavenging pressure was within a "normal" operating mode and two cases where the scavenging pressure was increased. The impact on the scavenging process was in conjunction with earlier results. Increasing the scavenging pressure, increase the density of the scavenge air which in turn reduce the scavenging efficiency. Note that the influence of the scavenging time, t_{scav}, is removed from this study as the engine speed is constant.

The scavenge port angle was varied to investigate the influence of the in-cylinder swirl. A known characteristics of swirling flow is a radial velocity deficit towards the center axis caused by a low pressure region in the center of the swirl. This phenomenon can create a central recirculation zone where the exhaust gas is trapped in a cone like shape in the center of the cylinder. A total of 7 port angles (0°, 10°, 15°, 18°, 20°, 25° and 30°) was used to evaluate the influence of swirl. Inspecting the visualizations of the passive scalar showed that the flow fields in the cylinder was influenced by the port angles. At $\alpha = 0°$ the flow was dominated by a central jet like profile while at $\alpha = 30°$ the flow was dominated by a wake like profile with a vortex breakdown occurring at the center axis. Still, when quantifying the scavenging efficiency and the purity of air as function of the volume flow rate it appeared that the port angle did not affect the scavenging process. The scavenging efficiency did not change due to the internal flow field and the bulk purity of air in the cylinder was in good agreement with the perfect displacement model.

A simple and preliminary scavenging model was derived in an attempt to be able to quantify the scavenging efficiency prior to a CFD simulation. The scavenging model was divided into two parts, one calculating the volumetric contribution to the scavenging efficiency and a second part calculating the con-

tribution from the push out process. The model was tuned by making a linear fit with the results obtained in the engine load sweep. The model was able to predict the scavenging efficiency with good accuracy for the 25%, 50% and 75% engine load case. The 100% was underestimated due to limitations in the model for the push out process.

6.2 Conclusions

This section will present some of the most important conclusions based on the results presented in this thesis.

- A CFD model embedded in the R&D framework at MAN Diesel & Turbo has been developed, tested and validated with high quality quantitative data obtained experimentally at the T50ME-X test engine and at a production engine during engine commissioning.

- The most important conclusion obtained during the Ph.D. project is the strong link between the scavenging efficiency and the volume flow (delivery ratio). The CFD simulations have shown that the gas exchange during the scavenging process depends on the delivery ratio regardless of operating conditions and in-cylinder flow conditions.

- The scavenging process consists of two sub processes. The volumetric scavenging, where the scavenge air flush the cylinder displacing the exhaust gas through the exhaust valve. And the push out process, where the piston displace some of the cylinder content from inlet port closing (IPC) to exhaust valve closing (EVC).

- Although heat transfer is beyond the scope of this project, the knowledge obtained in the port angle study showed that the scavenging process appears to be invariant to the in-cylinder swirl. This implies that the in-cylinder swirl can be used to influence the engine heat balance as the swirl affects the convective heat transfer. A separate study of the swirl's influence on the combustion process must be made, but there is no apparent limitations to this approach from a scavenging perspective.

- A preliminary scavenging model has been presented, which includes the contribution from the volumetric scavenging and the push out process. The model is based on a modified perfect displacement model and an expression that calculates the volume displaced by the piston during the push out process using an isentropic compression. The model presented in this thesis is modified to fit the engine load sweep case and is not general.

6.3 Future work

This industrial Ph.D. project is currently the last of a series of research conducted at MAN Diesel & Turbo in collaboration with the Technical University of Denmark. Several B.Sc. and M.Sc. theses as well as at least three Ph.D. projects have focused on the scavenging process over the past decade. The research involve both experimental work and CFD modelling on scaled down models as well as sector models of a full scale engine. This project aimed to use this knowledge and to apply it in developing a CFD model of a full scale two-stroke engine with realistic boundary conditions and the full 3D geometry.

The results obtained in this project are quite conclusive and have increased the understanding of the scavenging process significantly. The next step, in the authors opinion, is to use this knowledge to create a simple scavenging model which can be included as a design parameter when designing future marine two-stroke engines. Such a model, would manifest a design criteria at which an adequate scavenging process is guaranteed.

It is stated explicitly in the MAN Diesel & Turbo's R&D strategy that "full cycle" CFD simulations of the two-stroke diesel engine cycle shall be conducted in the near future. Parallel to this Ph.D. project, research engineers in the R&D department have been developing a combustion CFD model for the closed cycle portion of the engine cycle (see figure 1.6). The next step is to couple the closed cycle CFD model together with the scavenging model in order to conduct full cycle CFD. The strategy is to run the scavenging CFD model and then use the in-cylinder flow fields as initial conditions for the combustion CFD model, the results from the combustion CFD model will then be interpolated back to the scavenging model and thus form the initial conditions for the subsequent engine cycle. Full cycle CFD is an integral tool when evaluating the heat transfer in the engine.

Appendix A

Conference papers

A.1 Numerical Investigation of the Scavenging Process in Marine Two-Stroke Diesel Engines

SAE INTERNATIONAL

Numerical Investigation of the Scavenging Process in Marine Two-Stroke Diesel Engines

2013-01-2647
Published
10/14/2013

Fredrik Herland Andersen
MAN Diesel & Turbo / DTU

Johan Hult, Karl-Johan Nogenmyr, and Stefan Mayer
MAN Diesel & Turbo

doi:10.4271/2013-01-2647

ABSTRACT

The scavenging process is an integral part of any two-stroke internal combustion engine cycle whether it is spark ignited or compression ignited. The scavenging process is responsible for transporting the burned gases from the previous working stroke out of the combustion chamber to allow for the fresh charge or fresh air to enter for the next combustion/working stroke. This implies that the scavenging process is responsible for setting the initial condition for the combustion process, consequently affecting fuel economy, power output and emission of hazardous gases. Two-stroke diesel engines for marine propulsion are usually uniflow scavenged cross-head engines. In uniflow scavenged engines the scavenge air enters the cylinder via ports located near the bottom dead center and exits through an exhaust valve located in the cylinder head. The in cylinder flow is therefore concentrated in one direction which gives the method its name.

In this study a CFD analysis of the scavenging process in the 4T50ME-X test engine at MAN Diesel & Turbo is presented. The CFD model uses the full engine geometry including a moving piston and valve combined with time resolved measurement data as boundary and initial conditions. The results are then validated with experimental data from the engine. Optical velocity measurements have been performed through a specially designed engine cover with optical access.

INTRODUCTION

The scavenging process in marine two stroke diesel engines are responsible for transporting the burned gases from the working stroke out of the cylinder via the exhaust valve located in the cylinder head. This will replace the burned gases with fresh air plus possible Exhust Gas Resirculation (EGR) for the next compression stroke. From this it is clear that the scavenging processes is, to a great extend, responsible for setting the initial conditions for the combustion process that in turns affect the engine performance, thermal efficiency, specific fuel oil consumption (SFOC) and emission of hazardous gases. In uniflow scavenged engines compressed air enters the cylinder via multiple scavenge ports located in the lower part of the cylinder liner. The scavenge ports are cut at an angle with respect to the radial direction to create a confined swirling flow. Swirling flow is favorable for the mixing of air and fuel at the end of the compression stroke as it provides a more homogenous distribution of the fuel in the combustion chamber.

The uniflow scavenging process is characterized by a transient confined port-generated turbulent swirling flow, with complex phenomenon such as recirculation zones, vortex breakdown and vortex precession. Understanding the in cylinder flow field is essential for optimization of the scavenging and combustion processes. Investigations of the uniflow scavenging process are few compared to scavenging of smaller two and four stroke engines. An overview of previous studies can be found in (Heywood & Sher, 1999)[1]. Experimental studies of the scavenging process include

visualization (Ferro, 1958)[2], pitot measurements (Persival, 1955)[3] and hotwire measurements (Sher et al, 1991)[4]. Influence of the shape and angle of the scavenge ports have been investigated by Litke (1999) [5]. Over the past two decades computational resources have become reasonably inexpensive and as a result of this CFD modeling of the in-cylinder flow has become increasingly popular. Early models includes the work of Nakaawa et.al (1990)[18]. In the later years there have been several CFD analyses on the MAN Diesel & Turbo engines. Sigurdsson (2011)[19] performed CFD analysis on the scavenging process in the MAN Diesel & Turbo test engine 4T50ME-X using STAR-CD. To save computational time he used a 12 deg sector of the geometry including only one of the scavenge ports. Al-Mousawi (2012) performed a CFD analysis on an extended model based on Sigurdsson but focused on testing turbulence model for a scaled down model engine. Lamas et al. (2012)[6] performed a CFD analysis on the 7S50MC engine. This work included the full geometry for the cylinder and exhaust region, but does not take the asymmetric inlet conditions into account. The work presents an indication of the scavenging efficiency by use of a transport equation of a passive scalar. The model presented in this paper is based on the 4T50ME-X test engine located in Copenhagen, the model is 3D and includes the scavenge box to address the asymmetric inlet conditions. Time resolved as well as cycle averaged data is used as initial and boundary conditions and a validation study is performed by comparing experimental velocity measurements with CFD.

MAIN PART

Engine Operation

The numerical analysis presented in this paper corresponds to an optical measurement campaign conducted on the 4T50ME-X test engine. The objective for the measurement campaign was to investigate if performing PIV (Particle Image Velocimetry) measurements would yield trustworthy data and if so to perform preliminary velocity measurements inside the combustion chamber. The tangential and axial velocity component was successfully extracted from this measurement series.

Optical access to the combustion chamber was obtained through a specially designed engine cover with sapphire windows. A laser sheet could be placed inside the combustion chamber allowing PIV measurements. The size of the PIV window was small compared to engine scales and the data extracted is the axial and tangential velocity component from a 50×50 mm laser sheet. The velocities within this sheet were reasonably uniform and the data presented in this paper is the averaged value of the velocity components within this sheet. A detailed description of the experimental setup can be found in [11] and [12]. A sketch of the PIV set up can be seen in Figure 10. The numerical model used in this study will use these velocity measurements as validation and initial condition and will use time resolved and cycle averaged pressure data from the specific test run as initial and boundary conditions. For this specific measurement campaign a special belt designed to close every other scavenge port is mounted to increase the in-cylinder swirl.

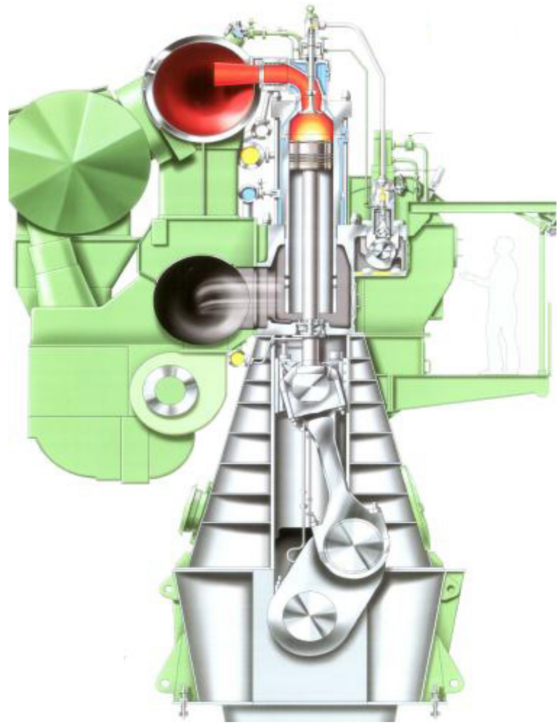

Figure 1. Cross section of a uniflow scavenged two-stroke cross-head diesel engine (MAN Diesel & Turbo SE

Figure 1 shows a cross section of the 4T50ME-X test engine located at the Diesel Research Center in Copenhagen. The engine is unique as it is a fully functional large bore, cross-head, uniflow scavenged, two-stroke diesel engine. Some of the engine specifications can be found in table 1.

Table 1. Engine specifications

Engine type	**Diesel, two-stroke**
Bore	500 mm
Stroke	2 200 mm
Connecting rod length	2 885 mm
cylinders	4
Ports per cylinder	30 (15)
Port angle	20^{o}
Max power	~ 7 MW
Max engine speed	123 RPM
Valve operation	electronic / hydraulic
Max pressure	190 bar
Charging	Turbo-charged

The two-stroke operation principle differs from four-stroke as it has a power stroke within every engine cycle compared to every other cycle as in a four-stroke engine. High power to weight ratio compared to four-stroke and fewer moving parts makes it a good candidate for marine propulsion systems as the engine room is confined with limited volume. Since the construction is relatively simple, and has fewer moving parts, two-stroke engines are very robust and reliable. The low engine speed closely matches the optimum revolution speed for the propeller so the costly and complicated transmission system can omitted and the propeller and crank-shaft is directly coupled via the drive shaft. A short description of the two-stroke engine cycle will follow.

The airflow through the engine goes from the scavenge air receiver trough the angled scavenge ports and into the cylinder. The angled port adds a tangential velocity component to the velocity thus creating a confined swirling flow. The fresh air moves in a helical motion upwards the cylinder and exits through the exhaust valve located in the cylinder head. In this process the fresh air will flush out the residual gases from the combustion process. After exiting the exhaust bend located downstream the exhaust valve the gases enter a large volume called the exhaust receiver. This volume is created to provide constant pressure to the turbines. The compressor is fed with ambient air which is pressurized before reaching the scavenge air receiver via a inter cooler. The scavenge receiver is a volume, like the exhaust receiver, designed to damp out pressure fluctuations created by the adjacent cylinders. There is a pressure difference between the scavenge receiver and the exhaust receiver which acts as the driving pressure for the scavenging process.

During the combustion process close to the top dead center there is a large build up of pressure in the combustion chamber / cylinder. This pressure acts on the piston, forcing it downwards thus expanding the volume and lowering the pressure in the cylinder. Approximately 20-30 CAD before uncovering the scavenging ports, the exhaust valve is opened. The period following is known as the blow down period where the combustion gases in the cylinder starts to escape the cylinder via the exhaust valve due to the pressure difference between the cylinder and the exhaust receiver. The optimum condition for scavenging is that the pressure in the cylinder and the pressure in the scavenge box is close to equal at inlet port opening [7] [8]. If the pressure in the cylinder is higher than the scavenge box the flow over the ports will be shortly reversed back into the scavenge box. This is undesirable as the back flow contains a lot of residual gases from the combustion process as well as lubricating oil that over time can lead to a shorter service interval for the engine. However, a higher cylinder pressure at scavenge port opening has its benefits as more work is performed on the piston and the working stroke is better utilized. Standard practice is therefore to allow some blow back, usually in the order of 1% of the total cylinder mass. The scavenge ports are uncovered approximately 40 CAD before bottom dead center (BDC) and close approximately 40 CAD after BDC. During this period the fresh air is flushing the cylinder for burned gases. After the scavenge ports are closed the piston moves upwards while the exhaust valve remains open. Timing of exhaust valve closing is used to set the compression ratio and consequently the compression pressure.

Figure 2 is a schematic overview of the processes described in the above section. The figure divides the two-stroke engine cycle into 5 processes; expansion (combustion/work), blow down (adjusting pressure), scavenging (flushing cylinder), push out (setting compression ratio) and compression (pressure build up). Those 5 processes can be clustered into two phases; closed volume (when the cylinder is a closed volume) and open volume (when there is gas exchange in the cylinder). The study presented in this paper is focused only on the open volume phase of the cycle.

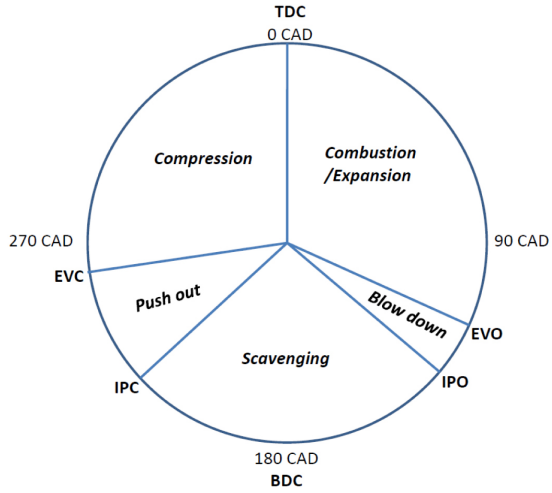

Figure 2. Two stroke engine cycle processes

Numerical Model

The numerical investigation presented in this paper is carried out using the open source C++ tool box OpenFOAM 1.6-ext [22].

Simplifications

• Only the open volume phase is considered. The simulation starts at EVO and ends at EVC. For this specific case the simulation starts at 128 CAD ATDC and ends at 261 CAD ATDC. Solving for the combustion and compression stroke is out of scope for this study. Boundary conditions are set by measurement data while the initial conditions are found by use of an in-house engine simulator.

• A transport equation for a passive scalar is solved to evaluate the mixing of burned gases with the fresh air

• Experience with the Reynolds Average Navier-Stokes (RANS) approach for solving turbulent swirling flows have proven to be inadequate for solving confined swirling flow problems as it fails to capture the vortex core appropriately

[9][20]. It has therefore been decided to use a Large Eddy Simulation (LES) turbulence model to model the turbulence. The simulation presented does not formally fulfill the requirements for engine LES [10] as the mesh is relatively coarse and cycle averaging is not performed at this stage. The author and his colleagues are aware of this simplification and has therefore named the approach "pseudo LES".

Governing Equations

The governing equations are the compressible Navier-Stokes equations:

$$\frac{\partial \rho}{\partial t} + \frac{\partial}{\partial x_j}\left(\rho u_j\right) = 0 \tag{1}$$

$$\frac{\partial (\rho u_i)}{\partial t} + \frac{\partial}{\partial x_j}\left[\rho u_i u_j + p\delta_{ij} - \tau_{ij}\right] - F_i = 0 \tag{2}$$

$$\frac{\partial e_0}{\partial t} + \frac{\partial}{\partial x_j}\left[\rho u_j e_0 + u_j p + q_j - u_j \tau_{ij}\right] = 0 \tag{3}$$

Where F_i is the body forces, ρ is the density of the fluid, u_j is the velocity, p is the pressure, μ is the dynamic viscosity of the fluid, δ_{ij} is the Kronecker delta ($\delta_{ij} = 1$ if i=j and $\delta_{ij} = 0$ if i≠j). e_0 is the energy per unit mass, q_j is heat flux given by Fouriers law

$$q_j = -C_p \frac{\mu}{Pr}\frac{\partial T}{\partial x_j} \tag{4}$$

Pr is the laminar Prantl number, the ratio of viscous and thermal diffusion rate. For a Newtonian fluid the viscous stress is given by:

$$\tau_{ij} = 2\mu S_{ij} \tag{5}$$

Where the trace-less viscous strain-rate tensor is defined as:

$$S_{ij} = \frac{1}{2}\left(\frac{\partial u_i}{\partial x_j} + \frac{\partial u_j}{\partial x_i}\right) - \frac{1}{3}\frac{\partial u_k}{\partial x_k}\delta_{ij} \tag{6}$$

Perfect gas assumption is made to specify an equation of state, the following relations is valid for this assumption.

$$\gamma \equiv \frac{C_p}{C_v}, \qquad P = \rho R T, \qquad e = C_v T, \qquad C_p - C_v = R$$

Where γ is the heat capacity ratio and R is the specific gas constant. As stated earlier the turbulence modeling approach in this study is "pseudo LES". In Large Eddy Simulation the larger energy carrying motions are resolved by the mesh while the smaller scales are modeled via e.g. an eddy viscosity model. In most cases, including the presented model, the scales of motions that are resolved are governed by the grid size and hence the navier-stokes equations (1), (2) and (3) are implicitly filtered by the cell size. The scales that is smaller than the cell size has to be modeled and is referred to as Sub Grid Scales (SGS) or more correctly Sub Filter Scales (SFS). For the compressible navier-stokes equation it is beneficial to use Favre-filtering [13],[21].

Performing the filtering operations on the governing equations (1), (2) and (3) yields the following closed set of filtered equations:

$$\frac{\partial \bar{\rho}}{\partial t} + \frac{\partial}{\partial x_i}\left(\bar{\rho}\widetilde{u_i}\right) = 0 \tag{7}$$

$$\frac{\partial}{\partial t}\left(\bar{\rho}\widetilde{u_i}\right) + \frac{\partial}{\partial x_j}\left[\bar{\rho}\widetilde{u_j}\widetilde{u_i} + \bar{p}\delta_{ij} - \widetilde{\tau_{ji}^{tot}}\right] - \bar{F}_i = 0 \tag{8}$$

$$\frac{\partial}{\partial t}\left(\bar{\rho}\widetilde{e_0}\right) + \frac{\partial}{\partial x_j}\left[\bar{\rho}\widetilde{u_j}\widetilde{e_0} + \widetilde{u_j}\bar{p} + \widetilde{q_j^{tot}} - \widetilde{u_j}\widetilde{\tau_{ji}^{tot}}\right] = 0 \tag{9}$$

There are now some additional terms that needs modeling in order to close the system of equations. The momentum equation (8) includes a turbulent contribution in the viscous stress tensor, $\widetilde{\tau_{ji}^{tot}} = \widetilde{\tau_{ji}^{laminar}} + \widetilde{\tau_{ji}^{turbulent}}$. The turbulent contribution to the viscous stress tensor is given by the following expression:

$$\widetilde{\tau_{ji}^{turbulent}} \equiv -\bar{\rho}\left(\widetilde{u_i u_j} - \widetilde{u_i}\widetilde{u_j}\right) \tag{10}$$

This term needs to be modeled and can be approximated with the following expression:

$$-\bar{\rho}\left(\widetilde{u_i u_j} - \widetilde{u_i}\widetilde{u_j}\right) \approx \mu_t\left(\frac{\partial \widetilde{u_i}}{\partial x_j} + \frac{\partial \widetilde{u_j}}{\partial x_i} - \frac{2}{3}\frac{\partial \widetilde{u_k}}{\partial x_k}\delta_{ij}\right) - \frac{2}{3}\bar{\rho}k\delta_{ij} \tag{11}$$

In the energy equation (9) there is also an additional term that must be addressed $\widetilde{q_j^{tot}} = \widetilde{q_j^{laminar}} + \widetilde{q_j^{turbulent}}$ where the turbulent contribution is expressed by:

$$\widetilde{q_j^{turbulent}} \equiv C_p\overline{\rho u_j' T} \tag{12}$$

The right hand side of (12) can be approximated by:

$$C_p\overline{\rho u_j' T} \approx C_p\frac{\mu_t}{Pr_t}\frac{\partial \tilde{T}}{\partial x_j} \tag{13}$$

The two additional terms (11) and (13) includes a new variable, μ_t turbulent viscosity, also known as eddy viscosity.

The turbulence model applied in this study is a so called eddy viscosity model where the effects of the unresolved, sub filtered scale, motions of the turbulent flow is accounted for with added viscosity. The eddy viscosity model applied in this study is the Smagorinsky model where the eddy viscosity is calculated by the following algebraic expression:

$$\mu_t = C_s^2 \rho \Delta^2 |\bar{S}| \tag{14}$$

Where C_s is a model constant and Δ is filter length scale, equal to the cell size for implicit filtering. In addition to the governing equations (7), (8) and (9) an additional transport equation is solved to address the presence of the two gases in the cylinder.

$$\frac{\partial(\rho S_0)}{\partial t} + \frac{\partial\left(\rho S_0 u_j\right)}{\partial x_j} - \frac{\partial}{\partial x_j}\left((\mu + \mu_t)\frac{\partial(\rho S_o)}{\partial x_j}\right) = 0 \tag{15}$$

Where S_0 is the mass fraction of fresh air. The mass fraction of burned gases, S_1, is found from the relation of unity:

$$S_1 = 1 - S_0 \tag{16}$$

Initially the cylinder and exhaust bend is filled with burned gases $S_0 = 0$ while the scavenge box is initiated with $S_0 = 1$.

Computational Domain

The computational domain used for the simulation presented in this study was generated using the native OpenFOAM meshers; blockMesh and snappyHexMesh. The mesh is constructed in different sections and then assembled afterwards into the final mesh. This approach was chosen in order to ensure the quality of cells in regions where the mesh modifiers are active. The exhaust valve mesh was generated using blockMesh where a in-house python utility reads object files describing the surfaces of the valve, stem and diffuser and writes a blockMeshDict file (the input file for the mesh utility). The exhaust bend, cylinder and scavenge box was generated with snappyHexMesh using an appropriate background mesh generated with blockMesh. Both meshes generate hexahedral dominated meshes which ensure higher accuracy and stability for the simulations. Some polyhedral cells are created by snappyHexMesh in order to resolve feature edges.

Figure 3 shows the computational mesh used in the simulation. The number of cells in the domain changes as cells are added and removed with the motion of the exhaust valve and piston. The number of cells is in the order ~1- 1.15 million cells depending on the crank angle. The base resolution for the cylinder cells is approximately 13 mm. The domain was decomposed by manual decomposition and solved in parallel on 25 XENON X5675 (Westmere) CPU's. Total simulation time was 165 hours.

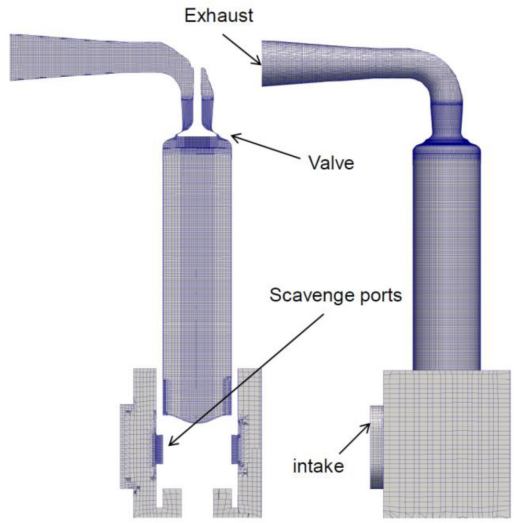

Figure 3. Cross section (left) and side view (right) of the computational domain

Mesh Modifiers

The mesh experiences topological changes during the simulation due to the movement of the exhaust valve and piston. To accommodate this, an additional engine library is needed. This library inherits most of its functions from the original engine library in OpenFOAM.

Table 2. list of mesh modifiers for the simulation

Mesh modifier	*Operates on*
Generalized Grid Interface	Valve
Add/Remove layers	Piston + valve
Sliding Interface	Scavenge ports

Generalized Grid Interface (GGI) is a utility in OpenFOAM 1.6-ext that allows mesh regions to slide across one another. Two interfaces slide across each other and within each time step the overlapping faces are cut into smaller sets to allow interpolation between the two regions. The implementation and functionality can be found in [15]. Sliding Interface has similar capabilities as the GGI plus the capability to handle non overlapping regions. The mesh contains 15 scavenge ports patches on the scavenge box geometry with a corresponding 15 patches on the cylinder. When the cylinder mesh slides past the scavenge ports the 15 corresponding patches must be coupled together in order to allow the fluid in the scavenge box to enter into the cylinder. This is obtained by use of the Sliding Interface, where the corresponding patches are merged together in each time step. Motion of the valve and piston is accommodated by adding and removing layers of cells as the boundaries are moved

according to the crank angle of the engine and prescribed motion of the valve. Figure 4 show the cells that are affected by the mesh modifiers. The user defines cellSets that are converted to cellZones and updated run time by the engine class.

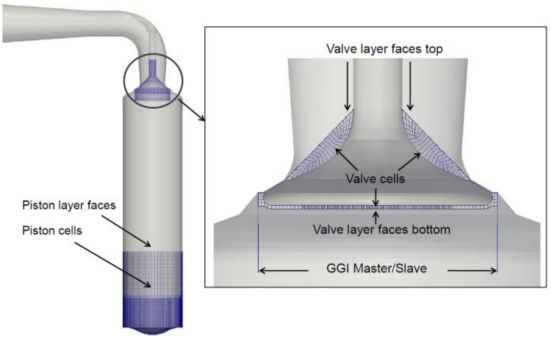

Figure 4. Location of mesh modifiers

Boundary and Initial Conditions

Initial conditions and boundaries are set by use of experimental data. The 4T50ME-X test engine is fitted with numerous temperature and pressure probes that are used for determining the initial conditions and the boundaries. Cycle averaged pressure signals from the scavenge box are used for the inlet pressure patch. The pressure on the exhaust patch is set to be the mean value of the input signal minus the measured pressure drop over the engine. This is to ensure that the driving pressure difference is correct. The initial temperature fields in the scavenge box and exhaust patch is set equal to the ones measured quantities in the scavenge receiver and exhaust receiver respectively. The initial temperature and pressure in the cylinder is calculated with the in-house engine simulator cycsim.

Table 3. Boundary conditions

Patch	*Pressure*	*Velocity*
Intake	timeVaryingTotalPressure	zeroGradient
Exhaust	totalPressure	inletOutlet
Walls	zeroGradient	fixedValue / moving wall

The main boundary conditions used in the simulation is shown in table 3. The total pressure is defined at the inlet and outlet patches and the velocity is defined as a Neumann boundary condition. The inletOutlet boundary that is defined on the outlet is similar to the zeroGradient, the only difference is that it does not allow negative flux over the patch. If a face in the patch has negative flux, indicating reversed flow over the patch, the flux is changed to the fixed value of zero. It is therefore a mix of a Dirichlet and a Neumann boundary condition.

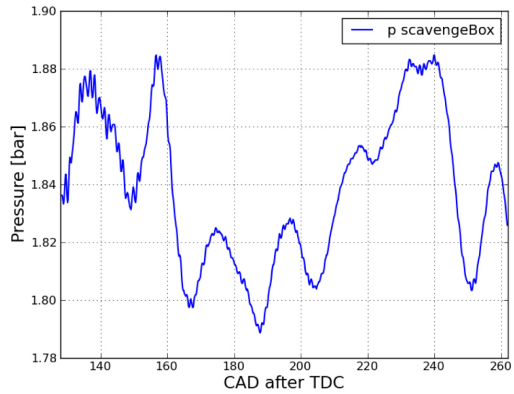

Figure 5. Inlet pressure signal

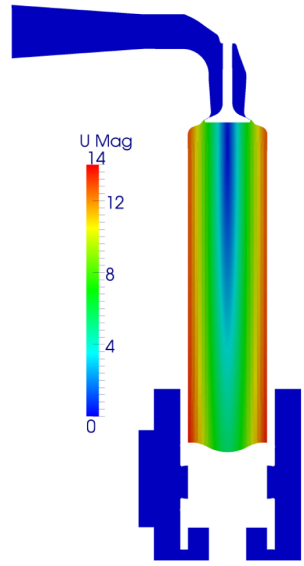

Figure 6. initial velocity distribution before applying turbulent fluctuations

The inlet pressure signal is shown in figure 5. The signal has fluctuations from pressure waves that are present in the scavenge box. The pressure fluctuations possibly originate from the other cylinders that are firing at different crank angles. As the engine has 4 cylinders there is 90 CAD between each occurrence of combustion. Also the underside of the piston acts as a pump when the piston is moving. The void between the stuffing box and the underside of the piston sucks air from the scavenge box when moving upwards and push it back into the scavenge box when the piston is moving down towards BDC. This effect is also accounted for in the solver as it imposes a volume flux over the port patches

equivalent with the volume displaced by the underside of the piston.

The initial velocity distribution used in this study is based on the PIV measurements from the measurement campaign [11]. The velocity field shown in figure 6 is a solid body rotation combined with an axial velocity component that is stationary at the top of the cylinder and equal to the piston velocity at the piston surface. This will not create pressure waves through the domain when starting the simulation. If the fluid in the cylinder is stationary when the piston starts to move it is plausible that waves will start to propagate in the axial direction of the cylinder. A turbulence generator is used to set the initial turbulence in the domain. The generator inserts turbulent spots with a homogenous distribution in the domain, a description of the generator can be found in [16]. Wall modeling is used for the turbulent viscosity and turbulent diffusion rate. The passive scalar is initialized to one (only air) in the scavenge box and with a fixed value at the inlet and to zero (only burned gases) in the rest of the domain. The boundary condition at the exhaust patch and the walls is zeroGradient.

Results

As stated earlier this specific test series has a special belt mounted around the liner that is blocking every other scavenge port. This was done to increase the swirl for comparison with standard design. The degree of swirl can be quantified by a swirl number, Sw, Gupta [17] suggested the following formulation for the swirl number:

$$S_w = \frac{2F_{\theta,z}}{F_{z,z}D} \tag{17}$$

Where $F_{\theta,z}$ is the flux of angular momentum, $F_{z,z}$ is the flux of axial momentum and D is a geometrical scale. As the velocity field usually is unknown it is difficult to determine an accurate swirl number a priori. By assuming that the flux of tangential momentum in the axial direction is equal to the flux of radial momentum in the axial direction and further assuming that the flow on the port exits has a uniform velocity distribution allows the port velocity to be decomposed with the port angle. Performing simple algebra on equation (17) then yields the following expression that only contains geometric properties [9].

$$S_w = \frac{A_{cylinder}}{A_{ports}} \cdot \tan(\alpha) \tag{18}$$

Where α is the port angle and $A_{cylinder}$ is the cross sectional area of the cylinder. The aforementioned belt is fitted to increase the swirl and according to (18) where A_{ports} is cut in half the geometric swirl number is twice as high in this setup compared to normal configuration for the 4T50ME-X engine. The swirl number for this cylinder in this test case is S_w = 0.52 which according to Gupta [17] is categorized as strong swirl. An unfortunate aspect of this method of increasing the swirl is that since the effective flow area through this specific cylinder is reduced to half it is not possible to accurately measure the airflow through this cylinder. Normally the airflow through the engine is determined from the turbocharger and it is assumed that an equal amount of air goes through all the cylinders. Consequently the mass flow through this specific cylinder is not possible to obtain from measurements with a sufficient accuracy.

Mass Flow and Scavenging Efficiency

The mass flow rate through the cylinder is measured at different places in the computational domain. The mass flow rate is integrated over the intake patch, the scavenge ports and the exhaust patch with the following expression:

$$\dot{m} = \int_A (\rho u) \cdot dA \tag{19}$$

The most interesting mass flow rate is the ones over the scavenging ports as these represent directly the rate of air that enters the cylinder. The total amount of air that enters the engine is found by extracting the mass flow rates and perform the following operation

$$m_{tot} = \sum_{i=1}^{N_{ports}} \left(\sum_{j=1}^{N_{time\,step}} \dot{m}_{port} \cdot dt \right) = 1.241\ kg \tag{20}$$

The total amount of air that entered the cylinder via the scavenge ports is shown in equation (20). The mass flow rates for the individual scavenge ports can be seen in figure 7.

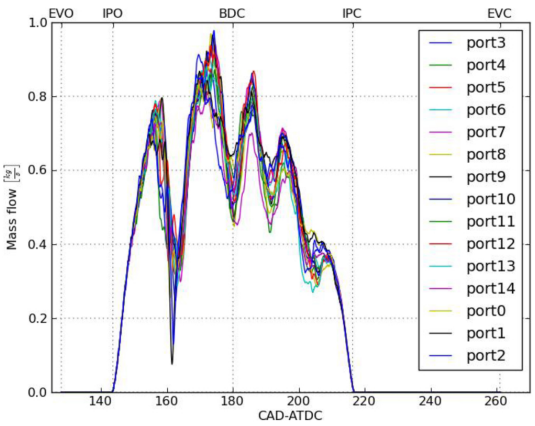

Figure 7. Mass flow rate over the scavenge ports

Figure 7 show the mass flow rates over the scavenge ports during the simulation. It is apparent that there is a presence of fluctuations both globally and with respect to variations between ports. The global oscillations corresponds relatively well with the oscillations that can be observed in the input

pressure shown in figure 5. It is worth mentioning that 5 peaks are observed in the mass flow rates in Figure 7, while only 4 distinct peaks are observed in the inlet pressure from Figure 7. This artifact baffles the author as one would expect the mass flows over the scavenge ports to be directly governed by the inlet pressure signal. One possible explanation is that the boundary condition on the outlet patch is a fixed pressure that omits pressure fluctuations that occur in the exhaust receiver. The measured pressure signal that is imposed on the inlet patch is affected by the exhaust receiver fluctuations while the CFD calculation is only affected by fluctuations in one end of the domain. Other pressure waves propagating in the cylinder might affect the frequencies observed in the mass flow rate. Counting the peaks reveal a frequency of approximately 45.5 Hz. This frequency corresponds well with the fundamental frequency of a cylinder with only one open end. The fundamental wavelength for such an arrangement is ¼ L where L is the length of the pipe. The fundamental frequency for the cylinder based on the stroke and the speed of sound of the mixture in the cylinder is:

$$f_0 = \frac{c}{4 \cdot L} = \frac{410\ m/s}{4 \cdot 2.2m} = 46.6\ Hz \tag{21}$$

The in-cylinder flow should be asymmetric when considering the location of the inlet patch compared to the distribution of the scavenge port patches. The cylinder is perfectly symmetric from the scavenge ports up to the exhaust valve while the inlet patch and outlet patch is oriented to one side. The location of the inlet compared to the scavenge ports is expected to influence the mass flow over the scavenge ports. The location of the inlet and outlet patch compared to the scavenge ports is shown in figure 3.

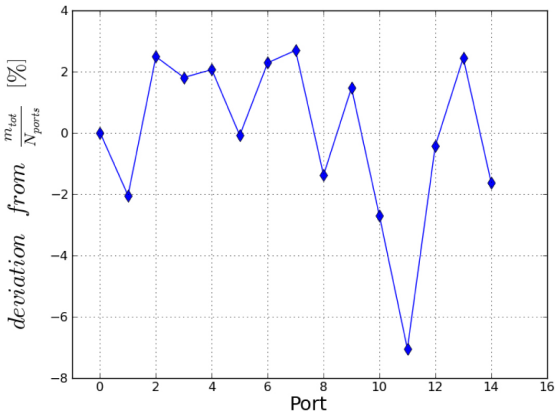

Figure 8. deviation of mass flow between the scavenge ports

Figure 8 shows the deviation in mass flow for the different scavenge ports. The figure show the difference between the total mass of air that has passed through the scavenge ports divided by the number of ports and the total mass of air that has passed through the individual port. There is a difference between the individual mass flows where the differences is ~ 2% from the average mass flow. The largest difference is for scavenge port 11 where the deviation is ~7% from the mean. It is difficult to make a quantitative conclusion of why port 11 experiences a larger deviation from the mean flow compared to the other ports. Other simulations not presented in this paper show a larger difference in mass flow over the ports depending on the engine load and configuration. The expected shape of the curve in Figure 8 would be horse shoe shaped, where the pressure build up across the scavenge box would be analogue with the mass flow rates. The orientation of the ports to the location of the inlet is that port 0 is roughly perpendicular to the inlet and the port numbers increases clockwise when observing in the positive z direction (looking up at the exhaust valve from underneath). The simulation is highly transient both in terms of the shape changes to the domain and the transient inlet condition, but also due to the turbulence modeling. The large deviation of port 11 is possibly a result of a transient phenomenon when the vortex center in the cylinder is formed after scavenging port opening. Short moments of reversed flow over some of the scavenge ports have been observed during this process.

The scavenging efficiency, charging efficiency and delivery ratio is calculated based on the passive scalar from equation (15). Due to this passive scalar the exact mass of fresh air in the cylinder can be calculated at any time. The following calculations are added to the source code and outputted to the log file.

$$m_{air} = \sum_{i=1}^{N_{cylinder}} S_{cell} \cdot \rho_{cell} \cdot V_{cell} \tag{22}$$

$$m_{gas} = \sum_{i=1}^{N_{cylinder}} (1 - S_{cell}) \cdot \rho_{cell} \cdot V_{cell} \tag{23}$$

Where $N_{cylinder}$, ρ_{cell} and V_{cell} are the number of cells in the cylinder, density in the specific cell and cell volume respectively. Equation (21) allows for the calculation of the most common engine parameters

$$\eta_{sc} = \frac{mass\ of\ delivered\ air\ retained}{mass\ of\ trapped\ cylinder\ charge} \tag{24}$$

$$\eta_{ch} = \frac{mass\ of\ delivered\ air\ retained}{swept\ volume\ \times ambient\ density} \tag{25}$$

$$DR = \frac{mass\ of\ delivered\ air}{swept\ volume\ \times ambient\ density} \tag{26}$$

The ambient density is calculated from the temperature and pressure from the scavenge receiver. The swept volume is

equal to the piston area times the stroke. Mass of delivered air is the total amount of air that has been introduced into the cylinder i.e. the same mass that is calculated with equation (20).

Table 4. Engine parameters

Parameter	*Value*
η_{sc}	0.981
η_{sc}	0.678
DR	1.346

Table 4 shows some of the most prominent two stroke engine parameters. The scavenging efficiency tells how effectively the cylinder is scavenged as it relates the ratio of fresh air to mixture in the cylinder. The scavenging efficiency for this simulation is very good and indicates that almost all of the burned gases are replaced with fresh air for the next working stroke. The charging efficiency relates the amount of fresh air trapped in the cylinder with a reference mass. It gives an indication of how effectively the cylinder has been charged. It relates the mass of trapped fresh air in the cylinder with a theoretical reference mass. The delivery ratio relates the total amount of air that goes through the cylinder with the theoretical reference mass. The delivery ratio differs from the efficiencies since it accounts for the amount of fresh air that is transported out with the burned gases. It includes the air that is lost (short circuited) during the scavenging process. Unfortunately the data needed to validate these parameters was not measured during this measurement campaign.

Visualization of the Passive Scalar

In order to evaluate the gas exchange in the cylinder the transport equation for the passive scalar is calculated (15). The passive scalar acts as an indication for the mass fraction of fresh air and burned gases. The color scheme is chosen for the visual effect of burned gases being red and cold air being blue.

Figure 9 show some instantaneous distributions of the passive scalar at some relevant crank angles during the simulation. The first snapshot is the initial condition where the cylinder is filled with hot gases and the scavenge box is filled with fresh air. The second snapshot is shortly after the scavenge ports are uncovered and it shows how the fresh air is entering the cylinder. The subsequent snapshots show how the fresh air is propagating through the cylinder, flushing the burned gases out. The flow is highly transient and since there is no cycle averaging it is not possible to show mean fields. The effect of in-cylinder swirling flow is seen as some exhaust gas is trapped in the center of the cylinder. The snapshot at 190 CAD show that some of the exhaust gases are trapped under the 15 jets that forms a recirculation vortex core at some distance above the piston surface. This mixture of burned gases and fresh air is dissolved as the simulation continues and by the 230 CAD frame it seems to have vanished. The valve also seems to restrict the mixture from escaping. Throughout the simulation there is a presence of burned gases underneath the valve. At exhaust valve closing, 261 CAD, there is still a presence of burned gases mixed with fresh air. This suggests that the swirl is strong when the belt is mounted.

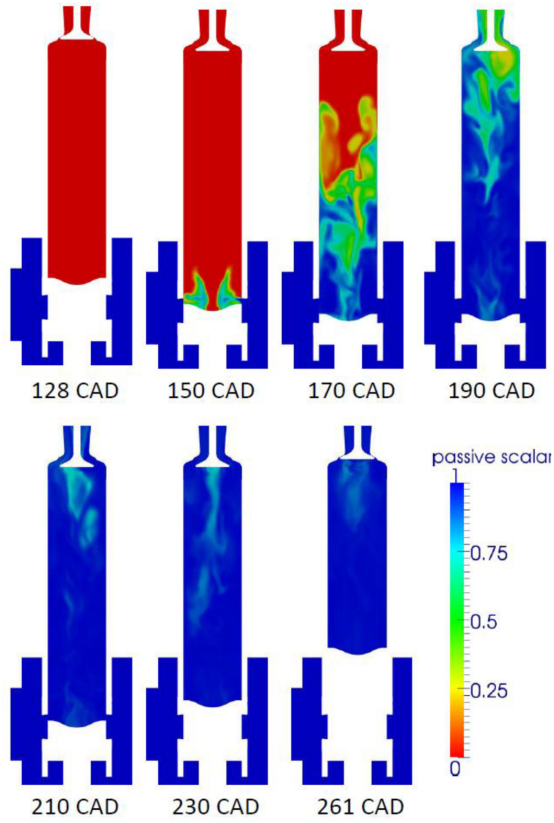

Figure 9. Snapshots of the passive scalar at relevant crank angles after Top Dead Center (TDC)

Velocity Fields and Comparison with PIV

The tangential and axial velocity component was measured with PIV during the measurement campaign. The velocities were measured at a point inside the combustion chamber, close to the valve. The position of the velocity "probe" is r = 195 mm from the geometric center of the cylinder. A detailed description of the methodology and work can be seen in [11].

Figure 10 shows a sketch of the PIV setup. The optical engine cover, described in [12], is fitted with a laser and a CCD camera that allows for the velocity field in the laser sheet to be measured. The velocities from the measurements are cycle averaged over many cycles. The laser sheet is relatively small, approximately 50×50 mm, and the measured velocities

in the sheet was quite homogenous. The measurements presented in Figure 11 are the average of the velocities from the laser sheet. The experimental data can be considered to be averaged in both time and space. Due to limitations from computational expenses and the lack of sufficient initial conditions the data presented in this study is not cycle averaged which will give an inherent inaccuracy in the comparison that follows. Probes located in the computational domain are used to extract the tangential and axial velocity component. A total of nine probes are used to calculate a local spatial average value in the region of interest. Three points along the radius spaced 10 mm apart and three points in the axial direction spaced 10 mm apart. Since the experimental data and the data from the numerical model are not post processed in the same way they are not expected to match perfectly in terms of absolute values. However, the most important feature for validating the simulation will be to check if the timing is correct. As the location of the laser sheet is far away from the scavenge ports the introduced fresh air will not reach the laser sheet immediately, but a delay will be present. The axial velocity component will increase immediately after the exhaust valve is opened due to the pressure difference between the exhaust receiver and the cylinder pressure. When timing the scavenge air it is more obvious to use the tangential velocity as a reference. When the tangential velocity component experiences a sudden rise it is evident that the incoming scavenge air has arrived at the location of the measurements in the cylinder. Figure 11 show the measured PIV velocity plotted together with the velocity from the simulation. As expected the axial velocity component experience heavy acceleration as the exhaust valve is opened. There is a large pressure difference between the exhaust receiver and the cylinder pressure and this combined with a small effective flow area before the valve is fully opened yields very high velocities. The flow over the valve is highly compressible with a peak mach number of ~1.4. The flow over the exhaust valve is transonic/supersonic approximately between 130-145 CAD ATDC.

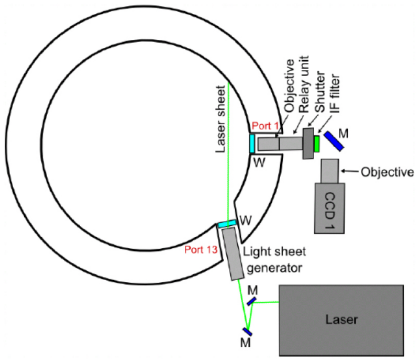

Figure 10. schematic of the experimental setup (MAN Diesel & Turbo)

The Mach number is not a measured quantity, but is calculated by the CFD solver based on the velocity, temperature and heat capacities in the domain divided by the speed of sound. The maximum value for the Mach number is then outputted to the log files.

$$Ma = \frac{mag(\vec{U})}{\sqrt{\frac{c_p}{c_v} \cdot (c_p - c_v) \cdot T}} \qquad (27)$$

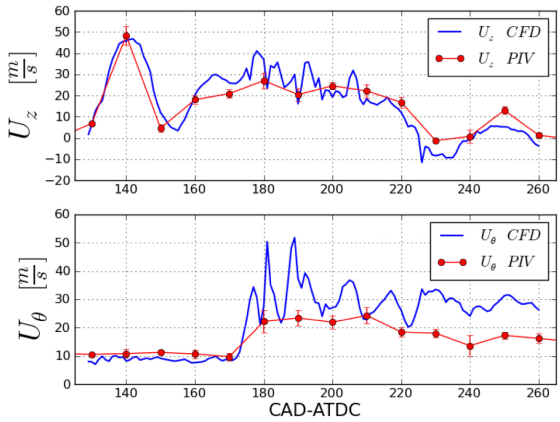

Figure 11. tangential and axial velocity component as function of crank angle

The velocity probes are located 75 mm above the top of the liner so the flow field in this region is affected by the flow over the exhaust valve. There are only small differences between the 9 probes in the computational domain and the curve in Figure 11 is an average of the probes. The axial velocity seems to fit the experimental data quite well both in terms of timing, trends and absolute values. The tangential velocity components are of higher relevance in terms of model validation since it is not as influenced by suction from the valve and can therefore give more information of the scavenging air. The tangential velocity is relatively unchanged after the opening of the exhaust valve and is relatively stable at the initial value. The scavenging ports open at ~143.25 CAD ATDC, but the sudden rise in the tangential velocity is not before ~ 170 CAD ATDC. This indicates that it takes almost 27 CAD for the introduced fresh air to travel trough the cylinder and reach the probes located in the engine cover. The magnitude of the tangential velocity component is over predicted by the numerical model compared to the PIV measurements, but the timing is very good. The rise in magnitude for the tangential velocity component is more or less instantaneous for the CFD model and the PIV measurements. From this it is possible to assume that the mass flow rate through the engine is reasonably well predicted, otherwise the time it takes the introduced fresh air to travel this distance (which is close to 2 meters) would be inconsistent with the measured data. As stated earlier in the paper the CFD model is non cycle averaged “pseudo-LES” and it is apparent from Figure 11 that some large turbulent structures are resolved in the simulation. The oscillatory

nature of the velocity measurements must be attributed to the fact that the results presented in this paper has not been filtered for frequencies or averaged. The difference in magnitude for the measured and calculated velocities is more difficult to explain as the measured data in confined to one location in the cylinder and does not tell anything about the tangential velocity profile. It is possible that even if the magnitude of the calculated tangential velocity is over predicted the integrated swirl is correctly simulated.

SUMMARY/CONCLUSIONS

In this study a CFD model that is able to predict the scavenging process in a uniflow scavenged cross-head two-stroke diesel engine has been presented. The model includes the full 3D geometry and utilizes experimentally measured quantities as initial conditions and boundary conditions. The case that is presented in this paper corresponds to a test run during an optical measurement campaign where the tangential and axial velocity components were measured experimentally by use of a PIV system. The CFD model is able to handle topological changes due to the motion of piston and valves and can perform run time analysis on the specific cells that are present in the cylinder. Mass flow rates are calculated on both the inlet and outlet patch as well as for all the scavenge ports. The total mass in the domain can be extracted as well as the total mass of the fluid present in the cylinder at all times. This combined with solving a transport equation for a passive scalar makes it possible to make a detailed investigation of the mixing and gas exchange in the cylinder during the scavenging process. Validation of the model is difficult without accurate knowledge of the mass flow rates at this test case. Comparison between the experimental velocities and the numerical is in relative good agreement. The absolute numbers is not necessarily accurate and the swirling component is clearly over predicted by the numerical model. However, when considering the timing of the swirling components it is in quite good agreement with the experimental data. This implies that the mass flows are reasonably correct otherwise a discrepancy between how long it takes the introduced fresh air to travel from the scavenge ports to the engine cover would be apparent. Future studies will include a comparison with experimental mass flows as these can be obtained from a mass balance calculation over the turbocharger. Also a comparison with a test run without blocking half of the scavenge ports will yield an opportunity to investigate the influence the swirl has on the scavenging process.

REFERENCES

1. Heywood JB, and Sher E,, The Two-stroke cycle engine: its Development, Operation and Design, Taylor and Francis, Philidelphia, 1999.

2. Ferro, A. Investigation by means of models into the scavenging of two-stroke internal combustion engines, The engineers' Digest, Vol 19, 1958, pp.512-522

3. Percival WH, Method of scavenging analysis for 2-cycle diesel engines, Society of Automotive engineers-papers, Vol 63, pp. 737-751, 1955

4. Sher, E, Hossain, I, Zhang, Q and winterbone, D.E, Calculations and Measurments in the Cylinder of a Two-Stroke Uniflow-Scavenged Engine Under Steady Flow Conditions, Experimental Thermal and Fluid Science, pp. 418-431, 1991

5. Litke, B, The influence of inlet angles in inlet ports on the scavenging process in two-stroke uniflow-scavenged engine, Marine technology III Volume 45, 1999.

6. Lamas, I.L. and Vidal, C.G.R, Computational Fluid Dynamics Analysis of the Scavenging Process in the MAN B&W 7S50MC Two-Stroke Marine Diesel Engine, Journal of Ship Research, vol 56, pp. 154-161, 2012

7. Stone, R. Introduction to Internal Combustion Engines. Macmillan press LTD, 1999.

8. Heywood, J.B. Internal Combustion Engine Fundamentals, McGraw-Hill Book Company, 1988

9. Al-Mousawi N,M,J. Numerical Simulation in a model Diesel engine using RANS and LES turbulence models. Master thesis, Technical University of Denmark, 2012

10. Rutland, C.J. Large-eddy simulations for internal combustion engines-a review. International Journal of Engine Research, 2011.

11. Mayer. S, Clausen. S, Hult. J, Nogenmyr. K.J, Advanced optical development tools for two-stroke marine diesel engines. CIMAC conference 2013, paper 53. 2013

12. Hult. J, Mayer. S, A methodology for laser diagnostics in large-bore two-stroke diesel engines, Measurement Science and Technology, 2013, doi:10.1088/0957-0233/24/4/045204.

13. Favre. A, Equations des gaz turbulent compressibles, Journal de Mechanique, vol 4, pp.361-421, 1965

14. Ferziger J.H, Peric M. Computational Methodes for Computional Fluid Dynamics. Third edition, Springer, 2002.

15. Beaudoin. M, Jasak. H, Development of a Generalized Grid Interface for Turbomachinery simulations with OpenFOAM. Open source CFD international conference. 2008

16. Kornev. N, Kröger. H and Hassel. E, Synthesis of homogenous anisotropic turbulent fields with prescribed second-order statistics by the random spots method. Communications in numerical methods in engineering, pp. 875-877, 2008. Doi:10.1002/cnm.1009.

17. Gupta, A.K. Lilley, D.G, Syred, N. Swirl Flows. Turnbridge Wells, Kent, Abacus press, 1984

18. Nakagawa. H, Kato. S, Tataishi. M, Adachi. T, Tsujimura. H and Nakashima. M, Airflow in the Cylidner of a 2-stroke Cycle Uniflow Scavenging Diesel Engine During compression Stroke. Japan society of mechanical enginers, Series III, Vol 3, No 3, 1990.

19. Sigurdsson. E. Scavenging flow in a Two-Stroke Diesel Engine, Master thesis, Technical University of Denmark, 2011.

20. Haider. S, Experimental and Numerical Study of Swirling Flow in Scavenging Process for 2-Stroke Marine Diesel Engines, Ph.D. thesis, Technical University of Denmark, 2011,

21. Veynante. D, Turbulent Combustion Modeling, Progress in energy and combustion science 28.3 (2002)

22. OpenFOAM User Guide Version 1.6, 14.July 2009. OpenCFD LDT. (www.openfoam.org) (www.extend-project.de)

ACKNOWLEDGMENTS

The author will like to thank:

Danish ministry of Science, Innovation and Higher Education for partially funding the industrial Ph.D. project.

Internal Combustion Engine Group, Dipartemento di Energia, Politecnico Di Milano for development of the Engine mesh motion Class in OpenFOAM.

DEFINITIONS/ABBREVIATIONS

CFD - Computational Fluid Dynamics

CAD - Crank Angle Degree

ATDC - After Top Dead Center

PIV - Particle Image Velocimetry

LES - Large Eddy Simulation

RANS - Reynolds Averaged Navier Stokes Equation

SFOC - Specific Fuel Oil Consumption

LES - Large Eddy Simulation

TDC - Top Dead Center

BDC - Bottom Dead Center

EVO - Exhaust Valve Opening

EVC - Exhaust Valve Closing

IPO - Inlet Port Opening

IPC - Inlet Port Closing

SGS - Sub Grid Scale

SFS - Sub Filter Scale

GGI - Generalized Grid Interface

CCD - Charged-Coupled Device

EGR - Exhaust Gas Recirculation

The Engineering Meetings Board has approved this paper for publication. It has successfully completed SAE's peer review process under the supervision of the session organizer. This process requires a minimum of three (3) reviews by industry experts.

ISSN 0148-7191

SAE Customer Service:
Tel: 877-606-7323 (inside USA and Canada)
Tel: 724-776-4970 (outside USA)
Fax: 724-776-0790
Email: CustomerService@sae.org
SAE Web Address: http://www.sae.org
Printed in USA

A.2 CFD analysis of the Scavenging Process in Marine Two-Stroke Diesel Engines

Proceedings of the ASME 2014 Internal Combustion Engine Division Fall Technical Conference
ICEF2014
October 19-22, 2014, Columbus, Indiana, USA

ICEF2014-5438

CFD ANALYSIS OF THE SCAVENGING PROCESS IN MARINE TWO-STROKE DIESEL ENGINES

Fredrik H. Andersen
MAN Diesel & Turbo SE
Teglholmsgade 41, 2450 Copenhagen SV,
Denmark

Technical University of Denmark
Anker Engelunds vej 1,2800, Kgs. Lyngby,
Denmark

Mail: Fredrik.Andersen@man.eu,
phone:(+45) 33 85 17 66

Johan Hult, Karl-Johan Nogenmyr and Stefan Mayer
MAN Diesel & Turbo SE
Teglholmsgade 41, 2450 Copenhagen SV,
Denmark

Draft

ABSTRACT

The scavenging process is an integral part of any two-stroke internal combustion engine regardless of being spark ignited (SI) or compression ignited (CI). The scavenging process is responsible for replacing the burned gas from the combustion process from the previous working stroke with fresh air/charge before the subsequent compression stroke. This implies that the scavenging process is integral to engine performance as it to a large extent influences the initial condition for the combustion process, thus affecting the fuel economy, power output and emission of hazardous gases.

Two-stroke diesel engines for marine propulsion normally operates by the uniflow scavenging method, where the scavenge air enters the cylinder via inlet ports located near the bottom dead center and exits through one or several exhaust valves located in the cylinder head. This arrangement concentrates the airflow in one direction through the cylinder thus giving the method its name. The inlet ports are angled with respect to the local radius which will introduce a tangential velocity component to the air flow. The air moves axially through the cylinder in a swirling motion that favors mixing of fuel and air as the injected fuel is transported with the swirling air in the combustion chamber during fuel injection.

A known characteristic of swirling flows is an adverse pressure gradient in the center of the rotating flow which might lead to a local deficit in axial velocity and the formation of central recirculation zones, known as vortex breakdown. Optimal scavenging is achieved when the gas exchange is done by displacement, the local deficit in axial velocity will increase the mixing of burned gas and scavenge air thus decreasing the amount of pure displacement.

INTRODUCTION

In this study a CFD analysis of the scavenging process in the 4T50ME-X test engine at Diesel Research Center Copenhagen is performed for two different swirl numbers. The CFD model includes the full, asymmetric three-dimensional, geometry from the scavenge box to the end of the exhaust diffuser and employ measured transient pressure signals as boundary condition for the airflow through the cylinder. In-cylinder velocity measurements (PIV) have been conducted for the specific engine operating conditions which will be used for both initial conditions and for validation of the simulations.
The influence of swirl on the scavenging process is investigated by blocking every second scavenging port with a specially designed belt that can be mounted on the lower part of the liner. Reducing the effective flow area will increase the in-cylinder swirl and the two cases are compared in terms of scavenging performance parameters and by investigation of the in-cylinder flow fields. Increasing the in-cylinder swirl has a negative

effect on the scavenging efficiency, and an investigation of the flow field indicated increased mixing of the burned gases and introduced air in the center line region of the cylinder.

The literature on research for marine two-stroke diesel engines is scarce compared to smaller due to the cost and complexity involved with research on ship engines. There are relatively few engines worldwide and there are few test engines. A consequence of this is that research often is conducted on scaled down models. Previous studies include visualization (Ferro, 1958)[2], pitot measurements (Persival, 1955)[1] and hotwire measurements (Shear et al, 1991)[4].

The influence of in-cylinder swirl have been investigated by (Litke, 1999)[5] where he used a model scaled to ¼ and water as the fluid. Various port angles and port shapes was investigated and it was concluded that the optimum angle for the scavenge ports was 20 degrees which is the industry standard.

The scavenging process in marine two-stroke engines have been subject for research at the Technical University of Denmark over the last years spawning several publications such as (Haider et al, 2011)[6] who performed PIV (Particle Image Velocimetry) measurements on a scaled down stationary set up. (Ingvorsen et al, 2013)[7][8] expanded the scaled down engine model by redesign of the scavenge port section to match that of the engine and to install a linear actuator in order to include the dynamic behavior of port opening and closing as well as investigating the influence of swirl number by changing the port angle.

Over the last decades computational resources have become reasonably inexpensive, this in turn has made CFD studies of the in-cylinder flow manageable and increasingly popular. Early numerical work includes the work of Nakaawa et al (1990)[9].

In later years several numerical studies have been conducted on MAN Diesel & Turbo's engines, or setups based on the design of a MAN engine. Sigurdsson (2011)[10] performed CFD analysis using Star-CD on a 12 degree sector (including only one scavenge port) of a heavily simplified version of the 4T50ME-X test engine. Al-Mousawi (2012)[11] used the commercial CFD software, Star-CCM+, to do calculations on the model engine from [7] investigating the influence of turbulence models. He tested both Reynolds Averaged Navier Stokes (RANS) and Large Eddy Simulation (LES). The study showed that RANS models struggles to resolve the vortex core and that if possible LES should be used. Most studies of the scavenging process in marine two-stroke diesel engine neglects to include the asymmetric component of the in-cylinder flow due to the 90 degree exhaust bend and the location of the scavenge air receiver and the scavenge ports. Lamas et al. (2012)[12] investigated the scavenging process in the 7S50MC engine using ANSYS Fluent. This study use the RANS turbulence modeling approach, includes the asymmetry from the exhaust bend and uses a transport equation of a passive scalar to distinguish between the burned gas and the fresh scavenge air used to flush the cylinder.

The aim for this study is to investigate how the scavenging process is affected by increasing the in-cylinder swirl. The in-cylinder swirl is changed by mounting a specially designed belt around the lower part of the liner, blocking every other port. Two cases will be presented in this paper, one where the scavenge ports are uncovered (which is the normal operating condition) and one where half of the scavenge ports are blocked. It is expected that increasing the swirl will have a negative effect on scavenging efficiency due to central recirculation zones which will increase mixing of the burned gas and the scavenge air.

4T50ME-X TEST ENGINE

The numerical investigation presented in this paper corresponds to an optical measurement campaign conducted on the 4T50ME-X test engine. The 4T50ME-X test engine is a full scale, operational, uniflow scavenged, cross head two-stroke diesel engine. It has 4 cylinders, a bore of 0.5 meters and a stroke of 2.2 meters. A time resolved signal from a pressure transducer in the scavenge box was ensemble averaged and applied as boundary condition in the CFD model. Time averaged pressure and temperature for the exhaust receiver is used as boundary conditions at the outlet of the computational domain. A time averaged temperature for the scavenge box is used to initialize the temperature field in the scavenge box. A transient pressure signal is measured in the cylinder head and is used for validation of the numerical model as well as initializing the simulations.

The optical measurement campaign was conducted to investigate the possibility of obtaining valuable velocity measurements inside the cylinder during operating condition. Optical access was provided through a specially designed engine cover with Ø60 sapphire windows which makes it possible to apply particle image velocimetry (PIV) to assess the flow field. Due to the limited size of the windows and the little space available, the field of view for the measurement was only 50x50 m, which is small compared to the scales of the in-cylinder motions. The laser sheet is located 55 mm from the cylinder wall as shown in figure 1.

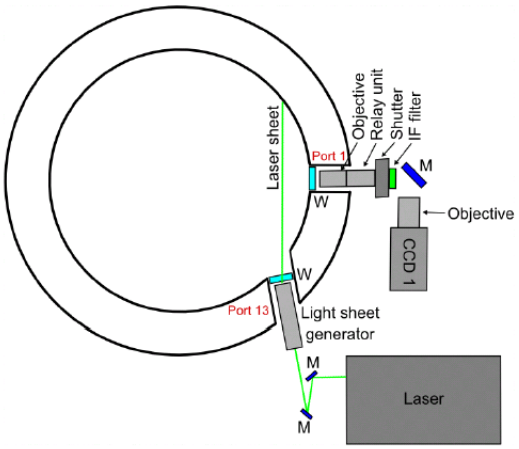

Figure 1: Schematic of the experimental setup (MAN Diesel & Turbo SE)

The velocity vectors that appeared in the 50x50 mm laser sheet was, except for crank angles close to top dead center (TDC), close to homogeneous and the velocity component used for validation is the mean value for the extracted sheet. Both the axial velocity component and the tangential velocity component are extracted and will be compared with velocity measurements from the CFD model. A more detailed description of the optical measurement campaign can be found in [14] and [15].

Table 1 contains the most prominent specifications of the test engine. Note that the slot containing the number of scavenge ports states both the default design number of 30 ports and the reduced number of ports, 15, which is used to increase the in-cylinder swirl.

Table 1. Engine specifications for 4T50ME-X

Bore	500 mm
Stroke	2 200 mm
Connecting rod length	2 885 mm
Cylinders	4
Ports per cylinder	30 (NS) / 15 (HS)
Port angle (deg)	20
Max Power	~7 MW
Max engine speed	123 RPM
Valve operation	Electronic / hydraulic
Max pressure	190 bar
Charging	Turbo charged

ENGINE OPERATION

Figure 2 show a schematic drawing of a uniflow scavenged, cross head, two-stroke diesel engine which is the de facto standard for propulsion of large marine vessels such as container ships and tankers.

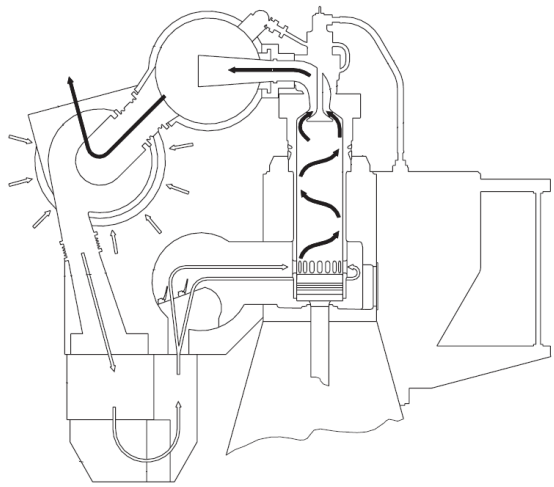

Figure 2. Schematic drawing of uniflow scavenged, cross-head marine diesel engine (MAN Diesel & Turbo)

The airflow enters the cylinder from the scavenge air receiver trough the angled scavenge ports and into the cylinder. The angled port adds a tangential velocity component to the velocity thus creating a confined swirling flow. The fresh air moves in a helical motion upwards through the cylinder and exits through the exhaust valve located in the cylinder head. In this process the fresh air will flush out the residual gas from the combustion process. After exiting the exhaust bend located downstream of the exhaust valve, the gas enters a large volume denoted exhaust receiver. This volume is created to provide constant pressure to the turbines. The compressor is fed with ambient air which is pressurized before reaching the scavenge air receiver via a cooling unit. The scavenge receiver is a buffer volume, like the exhaust receiver, designed to damp out pressure fluctuations created by the adjacent cylinders. There is a pressure difference between the scavenge receiver and the exhaust receiver which acts as the driving pressure for the scavenging process.

During the combustion process close to the top dead center there is a large build up of pressure in the combustion chamber / cylinder. This pressure acts on the piston, forcing it downwards thus expanding the volume and lowering the pressure in the cylinder. Approximately 110-130 CAD ATDC the exhaust valve opens. The following period is known as the blow down period where the combustion gas in the cylinder starts to escape the cylinder via the exhaust valve to balance the pressure difference between the cylinder and the exhaust receiver. The optimum condition for scavenging is that the pressure in the cylinder and the pressure in the scavenge box is close to equal at inlet port opening [16] [17]. If the pressure in the cylinder is higher than the scavenge box pressure the flow over the ports will be shortly reversed back into the scavenge box. This is undesirable as the back flow contains residual gas from the combustion process as well as liner lubricating oil.

This cause fouling that over time can lead to a shorter service interval for the engine. However, a higher cylinder pressure at scavenge port opening has the benefit that more work imposed on the piston. Standard practice is to allow some blow back, usually in the order of 1% of the total cylinder mass. The scavenge ports are uncovered approximately 40 CAD before bottom dead center (BDC) and close approximately 40 CAD after BDC. During this period the fresh air is flushing the cylinder for burned gas. After the scavenge ports are closed the piston moves upwards while the exhaust valve remains open. Timing of exhaust valve closing is used to set the compression pressure.

Figure 3 is a schematic overview of the processes described in the above section. The figure divides the two-stroke engine cycle into 5 processes; expansion (combustion/work), blow down (adjusting pressure), scavenging (flushing cylinder), push out (determining compression pressure) and compression (pressure build up). Those 5 processes can be clustered into two phases; closed volume (when the cylinder is a closed volume) and open volume (when there is gas exchange in the cylinder). The study presented in this paper is focused only on the open volume phase of the cycle.

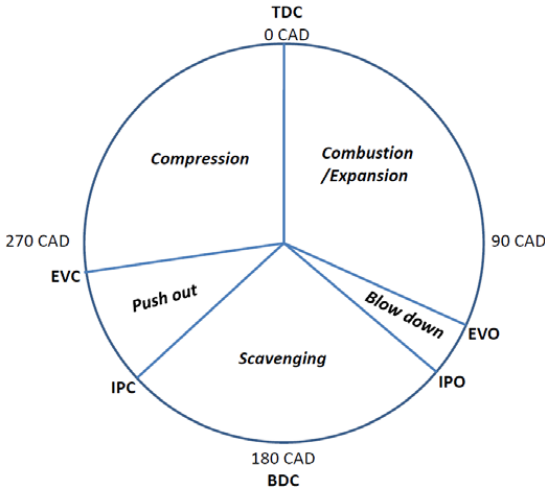

Figure 3. Two-stroke engine cycle processes

NUMERICAL MODEL

The software used in this numerical investigation is the open source tool box OpenFOAM 1.6-ext [18] which contains the necessary functionalities needed to solve the Navier-Stoke equations by the finite volume method (FVM). This particular version of OpenFOAM is used due to its extended engine libraries needed to handle shape and topological changes to the computational domain from the motion of the piston and valve. A special engine wrapper class, which inherits most of its functionalities from the native engine library, is written specifically to handle cross head, uniflow scavenged two-stroke engine simulations. The engine class generates mesh modifiers and calculates the piston position as a function of RPM, crank angle and geometry. The timing of exhaust valve opening and closing is electronically controlled and is a measured quantity and is read by the mesh class from an input script. Three mesh modifiers are implemented to handle the shape and topological changes to the mesh:

1. ***Sliding Interface***

   During the blow down period shown in figure 3 the cylinder and scavenge box is separated in space. The sliding interface algorithm is used to join together the two mesh regions as the piston uncovers the scavenge ports and the fresh air from the scavenge box enters the cylinder. The sliding interface algorithm allows for relative sliding of components. Each scavenge port has a patch (master) with a corresponding patch on the cylinder (slave). The master and slave faces are merged together and the faces are changed from a boundary to internal faces. The uncovered faces of the master and slave patch remains as boundaries.

2. ***Add / Remove layers***

   To maintain uniform cell sizes as the exhaust valve moves, layers of hexahedral cells are either added or removed, depending on local cell sizes. During opening of the valve, layers are removed below the valve, while added above the valve. A set of cells is generated by the user that contains the cells that translates as well as two sets of faces where layers of cells are to be added or removed. The cells and faces involved in this operation can be seen in figure 4.

3. ***Generalized Grid Interface (GGI)***

   A consequence of the valve motion is that a part of the mesh will be sliding along a stationary part of the mesh in the cylinder. The generalized grid interface (GGI) is a utility that enables communication over two non-conforming patches. Its functionality is somewhat similar to the sliding interface, but it does not make a topological change to the mesh and thus it does not re-write the mesh at every time step. It merely accommodates to interfaces to slide across eachother. Two interfaces, master and slave, are defined and the algorithm will go through the faces in the interface, calculate a weighting function and interpolate between the overlapping faces.

The motion of the piston is performed by stretching the in-cylinder mesh points according to the piston displacement calculated by the engine class and a weighting function. Only the open volume phase from figure 3 is considered in this study.

The simulations start at EVO and ends at EVC. Including the compression and modeling the fuel spray and combustion is out of scope for this study and due to the size of the simulation it is considered to computationally expensive to simulate several cycles even though this would make the simulations less sensitive to the initial and boundary conditions.

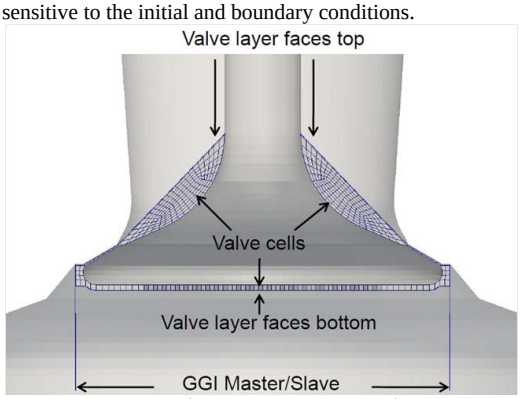

Figure 4. Cross section of the exhaust valve region of the mesh. The visible cells are subjected to topological changes by the add/remove layer algorithm

GOVERNING EQUATIONS

The governing equations are the compressible Favre Averaged Navier-Stokes (FANS) equations. FANS equations is closely related to the Reynolds Averaged Navier Stokes (RANS) equations, however as the density varies it is beneficial to use the density weighted favre averaging to avoid suppressing fluctuations in terms including density [19],[20],[23].

Turbulent fluid motions can be decomposed into a mean and a fluctuating component.

$$\phi = \bar{\phi} + \phi' \qquad (1)$$

To account for density variations the quantity of interest is favre averaged:

$$\tilde{\phi} = \frac{\overline{\rho\phi}}{\bar{\rho}} \qquad (2)$$

Where ρ denotes the fluid density. The fluctuation from the favre average reads:

$$\phi'' = \phi - \tilde{\phi} \qquad (3)$$

The Navier-Stokes is averaged according to equation (1), (2) and (3) to produce the governing equations for conservation of mass, momentum and energy.

$$\frac{\partial \bar{\rho}}{\partial t} + \frac{\partial}{\partial x_i}(\bar{\rho}\widetilde{u_i}) = 0 \qquad (4)$$

$$\frac{\partial}{\partial t}(\bar{\rho}\widetilde{u_i}) + \frac{\partial}{\partial x_j}\left[\bar{\rho}\widetilde{u_j}\widetilde{u_i} + \bar{p}\delta_{ij} + \rho\widetilde{u_i''u_j''} - \widetilde{\tau_{ij}}\right] - \tilde{F}_i = 0 \quad (5)$$

$$\frac{\partial(\bar{\rho}\tilde{h})}{\partial t} + \frac{\partial}{\partial x_j}\left[\bar{\rho}\tilde{h}\widetilde{u_i} - \widetilde{u_i}\bar{p} - \frac{\partial(\alpha_{eff}\tilde{h})}{\partial x_i}\right] - \frac{\partial \bar{p}}{\partial t} = 0 \qquad (6)$$

Equation (4) is the continuity equation where $u_i = [u_1, u_2, u_3]$ and $x_i = [x_1, x_2, x_3]$.

Equation (5) is the momentum equation which after averaging contains an additional term that requires modeling in order to close the set of equations. This term is the non-linear term $\rho\widetilde{u_i''u_j''}$ known as the Reynolds stress tensor [20]. The Reynolds stress tensor can be modeled by use of the Boussinesq approximation which relates the Reynolds stresses with an artificial eddy viscosity that accounts for the transport and dissipation of turbulence in the smaller scales of the flow [24]. The Reynolds stress tensor and the viscous stress tensor can be joined together and written as follows:

$$\rho\widetilde{u_i''u_j''} - \widetilde{\tau_{ij}} = \tilde{\mu}_{eff}\left[\left(\frac{\partial \widetilde{u_i}}{\partial x_j} + \frac{\partial \widetilde{u_j}}{\partial x_i}\right) - \frac{2}{3}\delta_{i,j}\frac{\partial \widetilde{u_k}}{\partial x_k}\right] \qquad (7)$$

Which contains a term for the effective viscosity, $\mu_{eff} = \mu_l + \mu_t$, where μ_l denotes laminar (molecular) viscosity and μ_t denotes the turbulent (eddy) viscosity. The eddy viscosity is calculated from the specific turbulence model. The remaining terms in equation (5) is the pressure term $\bar{p}\delta_{ij}$ where δ_{ij} is the Kronecker delta ($\delta_{ij} = 1\ if\ i = j\ \ and\ \delta_{ij} = 0\ if\ i \neq j$) and $\tilde{F}_i$ is the body forces.

Equation (6) is the energy equation written with respect to enthalpy. The last term in the bracket contains the effective thermal diffusivity $\alpha_{eff} = \alpha_l + \alpha_t$ where $\alpha_l$is the molecular thermal diffusivity and α_t is the thermal diffusivity added by the turbulent fluctuations in the fluid flow. The turbulent thermal diffusivity is calculated by the following equation:

$$\alpha_t = \frac{\mu_t}{Pr_t} \qquad (8)$$

Where Pr_t is the turbulent Prantl number which is equal to one. Perfect gas assumption is made to specify an equation of state, the following relations are valid for this assumption.

$$\gamma \equiv \frac{C_p}{C_v}, \qquad P = \rho RT, \quad C_p - C_v = R$$

Where γ is the heat capacity ratio, equal to 1.358 which corresponds to typical exhaust gas mixtures. R is the specific gas constant and T is the temperature.

The turbulent viscosity is calculated by the RNG $k-\varepsilon$ model. The RNG $k-\varepsilon$ turbulence model solves two additional

transport equations for turbulent kinetic energy k and turbulent dissipation rate ε. Where the eddy viscosity is only determined by a single length scale in the standard $k-\varepsilon$ model the RNG model tries to account for the different scales of motion through a re-normalization approach [25]. The eddy viscosity, μ_t, is calculated by combining k and ε as follows:

$$\mu_t = \rho C_\mu \frac{k^2}{\varepsilon} \tag{9}$$

In addition to the governing equations (4), (5) and (6) an additional transport equation is solved to address the presence of the two gases in the cylinder.

$$\frac{\partial(\bar{\rho}\widetilde{S_0})}{\partial t} + \frac{\partial\left(\bar{\rho}\widetilde{S_0}\widetilde{u_j}\right)}{\partial x_j} - \frac{\partial}{\partial x_j}\left((\tilde{\mu}+\tilde{\mu}_t)\frac{\partial(\bar{\rho}\widetilde{S_o})}{\partial x_j}\right) = 0 \tag{10}$$

Where S_0 is the mass fraction of fresh air. The mass fraction of burned gases, S_1, is found from the relation of unity:

$$S_1 = 1 - S_0 \tag{11}$$

Initially the cylinder and exhaust bend is filled with burned gases $S_0 = 0$ while the scavenge box is initiated with $S_0 = 1$

COMPUTATIONAL DOMAIN

The computational domain used in the simulations was generated with the native mesh generators snappyHexMesh and blockMesh. This result in a hexahedral dominated mesh which is beneficial for these kinds of simulations due to numerical accuracy and stability. The mesh was generated in 4 separate components that are later merged and stitched together into the full geometry. This was done to meet the special requirements for the mesh modifiers that act in the valve region. The mesh in the valve and the cylinder regions was generated using an in-house python utility that generates input scripts for the blockMesh utility. The scavenge box and the exhaust bend mesh was generated using snappyHexMesh using an appropriate back ground mesh generated with blockMesh. The total number of cells in the computational domain is 1.23 million. The computational domain is can be seen in figure 5. The computational domain is decomposed into 30 partitions that is solved in parallel using 30 XENON X5675 (Westmere) CPU's with high speed interconnection. Total simulation time is in the range of 120-130 hours.

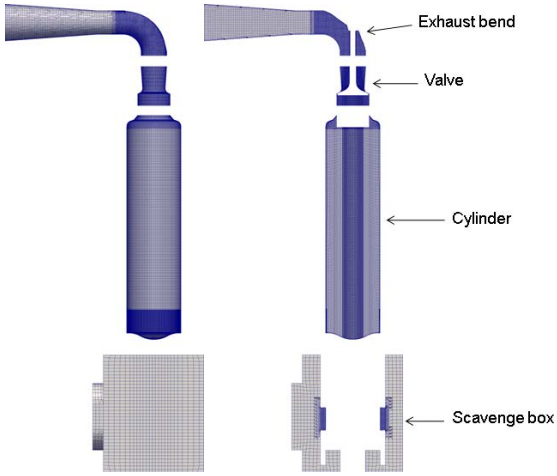

Figure 5. Mesh components and cross section

BOUNDARY AND INITIAL CONDITIONS

The initial and boundary conditions used in the simulations are a combination of time resolved and cycle averaged experimental data from the 4T50ME-X test engine as well as calculated quantities. The flow through the cylinder is pressure driven and subjected to pressure fluctuations from the other cylinders, acoustic waves and the fundamental frequency of a gas in a cylinder when subjected to a sudden opening in one end. To include some of these phenomena a time resolved pressure signal is used at the inlet boundary. Ideally the same should be done for the outlet boundary, but as the flow exits directly into the large exhaust receiver it is not straight forward to measure a time resolved pressure signal for the outlet patch.

The pressure in the cylinder is also a time resolved quantity and the in-cylinder pressure is initialized accordingly to the measurement. The in-cylinder temperature at the initial time step is more difficult to set as the gas temperature is not measured experimentally. The in-cylinder temperature is calculated by the ideal gas law

$$T_{EVO} = \frac{p_{EVO}}{\rho_{EVO} \cdot R} \tag{12}$$

The density at EVO needs to be evaluated. Since the compression and combustion processes from figure 3 is in the closed volume phase no mass other than the injected fuel is added or removed from the cylinder. The amount of fuel injected to the cylinder can be calculated with the following formula:

$$m_{fuel} = \frac{sfoc \cdot P}{60 \cdot RPM \cdot n_{cyl}} \tag{13}$$

Where sfoc is the specific fuel oil consumption, P is power output, RPM is the engine speed and n_{cyl} is the number of cylinders. The cylinder mass and volume is known at EVC and can be calculated at EVO like

$$\rho_{EVO} = \frac{m_{cyl,EVC} + m_{fuel}}{V_{cyl,EVO}} \qquad (14)$$

The flow through the cylinder is pressure driven and it is important to get the correct pressure drop over the engine. The average pressure drop over the engine is measured and to ensure the correct driving pressure in the model the outlet pressure boundary is calculated by the mean scavenge pressure subtracted the measured mean pressure drop.

$$p_{exhaust} = \overline{p_{scav}(t)} - \Delta p_{engine} \qquad (15)$$

The effective pressure drop over the engine is shown in figure 6 and show that there are some differences in driving pressure during the scavenging process that should be observable in the mass flow rates over the cylinder. The in-cylinder velocity field must be initialized to avoid a sudden pressure wave that would start propagating when the piston suddenly moves. To counter this artifact a utility that initialize the flow in the cylinder cells is developed. The utility reads in the engine speed, bore, stroke and length of connecting rod from the engine dictionary and calculates the piston position and velocity. The axial velocity in the cylinder is then set by a linear distribution of this value. The cells immediately adjacent to the piston are given the piston velocity and the axial velocity linearly decreases towards stationary in the top of the cylinder. The in-cylinder swirl is set according to the measured velocity from the experiments. As the velocity is only known at one point in the cylinder a solid body rotation is set to match this point. The passive scalar is initialized to be zero (only burned gas) in the cylinder and exhaust bend and to one (only air) in the scavenge box.

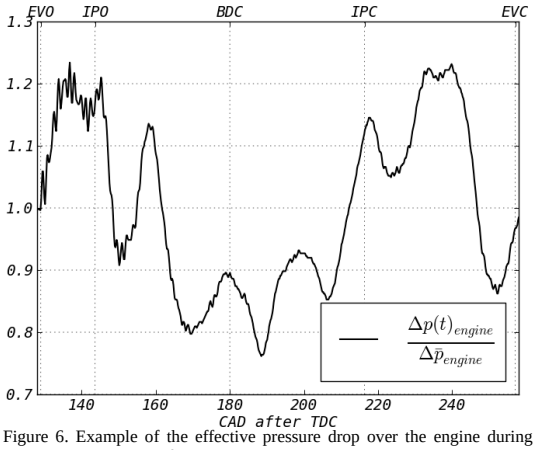

Figure 6. Example of the effective pressure drop over the engine during the simulation, normalized for the mean pressure drop

RESULTS FROM THE CFD ANALYSIS

The results from the investigations will be presented in this section. As the title implies the study is focused on investigating the influence of increasing the in-cylinder swirl component on the scavenging process of marine two-stroke diesel engines. As mentioned earlier, the in-cylinder swirl is increased by blocking every second scavenge port. This will increase the tangential momentum in the cylinder. The degree of swirl can be quantified by a swirl number, Sw, Gupta [22] suggested the following formulation for the swirl number:

$$S_w = \frac{2F_{\theta,z}}{F_{z,z}D} \qquad (16)$$

Where $F_{\theta,z}$ is the flux of angular momentum, $F_{z,z}$ is the flux of axial momentum and D is a geometrical scale. As the velocity field usually is unknown it is difficult to determine an accurate swirl number a priori. Equation (16) can be expressed only by geometric properties [11]:

$$S_w = \frac{A_{cylinder}}{A_{ports}} \cdot \tan(\alpha) \qquad (17)$$

Where α is the port angle and $A_{cylinder}$ is the cross sectional area of the cylinder. The aforementioned belt is fitted to increase the swirl and according to (17) where A_{ports} is cut in half, the geometric swirl number is twice as high with this setup compared to normal configuration for the 4T50ME-X engine. The two cases in this study will be denoted normal swirl (NS) and high swirl (HS).

Table 2. Geometric swirl numbers for the two test cases

Normal swirl (NS) S_w	**High swirl (HS) S_w**
0.26	0.52

According to Gupta (1984)[22] a swirl number above 0.4 is considered a strong swirl while a swirl number below 0.4 is considered weak. From table 2 it is clear that the NS case has a weak swirl while the HS has a strong swirl number.

MASS FLOW RATES AND SCAVENGING EFFICIENCY PARAMETERS

The mass flow rates over the scavenge port are integrated by the top level solver. This in conjunction with the transport equation for a passive scalar makes it possible to evaluate key performance parameters for the scavenging process. The mass flow rates is calculated by the following equation

$$\dot{m}_{port,i} = \int_{A_{port}} (\rho u) \cdot dA_{port,i} \qquad (18)$$

Where A_{port} is the area of the individual scavenging port i. The total mass flow over the ports is then calculated by adding together the mass flow rates multiplied with dt for each time step

$$m_{tot} = \sum_{i=1}^{N_{ports}} \left(\sum_{j=1}^{N_{time\,step}} \dot{m}_{port,i} \cdot dt_j \right) \quad (19)$$

Based on the knowledge of the mass flow rates and the passive scalar it is possible to calculate the most prominent scavenging parameters such as scavenging efficiency, delivery ratio and charging efficiency. The passive scalar is used to distinguish the burned gas from the introduced fresh air in the cylinder.

The engine class will generate a cell zone containing the numbering of the cells in the cylinder which is extracted by the top level solver and used to calculate the amount of fresh air and burned gas

$$m_{air} = \sum_{i=1}^{N_{cylinder}} S_{cell,i} \cdot \rho_{cell,i} \cdot V_{cell,i} \quad (20)$$

$$m_{gas} = \sum_{i=1}^{N_{cylinder}} (1 - S_{cell,i}) \cdot \rho_{cell,i} \cdot V_{cell,i} \quad (21)$$

Equation (20) and (21) is included in the top level solver and used to calculate the amount of combustion residue and fresh air. $N_{cyinder}$ is the number of cells in the cylinder, ρ_{cell} is the density of cell i and V_{cell} is the volume of cell i. Equation (20) and (21) allows for calculation of the scavenging parameters.

$$\eta_{sc} = \frac{mass\ of\ delivered\ air\ retained}{mass\ of\ trapped\ cylinder\ charge} \quad (22)$$

$$\eta_{ch} = \frac{mass\ of\ delivered\ air\ retained}{swept\ volume\ \times ambient\ density} \quad (23)$$

$$DR = \frac{mass\ of\ delivered\ air}{swept\ volume\ \times ambient\ density} \quad (24)$$

Equation (22), (23) and (24) show the equations for the scavenging efficiency, delivery ratio and the charging efficiency. The swept volume is calculated as the cross sectional area of the cylinder times the stroke and the ambient density is calculated with the ideal gas law using temperature and pressure from the scavenge receiver.

The scavenging efficiency is a measure of how effectively the cylinder has been scavenged. It relates the ratio of fresh air to mixture at the end of the scavenging process. This parameter is important as it contains information about the composition of the air in the cylinder that is used for the subsequent process. It affects the compression temperature and the amount of inert gas. Knowledge of the amount of combustion residue is also interesting for optimizing Exhaust Gas Recirculation (EGR) systems as a poor scavenging efficiency indicates the engine's amount of "internal EGR". Scavenging also affect the thermal load on engine components particularly the exhaust valve which is heavily subjected to high temperatures from the combustion process. If the scavenging process is sub optimal the exhaust valve is not cooled which affect the lifespan of the component.

The charging efficiency relates the amount of trapped fresh air to a theoretical reference mass and gives an indication of how effectively the cylinder is filled with the introduced air.

The delivery ratio relates the actual scavenging air mass to that required for an ideal charging process [17]. The reference mass equals the amount of air needed to fill the cylinder. This parameter gives an indication of excess air in the scavenging process. As mentioned in the introduction, the ideal scavenging process is by pure displacement where the introduced scavenge air displaces the burned gas without mixing. As mixing occurs in this process, additional air is required to ensure an acceptable scavenging efficiency. The scavenging parameters for both high and normal swirl can be seen in table 3.

Table 3. Scavenging performance parameters for the two test cases calculated with the results from the CFD analysis

Parameter	*Normal swirl (NS)*	*High swirl (HS)*
η_{sc}	99.9 %	97.9 %
η_{ch}	75.6 %	66.9 %
DR	1.48	1.22
m_{tot}	1.13 kg	1.13 kg

Both test cases have been run with similar operating conditions. There were some adjustments to fuel injection and exhaust valve timing to compensate for the reduced flow area over the ports in cylinder 4. Only one cylinder has the belt mounted so only small adjustments needed to be made to match engine speed and power output. The only notable difference between the two test series is the in-cylinder swirl. From table 3 it is clear that the additional swirl has an influence on the scavenging efficiency which is close to 100 % for the normal swirl case and 97.9 % in the high swirl case. It is important to note that the engine was run on low load during the measurements. At low loads the turbo charger is unable to generate a sufficient pressure drop across the engine and auxiliary blowers are used to increase the pressure in the scavenge receiver. As a result of this the pressure drop across the engine is high which yields beneficial conditions for the scavenging process as the flow rate over the cylinder is high enough to fully scavenge the cylinder despite the increased mixing of burned gas and fresh air in the high swirling case. The delivery ratio for both cases is well above 1 which

indicates that the engine is “over scavenged”. Figure 9 and 10 show cross sectional planes at various crank angles which show that both cases are well scavenged, but mixing of the two gases are increased for the high swirl case especially along the central region of the cylinder.

Swirling flow is widely used in industrial applications such as flame stabilization. Swirling flows have been extensively studied over several decades and its characteristics are well known. One characteristics of swirling flow is that is has an adverse pressure gradient in the core. This adverse pressure gradient causes an axial velocity deficit at the center of the swirl. If the swirl is strong enough the deficit can evolve into a central recirculation region. This lead to increased mixing of burned gases and air which, unless the delivery ratio is increased, will reduce the scavenging efficiency.

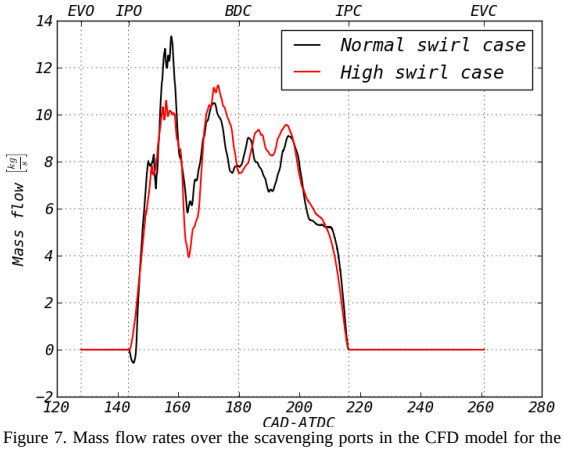

Figure 7. Mass flow rates over the scavenging ports in the CFD model for the NS and HS case

The mass flow rates over the scavenge port as a function of crank angle is shown in figure 7. The flow rates show the same behavior in both cases. Most notably there are 4 distinct peaks in mass flow that occurs roughly at the same crank angle for both cases. A slightly similar pattern is also observed in the input scavenge pressure signal shown in figure 6. The scavenge pressure also show 4 peaks within the EVO and EVC, but the timing does not align well with the mass flow rates in figure 7. As the flow is pressure driven it is expected that when imposing a fixed pressure on the inlet the mass flow rates should be directly correlated with the inlet pressure signal. However, the pressure signal is subjected to pressure waves that propagate between the exhaust receiver and the scavenge receiver that might influence the mass flow rates. The CFD simulation only contains one of two sources for pressure fluctuations as the outlet boundary has a fixed pressure. Counting manually the peaks in figure 7 reveal a frequency of approximately 45 Hz. This frequency corresponds very well with the fundamental frequency of a cylinder with one end open and the other closed. The fundamental wave length for such an arrangement is ¼ L, where L is the length of the cylinder. The fundamental frequency for the cylinder using the average speed of sound of the mixture in the cylinder and using the stroke as length is:

$$f_0 = \frac{c}{4 \cdot L} = \frac{410\ m/s}{4 \cdot 2.2\ m} = 47\ Hz \qquad (25)$$

The observed and theoretical frequencies are in quite good agreement and can with relative confidence bee concluded that the fluctuations in mass flow is due to the fundamental frequency of a pipe with one open and one close end.

TRANSIENT ANGULAR MOMENTUM

The angular momentum in the cylinder is evaluated to investigate the in-cylinder swirl. The top level solver grabs the cells in the cylinder and calculates the volume integrated angular momentum by the following formula:

$$L_z = \int_V r \rho u_\theta \, dV \qquad (26)$$

Where V is the instantaneous cylinder volume, ρ is the cell density, r is the radius from the cylinder center axis to the current cell and u_θ is the tangential velocity component.

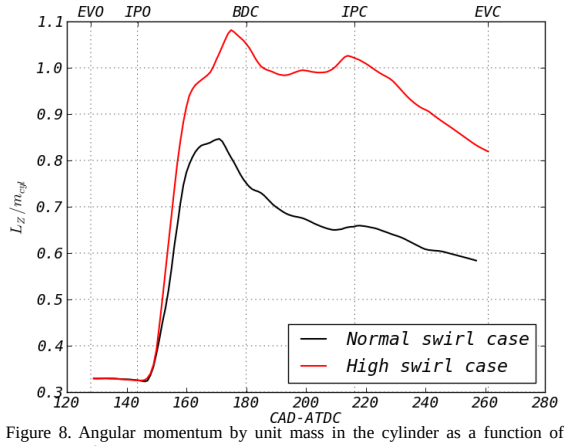

Figure 8. Angular momentum by unit mass in the cylinder as a function of crank angle for the normal swirl case and the high swirl case

The angular momentum in the cylinder is shown in figure 8. The angular momentum is divided by the instantaneous total mass in the cylinder and is therefore the angular momentum in the cylinder per unit mass. This is beneficial when analyzing the swirling flow as the influence of mass that is added and removed mass from the cylinder is masked. The angular momentums presented in figure 8 therefore describe the degree of swirl in the cylinder flow.

The angular momentum at EVO is a result of the initialization based on the solid body rotation. There is a small reduction of angular momentum until the scavenge ports are

opened and the scavenging air enters the cylinder. The angular momentum then increase as the cylinder is flushed with the scavenge air. The peak in angular momentum is reached shortly before BDC when the cylinder is filled with fresh air. This is in conjunction with the measured data that show a sudden rise in the tangential velocity component at approximately 170 CAD after top dead center. This can be seen in figure 11 and 12. The angular momentum then decrease as the swirl decays due to wall friction.

Shortly before IPC the angular momentum increases for the high swirl case and stabilizes for the normal swirl case. This is due to the reduction in flow area over the scavenge port that increase the swirl that is introduced into the cylinder when the ports are closing. After scavenge port closing the swirl continues to decay due to wall friction. As expected the angular momentum in the cylinder is higher for the high swirl case.

FLOW VISUALIZATION

The passive scalar is used to visualize the gas exchange in the cylinder during the scavenging process. The passive scalar acts as an indication of the mass fraction for the burned gas and the fresh air in the cylinder.

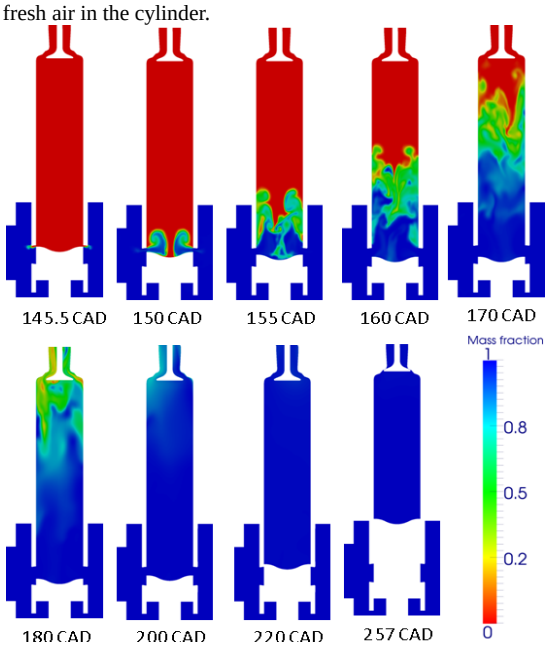

Figure 9. Distribution of the passive scalar in a cross sectional plane at relevant crank angles (Normal swirl case)

The visualization of the passive scalar for the normal swirling case is shown in figure 9. The color scheme is chosen in order to show the cold scavenge air as blue and the hot burned gases as red. From figure 9 it is clear that the scavenging process is dominated by displacement, where the introduced scavenge air replace the burned gases with moderate mixing. Also it is clear that the cylinder is well scavenged shortly after 200 CAD after top dead center.

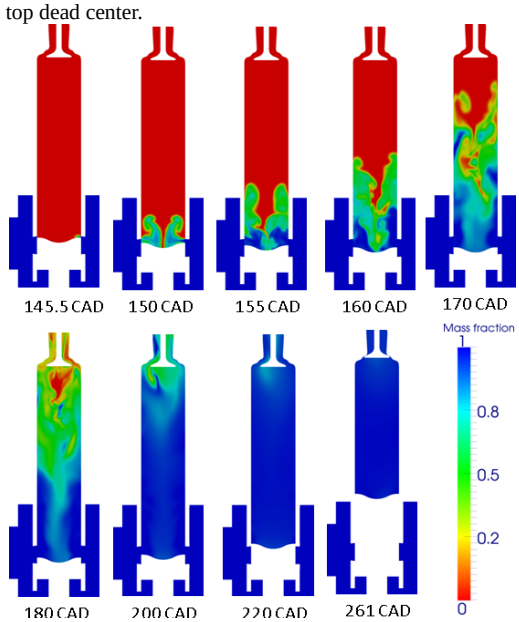

Figure 10. Distribution of the passive scalar in a cross sectional plane at relevant crank angles (High swirl case)

Visualization of the passive scalar for the high swirl case is shown in figure 10. Comparing the mixing phases with the normal swirl case from figure 9 it is obvious that the increased swirl enhance mixing of the two gases. As stated earlier the increased mixing of the two gases is the result from the adverse pressure gradient in the center of the swirling flow. The mass flow rates, and hence the axial momentum is close to equal for the two cases which implies that the increased angular velocity is responsible for the mixing. The scavenging air travels axially at the same rate in both figure 9 and 10 which can be seen as the scavenge air extends equally into the cylinder for both cases. The scavenge air reach the exhaust valve around BDC, but the purity of the cylinder gas is different. The high swirl case has a larger amount of burned gases trapped along the center axis of the cylinder which is due to the central axial velocity deficit. Even at BDC the high swirl case has a mixture in the order of 50-60 % burned gases all the way down to the piston while the normal swirling case has a close to pure scavenge air mixture covering most of the cylinder.

A significant amount of burned gas is also trapped under the exhaust valve at BDC. At EVC both cases are close to fully scavenged, this is, as mentioned earlier, caused by the engine load where auxiliary blowers provides a beneficial scavenge pressure which ensures high delivery ratios. It is expected that if the engine was run with high load the

scavenging process would be more influenced by the additional in-cylinder swirl.

COMPARISON AND VALIDATION WITH PIV MEASUREMENTS

The tangential and axial velocity components were measured in the cylinder by use of the non intrusive optical method Particle Image Velocimetry (PIV). The method was briefly introduced in the introduction and the set up can be seen in figure 1. A detailed description of the method and further results from the optical measurement series can be found in [14] and [15]. These measurements are valuable for validating the simulations. Mass flow rates could not be determined in the experiments, as the turbo charger operated on low mass flows. As mentioned earlier the tangential and axial velocity components are measured in a relatively small laser sheet where the velocity vectors are quite homogenous. The vectors in the sheet is then averaged and presented as a single point value. The PIV data can therefore be considered to be averaged in both space and time as the data is cycle averaged. Due to high computational expenses it is not feasible to perform full cycle. The velocity that is extracted from the CFD model is therefore subjected to oscillations and comparing absolute values is not of large interest.

The timing of the tangential velocity increase is more relevant as validation of the simulations. The velocity shown in figure 11 and 12 is extracted at a single location in the combustion chamber 50 mm from the liner wall. The figures show both the axial velocity component and the tangential velocity component at this point. The timing of the tangential velocity component is the most relevant because it signal the time it takes the introduced scavenge air to travel from the scavenge ports up to this point in the liner. Both figures show a good agreement between the point of acceleration of the tangential velocity for the experimental and calculated results. It is further assumed that if the time it takes the scavenge air to reach this location is correct, the mass flow rates must be reasonable.

The axial velocity component experience large acceleration when the exhaust valve is opened as the pressure difference between the cylinder and the exhaust receiver is large. After the initial acceleration the axial velocity component drops down before slowly being accelerated up to about 20 m/s. After IPC the axial velocity decrease and is actually negative or a brief moment around 230 CAD. This indicates that at this point exhaust gas from the exhaust receiver can be sucked back into the cylinder. It is however unlikely that this has any notable effect on the scavenging process as the flow is only negative for a short period. The rise in axial velocity towards the end of the scavenging process is due to acceleration of the flow as the exhaust valve is closed and the effective flow area is decreasing, while the piston pushes from below.

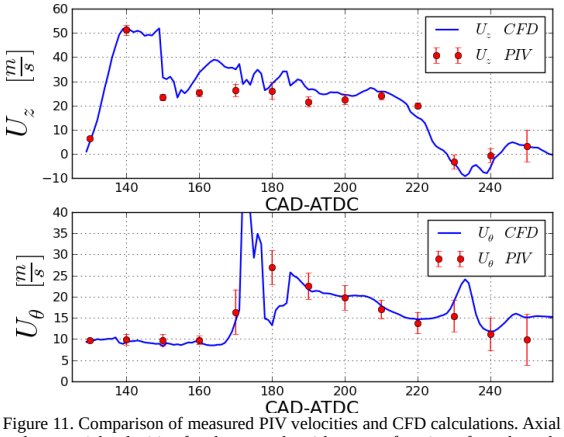

Figure 11. Comparison of measured PIV velocities and CFD calculations. Axial and tangential velocities for the normal swirl case as function of crank angle after top dead center

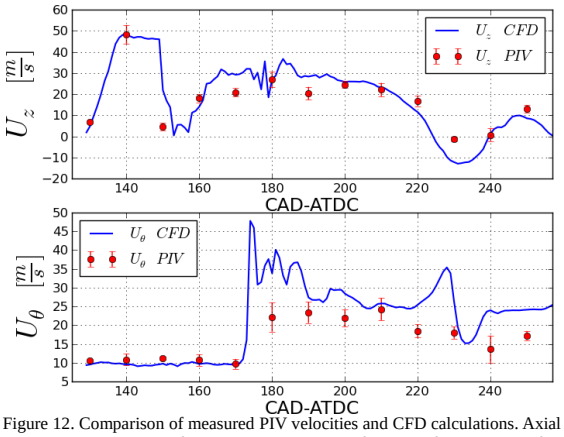

Figure 12. Comparison of measured PIV velocities and CFD calculations. Axial and tangential velocities for the high swirl case as function of crank angle after top dead center.

The tangential velocity component is relatively stable before the scavenge air reach the probe location. By analyzing the tangential velocities from figure 11 and 12 it is clear that the introduced scavenge air takes ~ 25-27 CAD to travel from the scavenge ports through the cylinder and up to the probe location which is located in the engine cover.

The PIV measurements has a resolution of 5 CAD so it is difficult to verify the exact timing on the arrival of the scavenge air at the measurement position. However, when studying the tangential velocity in figure 11 and 12 it seems that the experimental and calculated predictions are in good agreement. The agreement is good for the normal swirling case, but the calculated tangential velocities for the high swirl case is over predicted. Ideally several radial positions should be measured as only one measurement point cannot be used to evaluate the integrated swirl. Even if the tangential velocity is

over predicted the integrated swirl might be correct. This is depending on the shape of the tangential velocity profile.

SUMMARY/CONCLUSION

In this paper a CFD model used to simulate the scavenging process in marine two-stroke diesel engines is presented, validated and used to investigate the influence of the in-cylinder swirl. The model is full 3D and use time resolved as well as cycle averaged measured data as initial conditions, boundary conditions and as validation. The motion solver is able to handle topological changes due to the motion of the piston and exhaust valve. The transport equation of the passive scalar makes it possible to distinguish between the two gases in the cylinder and to investigate the mixing of the burned gas and the scavenge air for comparison with the scavenging efficiency parameters.

The CFD simulation is validated by comparing the measured velocities with the calculated. In both the high and normal swirl case the timing of the tangential velocity is relatively accurate which indicates that the mass flow rates are acceptably accurate for the CFD simulation.

The trends are captured by the model for both the normal swirl and the high swirl case. The absolute values for the normal swirl case are in better agreement than for the high swirl case, especially when considering the tangential velocity. This might indicate that the swirl is over predicted in the high swirl case, but it is difficult to conclude as the measured velocity does not quantify the swirl profile. The integrated swirl might still be reasonable even if the swirl at this point is over predicted.

The flow visualization shows increased mixing of the two gases for the high swirling case which is a result of central recirculation zones in the cylinder due to the adverse pressure gradient which is characteristic for high swirling flows. The flow is validated by comparing the timing of the tangential velocity component.

The sudden rise in tangential velocity indicates that the introduced scavenge air has traveled from the scavenge ports, through the cylinder, to the engine cover where the laser sheet is located. The measured data and the calculated data is in good agreement when considering the timing, which indicate that the mass flow rates is relatively accurate for the CFD simulations. This indicates that CFD modeling can produce relevant and trustworthy insight to the flow fields in the cylinder for large marine engines and can be used as a mean for better understanding the processes that takes place in the cylinder.

REFERENCES

1. Percival WH, Method of scavenging analysis for 2-cycle diesel engines, Society of Automotive engineers-papers, Vol 63, pp. 737-751, 1955
2. Ferro, A. Investigation by means of models into the scavenging of two-stroke internal combustion engines, The engineers' Digest, Vol 19, 1958, pp.512-522
3. JB, Heywood and E, Sher, The Two-stroke cycle engine: its Development, Operation and Design, Taylor and Francis, Philidelphia, 1999.
4. Sher. E, Hossain. I, Zhang. Q and winterbone. D.E, Calculations and Measurments in the Cylinder of a Two-Stroke Uniflow-Scavenged Engine Under Steady Flow Conditions, Experimental Thermal and Fluid Science, pp.418-431, 1991
5. Litke.B, The influence of inlet angles in inlet ports on the scavenging process in two-stroke uniflow-scavenged engine, Marine technology III Volume 45, 1999
6. Haider. S, Experimental and Numerical Study of Swirling Flow in Scavenging Process for 2-Stroke Marine Diesel Engines, Ph.D. thesis, Technical University of Denmark, 2011
7. Ingvorsen K. M, Meyer K. E. Walther J. H, Mayer S, Turbulent swirling flow in a model of a uniflow scavenged two-stroke engine, Experiments of Fluids-2013, Volume 54, Issue 3, pp 1-7
8. Ingvorsen K. M. Meyer K. E. Walther J. H, Phase-locked stereoscopic PIV measurements of the turbulent swirling flow in a dynamic model of a uniflow-scavenged two-stroke engine cylinder, Proceeding of the 10th International Symposium on Particle Image Velocimetry. TU Delft, 2013
9. Nakagawa. H, Kato. S, Tataishi. M, Adachi. T, Tsujimura.H and Nakashima.M, Airflow in the Cylidner of a 2-stroke Cycle Uniflow Scavenging Diesel Engine During compression Stroke. Japan society of mechanical engineers, Series III, Vol 3, No 3, 1990.
10. Sigurdsson. E. Scavenging flow in a Two-Stroke Diesel Engine, Master thesis, Technical University of Denmark, 2011
11. Al-Mousawi N,M,J. Numerical Simulation in a model Diesel engine using RANS and LES turbulence models. Master thesis, Technical University of Denmark, 2012
12. Lamas. I.L. and Vidal. C.G.R, Computational Fluid Dynamics Analysis of the Scavenging Process in the MAN B&W 7S50MC Two-Stroke Marine Diesel Engine, Journal of Ship Research, vol 56, pp. 154-161, 2012
13. Andersen F. H. Hult J. Nogenmyr K-J. and Mayer S. Numerical investigation of the Scavenging Process in Marine Two-stroke Diesel Engines, SAE technical paper (2013-01-2647), SAE Powertrain, Fuels and lubricants meeting, Seoul Korea, 2013.
14. Hult.J, Mayer.S, A methodology for laser diagnostics in large-bore two-stroke diesel engines, Measurement Science and Technology, 2013, doi:10.1088/0957-0233/24/4/045204
15. Mayer.S, Clausen.S, Hult.J, Nogenmyr.K.J, Advanced optical development tools for two-stroke marine diesel engines. CIMAC conference 2013, paper 53. 2013
16. Stone, R. Introduction to Internal Combustion Engines. Macmillan press LTD, 1999.
17. Heywood, J.B. Internal Combustion Engine Fundamentals, McGraw-Hill Book Company,1988
18. OpenFOAM User Guide Version 1.6, 14.July 2009. OpenCFD LDT. (www.openfoam.org) (www.extend-project.de)

19. Favre.A, Equations des gaz turbulent compressibles, Journal de Mechanique, vol 4, pp.361-421, 1965
20. Ferziger J.H, Peric M. Computational Methodes for Computional Fluid Dynamics. Third edition, Springer, 2002.
21. Rutland, C.J. Large-eddy simulations for internal combustion engines-a review. International Journal of Engine Research, 2011.
22. Gupta, A.K. Lilley, D.G, Syred, N. Swirl Flows. Turnbridge Wells, Kent, Abacus press, 1984
23. Oliver, Todd A. Favre-Averaged Navier-Stokes and Turbulence Model Equations Documentation. Predictive Engineering and Computational sciences, University of Austin Texas. 2009.
24. White, Frank M. Viscous Fluid Flow, Third edition, McGraw Hill, International edition, 2006.
25. Yakhot, V., Orszag, S.A., Thangam, S., Gatski, T.B. & Speziale, C.G. (1992), "Development of turbulence models for shear flows by a double expansion technique", Physics of Fluids A, Vol. 4, No. 7, pp1510-1520.

ACKNOWLEDGEMENTS

The author would like to thank:
Danish ministry of science, innovation and higher education for partially funding the industrial Ph.D. project

Internal Combustion Engine Group, Dipartemento di Energia, Politecnico Di Milano for development of the engine mesh motion class in OpenFOAM

A.3 Parametric study of the Scavenging process in Marine Two-Stroke Diesel Engines

Proceedings of the ASME 2015 Internal Combustion Engine Division Fall Technical Conference
ICEF2015
November 8-11, 2015, Houston, Texas , USA

ICEF2015-1075

PARAMETRIC STUDY OF THE SCAVENGING PROCESS IN MARINE TWO-STROKE DIESEL ENGINES

Fredrik Herland Andersen
MAN Diesel & Turbo SE
Teglholmsgade 41, 2450 Copenhagen SV,
Denmark

Technical University of Denmark
Anker Engelunds vej 1,2800, Kgs. Lyngby,
Denmark

Mail: Fredrik.Andersen@man.eu,
phone:(+45) 33 85 17 66

Stefan Mayer
MAN Diesel & Turbo SE
Teglholmsgade 41, 2450 Copenhagen SV,
Denmark

ABSTRACT

Large commercial ships such as container vessels and bulk carriers are propelled by low-speed, uniflow scavenged two-stroke diesel engines. The integral in-cylinder process in this type of engine is the scavenging process, where the burned gas from the combustion process is evacuated through the exhaust valve and replaced with fresh air for the subsequent compression stroke. The scavenging air enters the cylinder via inlet ports which are uncovered by the piston at bottom dead center (BDC). The exhaust gas is then displaced by the fresh air. The scavenging ports are angled to introduce a swirling component to the flow. The in-cylinder swirl is beneficial for air-fuel mixture, cooling of the cylinder liner and minimizing dead zones where pockets of exhaust gas are trapped. However, a known characteristic of swirling flows is an adverse pressure gradient in the center of the flow, which might lead to a local deficit in axial velocity and the formation of central recirculation zones, known as vortex breakdown. This paper will present a CFD analysis of the scavenging process in a MAN B&W two-stroke diesel engine. The study include a parameter sweep where the operating conditions such as air amount, port timing and scavenging pressure are varied. The CFD model comprise the full geometry from scavenge receiver to exhaust receiver. Asymmetric inlet and outlet conditions is included as well as the dynamics of a moving piston and valve. Time resolved boundary conditions corresponding to measurements from an operating, full scale production, engine as well as realistic initial conditions are used in the simulations. The CFD model provides a detailed description of the in-cylinder flow from exhaust valve opening (EVO) to exhaust valve closing (EVC). The study reveals a close coupling between the volume flow (delivery ratio) and the in-cylinder bulk purity of air which appears to be independent of operating conditions, rpm, scavenge air pressure, BMEP etc. The bulk purity of air in the cylinder shows good agreement with a simple theoretical perfect displacement model.

INTRODUCTION

The literature on research for marine large bore, uniflow scavenged, two-stroke diesel engines are scarce compared to four-stroke engines, as found in the automotive and truck industry. This is primarily due to the cost and complexity involved with test facilities and operation of large engines. There are relatively few engines worldwide and there are few test engines available compared to engines used in the automotive and truck industry .

Previous studies include visualization by Ferro (1958)[2], pitot measurements by Percival (1955)[1] and hotwire measurements by Sher et al (1994)[4]. The influence of in-cylinder swirl have been investigated by Litke (1999)[5] who used a scaled down model engine with water as working fluid. The port angle and port shape was varied concluding that a port angle of 20 degrees provided the best scavenging efficiency. 20 degree port angle is within the span of the industry standard.

Haider (2011)[6] performed Particle Image Velocimetry (PIV) measurements on a scaled down stationary model based on the T50ME-X test engine at MAN Diesel & Turbo SE, located in Copenhagen, Denmark. Ingvorsen et al [7],[8][26] expanded the model engine to include a more realistic scavenge port configuration as well as a moving piston. Al-Mousawi [11] and Hemmingsen [27] performed CFD analysis on the model engine using both Reynolds Average Navier Stoke (RANS) and Large Eddy Simulation (LES) based turbulence models. Andersen et al (2013)[13], Andersen et al (2014)[28} and Lamas et al (2012)[12] performed CFD analysis on full scale engines, the T50ME-X and the S50MC engine respectively.

The aim for this study is to investigate the scavenging process in a full scale MAN B&W engine at different engine configurations. Four different engine loads are investigated corresponding to 25%, 50%, 75% and 100% engine load, following a propeller curve according to the specific engine lay-out. 75% engine load can be understood as 75% of the maximum continuous rating point (MCR) in the engine lay out diagram. Both engine speed and mean effective pressure varies with engine load. When increasing engine load the cylinder pressure, exhaust receiver and scavenge receiver pressure and the mean effective pressure increase. The driving pressure through the cylinder, the scavenging gradient, is the difference between the exhaust and scavenge receiver pressures. The in-cylinder pressure increase with engine load as more fuel is burned during the combustion process, this increase the driving pressure for the turbocharger turbine. A higher turbocharger back pressure increases the mass flow rate through the compressor, and consequently though the engine's cylinders.

Two-stroke engine operation

The operating cycle for low speed, uniflow-scavenged, marine two-stroke diesel engines differs significantly from conventional four-stroke engines. A very short introduction to the most significant aspects will be presented in this section.

A cross sectional drawing of a two-stroke marine diesel engine is shown in figure 1. Exhaust gas in the exhaust receiver provides a boost pressure for the turbine side of the turbocharger. The compressor aspirate ambient air, typically from the engine room, and compresses it before the diffusor, a cooler unit and a water-mist catcher located between the turbo charger and the scavenge air receiver. The scavenge air receiver is a large volume designed to dampen pressure oscillations and provide a steady driving pressure for the scavenging process. The scavenge ports are uncovered by the piston close to BDC. The pressure difference between the exhaust receiver and the scavenge receiver drives the flow of scavenge air, in a swirling motion, through the cylinder and through the centered exhaust valve. This motion of scavenge air displaces the exhaust gas in the cylinder and replace it with cooled scavenge air.

The uniflow-scavenged two-stroke diesel engine cycle can be divided into two phases consisting of 5 sub processes as shown in figure 2. The two phases are the closed volume phase and the open volume phase. The closed volume phase starts at exhaust valve closing (EVC) and ends at exhaust valve opening (EVO) where no mass transfer, except for the injected fuel, takes place in the cylinder. The open volume phase starts at exhaust valve opening (EVO) and ends at exhaust valve closing (EVC). The open volume phase consist of three different processes: the blow down process, where the valve opens to adjust the cylinder pressure with the scavenge pressure. The volumetric part of the scavenging process, where the cylinder is flushed with fresh air, and the push out process where the compression pressure is set according to the exhaust valve closing strategy. This study only comprise the open volume phase, thus the simulations are initialized at EVO and ends at EVC.

The specific engine which is simulated in this study is a MAN B&W ME type engine. The ME type engine does not have a camshaft for exhaust valve control, but instead the exhaust valve (and fuel injection system) is electronically controlled with hydraulic actuation. This means that the exhaust valve opening, EVO, and closing, EVC, is not fixed, but varies with engine load to ensure a continuous optimized engine performance.

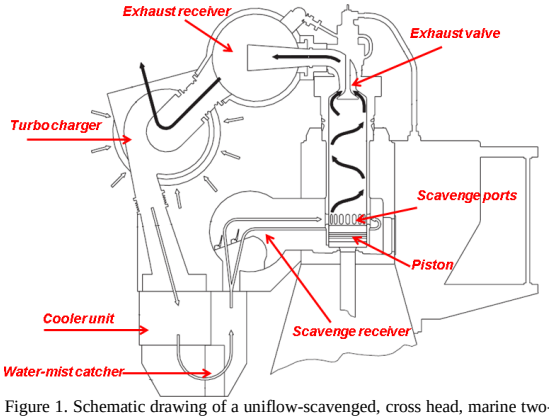

Figure 1. Schematic drawing of a uniflow-scavenged, cross head, marine two-stroke diesel engine (MAN Diesel & Turbo).

.

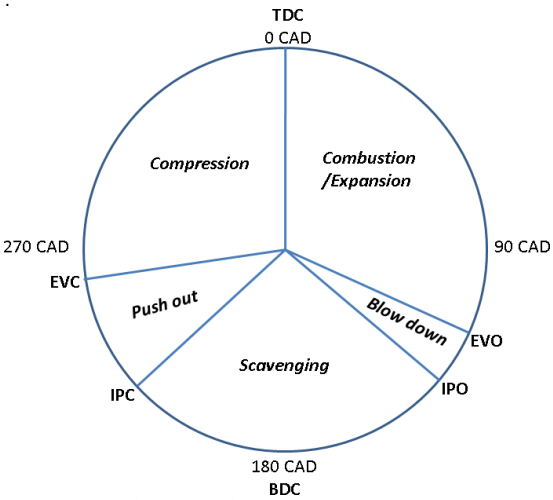

Figure 2. Two-stroke engine cycle

Numerical Model

The software used in this numerical investigation is the open source C++ tool box OpenFOAM[18] which contains functionalities to solve the Navier-Stoke equations by the finite volume method (FVM). A customized engine wrapper class has been written to handle shape and topology changes to the

mesh due to the moving piston and valve. The wrapper class is specifically designed for uniflow-scavenged, two-stroke diesel engines. The engine class generates mesh modifiers and calculates the piston position as function of crank angle, RPM and geometry. The exhaust valve lift curve is measured experimentally on the engine at test bed and used as input for the simulations.

Three simple mesh utilities is used to handle the shape and topological changes to the mesh. The coupling of scavenging ports and the cylinder is done by an algorithm called "slidingInterface" which is designed to allow relative sliding of components. The slidingInterface algorithm perform topological changes to the mesh as it rewrite the faces in the fully or partially overlapping corresponding patches. The second mesh modifier is the "add/remove layers" algorithm which is used facilitate the motion of the valve. When the exhaust valve moves, a hexahedral layer of cells are added or removed depending on a specified maximum and maximum cell size. The third mesh modifier is called the "Generalized Grid Interface" (GGI) which has similar functionalities as the slidingInterface. When the valve moves up and down, parts of the internal mesh have to slide across each other. The GGI allows non-conformal patches to slide across each other. The algorithm does not stitch the mesh together, communication is performed by a weighted interpolation scheme across the two interfaces. The cells affected by the mesh modifiers can be seen in figure 3. The motion of the piston is done by stretching and compressing the cells in the cylinder region. This is only a shape change to the mesh and does not require a topological change.

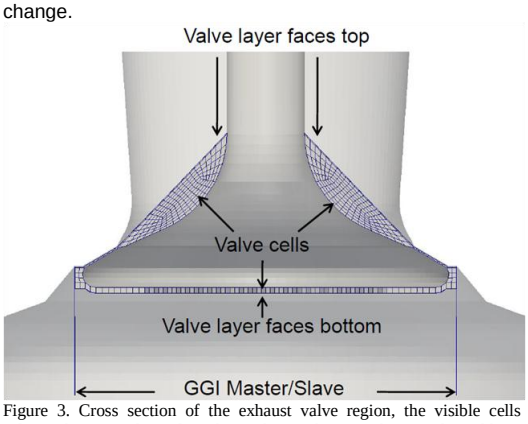

Figure 3. Cross section of the exhaust valve region, the visible cells are subjected to topological and or shape changes due to the add/remove algorithm.

Govering equations

The governing equations are the compressible Favre Averaged Navier-Stokes (FANS) equations.

$$\frac{\partial \bar{\rho}}{\partial t} + \frac{\partial}{\partial x_i}(\bar{\rho}\widetilde{u_i}) = 0 \qquad (1)$$

$$\frac{\partial}{\partial t}(\bar{\rho}\widetilde{u_i}) + \frac{\partial}{\partial x_j}\left[\bar{\rho}\widetilde{u_j}\widetilde{u_i} + \bar{p}\delta_{ij} + \rho\widetilde{u_i''u_j''} - \widetilde{\tau_{ij}}\right] - \tilde{F}_i = 0 \qquad (2)$$

$$\frac{\partial(\bar{\rho}\tilde{h})}{\partial t} + \frac{\partial}{\partial x_j}\left[\bar{\rho}\tilde{h}\widetilde{u_i} - \widetilde{u_i}\bar{p} - \frac{\partial(\alpha_{eff}\tilde{h})}{\partial x_i}\right] - \frac{\partial \bar{p}}{\partial t} = 0 \qquad (3)$$

Equation (1) is the continuity equation where $u_i = [u_1, u_2, u_3]$ and $x_i = [x_1, x_2, x_3]$.

Equation (2) is the momentum equation which after the averaging contains an additional term that requires modeling in order to close the set of equations. This term is the non-linear term $\rho\widetilde{u_i''u_j''}$ known as the Reynolds stress tensor [20]. The Reynolds stress tensor can be modeled by use of the Boussinesq approximation which relates the Reynolds stresses with an artificial eddy viscosity that accounts for the transport and dissipation of turbulence in the smaller scales of the flow [24]. The Reynolds stress tensor and the viscous stress tensor can be joined together and written as follows:

$$\rho\widetilde{u_i''u_j''} - \widetilde{\tau_{ij}} = \tilde{\mu}_{eff}\left[\left(\frac{\partial \widetilde{u_i}}{\partial x_j} + \frac{\partial \widetilde{u_j}}{\partial x_i}\right) - \frac{2}{3}\delta_{i,j}\frac{\partial \widetilde{u_k}}{\partial x_k}\right] \qquad (4)$$

Which contains a term for the effective viscosity, $\mu_{eff} = \mu_l + \mu_t$, where μ_l denotes laminar (molecular) viscosity and μ_t denotes the turbulent (eddy) viscosity. The eddy viscosity is calculated from the specific turbulence model. The remaining terms in equation (4) is the pressure term $\bar{p}\delta_{ij}$ where δ_{ij} is the Kronecker delta ($\delta_{ij} = 1\ if\ i = j\ \ and\ \delta_{ij} = 0\ if\ i \neq j$) and $\tilde{F}_i$ is the body forces.

Equation (3) is the energy equation written with respect to enthalpy. The last term in the bracket contains the effective thermal diffusivity $\alpha_{eff} = \alpha_l + \alpha_t$ where $\alpha_l$is the molecular thermal diffusivity and α_t is the thermal diffusivity added by the turbulent fluctuations in the fluid flow. The turbulent thermal diffusivity is calculated by the following equation:

$$\alpha_t = \frac{\mu_t}{Pr_t} \qquad (5)$$

Where Pr_t is the turbulent Prantl number which is equal to one. The turbulent viscosity is calculated by the RNG k-ε turbulence model which solves two transport equations for turbulent kinetic energy, k, and turbulent diffusion rate, ε.
A transport equation for a passive scalar is solved to distinguish between the exhaust gas in the cylinder and the scavenge air.

$$\frac{\partial(\bar{\rho}\widetilde{S_{air}})}{\partial t} + \frac{\partial(\bar{\rho}\widetilde{S_{air}u_j})}{\partial x_j} - \frac{\partial}{\partial x_j}\left((\tilde{\mu} + \tilde{\mu}_t)\frac{\partial(\bar{\rho}\widetilde{S_{air}})}{\partial x_j}\right) = 0 \qquad (6)$$

Where S_{air} is the mass fraction of fresh air. The mass fraction of burned gases, S_{gas}, is found from the relation of unity:

$$S_{gas} = 1 - S_{air} \qquad (7)$$

Initially the cylinder and exhaust bend is filled with burned gases $S_{air} = 0$ while the scavenge box is initiated with $S_{air} = 1$.

Computational domain

The computational domain used for the simulations in this study is generated using the native OpenFOAM mesh generators: blockMesh and snappyHexMesh. The valve and cylinder meshes are generated with blockMesh where an in-house python utility reads a dictionary containing geometric data and generates an input file for blockMesh. The exhaust duct and the scavenge box mesh is generated with snappyHexMesh. The computational domain then consist primarily of hexahedral cells which is beneficial for numerical stability and accuracy. A base size of 13.5mm is used in the cylinder and 4.8mm in the exhaust valve region are used for the simulations.

Initial and boundary conditions

The initial and boundary conditions are based on data obtained at test bed during engine commissioning. Time averaged temperature and pressure in the cylinder and exhaust receiver is used as initial and boundary conditions. A time resolved pressure trace from the scavenge box is used as inlet boundary condition to include the oscillations from pressure waves which originates from cylinder to cylinder interactions and blow back of exhaust gas at IPO. The cylinder pressure is known at EVO from a measured pressure trace and the corresponding temperature is calculated using the ideal gas law. The mass flow rate of scavenge air is known from the emission measurement and is used to calculate the scavenging gradient, Δp_{engine} to ensure a correct mass flow rate in the CFD simulations. A time (CAD) resolved pressure trace from the measurements is used to include the pressure fluctuations and to impose the scavenging gradient the outlet boundary condition is calculated from the scavenging gradient and the average scavenge pressure:

$$p_{exhaust} = \overline{p_{scav}(t)} - \Delta p_{engine}. \qquad (8)$$

The in-cylinder velocity field is initialized with a solid body rotation according to a measured tangential velocity component which was obtained by Particle Image Velocimetry (PIV) though a specially designed cover with optical access [14][15].

Results

This section will present some results from the CFD analysis. Variations in engine load has an influence on the scavenging process primarily due to two factors. The increased RPM will reduce the scavenging time, t_{scav}, which will reduce the integrated flow area through the cylinder. Another factor is the pressure in the receivers which increase with load. The pressure difference between the scavenge receiver and the exhaust receiver drives the flow through the cylinder, thus being the most important parameter regarding the scavenging process. The temperature in the scavenge receiver is, due to the cooler unit, invariant to the operating conditions, thus the scavenge pressure determines both the mass flow rate and the volume flow rate across the cylinder.

Table 1: Scavenge pressure, density in scavenge receiver and rpm for the four engine loads.

Engine Load	25 %	50%	75%	100%
p_{scav}	Ref.	1.51	2.12	2.40
ρ_{scav}	Ref.	1.53	2.16	2.41
m_{scav}	Ref.	1.29	1.52	1.6
RPM	Ref.	1.26	1.44	1.6

The operating conditions for the four engine loads in the sweep can be found in table 1. The scavenging pressure and corresponding density is given according to the reference case of 25% engine load. The scavenge pressure, p_{scav}, is increased in the four load cases to investigate the influence on bulk purity of scavenge air in the cylinder and the delivery ratio. The bulk purity of scavenge air in the cylinder is defined as the ratio of fresh air and total mixture in the cylinder [17]:

$$\psi = \frac{mass\ of\ delivered\ air\ retained}{mass\ of\ trapped\ cylinder\ charge}. \qquad (9)$$

The bulk purity is calculated using the passive scalar from equation 7. The scavenging efficiency, η_{scav}, is a measure of the bulk purity of scavenge air in the cylinder at exhaust valve closing (EVC). The delivery ratio is defined as the total amount of scavenge air introduced to the cylinder divided with a reference volume $V_{ref} = V_{swept} + V_{compression}$.

$$DR = \frac{mass\ of\ delivered\ air}{reference\ volume \times density\ of\ scavenge\ air} \qquad (10)$$

The delivery ratio depict the volume flow through the cylinder. It directly states the ratio of introduced volume to the volume which shall be displaced. If the delivery ratio is larger than unity the introduced volume flow should be adequate for displacing the exhaust gases in the cylinder. The scavenging efficiency, bulk purity at IPC and delivery ratio from the CFD analysis are listed in table 2.

Table 2: Scavenging efficiency, bulk purity at IPC and delivery ratio from the CFD analysis

Engine Load	25 %	50 %	75%	100%
η_{scav} (%)	99.3	98.2	98.6	96.1
ψ_{IPC} (%)	94.8	92.8	88.0	83.6
DR	1.0	0.91	0.76	0.67

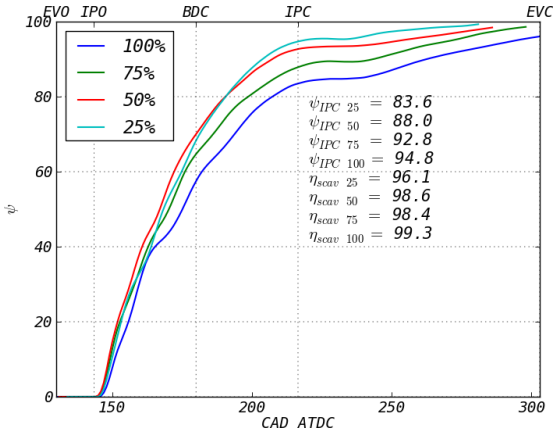

Figure 4: The bulk purity of air in the cylinder as function of crank angle.

The bulk purity of scavenge air in the cylinder as function of the crank angle is shown in figure 5. From the figure it is clear that

the engine load influences the scavenging process. The scavenging efficiency appears inversely proportional with engine load. The highest scavenging efficiency is found for the 25% load case while the lowest scavenging efficiency is found for the 100% engine load case. Another interesting observation from figure 4 is that the scavenging process is dependent to the push out process. After the scavenge ports are closed, IPC, the driving pressure is removed and the in-cylinder gas is displaced by the piston motion. The bulk purity of fresh air in the cylinder at IPC is as low as 83.6 % for the 100% load case. The remaining 12.5 % of scavenging is done purely by displacing the cylinder content by piston motion. This is possible as the residual exhaust gas is normally located in the top of the cylinder at IPC while the rest of the cylinder consist of scavenge air.

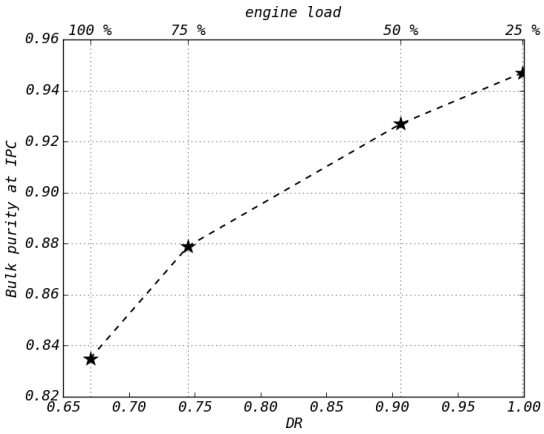

Figure 5: Bulk purity of air in the cylinder at inlet port closing (IPC)

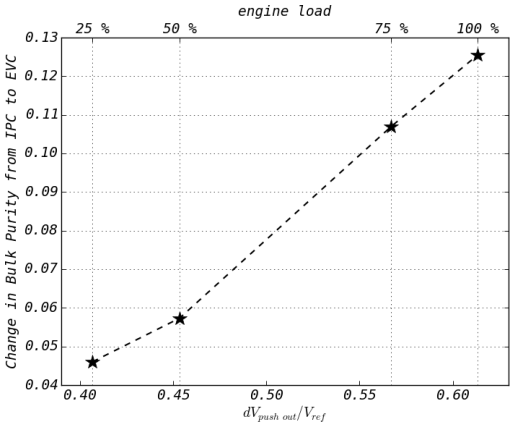

Figure 6: Contribution to the bulk purity of air in the cylinder from the push out process.

Figure 5 show the bulk purity at IPC, ψ_{IPC}, as function of engine load and delivery ratio. The figure shows that the purity of air at IPC scales with the delivery ratio. The increase in purity at IPC is also close to linear, with the exception of the 100% engine load case. The purity at IPC represents the contribution for the volumetric scavenging, where only the volumetric displacement is included. Figure 6 shows the contribution from the push out process where the scavenge ports are closed, but the cylinder content is being displaced by the piston motion. The change in purity is calculated as:

$$d\psi_{push\ out} = \eta_{scav} - \psi_{IPC} \quad (11)$$

Where η_{scav} is the bulk purity of scavenge air at EVC and ψ_{IPC} is the bulk purity at IPC. The volume displaced by the piston during the push out process is calculated by:

$$dV_{push\ out} = V_{IPC} - V_{EVC} \quad (12)$$

Where V_{IPC} and V_{EVC} is the cylinder volume at IPC and EVC respectively. V_{ref} is the same as for the calculation of delivery ratio, equation 10.

Figure 7 and 8 shows the bulk purity of scavenge air in the cylinder as a function of the added mass and volume (delivery ratio) through the scavenge ports during the scavenging process. Figure 7 shows that the displacement of exhaust gases does not scale with the mass flow. The mass flow over the engine increase with engine load, but the overall scavenging efficiency decrease. The engine consumes over 50 % more mass of air at full load than at low load, but still it cannot displace the exhaust gases in the cylinder. The rate of change for the bulk purity is also decreasing for increased engine load when comparing with mass flow rate.

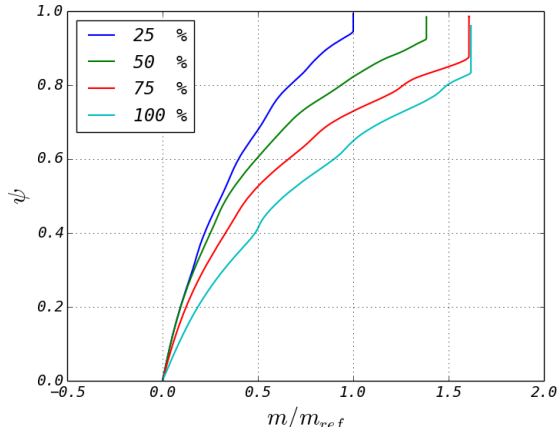

Figure 7: Bulk purity of air as function of introduced mass flow. The vertical part correspond to the contribution of the push out process where no mass is added to the cylinder, but the bulk purity is affected by the piston displacement.

Figure 8 compares the bulk purity of scavenge air in the cylinder with the volume flow of scavenge air. The figure shows that the bulk purity of scavenge air in the cylinder appears to scale with the volume flow rather than the mass flow rate from figure 7. Figure 8 shows that the high load case (100% engine load) receives approximately 30 % less volume flow than the reference case of 25% engine load. The reason for this decay in volume flow comes from change in density of the air in the scavenge receiver. The density in the scavenging receiver increase with the pressure, which in turn increase with the engine load. This is an important point as it can shed some light over the consequence of increasing the scavenging pressure in two-stroke marine diesel engines.

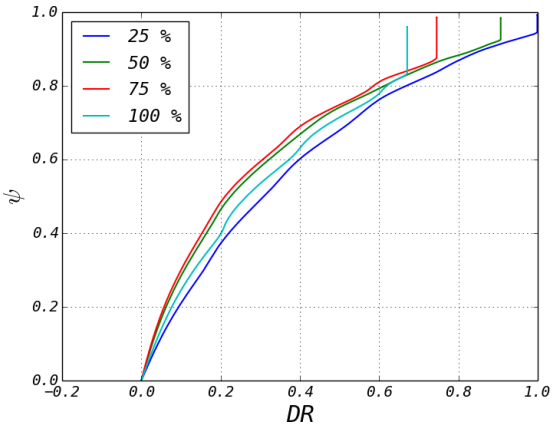

Figure 8: Bulk purity of air as function of delivery ratio. The vertical part correspond to the contribution of the push out process where no mass is added to the cylinder, but the bulk purity is affected by the piston displacement.

There are some deviations between the rate of change of the bulk purity of scavenge air as function of delivery ratio in figure 8. All the graphs appears to join the same trajectory at the later stage of the scavenging process, but from DR=0 to DR=0.8 the different load cases follows different trajectories. This difference was found to be caused by the density differences between the exhaust gas in the cylinder and the introduced scavenge air. Sher (1990)[29], proposed an extension to the perfect displacement model which included the density difference between the exhaust gas and the scavenge air.

$$\eta_{scav} = \left[1 + \frac{\rho_{ex}}{\rho_{scav}}\left(\frac{1}{DR} - 1\right)\right]^{-1} \qquad (13)$$

Equation 13 show the perfect displacement model from [29] where the density ratio ρ_{ex}/ρ_{scav} is included.

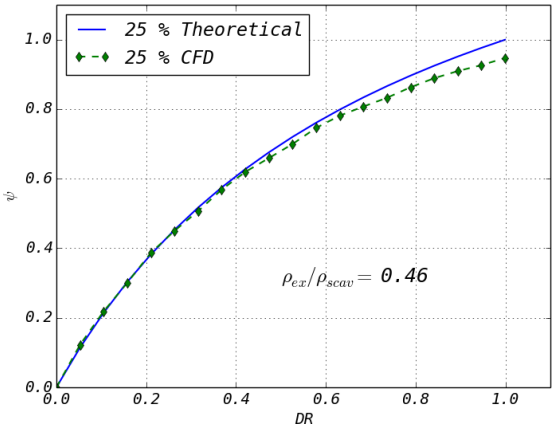

Figure 9: bulk purity of scavenge air, calculated with the CFD model and the perfect displacement model, equation 13, for the 25% engine load case.

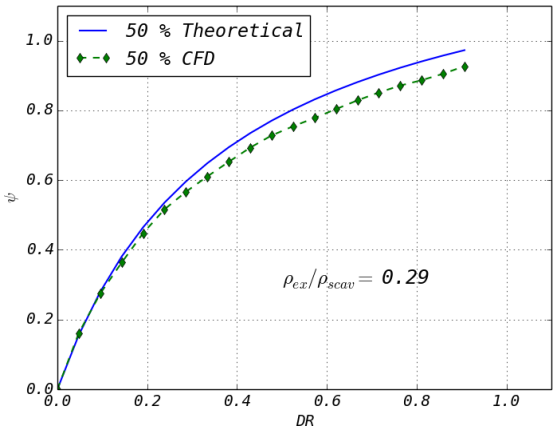

Figure 10: bulk purity of scavenge air, calculated with the CFD model and the perfect displacement model, equation 13, for the 50% engine load case.

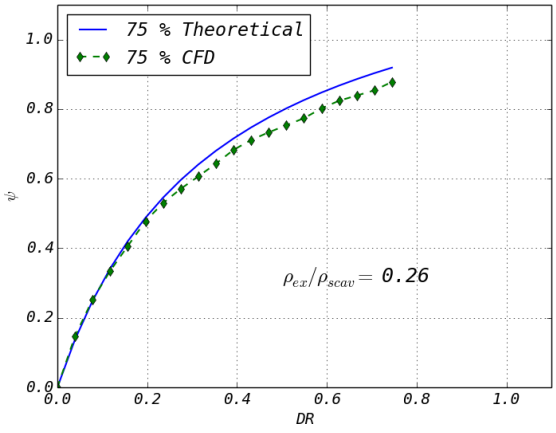

Figure 11: bulk purity of scavenge air, calculated with the CFD model and the perfect displacement model, equation 13, for the 75% engine load case.

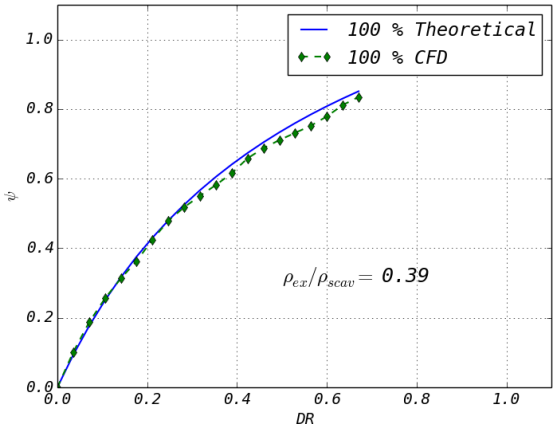

Figure 12: bulk purity of scavenge air, calculated with the CFD model and the perfect displacement model, equation 13, for the 25% engine load case.

Figure 9, 10, 11 and 12 show the bulk purity of scavenge air in the cylinder calculated with the CFD model and with the theoretical perfect displacement model of Sher [29]. The figures show good agreement between the CFD model and the perfect displacement model, especially in the initial stages of the volumetric scavenging. The perfect displacement model does not include the mixing between the scavenge air and the exhaust gas which explain why the perfect displacement model and the CFD model separates. Comparing the bulk purity calculated with the CFD model and the perfect displacement model shows the influence of the density ratio $\boldsymbol{\rho_{ex}/\rho_{scav}}$. The different engine loads in figure 8 showed different trajectories, but when plotting them with the perfect displacement model including the density ratio, they show good agreement.

Table 3: The density ratios used when calculating the bulk purity of scavenge air with the perfect displacement model, equation 13.

Engine Load [%]	**100**	**75**	**50**	**25**
$\boldsymbol{\rho_{ex}/\rho_{scav}}$	0.39	0.26	0.29	0.46

The density ratios used when calculating the bulk purity with the perfect displacement model is shown in table 3. The 75% and 50% engine load case have similar values for $\boldsymbol{\rho_{ex}/\rho_{scav}}$. This can be seen in figure 8 where the 75% and 50% engine load cases have similar trajectories. The bulk purity of scavenge air in the cylinder is defined as the ratio of the mass of scavenge air to the total mass in the cylinder. The delivery ratio is defined in terms of volume added to the cylinder to a reference volume. The compressed, cooled scavenge air has a higher density than the hot exhaust gas. The density ratio therefore influence the shape of the purity as function of delivery ratio curve.

The perfect displacement model does not include the mixing between the scavenge air and the exhaust gas. This is why the purity calculated with the CFD results and the perfect displacement model separates. The figures suggests that the mixing between the scavenge air and exhaust gas increase with the density difference between the two gases.

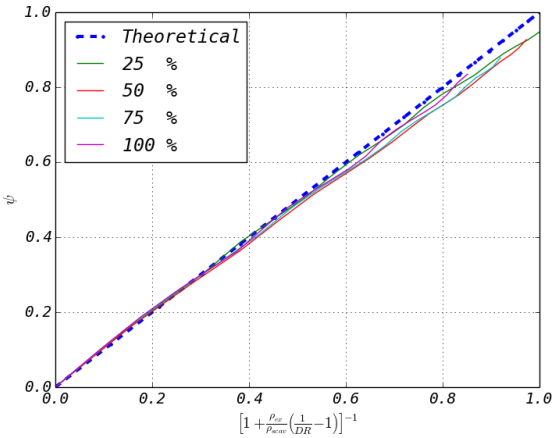

Figure 13: Comparison between the bulk purity in the cylinder, calculated with the CFD model results and the perfect displacement model.

Figure 14 show the distribution of fresh air (blue) and exhaust gas (red) at bottom dead center. The figure is consistent with the results presented in figure 4, 5 and 6 where the bulk purity of fresh air is decaying for increased engine load. While the 25 % load case have a mixture of fresh air and exhaust gas stretching from the scavenge ports to the exhaust valve, the fresh air in the 100 % load case only span half of the cylinder.

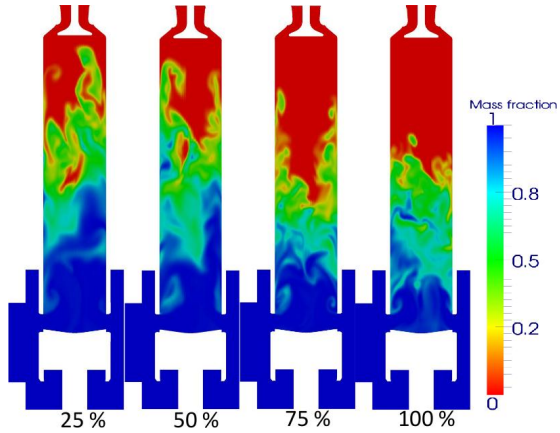

Figure 14: A cross section of the cylinder showing the distribution of fresh air and exhaust gas at BDC. Blue represent the cool fresh air and red represent hot exhaust gas.

Conclusion

A parametric study of the scavenging process is presented in this paper. A CFD model, capable of shape and topological changes due to the motion of piston and valve is presented. The CFD model was presented and validated in Andersen et al (2014)[29].

An engine load sweep was presented in this study. The load sweep was conducted as the scavenging pressure, and the mass and volume flow across the engine varies. The mass flow rate through the engine increase with engine load. This is good as the combustion process needs more air to burn the extra fuel injected at higher engine loads. However, this study has shown that the increase in mass flow might not benefit the scavenging process if the scavenge pressure is increased too much. This study shows that the gas exchange in the cylinder is not dependent on the mass flow rate, but the volume flow rate (delivery ratio). The study also showed that the push out process, where the piston displace the cylinder content after inlet port closing (IPC) has a significant influence on the scavenging process.

Further, the CFD model results was compared with a theoretical perfect displacement model with good agreement. The theoretical model did not include the mixing between the scavenge air and the exhaust gas, but it showed that the volumetric part of the scavenging process is dominated by a perfect displacement of the exhaust gas with the scavenge air.

Nomenclature

$\boldsymbol{\rho}$	Density
$\boldsymbol{u_i = [u_1, u_2, u_3]}$	Velocity
$\boldsymbol{x_i = [x_1, x_2, x_3]}$	Cartesian coordinates
$\boldsymbol{p}$	Pressure
$\boldsymbol{h}$	Enthalpy
$\boldsymbol{\tau_{i,j}}$	Viscous stress tensor
$\boldsymbol{F}$	Body forces
α_{eff}	Effective thermal diffusivity
$\boldsymbol{\mu_{eff}}$	Effective dynamic viscosity
$\boldsymbol{\delta_{i,j}}$	Kronecker delta
$\mathbf{s}$	Passive scalar
$\boldsymbol{\nabla p_{engine}}$	Scavenging gradient
$\boldsymbol{\psi}$	Bulk purity of air
$\boldsymbol{DR}$	Delivery ratio
$\boldsymbol{\eta_{scav}}$	Scavenging efficiency
$\boldsymbol{m_{scav}}$	Mass of scavenge air
$\boldsymbol{t_{scav}}$	Scavenging time
$\boldsymbol{p_{scav}}$	Scavenging pressure
$\boldsymbol{p_{exhaust}}$	Exhaust pressure
$\boldsymbol{V_{IPC}}$	Cylinder volume at IPC
$\boldsymbol{V_{EVC}}$	Cylinder volume at EVC
$\boldsymbol{V_{ref}}$	Reference volume
$\boldsymbol{\rho_{scav}}$	Density of scavenge air
$\boldsymbol{\rho_{ex}}$	Density of exhaust air

References

1. Percival WH, Method of scavenging analysis for 2-cycle diesel engines, Society of Automotive engineers-papers, Vol 63, pp. 737-751, 1955
2. Ferro, A. Investigation by means of models into the scavenging of two-stroke internal combustion engines, The engineers' Digest, Vol 19, 1958, pp.512-522
3. JB, Heywood and E, Sher, The Two-stroke cycle engine: its Development, Operation and Design, Taylor and Francis, Philidelphia, 1999.
4. Sher. E, Hossain. I, Zhang. Q and winterbone. D.E, Calculations and Measurments in the Cylinder of a Two-Stroke Uniflow-Scavenged Engine Under Steady Flow Conditions, Experimental Thermal and Fluid Science, pp.418-431, 1991
5. Litke.B, The influence of inlet angles in inlet ports on the scavenging process in two-stroke uniflow-scavenged engine, Marine technology III Volume 45, 1999
6. Haider. S, Experimental and Numerical Study of Swirling Flow in Scavenging Process for 2-Stroke Marine Diesel Engines, Ph.D. thesis, Technical University of Denmark, 2011
7. Ingvorsen K. M, Meyer K. E. Walther J. H, Mayer S, Turbulent swirling flow in a model of a uniflow scavenged two-stroke engine, Experiments of Fluids-2013, Volume 54, Issue 3, pp 1-7
8. Ingvorsen K. M. Meyer K. E. Walther J. H, Phase-locked stereoscopic PIV measurements of the turbulent swirling flow in a dynamic model of a uniflow-scavenged two-stroke engine cylinder, Proceeding of the 10th International Symposium on Particle Image Velocimetry. TU Delft, 2013
9. Nakagawa. H, Kato. S, Tataishi. M, Adachi. T, Tsujimura.H and Nakashima.M, Airflow in the Cylidner of a 2-stroke Cycle Uniflow Scavenging Diesel Engine During compression Stroke. Japan society of mechanical engineers, Series III, Vol 3, No 3, 1990.
10. Sigurdsson. E. Scavenging flow in a Two-Stroke Diesel Engine, Master thesis, Technical University of Denmark, 2011
11. Al-Mousawi N,M,J. Numerical Simulation in a model Diesel engine using RANS and LES turbulence models. Master thesis, Technical University of Denmark, 2012
12. Lamas. I.L. and Vidal. C.G.R, Computational Fluid Dynamics Analysis of the Scavenging Process in the MAN B&W 7S50MC Two-Stroke Marine Diesel Engine, Journal of Ship Research, vol 56, pp. 154-161, 2012
13. Andersen F. H. Hult J. Nogenmyr K-J. and Mayer S. Numerical investigation of the Scavenging Process in Marine Two-stroke Diesel Engines, SAE technical paper (2013-01-2647), SAE Powertrain, Fuels and lubricants meeting, Seoul Korea, 2013.
14. Hult.J, Mayer.S, A methodology for laser diagnostics in large-bore two-stroke diesel engines, Measurement Science and Technology, 2013, doi:10.1088/0957-0233/24/4/045204

15. Mayer.S, Clausen.S, Hult.J, Nogenmyr.K.J, Advanced optical development tools for two-stroke marine diesel engines. CIMAC conference 2013, paper 53. 2013
16. Stone, R. Introduction to Internal Combustion Engines. Macmillan press LTD, 1999.
17. Heywood, J.B. Internal Combustion Engine Fundamentals, McGraw-Hill Book Company,1988
18. OpenFOAM User Guide Version 1.6, 14.July 2009. OpenCFD LDT. (www.openfoam.org) (www.extend-project.de)
19. Favre.A, Equations des gaz turbulent compressibles, Journal de Mechanique, vol 4, pp.361-421, 1965
20. Ferziger J.H, Peric M. Computational Methodes for Computional Fluid Dynamics. Third edition, Springer, 2002.
21. Rutland, C.J. Large-eddy simulations for internal combustion engines-a review. International Journal of Engine Research, 2011.
22. Gupta, A.K. Lilley, D.G, Syred, N. Swirl Flows. Turnbridge Wells, Kent, Abacus press, 1984
23. Oliver, Todd A. Favre-Averaged Navier-Stokes and Turbulence Model Equations Documentation. Predictive Engineering and Computational sciences, University of Austin Texas. 2009.
24. White, Frank M. Viscous Fluid Flow, Third edition, McGraw Hill, International edition, 2006.
25. Yakhot, V., Orszag, S.A., Thangam, S., Gatski, T.B. & Speziale, C.G. (1992), "Development of turbulence models for shear flows by a double expansion technique", Physics of Fluids A, Vol. 4, No. 7, pp1510-1520.
26. Ingvorsen KM, Meyer KE, Walther JH, Mayer S. 2014. Turbulent swirling flow in a dynamic model of a uniflow-scavenged two-stroke engine. Experiments in Fluids. 55. Available from: 10.1007/s00348-014-1748-y
27. Hemmingsen C.S Numerical Simulation of Convective Heat Transfer During Scavenging in a Model Diesel Engine. M.Sc. thesis, Technical University of Denmark 2014.
28. Andersen FH, Hult J, Nogenmyr K-J, Mayer S. CFD analysis of the scavenging process in marine two-stroke diesel engines. In Proceedings of the ASME 2014 Internal Combustion Engine Division Fall Technical Conference (ICEF 2014). American Society of Mechanical Engineers. 2014. ICEF2014-5438.
29. E. Sher. Scavenging the Two-Stroke engine. Prog. Energy Combust. Sci., 16(2):95-124, 1990

Acknowledgments

The author would like to thank:
The Danish minestry of science, innovation and higher education for partially funding the industrial Ph.D. project.

Internal combustion engine group (ICEG), Dipartemento di Energia, Politecnico Di Milano for engine mesh motion class in OpenFOAM

Bibliography

Noufil Malik Jaffir Kadhum Al-Mousawi. Numerical simulation of swirling flow in a model diesel engine using RANS and LES turbulence models. Master's thesis, Technical University of Denmark, September 2012.

F. Andersen, J. Hult, K. Nogenmyr, and S. Mayer. Numerical investigation of the scavenging process in marine two-stroke diesel engines. In *SAE/KSAE 2013 International Powertrains, Fuels & Lubricants Meeting*, pages Paper No. 2013–01–2647, Seoul, South Korea, October 2013. SAE.

F. H. Andersen and S. Mayer. Parametric study of the scavenging process in marine two-stroke diesel engines. In *Proceedings of the ASME 2015 Internal Combustion Engine Division Fall Technical Conference, Americal Society of Mechanical Engineers (ASME)*, 2015.

F. H. Andersen, J Hult, K-J. Nogenmyr, and S. Mayer. CFD analysis of the scavenging process in marine two-stroke diesel engines. In *Proceedings of the ASME 2014 International Combustion Engine Division Fall Technical Conference, ICEF2014*, Columbus, Indiana, October 19-22 2014. ASME.

M. Beudoin and H. Jasak. Development of a generalized grid interface for turbomachinery simulations with openfoam. In *Open Surce CFD international conference*, 2008.

Gordon P. Blair. *Design and Simulation of Two-Stroke Engines.* SAE International, 400 Commonwealth Drive, Warrendale, 1996.

Michael A. Boles Cengel, Yunus A. and. *Thermodynamics, an engineering approach, sixth edition.* McGraw-Hill, 2007.

J.J. Corbett. Marine transportation and energy use. *Encyclopedia of Energy, edited by C.J Cleveland, pp. 745-748, Elesiver Science, San Diego, CA.*, 2004.

Nabi Dedeoglu. Scavenging model solves problems in gas burning engine. *SAE Tech. Paper Ser.*, page Paper No. 710579, 1971.

A. Favre. Equations des gaz turbulent compressibles. *Journal de Mechanique*, 4:361–421, 1965.

A. Ferro. Investigation by means of models into scavenging of two-stroke internal combustion engines. *Eng. Dig.*, 19(12):519–522+512, 1958.

Joel H. Ferziger and Milovan Perić. *Computational Methods for Fluid Dynamics.* Springer-Verlag, 1996.

A. K. Gupta, D. G. Lilley, and N. Syred. *Swirl Flows.* Abacus Press, 1984.

S. Haider, T. Schnipper, A. Obeidat, K. E. Meyer, V. L. Okulov, S. Mayer, and J. H. Walther. PIV study of the effect of piston position on the in-cylinder swirling flow during the scavenging process in large two-stroke marine Diesel engines. *J. Mar. Sci. Tech.*, 18:133–143, 2013. doi: 10.1007/s00773-012-0192-z.

Sajjad Haider. *Swirling flow in scavenging process for two-stroke Diesel engines.* Ph.D. thesis, Technical University of Denmark, May 2011.

Casper Schytte Hemmingsen. Numerical simulation of convective heat transfer during scavening in a model diesel engine. Master's thesis, Technical University of Denmark, February 2014.

J. B. Heywood. *Internal combustion engine fundamentals.* McGraw Hill, Inc., 1988.

J. B. Heywood and E. Sher. *The two-stroke cycle engine: Its development, operation, and design.* Taylor & Francis, 1999.

J . Hult, S. Matlok, and S. Mayer. Particle image velocimetry measurements of swirl and scavenging in a large marine two-stroke diesel engine. In *SAE Techincal Paper 2014-01-1173*, 2014.

J. Hult and S. Matlok. In-cylinder velocity measurements of swirl and scavenging using piv. Internal LDF1-report, not published, June 2013.

M. Peric I. Demirdzic. Scalar conservation law in finite volume calculations of fluid flow. *International Journal for Numerical Methods in Fluids*, 1988.

Holt. Julie. Ring-Hansen Ingenioren. Man's gigantiske slaglaengde skaerer syv procent af forbruget. *Nyhedsmagasinet Ingenioeren*, 02.05.2014.

K. M. Ingvorsen, K. E. Meyer, J. H. Walther, and S. Mayer. Turbulent swirling flow in a model of a uniflow-scavenged two-stroke engine. *Exp. Fluids*, 54(3): 1494, 2013.

K. M. Ingvorsen, K. E. Meyer, J. H. Walther, and S. Mayer. Turbulent swirling flow in a dynamic model of a uniflow-scavenged two-stroke engine. *Exp. Fluids*, 55:1748, 2014.

Kristian Mark Ingvorsen. *Investigations of the turbulent swirling flow in a two-stroke marine diesel engine.* PhD thesis, Department of Mechanical Engineering. Technical University of Denmark, November 2013. Unpublished.

International Maritime Organization. *Revised Marpol Annex VI: Regulations for the Prevention of Air Pollution from Ships and No_x Technical Code 2008.* International Maritime Organization, London, 2009.

H. Jasak. *Error analysis and estimation for the finite volume method with applications to fluid flows.* PhD thesis, Department of mechanical engineering, Imperial College of science, Technology and Medicin, University of London, 1996.

Hrvoje. Jasak. Turbo tools and genreal grid iterface, theoretical basis and implementation. In *Sixt OpenFOAM Workshop, Penn State University 13-16 June*, 2011.

W. P. Jones and B. E. Launder. The prediction of laminarization with a two-equation model of turbulence. *Int. J. Heat Mass Transfer*, 15:301–314, 1972.

Maria Isabel Lamas and Carlos Gervasio Rodriguez Vidal. Computational fluid dynamics analysis of the scavenging process in the MAN B&W 7S50MC two-stroke marine Diesel engine. *J. Ship. Res.*, 56(3):154–161, 2012.

Benedykt Litke. The influence of inlet angles in inlet ports on the scavenging process in two-stroke uniflow-scavenged engine. *Mar. Tech. III*, 45:247–252, 1999.

O. Lucca-Negro and T. O'Doherty. Vortex breakdown: a review. *Prog. Energy Combust. Sci.*, 27:431–481, 2001.

MAN Diesel & Turbo. Various internal documents, presentations and course material. 2015.

Hiroshi Nakagawa, Satoshi Kato, Mataji Tateishi, Takeshi Adachi, Harutaka Tsujimura, and Masayoshi Nakashima. Airflow in the cylinder of a 2-stoke cycle uniflow scavenging diesel engine during compression stroke. *Jpn. Soc. Mech. Eng.*, 33(3):591–598, 1990.

Anas Obeidat, Teis Schnipper, Kristian M. Ingvorsen, Sajjad Haider, Knud Erik Meyer, Stefan Mayer, and Jens H. Walther. Large eddy simulations of the influence of piston position on the swirling flow in a model two-stroke diesel engine. *Int. J. Num. Meth. for Heat & Fluid Flow*, 24(2):325–341, 2014.

OpenFOAM-UserGuide. *OpenFOAM UserGuide Version 1.6, 14. July 2009 OpenCFD LTD. (www.openfoam.org), (www.extend-project.de), (C++ source Code).*

W. H. Percival. Method of scavenging analysis for 2-stroke-cycle diesel cylinders. *SAE Trans.*, 63:737–751, 1955.

U. Piomelli. Lare-eddy simulation of turbulent flows, part one: Introduction. Lectrure notes for the course: "Large Eddy Simulation and related techniques: Theory and applications", Von Karmann Institute for Fluid Dynamics, February 6-10 2012.

Stephan. B. Pope. *Turbulent Flows.* Cambridge University Press, 2000.

A. McDonald R. Fox and P. Pritchard. *Introduction to Fluid Mechanics.* John Wiley and Sons, Inc, 2004.

W. Rizk. Experimental studies of mixing processes and flow configurations in two-cycle engine scavenging. *Proc. Inst. Mech. Eng.*, 172(10):417–427, 1958.

E Sher. Scavenging the two-stroke engine. *Prog. Energy Combust. Sci.*, 16(2): 95–124, 1990.

E. Sher, I. Hossain, Q. Zhang, and D. E. Winterbone. Calculation and measurements in the cylinder of a two-stroke uniflow-scavenged engine under steady flow conditions. *Exp. Therm. Fluid Sci.*, 4:418–431, 1991.

E. Sigurdsson, K. M. Ingvorsen, M. V. Jensen, S. Mayer, S. Matlok, and J. H. Walther. Numerical analysis of scavenge flow and convective heat transfer in large two-stroke marine diesel engines. *Appl. Energy*, 123:37–46, 2014.

Ole Soerensen. *B&W-dieselmotorens historie, 1898-2008.* Diesel House, 2008.

R. Stone. *Introduction to internal combustion engines.* MacMillian Press LDT, 1999.

Nak Won Sung and Donald J. Patterson. Air motion in a two stroke engine cylinder — the effects of exhaust geometry. *SAE Trans.*, pages 2534–2544, 1982. Paper No. 820751.

Frank M. White. *Viscous Fluid Flow.* McGraw Hill, Inc., 3. edition, 2006.

D. C. Wilcox. *Turbulence modeling for CFD.* DWC Industries, 2 edition, 1998.

D. F. Woodyard. *Pounder's marine diesel engines and gas turbines.* Elsevier/Butterworth-Heinemann, 9 edition, 2009.

V. Yakhot, S. A. Orszag, S. Thangam, T. B. Gatski, and C. G. Speziale. Development of turbulence models for shear flows by a double expansion technique. *Phys. Fluids*, 4(7):1510–1520, 1992.

DTU Mechanical Engineering
Section of Fluid Mechanics, Coastal and Maritime Engineering
Technical University of Denmark

Nils Koppels Allé, Bld. 403
DK- 2800 Kgs. Lyngby
Denmark
Phone (+45) 4525 1360
Fax (+45) 4588 4325
www.mek.dtu.dk
ISBN: 978-87-7475-433-6

DCAMM
Danish Center for Applied Mathematics and Mechanics

Nils Koppels Allé, Bld. 404
DK-2800 Kgs. Lyngby
Denmark
Phone (+45) 4525 4250
Fax (+45) 4593 1475
www.dcamm.dk
ISSN: 0903-1685